N 69 14338
NASA CR 98593

# UNIVERSITY OF

# MARYLAND

THERMALLY INSENSITIVE DETERMINATIONS OF TRANSITI
PROBABILITIES FOR CI , OI , NeI , AℓII , SiI ,
SiII , PI , PII , SI , SII , and CO*

CASE FILE COPY

by

Myron Howard Miller

University of Maryland
College Park, Maryland

## THE INSTITUTE FOR FLUID DYNAMICS

*and*

## APPLIED MATHEMATICS

OCT 1968
RECEIVED
NASA STI FACILITY
INPUT BRANCH

Technical Note BN-550 May, 1968

# THERMALLY INSENSITIVE DETERMINATIONS OF TRANSITION PROBABILITIES FOR CI , OI , NeI , AℓII , SiI , SiII , PI , PII , SI , SII , and CI*

CASE
CO

by

Myron Howard Miller

University of Maryland
College Park, Maryland

* Research supported primarily by NASA Grant NsG-359 (astronomy Program, Office of Space Science and Application). Publication of this 200 copy edition was supported by the National Science Foundation Grant NSF GP-8325.

This report was also a dissertation submitted in partial fulfillment of the requirements for the degree of Doctor of Philosophy in The University of Maryland, 1968.

ABSTRACT

Title of Thesis: Thermally Insensitive Determinations of Transition Probabilities for CI , OI , NeI , AℓII , SiI , SiII , PI , PII , SI , SII , and CℓI .

Myron H. Miller, Doctor of Philosophy, 1968

Thesis directed by: Research Associate Professor, Thomas D. Wilkerson

Absolute transition probabilities were measured for more than 150 lines in the visible spectra of CI, OI, NeI, AℓII, SiI, SiII, PI, PII, SI, SII and CℓI . Results varied in accuracy between 10% - 45%, being typically 20% for the stronger lines of each element studied. Stark widths were measured for 24 neutral lines and 28 ion lines. Stark shifts were also measured for 15 of 24 neutral lines.

The spectroscopic source was a luminous gas-driven shock tube, normally operated at temperatures 9,000-13,000°K and at pressures $5\text{-}40\times10^{6}$ dyne $cm^{-2}$. Electron densities varied over the range 2.5-$12\times10^{16}cm^{-3}$. Photographic and multi-channel photoelectric recording were simultaneously employed for time-resolved spectroscopy. Two independent methods of absolute intensity calibration were used: one was the traditional method relying on the DC carbon arc, and the other was a new method which relies on basic atomic parameters rather than laboratory standards. The thermodynamic state of the shock tube plasma was deduced from redundant data. Temperature was simultaneously measured four independent ways, using the following observations:

absolute integrated intensities of $H_\beta$ and NeI $\lambda 5852$ , the half-width of $H_\beta$ , and either the slit-integrated intensity from an optically thick portion of $H_\alpha$ or a line-reversal intensity. Absolute pressures were recorded with calibrated quartz transducers and compared with those predicted from measured shock speeds and real-gas thermodynamics. Most spectra were studied using two or three types of test gas and a variety of plasma temperatures and pressures.

Current results contain very little implicit dependence on measured source temperatures because they were deduced by "thermal balancing" -- a technique we have developed for circumventing the critical sensitivity of excited level populations to thermal errors.

The majority of our A-values agree with Coulomb approximations to within 30%. Results for 4s-4p transitions in SiI , PI and SI are factors of 2-8 smaller than predicted by Coulomb approximations. Marked departures from LS coupling are observed in the spectra of SiI, PII and SII . Stark broadening of neutral lines generally agrees with theory to better than 10%; while some ion lines agree with current theories to within 30%, others disagree by factors as large as 8.

ACKNOWLEDGMENTS

I wish to express my thanks to Professor T.D. Wilkerson for suggesting this thesis topic and for his advice throughout the experiment. The author's colleague, Roger Bengtson, participated in much of the work reported here, and his help, advice, and his checking of a great many calculations are gratefully acknowledged. I also value several discussions with Drs. R. Grieg, H. Griem and G. Charatis. I also would like to thank Messrs. G. Monahan and S. McPhillips for help with the experimental work, and Messrs. R. Roig and L. Goldstein for their attention to detail in the reduction of photographic data. I also appreciate the help of Dr. G. Oertel and Messrs. P.W. Murphy and M.W. Smith, whose computer calculations gave us theoretically predicted A-values for comparison purposes, and Dr. D. Koopman who initiated the computer coding of Rankine-Hugoniot calculations.

My appreciation also to Mrs. Francine Knox for the care she took in the typing of this thesis and to Mr. James Kempton who prepared the figures. I recall gratefully the craftsmanship and ingenuity of Mr. E. Grossenbacher and his staff in the building of the equipment. Thanks are also due to the Sand and Gravel Institute, University of Maryland, for their assistance in constructing the shock tube.

I thank my wife, Magdalene, for her patience and good humor during this protracted work.

Also, the author wishes to acknowledge N.A.S.A.'s support of this research under grant NSG-359, monitored by Dr. N. Roman, Astronomy Program, Office of Space Science and Applications.

TABLE OF CONTENTS


| Chapter | | Page |
|---|---|---|
| I. | INTRODUCTION AND OUTLINE OF DISSERTATION | 1 |
| | A. Introduction | 1 |
| | B. Review of Experimental A-Value Determinations | 2 |
| | C. Outline of Principle Results | 7 |
| | D. Outline of the Dissertation | 12 |
| II. | SUMMARY AND APPLICATION OF SPECTROSCOPIC THEORY | 15 |
| | A. Introduction | 15 |
| | B. Optically Thin Lines | 15 |
| | C. Formulation for Finite Optical Depth | 21 |
| | D. Utilization of Absolute Intensity Standards in A-Value Determinations | 28 |
| | E. Influence of Spectrograph Slit Widths on Accuracy of A-Value Determinations | 31 |
| III. | METHOD OF THERMALLY INSENSITIVE BALANCING | 33 |
| | A. Introduction | 33 |
| | B. Conceptual Outline of the New Methods | 34 |
| | C. Introductory TIB Example: the Line CI λ5052Å | 37 |
| | D. General Applicability of TIB to the Study of Light Elements | 47 |
| | E. Prospects for Extension of TIB to Other Laboratory Sources, Wavelength Regions and Plasma Temperatures | 67 |
| IV. | SPECTROSCOPICALLY ORIENTED DESCRIPTION OF THE LUMINOUS SHOCK TUBE | 69 |
| | A. Introduction | 69 |
| | B. Shock Tube Operation | 72 |

Chapter | Page


C. Hydrodynamic Predictions Compared with Direct Measurements on the Thermodynamic State of Reflected Shocks ..... 75

D. Spectroscopic Consequences of Breakdowns in the 1-D Flow Model ..... 82

E. Tailoring of Shock Conditions for Optimal Spectroscopic Observations ..... 87

V. EQUIPMENT ..... 93

A. The Shock Tube ..... 93

1. General Description and Design Considerations .... 93

2. Construction Details ..... 97

3. Diaphragm Selection, Preparation and Performance.. 104

4. Gas Delivery and Evacuation Systems and Equipment for Handling Driver Gas ..... 110

5. The Vacuum System ..... 112

6. Test Gas Handling Equipment ..... 115

B. Diagnostics ..... 117

1. Spectroscopic Instrumentation ..... 117

2. Pressure Transducers ..... 126

VI. EXPERIMENTAL METHOD ..... 128

A. Introduction ..... 128

B. Absolute Photometry ..... 129

1. Introduction ..... 129

2. Linearity Checks ..... 129

3. Absolute Intensity Calibration Using the A-value and Shape Function of $H_\alpha$ as Absolute Standards . 136

4. Absolute Intensity Calibrations Using the Carbon Arc ..... 141

Chapter Page


5. Comparison of Absolute Intensity Calibrations From the Carbon Arc With the New Internal Method ..... 143

6. Calibration of Photographic Emulsions ..... 146

7. Simultaneous Photographic and Photoelectric Measurement of CI $\lambda$5052 Integrated Intensity ... 151

8. Method of Recording Absolute Integrated Intensities of $H_\alpha$, $H_\beta$, NeI $\lambda$5852 and Lines Studied for A-values ..... 154

C. Temperature Measurements ..... 155

1. Introduction ..... 155

2. Measurement of $T_{neon}$ ..... 159

3. Measurement of $T_{\lambda\frac{1}{2}}$ ..... 160

4. Measurement of $T_\beta$ ..... 161

5. Measurement of $T_\alpha$ ..... 162

6. Comparison of the Redundant Temperature Measurements ..... 163

7. Reversal Temperatures and Shock Speed Temperature ..... 164

D. Pressure Measurements ..... 166

1. Calibration ..... 166

2. Measurements Behind the Reflected Shock ..... 166

E. Redundant Measurement of Electron Density ..... 168

F. Methods for Deducing Concentrations of Plasma Impurities ..... 171

G. Observations Supporting the Assumption of LTE ..... 173

H. Sample Data from a Typical Shock Tube Run ..... 174

Chapter | Page


VII. RESULTS ..... 177

A. Introduction ..... 177

B. Estimation of Experimental Errors ..... 181

C. Monitor on Overall Accuracy: Measured $H_\beta$ Transition Probability ..... 185

D. Transition Probabilities for CI ..... 187

1. Introduction ..... 187

2. Selection, Execution and Reduction of Data Runs .. 189

3. Results ..... 196

4. Check for Systematic Error: Invariance of Results with Changing Experimental Parameters .... 198

5. Comparison Between Present CI Results and the Literature ..... 202

E. SI and SII Transition Probabilities ..... 205

1. Introduction ..... 205

2. Design, Execution and Reduction of Data Runs ..... 205

3. Results ..... 213

4. Checks for Internal Consistency ..... 213

5. Comparison of Current SI and SII Results with Literature Values ..... 220

F. Transition Probabilities for SiI and SiII ..... 226

1. Introduction ..... 226

2. Selection of Methods, Experimental Problems, and Reduction of Data ..... 230

3. Results for Transition Probabilities of SiI and SiII ..... 238

4. Checks for Internal Consistency ..... 240

5. Comparison with Literature Values ..... 240

Chapter Page

G. Transition Probabilities for PI and PII ..... 247

1. Introduction ..... 247

2. Design, Execution and Reduction of Experimental Runs ..... 251

3. Checks for Internal Consistency ..... 256

4. Results ..... 256

5. Comparison of PI and PII Results with Literature Values ..... 256

H. Transition Probabilities for Selected Visible Lines of OI, NeI, AℓII, and CℓI ..... 257

1. Introduction ..... 257

2. Transition Probabilities for OI ..... 257

3. Transition Probabilities for NeI ..... 261

4. Transition Probability for AℓII λ5593.2 ..... 264

5. Transition Probability for CℓI λ4601.0 ..... 266

I. Stark Widths and Shifts for Neutral Lines ..... 267

1. Introduction ..... 267

2. Method ..... 272

3. Results ..... 277

J. Stark Broadening of Ion Lines ..... 282

1. Introduction ..... 282

2. Method ..... 283

3. Results and Discussion ..... 288

K. Relative Stark Widths of $H_\beta$ and $H_\gamma$ ..... 295

Chapter Page

VIII. CONCLUSIONS AND CRITIQUE ..... 300

A. Conclusions ..... 300

B. Critique of the Experiments Design ..... 308

C. Suggestions for Future Work ..... 309

SELECTED BIBLIOGRAPHY ..... 311

LIST OF TABLES


| Table | | Page |
|---|---|---|
| I. | COMPARISON OF ERROR PROPAGATION AND SCATTER FOR DIFFERENT METHODS OF OBTAINING PLASMA TEMPERATURE | 156 |
| II. | SCOPE OF RESULTS FOR A-VALUES | 178 |
| III. | TRANSITION PROBABILITIES STUDIED, ARRANGED BY WAVELENGTH | 179 |
| IV. | TRANSITION PROBABILITIES FOR CI | 197 |
| V. | COMPARISON OF MEASURED CI TRANSITION PROBABILITIES WITH LITERATURE VALUES | 203 |
| VI. | TRANSITION PROBABILITIES FOR MERGED SI MULTIPLETS | 214 |
| VII. | COMPARISON OF MEASURED SI TRANSITION PROBABILITIES WITH LITERATURE VALUES | 215 |
| VIII. | TRANSITION PROBABILITIES FOR SII | 216 |
| IX. | COMPARISON OF MEASURED SII TRANSITION PROBABILITIES WITH LITERATURE VALUES | 222 |
| X. | COMPARISON OF MEASURED SII LINE STRENGTHS TO STRENGTHS PREDICTED BY LS COUPLING AND INTERMEDIATE COUPLING | 224 |
| XI. | TRANSITION PROBABILITIES FOR SiI AND SiII | 239 |
| XII. | COMPARISON OF SiI TRANSITION PROBABILITIES WITH LITERATURE VALUES | 241 |
| XIII. | APPLICATION OF CURRENT RESULTS TO SiI SOLAR ABUNDANCE DETERMINATIONS, SHOWING DECREASED SCATTER FROM IMPROVED RELATIVE gf VALUES | 243 |
| XIV. | COMPARISON OF SiII TRANSITION PROBABILITIES WITH LITERATURE VALUES | 246 |
| XV. | TRANSITION PROBABILITIES FOR PI | 253 |
| XVI. | TRANSITION PROBABILITIES FOR PII | 254 |

| Table | | Page |
|---|---|---|
| XVII. | COMPARISON OF PI AND PII TRANSITION PROBABILITIES WITH COULOMB APPROXIMATIONS ..... | 255 |
| XVIII. | TRANSITION PROBABILITIES FOR OI, NeI, AℓII AND CℓI ..... | 258 |
| IXX. | TOTAL STARK SHIFTS AND WIDTHS FOR NEUTRAL LINES ..... | 278 |
| XX. | COMPARISON OF SII TOTAL STARK WIDTHS WITH LITERATURE VALUES ..... | 289 |
| XXI. | MEASURED STARK WIDTHS FOR STRONG ION LINES, INCLUDING COMPARISON WITH PREDICTED VALUES ..... | 292 |
| XXII. | RELATIVE LINE STRENGTHS WITHIN MULTIPLETS: PRESENT RESULTS COMPARED WITH LS COUPLING ..... | 306 |

LIST OF FIGURES


| Figure | | Page |
|---|---|---|
| 1. | Excited State Number Density of $H_\beta$ as a Function of Temperature and Pressure | 18 |
| 2. | Excited State Number Density of CI λ5052 as a Function of Temperature and Pressure | 19 |
| 3. | Effect of Readily Ionized Impurity Upon the Excited State Number Density of CI λ5052 | 22 |
| 4. | Absolute Intensity of the Central Portion of $H_\alpha$ as a Function of Plasma Temperature | 27 |
| 5. | Excited State Densities and Ratios of Excited State Densities as Functions of Temperature in a Typical Shock Tube Plasma | 36 |
| 6. | Relative Thermal Error Propagation in A-Value of CI λ5052 Measured Three Ways: $AE_c$ (Absolute Emission), $ARH_c$ (Trans-Species Relative to $H_\beta$) and $\frac{1}{2}[AE_c+ARH_c]$ (Thermally Insensitive Method) | 39 |
| 7. | Thermal Error in Results of Two Hypothetical Experiments Each Measuring the A-Value of CI λ5052 in a Variety of Ways | 41 |
| 8. | Current Results for the Transition Probability of CI λ5052: Data From First-Reflected Shocks Using $1\%CH_4$ or $\frac{1}{2}\%CH_4 + \frac{1}{2}\%CS_2$ Additives | 44 |

Figure | Page


9. Reduction in Scatter Due to TIB for an Experiment Employing a Single Means of Temperature Determination: Data for 37 Runs Shown in Figure 8 Re-Evaluated Using $T = T_{neon}$ Rather Than $\tilde{T} = T = \frac{1}{4}(T_{neon} + T_{\alpha} + T_{\beta} + T_{\lambda\frac{1}{2}})$ ..... 48

10. Dependence of Thermal Balancing, $A(TIB)_C = [AE_C + ARH_C]$, Upon Absolute Plasma Pressure ..... 49

11. Dependence of Thermal Balancing on Concentration of Spectroscopic Additive Gas ..... 50

12. Dependence of Thermal Balancing on True Source Temperature: Relative Thermal Sensitivity in A(TIB)=(AE+ARH) for CI λ5052 and for SI λ4695 at $T_o$ = 10,000°K, 11,000°K and 12,000°K ..... 52

13-A. Relative Thermal Sensitivity in the A-Value of CI λ5052 Measured Five Ways, at 10,000°K True Source Temperature ..... 54

13-B. Relative Thermal Sensitivity in the A-Value of CI λ5052 Measured Five Ways, at 11,600°K True Source Temperature ..... 55

14. Thermal Balancing of SI λλ4695 Using the Trans-Species Measurement Relative to CI λ5052, $ARC_{SI}$ ..... 60

15. Relative Thermal Error in the A-Value of PII λ5253 Measured Four Ways ..... 63

16. Relative Thermal Error in the A-Value of AℓII λ5593 Measured Four Ways ..... 64

Figure | Page

17. Schematic Correlation Between Shock Tube Flows and Time-Resolved Spectroscopy Near the End Wall ..... 73

18. Rankine-Hugoniot Predictions for a Typical Spectroscopic Variable: The Excited State Density of $H_\beta$ Displayed as a Function of Incident Shock Speed ..... 77

19. Comparison of Temperatures for First-Reflected Shocks: Average of Four Independent Direct Determinations, $\tilde{T}$ , vs. Rankine-Hugoniot Predictions, $T(S_1)$ , Based on Observed Incident Shock Speed ..... 79

20. Measured Pressure Behind First-Reflected Shocks (Quartz Transducers) vs. Pressures Predicted from Rankine-Hugoniot Equations (Including Real Gas Effects) Using Measured Incident Shock Speeds ..... 80

21. Measured Incident Shock Speed as Function of Initial Pressure Ratios Across Diaphragm: Hydrogen Driver Gas into Neon + 1% Light Hydrocarbon ..... 89

22. Maximum Excited State Densities Attainable With Current Apparatus as Function of Test Gas Initial Pressure ..... 91

23. Maximum Excited State Density of CI λ5052 Attainable With Current Apparatus as Function of Spectroscopic Additive Gas Concentration in Neon Carrier Gas ..... 92

24. The Shock Tube, Viewed From the Rear of the Driver Section ..... 94

25. The Test Section; "SQUID" in Background ..... 95

| Figure | | Page |
|---|---|---|
| 26. | Schematic Cross Sectional Views of Shock Tube Driver and Expansion Sections | 99 |
| 27. | Dorsal View of Expansion Section, Showing Method of External Reinforcement, a Typical Test Port, and a Blank Diagnostic Plug | 100 |
| 28. | Face of the Breech Section, Before Installation of Catcher (right), and, Driver Flange, Showing Union of Thin-Walled Tube (left) | 102 |
| 29. | Diaphragm Breaking Pressures as a Function of (Scribe Depth/Thickness), with Method of Scribing, Material, and Diaphragm Thickness as Parameters | 106 |
| 30. | Spent Diaphragms, Without Catcher Installed (left) and with Catcher Installed (right) | 108 |
| 31. | Reproducability of Breaking Pressure for Two Types of Diaphragm Scribe Preparation | 109 |
| 32. | Cut-Away View of 4" Main Valve | 111 |
| 33. | Schematic Representation of Shock Tube and Associated Gas Handling Equipment | 113 |
| 34. | Apparatus for Time-Resolved Spectroscopy of Shock Tube Plasmas | 118 |
| 35. | Schematic Representation of Photoelectric Sequential Image Divider ("SQUID") | 120 |
| 36. | Two Types of Quartz Transducer Installations Used to Minimize Ringing Amplitudes During Shocks | 127 |

Figure Page


37. Schematic CRT Display Showing Slit-Integrated $H_\alpha$ Intensity and Line Reversal on $H_\alpha$ ..... 130

38. Optics to Illuminate Spectrograph for Absolute Intensity Calibrations ..... 131

39. Absolute Intensity Calibration Using $H_\alpha$ as Internal Standard: Reversal Intensity vs.(Slit Averaged $H_\alpha$ Intensity/Reversal Intensity)..... 137

40. Comparison of Independent Absolute Intensity Calibrations: Reversal Intensities (In Units of Carbon Arc Intensity) Calibrated by Slit-Averaged Emission Coefficient of $H_\alpha$ vs. Values Calibrated by Direct Comparison Against the Carbon Arc ..... 145

41. Fitting of Photographic Relative Intensities to Simulteneously Recorded Absolute Intensities of 8 Photoelectric ("SQUID") Channels ..... 148

42. Comparison of Simultaneous Measurements of Integrated Absolute Intensity of CI λ5052: Wing-Corrected Photoelectric Recording vs. "SQUID" Calibrated Photographic Recording ..... 153

43. Comparison of Four Simultaneous Temperature Measurements in First-Reflected Shocks ..... 158

44. Comparison of Electron Densities Deduced From the $H_\beta$ Half-width with Electron Densities Computed From Measured Temperatures and Pressure ..... 170

45. Typical Data From One Shock Tube Firing ..... 175

Figure | Page


46. Monitor for Overall Experimental Accuracy: A-Value of $H_\beta$ Measured Simultaneously with Data for A-Values of CI, SI and SII ..... 186

47. Densitometer Tracings, 4750Å - 5100Å, for Three Successive Steady State Regions Recorded During a Single Shock Tube Firing ..... 188

48. Grotrian Diagram for CI Lines Currently Studied ..... 190

49. Uncertainty in Line Intensity, $\Delta I_L(\lambda)/I_L(\lambda)$ , Arising from Emulsion Grain, Shown as a Function of Specular Transmission ..... 192

50. Results for Some CI A-Values Measured Relative to CI λ5052 ..... 195

51. Testing A-Value of CI λ5052 Results for Possible Systematic Dependance Upon Measured Thermodynamic Variables ..... 199

52. Testing A-Value of CI λ5052 Results for Possible Systematic Dependance Upon Operational Variables ..... 201

53. Time-Resolved Spectrogram of Shock in ½% $CH_4$ + ½% $CS_2$ + 99% Neon ..... 206

54. Grotrian Diagram for SI Lines Currently Studied ..... 207

55. Results for the Absolute A-Value of the Blended SI Multiplet, λλ4695 ..... 209

56. Results for the Absolute A-Value of SII λ5453 ..... 211

Figure Page

57. Relative Thermal Error in the A-Value of SII 5453 Measured Two Ways, and, Relative Thermal Error in the Ratio of TIB Results for SII λ5453 Relative to TIB Results for SI λλ4695 ..... 212

58. Discrepancies that Would Result From Unrecognized Loss (Adsorption) of $CS_2$ ..... 219

59. Time-Resolved Spectrogram of Shock in 0.21% $SiH_4$ + 99.79% Neon ..... 227

60. Excited State Densities of Some Visible Silicon Lines as Functions of Temperature ..... 228

61. Relative Thermal Error Propagated into AE of SiI λ5948, ARH of SiII λ6347, and AE, ARH of SiII λλ5056 at True Source Temperature ($T_o$) of 9,000°K ..... 229

62. Graphical Solution (Over Determination) for Temperature and Silane Concentration in Terms of the Four Observables: The Intensities of $H_\alpha$ and $H_\beta$, the Halfwidth of $H_\beta$, and the Ratio of $H_\beta$ to NeI λ5852 Intensities ..... 233

63. RMS Scatter Between Five Measured Temperatures as Function of Assumed Silane Concentration in a Silane + Neon Test Gas ..... 235

64. Histogram of Results for A-Values of SiI λ5948 and SiII λλ5056 ..... 237

65. Densitometer Tracings, 5200Å - 5500Å, for Two Shocks in 0.14% $PH_3$ + 99.86% Neon, Showing Strong Temperature Dependence in the Relative Brightness of PI and PII lines ..... 248

Figure | Page

66. Time-Resolved Spectrogram of Shock in 0.14% $PH_3$ + 99.86% Neon ..... 250

67. Densitometer Tracings, 5300Å - 5600Å, and 5900Å - 6200Å, for Multiply-Reflected Shock in 2% $O_2$ + 98% Neon ..... 260

68. Densitometer Tracing, 5300Å - 5650Å, for Shock in 0.11% $[CH_3]_3$ Aℓ + 99.89% Neon ..... 262

69. Time-Resolved Spectrogram of Shock in Pure Neon Test Gas ..... 263

70. Time-Resolved Spectrogram of Shock in 2% + $O_2$ + 98% Neon.. 269

71. (Full) Halfwidth vs. Red Shift for Blended Multiplets (11) and (12) of OI ..... 271

72. Instrument Profile for 0.75 Meter JACO Fast Spectrograph Using 50μ Slit (1.0Å Bandpass) ..... 273

73. (Full) Halfwidths of SI λλ4695 Measured as Functions of Electron Density ..... 275

74. (Full) Halfwidths of CI λ5052 Measured as Functions of Electron Density ..... 280

75. (Full) Halfwidth of SII λ5453 Measured as a Function of Electron Density ..... 287

76. Comparison of Measured Halfwidths of $H_\beta$ and $H_\gamma$ ..... 296

77. Comparison of Currently Measured Multiplet A-Values with Coulomb Approximation ..... 303

# CHAPTER I

# INTRODUCTION AND OUTLINE OF DISSERTATION

## A. Introduction

Astrophysics motivates much of the interest in atomic and molecular transition probabilities. Stellar abundances could not be determined without A-values, nor could quantitative models for stellar atmospheres be explored very far without them.[1-6] Transition probabilities, together with line broadening parameters and continuous absorption coefficients, are also essential for analysis of less remote plasmas, such as those produced by magnetic pinch devices or by the bow shocks of re-entry vehicles.[7-11] A rough correlation has also been demonstrated between the A-value of a line and the reproducibility of spectrochemical analysis based on that line.[12]

At present, the main application of A-values is to the study of atomic environments rather than the study of atomic structure *per se*. Atomic structure theory benefits from measurements which are accurate enough to distinguish good models from bad; the theory then becomes a more useful tool for estimating other line strengths needed in the future.

For the vast majority of astrophysically interesting lines, i.e., strong isolated lines lying in the visible region and in the near IR and near UV, neither experiment nor theory yet holds any clear-cut claim to superior reliability.[13] While there are transitions, for instance those between highly excited states of hydrogenic ions, where measured

values cannot improve upon Coulomb field predictions, many other transitions cannot be reliably treated using hydrogenic radial wave functions[7,14-16]

B. Review of Experimental A-Value Determinations

Progress in A-value determinations has been closely tied to refinement of spectroscopic sources. An investigation conducted in emission or absorption is meaningful only to the extent it can correlate the observed radiation with the number of emitters or absorbers in the line of sight -- that is, the number of atoms in the relevant excited states. The population of these states usually cannot be measured directly (precisely because the line strengths are not known) and must be deduced from the thermodynamic state of the source. The quality of the resulting A-value thus hinges directly on properties of the source: whether it is in LTE so a thermodynamic state is really defined, and if so, whether it is sufficiently homogeneous to warrant a space-averaged, or zoned, description. A turbulent or patchy thermal light source would clearly be very hard to interpret.

The capabilities of available laboratory sources, rather than astrophysical importance, often decides which transitions are studied. For instance, CsI, HgI, K I and NaI have each been subject to more than a score of investigations, while there have been no visible studies of BeI, FI, PI[17] and only three visible studies of SiI , despite its great astrophysical importance.[18] Experimental studies with neutrals outnumber studies of first ions by more than ten to one, yet it is the ion lines which are often the more important for analysis of hotter stars. No absolute A-values have yet been measured for visual lines of FeII or AℓII.

The early investigations of King[19,20] were performed in absorption, employing furnaces as spectroscopic sources. This work was limited to metallic spectra because furnace temperatures were so low (1500 - 2500°K) as to excite levels only a few eV above the ground state. Even for the metals, excitation energies were so much greater than kT that the assumed level populations were critically dependent on T . In addition, vapor pressures used in computing particle densities (and hence, absolute line strengths) were also critically dependent on T . The results of much of this pioneering work contained systematic discrepancies which were traced by later investigators to error in source temperature and lack of source homogeneity. Not being able to assess any set of these results a priori, astronomers found it necessary to use solar "curves of growth" to eliminate erroneous line strength data[4,5] for various levels of excitation and various stages of ionization for these elements.

The quest for transition probabilities for less readily excited atoms led to use of hollow cathode and similar discharge tubes. While the desired atoms can often be introduced as gases rather than vapors, and the desired lines made bright enough for time integrated study, it proves difficult to verify how closely these sources approach LTE . Glow discharges found wide employment by Rozhdestvenskii,[21] Prokofev[22] and co-workers during their development of the "hook" (anomalous dispersion) method for obtaining A-values. (This method circumvents the trouble of absolute photometric calibration but except for resonance lines does not remove the dependence of measured A-values on the temperature ascribed to the source.)

Free-burning DC arcs have also been used.[23] The electron densities in the arc column are adequate to insure LTE , and attainable temperatures

will excite the strong lines of many neutral atoms. These sources have the serious drawback that they are difficult to stabilize. Erratic, large scale wobble of the arc column confuses the data interpretation for a zoned, axially symmetric source no more than a millimeter in diameter.

Within the last decade A-value investigations have divided into two categories: those that are designed to utilize more sophisticated thermal sources (e.g. stabilized arcs, shock tubes) and those that do not rely directly on thermal excitation (e.g. radiative lifetime studies, Hanle effect, natural line width measurements).

Wall stabilized arcs use[25] a set of mechanical spacers to constrain the arc channel and flush the electrodes with an inert gas to reduce burning rates. Under optimal conditions these arcs can burn steadily and quiescently for periods of more than an hour--which affords the advantages that weak lines can be studied with time integrated recording and whole spectra can be scanned with a single photoelectric detector. Their main disadvantage is that radial thermal gradients demix plasma components in ways not yet susceptible to theoretical analysis. Also, a good deal of trial and error may be necessary to find those spectroscopic additive concentrations which allow the arc to burn quiescently. Side-on viewing of a cylindrically symmetric, zoned source (diameter $\lesssim$ 1 mm) also requires Abel inversion--but computer codes make this task far less tedious than in the past.

Liquid vortex arcs[24,26] constrain the arc column within the vortex center. Arc column wobble is greater than with wall-stabilization, but this may be offset by the fact that the turbulent liquid vortex surrounding the arc makes it less susceptible to demixing problems. Both types of arc are currently in use, with the wall-stabilized variety enjoying greater popularity.

There is no demixing problem in gas-driven shock tubes[27] where the bulk of the plasma is homogeneous except for thin ($\sim$ 1 mm) boundary layers. These layers do not separate plasma components since the duration of the plasma ($\sim$ 100μs) does not allow time for demixing to occur. Luminous shock tubes also have the advantage of allowing plasma conditions (temperature, pressure) to be widely varied in a predictable fashion by simple changes in the initial gas pressures selected. The necessity to simultaneously time-and wavelength-resolve spectra calls for elaborate instrumentation; it is also difficult to study lines of low brightness because signal-to-noise problems cannot be overcome by long sampling times. Laporte's group at Michigan made extensive use of the shock tube as a spectroscopic source[28-32] (complete reference to earlier work is given in these references). More recent references are listed by Byard[33] and by Parkinson[34].

Shock tubes using heated driver gases are employed to study lines whose excitation requires mean thermal energies in excess of the 1 eV produced by DC arcs or cold-driver (conventional) shock tubes. With either chemical heating (explosive drivers)[35] or electrical heating (T-tubes),[36] there is a trade off between plasma temperature and plasma duration, i.e., the higher the temperature achieved, the shorter the available test times. For T-tubes this does not present a serious handicap because their excellent reproducibility and fast duty cycles permit shot-to-shot scanning using short rise-time photomultipliers.

Lifetime studies yield the most reliable experimental A-values presently available. A-values are obtained directly from radiative lifetimes (typically $10^{-8}$sec), thus avoiding the presistent problems associated with thermal light sources. The radiative decay that follows impulsive

excitation can be timed in a variety of ways: by time-resolving the radiation[37,38] emitted subsequent to impulsive excitation of very short duration (coincidence method), by noting the phase shift[39] between emitted radiation and sinusoidily applied excitation (phase shift method), or by directing a monoenergetic beam of particles onto a very thin target foil and measuring the fall off in line intensity with distance behind the target (time-of-flight method).[40] These techniques are most readily applied to transitions in the UV and VUV because level-cascading problems usually become tractable only for deep-lying levels. Moreover for many astrophysically interesting lines, impulsive excitation cross sections are too small to yield the amount of light needed to measure decay times.

Transition probabilities deduced from a line's natural width do not depend in principle upon the thermodynamic state of the light source. The uncertainty principle[13,41] relates the natural width (i.e. in classical terms, the width due to damping of a harmonic oscillator) to the sums of A-values for transitions out of the upper and lower states of the line. Under favorable conditions, i.e. either the upper or lower state is metastable, or the lower state is ground, coscading problems are eliminated; if moreover, the sum of A-values for spontaneous emission out of a level is dominated by a single term, the line's halfwidth will be uniquely related to this single A-value. In practice however, Doppler broadening, and pressure broadening complicate the measurement of natural widths[†]. To unscramble the various contributions to total line widths, one can use the curve of growth[30,42] or combine high resolution spectroscopy

---

[†]Autoionizing[43] lines are an exception: their natural widths may be more than 1Å, ($10^4$ times greater than normal lines) so interference from completing broadening mechanisms is slight.

with very low density light sources[42]. The latter method has the advantage of reducing interference from induced emission, absorption and collisional processes.

The Hanle effect[44] has recently been utilized[45] to obtain A-values. This technique determines lifetimes of excited atomic states from variations in line intensity that accompany the level crossing of Zeeman sublevels under the influence of externally applied magnetic fields.

Since each of the methods discussed has its own strengths and weaknesses, the most convincing values of atomic line strengths will be those measured with good agreement by all methods. Short of this goal, one can use a fairly certain lifetime value, for example, as a secondary standard in reducing thermal light source data. In this way, advances in each method can be propagated into others. We believe that attainment of a reliable handbook of line strengths will have to proceed in this way; indeed the National Bureau of Standards has underway a critical survey of data of this type which is being continually revised as new data become available. The emphasis of our work is experimental with observations made only at the end as to how well theoretical treatments agree with the experimental results. The thrust of our experiments is to improve and cross-check the data from one thermal light source--the gas-driven shock tube. Methods discovered in these experiments will also be of great use in other thermal light sources.

## C. Outline of Principle Results

The initial and paramount objective of this work is to obtain the absolute transition probability of CI λ5052 to a reliability of ± 10% . Fully one half of our total experimental effort was directed towards this goal. While five previous CI investigations have been reported within

the past fifteen years, their results disagree by a factor of 4. If the current investigation is to meaningfully claim better accuracy than its predecessors, it must be demonstrably free from significant systematic (repeatable) errors. The methods we have adopted to demonstrate freedom from systematic errors effectively force us to perform several independent, simultaneous measurements of the same transition probability; i.e., to perform several of the conventional experiments simultaneously. This is done for each shock tube shot.

Our program to eliminate systematic errors had three distinct parts: all pertinent variables were measured redundantly; A-values were deduced in a new way (TIB) to circumvent the usual critical dependence on measured source temperature; and the experiment was executed over wide ranges of source temperature and pressure, using more than one type of test gas to introduce carbon into the plasma.

During the investigation of CI λ5052 each experimental run included four simultaneous and independent temperature measurements. The four temperatures were deduced from the absolute integrated intensity of NeI λ5852, the absolute integrated intensity of $H_\beta$, the halfwidth of $H_\beta$, and the slit-integrated optically thick portion of $H_\alpha$.

Plasma pressure was obtained both directly, from quartz transducers, and from Rankine-Hugoniot (real-gas) predictions based on observed incident shock speeds.

Our photometry was also redundant: two independent methods of absolute intensity calibration (one of them new) were routinely employed. The absolute integrated intensity of CI λ5052 was simultaneously recorded both photographically and photoelectrically. Two different

photographic emulsions were alternately used for time-resolved relative intensity measurements.

Enough data were collected during each shock tube shot to yield several independent estimates of the desired A-value. Amongst these simultaneous results for CI $\lambda 5052$ are certain pairs whose averages, according to the predictions of Saha-Boltzmann equilibrium, will contain only a small fraction of the critical dependence on source temperature normally implicit in measured CI A-values.

Our studies of CI were conducted at temperatures ranging between 9,500°K and 13,000°K and at pressures varying from $5\times10^{6}$ dynes $cm^{-2}$ to $20\times10^{6}$ dynes $cm^{-2}$. Electron densities varied between $2.5\times10^{16} cm^{-3}$ and $12\times10^{16} cm^{-3}$. The shock-heated gases routinely used consisted (initially) of 1% $CH_4$ + 99% neon and $\frac{1}{2}$% $CH_4$ + $\frac{1}{2}$% $CS_2$ + 99% neon: a few runs employed $\frac{1}{4}$% $CH_4$ + $\frac{3}{4}$% $CS_2$ + 99% neon.

As a control on overall accuracies, we measured the A-value of $H_\beta$ simultaneously with our determinations of CI A-values.

By being much less susceptible to systematic errors, this investigation would seem much more reliable in principle than the typical emission study which relies on the minimum complement of three measured variables (e.g., one temperature, one pressure and one absolute integrated intensity). While good equipment and reasonable attention to detail may insure a reproducible (small scatter) result for the latter type of experiment, systematic ("repeatable") errors easily go undetected. In fact, this must often have been the case, to judge from the marked discrepancies in the literature between authors each claiming small margins of error.

The present investigation, however, was specifically designed to counter systematic errors, both by setting up several ways to discover them

and by minimizing the consequences to the results should any escape detection. Each pair of redundant calibrations, of redundant measurements of state variables, of redundant photometric measurements, and each of the independently deduced A-value determinations (for the same line) is prone to its own peculiar set of systematic errors. Only in the absence of significant systematic error can there be internal self-consistency at all levels of the experiment from calibrations through final results. The self-consistency checks are made even more stringent by insisting that they hold over widely varying source conditions.

Transition probabilities for the visual lines of SI and SII were obtained at a considerable economy of effort compared to the CI results. Our "system" was calibrated and checked-out in the course of the CI studies: thereafter its capabilities for rapidly gathering data could be utilized in a more or less routine manner. At the beginning of this study, no published experimental results were available for either SI or SII. This is curious because the visual spectrum of SII is unusually rich in strong isolated lines, whose Coulomb approximation A-values led Aller[46] to conclude: "For no other element do so many lines yield so little data on stellar abundances." A-value determinations for SI and SII by Bridges and Wiese,[25] and for SI by Foster,[26] have been reported in the last two years. These authors disagree by 40% in their estimates of SI transition probabilities.

Compared to CI or SI, a relatively small number of data runs were devoted to each of the spectra SiI, SiII, PI, PII, NeI, AℓII, OI and CℓI. It was a deadline for relocating our equipment, rather than a lesser astrophysical importance, that was responsible for these spectra being alloted less laboratory time (fewer runs) than CI, SI or SII.

Because they were studied less exhaustively, our results for these elements are less accurate than for CI or SI : whether they are slightly less accurate, or grossly less accurate, depends both on the strengths of the individual lines and the particular susceptibility to systematic error of the type of A-value determination employed.

Experimental A-values have not been previously reported for any visual lines of PI or PII . Although there have been several recent works[47-50] devoted to the near UV spectrum of SiI , the sole prior investigation above 4100Å consists of Hey's measurement of SiI λ5948 . One half of the OI (multiplet) A-values we report have not been previously studied. Although the visual spectrum of NeI has been the object of many recent experiments,[13,17,51] none have dealt with the lines we report here.

Stark widths and shifts were measured as functions of electron density for a total of sixteen neutral lines from the spectra of CI , OI , NeI , SiI , PI , SI , CℓI and AI . While these data were obtained as free by-products of our A-value studies, the measurements were conducted under circumstances favorable to good accuracies, i.e., shifts and widths were often observed over a factor of 4 in electron density and a factor of 5 in peak line brightness; our source plasma is laminar and homogeneous (i.e., not zoned); and, in many cases, observed full-halfwidths exceed instrument widths by more than a factor of 5.

Stark widths were also measured for 27 ion lines from the spectra of SII , SiII , AℓII , and PII . Because our experimental procedure was always directed towards optimizing results for A-values, these narrow lines were usually measured with spectrograph slits several times broader than their total Stark widths. So accuracies are not high. However, in most cases tolerances are not so large as to preclude meaningful comparison with

the recently reformulated broadening theory for ion lines.[52-54]

Data for comparing the halfwidths of $H_\beta$ and $H_\gamma$ were also included as a bonus along with our transition probability data. While the precisions available from our time-resolved photographically recorded profiles do not compete with those obtained by Gerardo and Hill[55], plasma temperatures in the two experiments differ typically by a factor of 2, so results of the two experiments are not directly comparable. Accuracies of the current results are good enough to render them useful for comparison with Griem's[56] predictions for the Stark broadening of Balmer lines.

## D. Outline of the Dissertation

A brief review of spectroscopic concepts and formulas is given in Chapter II. Some of these relations are evaluated and presented in graphical form for later use in the analysis of our shock tube plasmas. We also discuss different methods of measuring A-values in emission using thermal light sources containing several atomic species. The last section treats the problems involved in selection of spectrograph slit widths for time resolved studies with light sources of limited brightness.

Chapter III describes the method of thermally insensitive balancing (TIB) which we employ to circumvent the usual critical sensitivity of measured A-values to errors in the temperature ascribed to the light source.

In Chapter IV we consider aspects of the conventional gas-driven shock tube that pertain to its use as a spectroscopic light source. The second section contains a brief heuristic account of shock tube operation intended to orient the reader not previously familiar with these devices. The third section compares thermo-hydrodynamic predictions for the state of first reflected shocks with direct measurements of state variables.

In the fourth section we consider the effects on our results of departures from the idealized,one-dimensional model of shock tube flows. Tailoring of plasma conditions to optimize spectral line brightness is discussed in the last section.

Chapter V deals with construction of the shock tube and its related equipment. The design and construction of this apparatus constituted a substantial portion of the present dissertation. In the first section we also discuss data correlating reproducibility of diaphragm breaking pressures with methods of diaphragm preparation: this information may prove of practical use to workers employing shock tubes. In the second section we describe equipment for photoelectric image dissection. Joining microscope cover-glass slides to formed, fibre-optic bundles produces sequential sampling channels of 50μ width that are simple and inexpensive.

The experimental techniques used to calibrate detectors and to collect data from the shock tube are described in Chapter VI. Data from redundant measurements of photometric and thermodynamic variables are presented and intercompared.

In Chapter VII we present results of A-value determinations for visible lines of CI, OI, NeI, AℓII, SiI, SiII, PI, PII, SI, SII and CℓI . Results are also given for Stark widths and shifts of 16 neutral lines or merged multiplets and for Stark widths of 28 ion lines selected from these spectra. In addition to comparing our results with previous experimental values and theoretical predictions, we discuss the particular experimental problems posed by each element and the various internal consistency checks applied to our data. In the last section we compare the observed halfwidth of $H_\beta$ and $H_\gamma$ .

Chapter VIII assesses the agreement between our collected results and Coulomb predictions for complete multiplets, and compares relative line strengths within multiplets with LS coupling predictions. The second section offers a brief critique of the current experiment's design, as viewed with hindsight. The last section suggests some areas for future investigation.

# CHAPTER II

## SUMMARY AND APPLICATION OF SPECTROSCOPIC THEORY

### A. Introduction

We discuss the formation of spectral lines by a thermal light source, the dependence of line features on properties of the source, operational definitions of types of A-value measurements and factors governing selection of the spectrographic slit width.

### B. Optically Thin Lines

A light source is said to be "optically thin" at a given wavelength if photons of that wavelength, emitted at any depth in the source, escape without subsequent interactions. Of course, statistically speaking an occasional photon will be reabsorbed no matter how tenuous or shallow the source is. However, radiative transfer assumes a particularly simple form once the photon mean free path is of order ten times the extent of the source along the line of sight. For example, the integrated energy in an emitted spectral line is then independent of the line profile. For a homogeneous, laminar source, the absolute integrated intensity along a line of sight of length $\underline{\ell}$ can be written:[6,7,57]

$$I = \frac{hc}{4\pi\lambda} \ell A_{mn} N_m \qquad \text{ergs cm}^{-2}\ \text{s}^{-1}\ \text{sterad}^{-1} \qquad [1]$$

where $N_m$ = number density of atoms in the excited state ,

$A_{mn}$ = transition probability per unit time (Einstein coefficient).

When, in addition to being homogeneous and free from strong externally applied fields, <u>all</u> atomic states in the plasma are populated essentially by collisions, i.e., when not more than one radiative transition occurs for each ten collisions affecting the occupation of the most tightly-bound atomic state in the plasma, then the number density of an excited state, $N_m$ , will be given by the Maxwell-Boltzmann distribution

$$N_m = N_q^p \frac{g_m}{Z_q^p} e^{-Em/kT} \qquad [2]$$

where $N_q^p$ = total number density of atoms (ions) of the $q^{th}$ element in the $p^{th}$ stage of ionization,

$g_m$ = $2J_m+1$ = statistical weight of the state $m$ ,

$E_m$ = energy of the state $m$ ,

and

$Z_q^p$ = $\sum_{i=n_o}^{n_\infty} g_i e^{-Ei/kT}$ = partition function, where the summation is over all allowed states of the atom from the ground state $n_o$ to the highest bound state of the atom in its particular plasma environment, $n_\infty$ .

If $n_\infty$ is taken as the most energetic state for which

$$E_n \leq \chi_q^p - \Delta\chi_q^p$$

where $\chi_q^p$ = ionization energy (in vacuo) of $q^{th}$ atom in its $p^{th}$ stage of ionization,

$-\Delta\chi_q^p$ = decrease in ionization potential due to plasma microfields,

Griem [58] shows that the uncertainty in this cutoff procedure, together with the error from neglecting plasma perturbations to the energy levels $E_{n_o} \cdots E_{n_\infty}$, causes much less than 1% error in $Z_q^p$ under normal laboratory conditions.

For an r-component plasma there are r Saha equations for ionization equilibrium. These are coupled together by the plasma electron density. Considering only neutrals (p = 0) and first ions (p = 1) :

$$\frac{NeN_q^1}{N_q^o} = \frac{(2\pi mkT)^{3/2}}{h^3} \frac{2Z_q^1}{Z_q^o} e^{-(\chi_q^o - \chi_q^o)/kT}, \quad q = 1,2,\cdots r \qquad [3]$$

For a closed thermodynamic system of known (initial) composition the following subsidiary conditions must be used with eqn. [3];

$$N_q^o + N_q^1 = \alpha_q(N-Ne), \quad q = 1,2,\cdots r \qquad [4]$$

where N = total particle number density,

$N = \frac{p}{kT}$ since departures from ideal gas behavior are negligible at $10^4$°K , [5]

$\alpha_q$ = constant = relative concentration of $q^{th}$ atoms in the test gas,

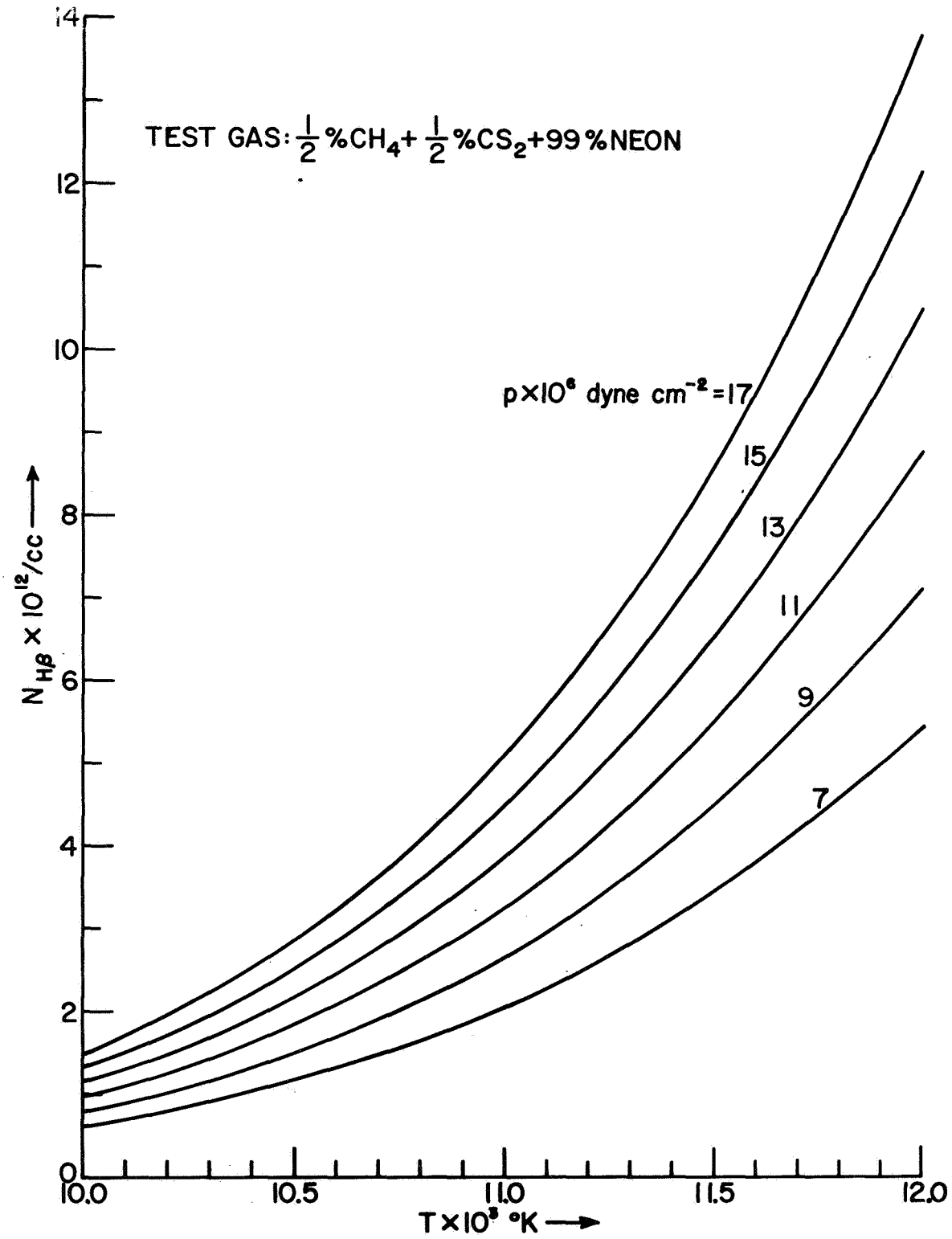


Fig. 1: Excited State Number Density of $H_\beta$ as a Function of Temperature and Pressure.

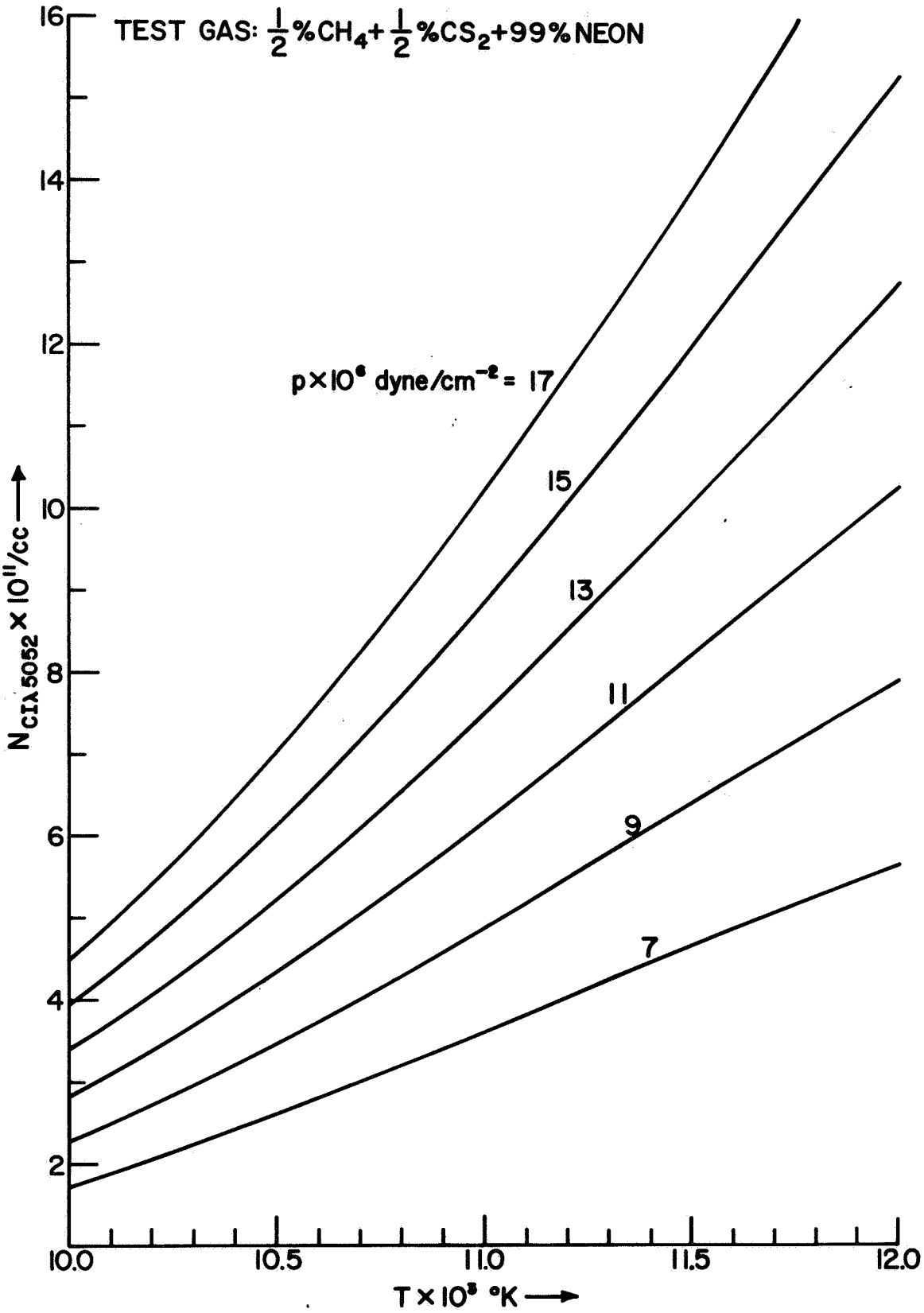


Fig. 2: Excited State Number Density of CI λ5052 as a Function of Temperature and Pressure.

and
$$\sum_{q=1}^{r} (N_q^o + 2N_q^1) \qquad [6]$$

where the factor of 2 enters through the requirement of plasma neutrality,

$$\sum_{q=1}^{r} N_q^1 = Ne \quad . \qquad [7]$$

Equations [1] - [7] are sufficient to uniquely determine any $N_m$ if p and T (or two equivalent thermodynamic state variables) are given together with the initial plasma composition. Because the Saha equations are coupled, their solution requires iteration in electron density: so for routine calculations,computer coding is almost a necessity. For example, if it typically requires 4 iterations to attain a 1% level of convergence, then to find the excited state number density for some carbon line in a plasma initially composed of ½% $CH_4$ + ½% $CS_2$ + 99% neon requires solution of 48 equations. The computer program employed in the current work was written for us by Koopman[59] and Bengtson along lines suggested by Rouse[60] .

Figures 1 and 2 show the dependence of excited stated densities on pressure and temperature for two lines, $H_\beta$ and CI λ5052 , that are typical of those we study.

In this treatment we have stated that the system is closed and have implicitly assumed that all molecules are completely dissociated. In the current shock tube studies these assumptions are valid to a good approximation.

Our plasmas are not strictly closed thermodynamic systems because small concentrations of impurities boil off the shock tube walls. Two kinds

of impurity can influence our determinations of an A-value, say that for CI λ5052: very readily ionized impurities which shift the Saha-equilibrium of $N_{CI\lambda5052}$, and impurity levels of carbon. In Fig. 3 we plot $N_{CI\lambda5052}$ as a function of temperature for different assumed impurity concentrations of aluminum.† The relative change in $N_{CI\lambda5052}$ is only a few percent for aluminum concentrations several times larger than could exist without causing significant discrepancies between the predicted and observed (cf. Chapter VI) electron densities. Impurity levels of carbon are estimated (cf. Chapter VI) to introduce not more than 3% error into A(CI λ5052). If carbon impurity levels were twice as large as we estimate, then CI lines would be observed in pure argon plasmas.

Since our customary plasmas are hotter than 10,000°K, less than 1% of the test gas remains undissociated.[61,62] We do not observe such features as $C_2$ Swan bands in the shock regions where we measure A-values.

### C. Formulation for Finite Optical Depth

The optically thin approximation, eqn. [1], is not valid for bright lines whose photons stand a good chance of being reabsorbed instead of emerging from the plasma without interacting. By invoking the laws of radiative transfer we can treat the interaction between these lines and the emitting plasma.[6,7] The treatment is exact if we have detailed knowledge of the <u>shape</u> of the line in a particular plasma environment. For a homogeneous source viewed through a small solid angle the observed intensity per wavelength interval per steradian is

---

†We use aluminum as a convenient lumped concentration to represent all types of impurity atoms which are more than 90% ionized at T = 11,000°K.

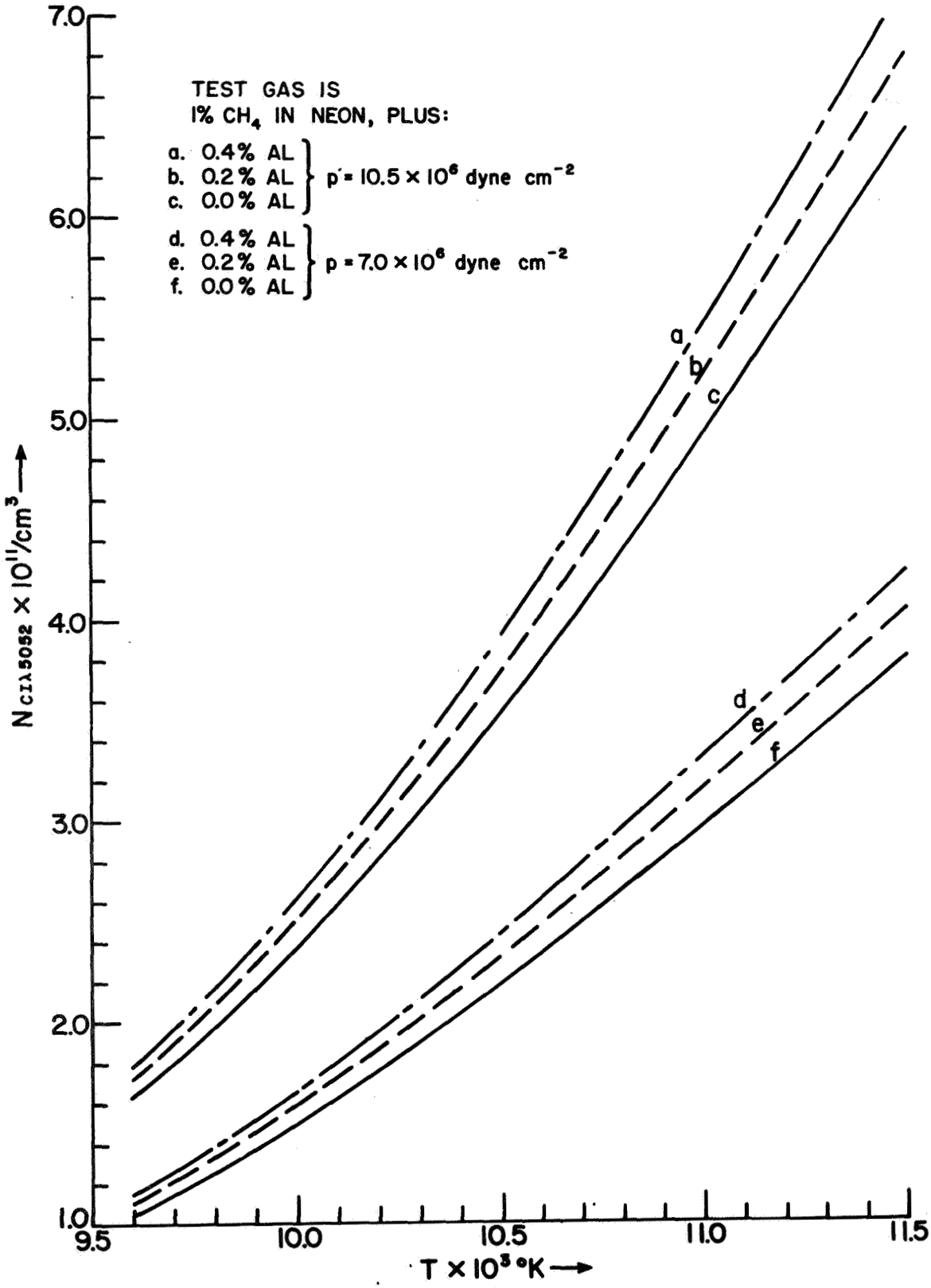


Fig. 3: Effect of Readily Ionized Impurity Upon the Excited State Number Density of CI λ5052.

$$I_\lambda = B_\lambda(T)\ [1 - e^{-\ell k'(\lambda)}] \qquad [8]$$

where $\ell k'(\lambda) = \tau(\lambda)$ = optical depth

$\ell$ = length of the light source along line of sight,

$$B_\lambda(T) = \frac{2hc^2}{\lambda^5}\ [e^{\frac{hc}{kT\lambda}} - 1]^{-1} = \text{the Planck function,} \qquad [9]$$

$k'(\lambda)$ = adsorption coefficient including induced emission.

and

$$k'(\lambda) = \frac{\lambda^4}{8\pi c}\ A_{mn}\ N_m\ e^{\frac{hc}{kT\lambda}}[1 - e^{-\frac{hc}{kT\lambda}}]\ L(\lambda,p,T) \qquad [10]$$

with $L(\lambda,p,T)$ = shape factor,

$$\int_{-\infty}^{\infty} L(\lambda,p,T)d\lambda = 1.0 \qquad [11]$$

The shape of the line is a function of $p$ and $T$ because Doppler broadening depends on $T$, while Stark[7,16] broadening depends on electron density (a function of $p$ and $T$) and $T$.

There are two ways of obtaining $L(\lambda,p,T)$ : if $p,T$ are known, together with the relevant Stark broadening parameters, $L(\lambda,p,T)$ can be computed: this must be done when the line is slit-integrated over a wavelength. If the spectrograph slit-width is small compared to the full halfwidth of the line, and the photometric detector is absolutely calibrated, and the instrumental profile is known, then $L(\lambda,p,T)$ can be recovered from the observed line profile. The latter method is usually the less tedious.

To compute $L(\lambda,p,T)$ we calculate the Doppler (full) halfwidth

$$\lambda_D = 2[\ln 2]^{\frac{1}{2}} \lambda_o \left(\frac{2kT}{Mc^2}\right)^{\frac{1}{2}} \qquad [12]$$

where $M$ = mass of atom

$\lambda_o$ = wavelength at line center.

Assuming that the Stark impact (electron) broadening parameter, $w$, and ion (quasi-static) broadening parameter, $\alpha$, of the line are known, the total (full) Stark halfwidth is[7,16] computed:

$$\Delta\lambda_S = 2\{1 + 1.75\alpha(1 - 0.75R)\}\ w\ Ne \qquad [13]$$

where $R = \left(\frac{3}{4\pi Ne}\right)^{1/3} \frac{1}{\rho_D}$

= mean distance between ions/Debye radius .

We assume $\Delta\lambda_D$ and $\Delta\lambda_S$ are the only significant components of the total line width: instrumental broadening has nothing to do with radiative transfer in the plasma, while the natural broadening and van der Waals broadening are usually negligible in laboratory plasmas. The intensity distribution in a Doppler broadened line has a Gaussian shape, $G(\lambda)$, while the intensity distribution in a Stark broadened line has a Lorentzian (dispersion) shape,[63] $L(\lambda)$. When both types of broading are present in a line, the intensity distribution will have the shape of a Voigt profile, $V(\lambda,\eta)$

$$V(\lambda,\eta) = \int_{-\infty}^{\infty} L(y)\ G(\lambda-y)\ dy \qquad [14]$$

where $\eta$ = a function of $\frac{\Delta\lambda_D}{\Delta\lambda_S}$

Davies and Vaughan[64] have tabulated numerical solutions to the convolution integral of eqn. [14]. With suitable normalization (cf eqn. [11]) $V(\lambda,\eta)$ becomes $L(\lambda,p,T)$ . Because $L(\lambda,p,T)$ is a complicated function, the integral $\int_{-\infty}^{\infty} I_\lambda d\lambda$ (cf. eqn. [8]) must either be approximated by a summation or else $L(\lambda,p,T)$ can be fitted to a polynomial in $\lambda$ .

When a line of non-negligible optical depth is recorded with slits much narrower than the line full halfwidth (i.e. when the recorded profile is not seriously distorted by instrumental broadening), the transition probability can often be obtained in a direct and simple way. For example, suppose the profile of $H_\beta$ has been photographically recorded in absolute intensity using 1.0Å spectrograph slits, and that pressure and temperature are known. If the halfwidth of $H_\beta$ is 20Å , then the intensity will vary only slightly within any 1Å wide segment of the profile, $\Delta\lambda$ , and is well approximated by its average, $\tilde{I}_\lambda$ , over $\lambda \mp \Delta\lambda/2$ . Since T is known, $\tilde{B}_\lambda(T)$ is also known. Substitution into eqn. [8] gives:

$$\{1 - e^{-k'(\lambda)\ell}\} \cong \frac{\tilde{I}_\lambda}{\tilde{B}_\lambda(T)} \qquad [15]$$

Since the right hand side of this equation is known, we can simply reconstruct the fictitious intensity segment $\tilde{I}^o_\lambda$ that would be obtained if none of the photons emitted in the plasma were reabsorbed:

$$\tilde{I}^o_\lambda = \tilde{I}_\lambda \ln\left\{1/(\tilde{I}_\lambda/\tilde{B}_\lambda(T) - 1)\right\} \left(\frac{\tilde{I}_\lambda}{\tilde{B}_\lambda(T)}\right)^{-1} \qquad [16]$$

If $\tilde{I}_\lambda/\tilde{B}_\lambda(T) = 0.1$ , then $\tilde{I}^o_\lambda/I_\lambda = 1.01$ , and if $\tilde{I}_\lambda/\tilde{B}_\lambda(T) = 0.5$ , then $\tilde{I}^o_\lambda/\tilde{I}_\lambda = 1.21$ . Applying eqn. [16] piecewise to span the entire line profile, one obtains

$$I \simeq \sum_{\Delta\lambda=-\infty} \tilde{I}^o_\lambda \, \Delta\lambda$$

which is substituted into eqn. [1] to find $A_{mn}$ .

While this cumbersome procedure was not required to determine A-values in the current work†, it was employed with 2 lines of known A-value, $H_\alpha$ and NeI λ5852 , for purposes of plasma diagnosis. We now show predictions for the absolute integrated intensity of an optically thick central portion of $H_\alpha$ as a function of temperature: these are later used (cf. Chapter VI) not only to estimate plasma temperatures but also to perform (in conjunction with a reversal flash lamp) in-situ absolute intensity calibrations and photomultiplier linearity checks.

Griem, Kolb and Shen [56] calculated the shape of $H_\alpha$ as a function of electron density and temperature with a reliability Griem estimates as 20%. For a plasma of known composition, then, we know $L(\lambda,p,T)$ . If the thickness and pressure of the plasma are also known, the absolute intensity passing through 2Å wide entrance slits centered on 6562.8Å becomes a unique function of temperature. Using wavelength segments $\Delta\lambda = .2$Å , this intensity can be well approximated by:

$$\int_{-1.0Å}^{1.0Å} I_\lambda(T)d\lambda \simeq B_{\lambda_o}(T) \sum_{-1.0Å}^{1.0Å} [1 - e^{-\tilde{k}'(\lambda)\ell}] \, \Delta\lambda \qquad [17]$$

---

†The bright lines we studied that were essentially integrated by 1Å wide slits were ion lines; if such lines were seen to require significant optical depth corrections, we reduced plasma temperatures. Since ion line population densities are very sensitive to T , a slight drop (5-10%) in T would reduce line brightness drastically, obviating the need for optical depth correction.

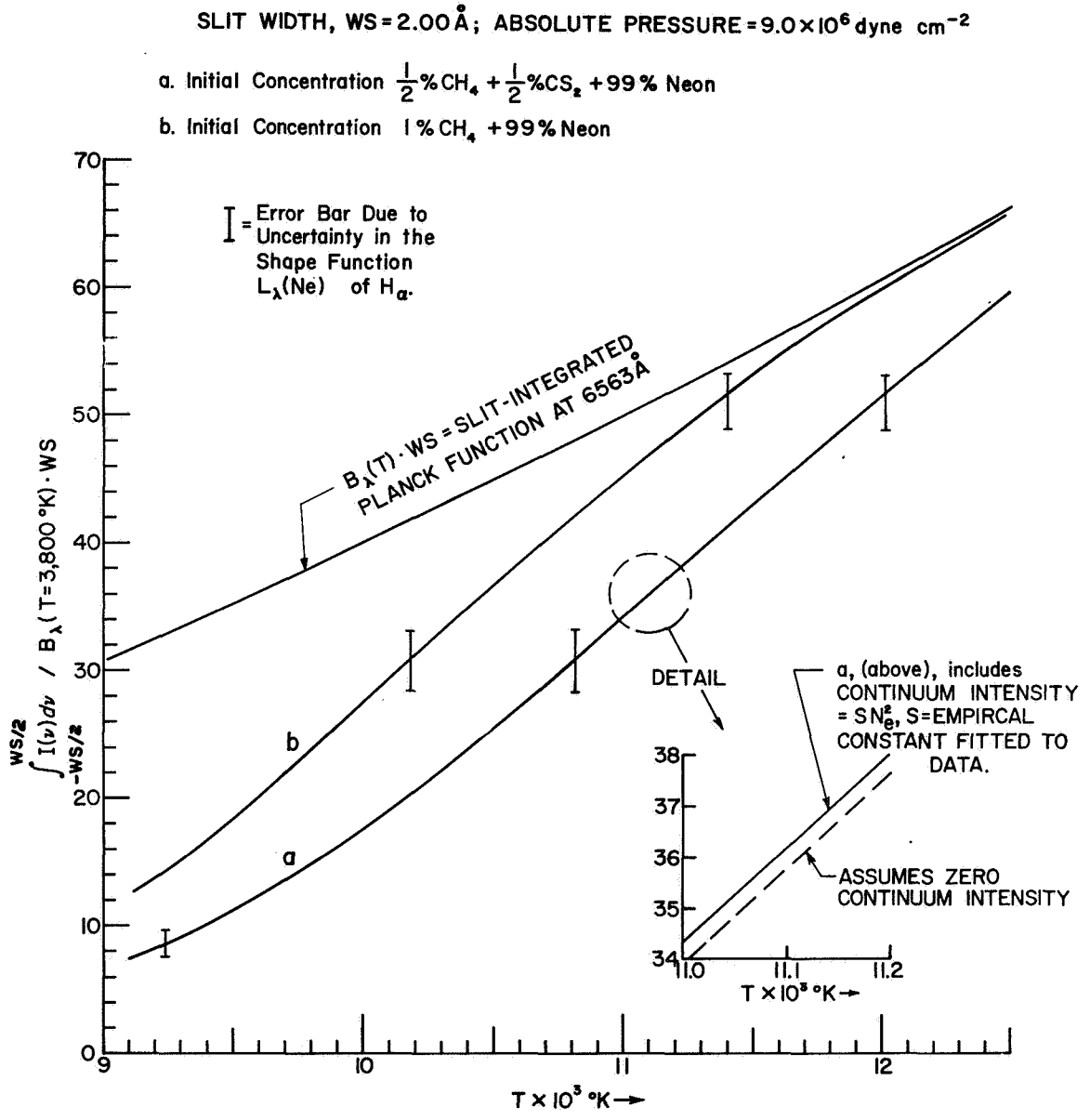


Fig. 4: Absolute Intensity of the Central Portion of $H_\alpha$ as a Function of Plasma Temperature.

where $\tilde{k}'(\lambda)$ = the average value of $k'(\lambda)$ within the wavelength interval $\lambda \pm 0.1\text{Å}$ .

In Fig. 4 we plot $\int_{-1.0\text{Å}}^{1.0\text{Å}} I_\lambda(T)d\lambda$ as a function of T for two plasmas of different composition†. Also shown is $B_{\lambda_o}(T)\times 2.0\text{Å}$ . The intensity scale of the ordinate is normalized to the absolute intensity of a carbon arc at 6562.8Å , $B_{\lambda_o}(3{,}800°\text{K})\times 2.0\text{Å}$ . The vertical error bars, typically ±8%, represent the uncertainty propogated into these optically thick, partially integrated, line intensities. Both $\int_{-1.0\text{Å}}^{1.0\text{Å}} I_\lambda(T)d\lambda$ curves would be steeper between 9,000 - 10,000°K were it not for the ionization of CI and SI which causes

$$\frac{\int_{-1.0\text{Å}}^{1.0\text{Å}} L(\lambda,p,T)d\lambda}{\int_{-\infty}^{\infty} L(\lambda,p,T)d\lambda}$$

to decrease rapidly in this temperature region.

### D. Utilization of Absolute Intensity Standards in A-Value Determinations

To measure $A_{mn}$ using a thermal light source requires observation of at least 3 variables: two to find the thermodynamic state of the source and an additional one to convey the required intra-atomic information, $A_{\tilde{mn}}$ . This last variable is not the integrated line intensity I of eqn. [1], but is rather a ratio of I to some standard intensity $I_s$ . Only because $I_s$ is known absolutely (in ergs $cm^{-2}s^{-1}sterad^{-1}$) is measurement of I

---

†As indicated in the figure, the curves actually plotted include a small (∿1%) correction for the finite intensity of the underlying continuum, $I_{cont.} \approx s(Ne)^2$ , where s is an approximate, experimentally determined, constant.

possible: sensitivity of detectors, spectrograph efficiency and transmission of the optical train cannot be quantitatively predicted from first principles.

The sources for $I_s$ belong to two classes. Either:

$$I_s = B_\lambda(T) \text{ --- with } T \text{ precisely known}$$

or

$$I_s = \frac{hc}{4\pi\lambda} \ell A^s_{mn} N_m(p,T) \text{ --- with } A^s_{mn}, \ell, p, T \text{ and plasma composition precisely known.}$$

To the first class belongs laboratory standards such as the DC carbon arc anode (where T is fixed by sublimation temperature of electrolyic carbon) and the tungsten filament lamp (where T is fixed by very sensitive current regulation). It also includes those portions of spectral lines where mean optical depths exceed 3, i.e.,

$$\frac{\int_{-\frac{ws}{2}}^{\frac{ws}{2}} I_\lambda(T)d\lambda}{ws \times B_\lambda(T)} \geqslant .95$$

where ws = bandpass of system, and where T is precisely known.

The most notable examples of the second class ("internal standards") are the Balmer lines of hydrogen, where $A^s_{mn}$ is known to be better than $\pm$ 1%. For use as internal standards, optically thin lines of known strength offer the advantages of calibration along the identical optical path, on the same time scale, and at roughly the same signal level as the line intensities of

interest. Their great disadvantage is a Maxwell-Boltzmann dependence on temperature--the absolute reference standard is then not really the precise $A^{s}_{mn}$ , as one would like, but rather an assortment of less precise quantities entering into the measured source temperature.

The majority of emission studies have relied on laboratory standards, turning to optically thin plasma lines (e.g. $H_\beta$ used by Doherty[29]) or optically thick plasma lines (e.g., Lyman $\alpha$ used by Lincke[65]) only when laboratory standards were unavailable.

We will have important reasons to distinguish between A-values relying on these two different classes of absolute intensity calibration. We therefore introduce the following notations and terminology. When the carbon arc is the photometric standard;

$$AE \equiv A_{mn} = \frac{\lambda 4\pi}{hc\ell} \frac{1}{N_m} \frac{I}{I_s} \times B_\lambda(3{,}800°K) \qquad [18]$$

AE = "the emission A-value," or "the conventional result."

and when the A-value of $H_\beta$ is the photometric standard;

$$ARH \equiv A_{mn} = \frac{N_{H_\beta}}{N_m} \frac{I}{I_{H_\beta}} \frac{\lambda}{\lambda_{H_\beta}} \times A_{H_\beta} \qquad [19]$$

ARH = "the A-value from trans-species relative intensity measurement."

## E. Influence of Spectrograph Slit Widths on Accuracy of A-Value Determinations

The selection of the spectrograph slit width will often directly affect the accuracy of measured A-values.[30] The optimal choice usually involves a compromise between mutually incompatible objectives. When lines are recorded with slits which essentially integrate the total line intensity, measurement of $I/I_s$ really consists of four plasma observations:

$$\frac{I}{I_s} = \frac{I_{L+B}}{I_{s_{L+B}}} - \frac{I_B}{I_{s_B}} \equiv \left(R_{L+B} - R_b\right) \qquad [20]$$

where

$$\left.\begin{array}{l} I = \text{the integrated line intensity} \\ I_s = \text{the standard intensity} \end{array}\right\} \text{as before}$$

and the four directly observed quantities are,

$I_{L+B}$ = the integrated line <u>plus</u> local background (continuum) intensity

$I_B$ = the integrated local background, i.e., the local continuum intensity

$I_{s_{L+B}}$ = calibration intensity for the line-plus-background monitoring channel

$I_{s_B}$ = calibration intensity for the background monitoring channel.

That is, the electron densities in thermal light sources produce non-negligible continuum intensities, so that the absolute integrated intensity $I$ of eqn. [1] is obtained by a difference measurement between two ratios

of observed intensities. To obtain ARH of eqn. [19] requires the additional difference measurement, $I_{H_{L-B}} - I_{H_B}$, as well.

For fixed source conditions, increasing the slit width, ws, will decrease the ratio $R_{L+B}/R_B$. (In the limit of infinitely wide slits, this ratio will go to unity). So to avoid a critical difference measurement for $R_{L+B} - R_B$, it is desirable to keep ws small.

However, unless WS is considerably greater than the lines' full halfwidth, $\lambda_{\frac{1}{2}}$, wing corrections will impart to the measured A-value some of the uncertainty in the line's broadening parameters. That is, the line's broadening parameters must be used to calculate the fraction of the total line intensity falling outside the measured bandpass. If the line shape is Lorentzian (Stark broadened), for example, this fraction is[66]:

$$\int_{-\frac{ws}{2}}^{\frac{ws}{2}} I_\lambda d\lambda \Big/ \int_{\infty}^{\infty} I_\lambda d\lambda = \frac{2}{\pi} \tan^{-1}\left(\frac{ws}{\Delta\lambda_S}\right) \qquad [21]$$

from which it is seen that the uncertainty in $\Delta\lambda_S$ becomes more crucial as ws decreases.

Choice of spectrograph slit width involves a second pair of conflicting objectives. Wide slits favor improved signal-to-noise† ratios; however, wide slits also favor inclusion of interfering spectral features within $I_{L+B}$ and $I_B$.

---

†In photographic recording the source of noise is the emulsion grain; in photoelectric recording it is random fluctuations in the emission of electrons from the photocathode.

# CHAPTER III

# METHOD OF THERMALLY INSENSITIVE BALANCING

## A. Introduction

Small errors in the temperature ascribed to a light source can easily undermine the reliability of transition probabilities obtained using thermal excitation. The excited state populations of light elements have a particularly critical dependence on temperature because excitation energies typically exceed mean thermal energies by a factor of 10.

For lines in the visible spectrum, experiments involving observation of refractive indices (hook method) will be only slightly less vulnerable to thermal errors than those involving observation of absolute line intensities (emission method) since energies of upper and lower states differ by only 2 eV.

Since the development of radiative decay experiments has not diminished the importance of thermal sources for the study of astrophysically interesting lines in the visual spectrum, we wish to point out that these sources have <u>not</u> traditionally been employed to fullest advantage. We have, in fact, found means for overcoming the persistent problem posed by the thermal sensitivity of many light elements and their ions.

<u>Section B</u> is devoted to a brief conceptual outline of the new thermally insensitive approach, making it clear at the outset that its use does not require any basic innovations in established laboratory technique.

Section C follows in detail the application of the thermally insensitive method to a particular CI line in a given shock tube plasma, and quantitative predictions are compared with results of the current experiment. Several features common to any application of the method will emerge at this time.

Section D enlarges upon the general applicability of thermally insensitive procedures, drawing examples from the present shock tube studies of CI , SI , SII , SiII , PII , and AℓII .

Section E offers guidelines for extrapolating the method for use in a wide variety of sources, and to various temperature and wavelength domains.

## B. Conceptual Outline of the New Methods

The experimental approach described here will often lift the strong implicit thermal dependence from measured A-values. It consists in simultaneously and independently performing a pair of customary A-value measurements the sum of whose results contain no net thermal dependence. That is, the pair of measurements is selected in a way which insures mutual cancellation of any thermal error propagated into the two independent results.

In a thermal light source, excited atomic states are populated in accordance with Saha-Boltzmann equilibrium. This imparts to emission lines a strong thermal dependence which cannot be circumvented while the plasma is in LTE .

Our method utilizes the differences between thermal dependences of various lines in multicomponent plasmas.

Some few spectral lines, such as the Balmer series of hydrogen, have precisely known A-values. In multicomponent plasmas of known temperature and composition, their known A-values serve as absolute standards for A-values deduced by trans-species relative intensity measurements (cf. eqn. [19]). In such a measurement the integrated intensity of $H_\beta$ is used for the same purpose as the carbon arc is in the traditional emission measurement (cf. eqn. [18]).

While both methods of determining an A-value are equivalent in principle, results from the two methods have entirely different dependence on source temperature. When the carbon arc is the absolute calibration standard, the absolute emission A-value, AE , derived from an observed line intensity is

$$AE \propto \frac{1}{N(T)} \propto e^{E/kT}$$

but when $H_\beta$ is the absolute calibration standard;

$$ARH \propto \frac{N_{H\beta}}{N}(T) \propto e^{(E-E_{H\beta})/kT}$$

If $E_{H\beta} > E$ , as is the case for most neutral lines, AE and ARH will have thermal dependence of opposite sign. If $E_H \simeq 2E$ , the thermal dependencies of AE and ARH will be not only opposite in sign but also equal in magnitude, so that the <u>sum</u> (or <u>average</u>) of these two independent determinations will have zero thermal dependence.

We refer to the combining of independent results for purposes of reducing (or eliminating) their joint thermal dependence as "thermally insensitive balancing" or TIB .

Pressure = $9.0 \times 10^6$ dyne $cm^{-2}$; Test Gas: $\frac{1}{2}$% $CH_4$ + $\frac{1}{2}$% $CS_2$ + 99% Neon

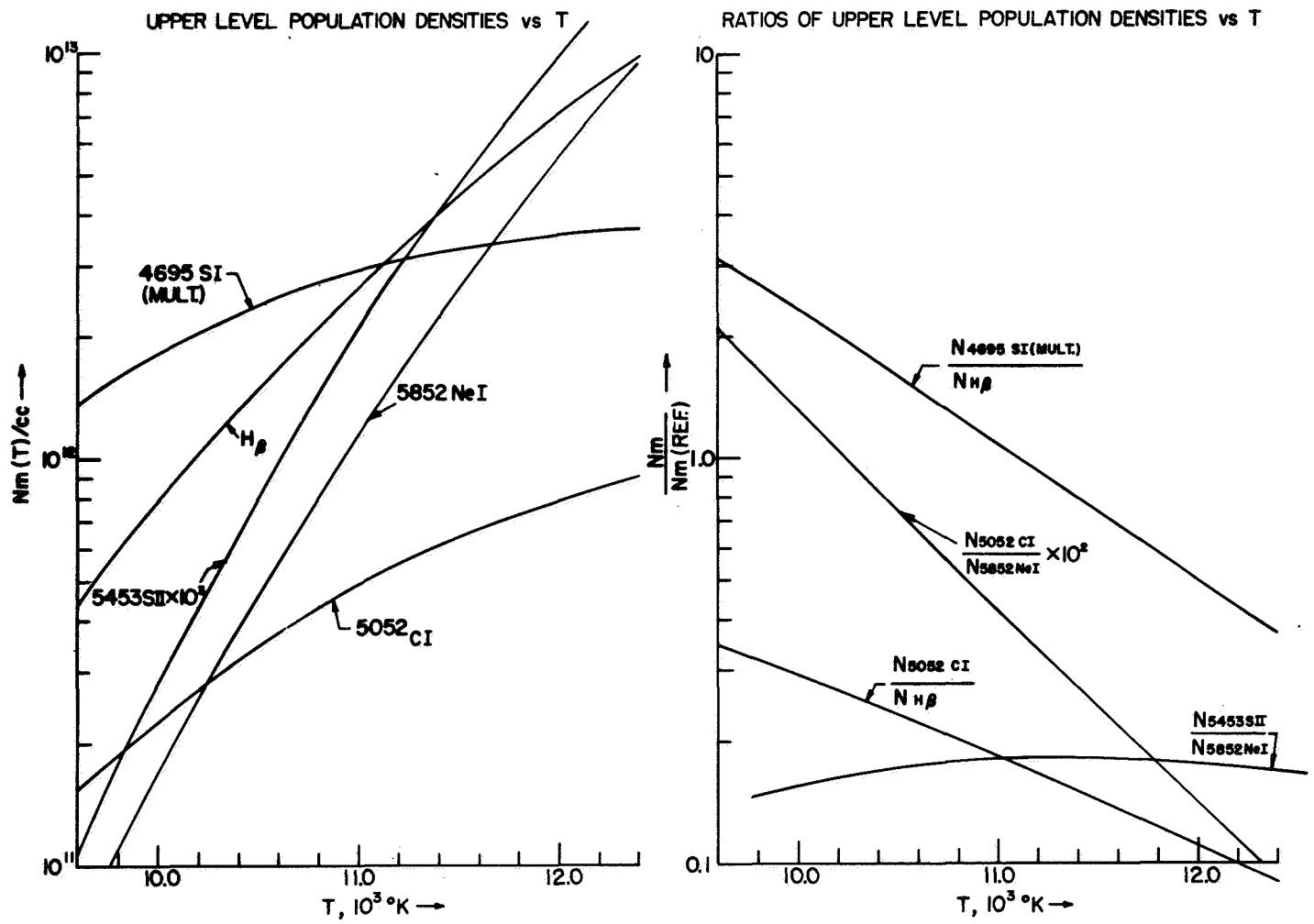


Fig. 5: Excited State Densities and Ratios of Excited State Densities as Functions of Temperature in a Typical Shock Tube Plasma.

C. Introductory TIB Example: The Line CI λ5052Å

The neutral carbon line CI λ5052, (3s - 4p), has an excitation energy of 10.09 ev. It is now singled out for special attention because it is the most easily observed isolated line in the visible CI spectrum.

The left side of Fig. 5 gives excited state population densities as functions of temperature for some prominent lines in a shock tube plasma. Slopes in this semi-logarithmic representation are roughly proportional to excitation energies, as one would expect from Boltzmann equilibrium. The convexity of the curves is due to ionization of neutrals and, to a lesser degree, the inverse relationship between temperature and number density for the assumed condition of constant pressure. Excited state densities for all five lines increase with temperature from 9,600°K to 12,400°K.

However, one can select pairs of these lines to give ratios of population densities which decrease with temperature throughout this 2,800°K range. Three such pairs are shown in the right half of Fig. 5 . In particular, compare the slope of $N_{5052CI}$ on the left with the slope of $N_{5052CI}/N_{H\beta}$ or the right. At 11,000°K these slopes have equal magnitude but opposite sign, i.e.

$$-\frac{\partial}{\partial T} \ln N_{5052CI} \cong \frac{\partial}{\partial T} \ln \frac{N_{5052CI}}{N_{H\beta}}$$

Substitution from eqn. [18] and eqn. [19] gives:

$$\frac{1}{AE_C} \frac{\partial AEc}{\partial T} + \frac{1}{ARH_C} \frac{\partial ARHc}{\partial T} = 0$$

or

$$\frac{\partial}{\partial T} A(TIB)_C = 0$$

where

$AE_C$ = A-value of CI λ5052 measured in absolute emission

$ARH_C$ = A-value of CI λ5052 measured relative to $H_\beta$

$A(TIB)_C \equiv \frac{1}{2}(AE_C + ARH_C)$

$A(TIB)_C$ is the adopted† result for the measurement of CI λ5052.

A quantitative description of how thermal error propagates into the various results $AE_C$, $ARH_C$, and $A(TIB)_C$, is given in Fig. 6 . In this figure T is the measured (or assumed) temperature and $T_o$ = 11,000°K is the true source temperature. The ordinate, $A(T)/A(T_o)$, is the transition probability obtained using the measured temperature normalized against its value when the true source temperature is used: i.e., $A(T)/A(T_o)$ is the relative error propagated into results by the errors $(T-T_o)$ in assumed source temperature.

The equations given at the top of the figure can be used in conjunction with Fig. 5 to extend the range of the display. For compactness we use $N_C = N_{5052CI}$ .

---

†Algebraically, of course, one finds $A(TIB)_C = AE_C = ARH_C =$ an atomic constant. What concerns us here are the inequalities:

$$\frac{\partial}{\partial T} A(TIB)_C \neq \frac{\partial}{\partial T} AE_C \neq \frac{\partial}{\partial T} ARH_C \neq 0.0$$

which are pertinent for computing the error propagated into measured A-values as the result of imperfect temperature determinations.

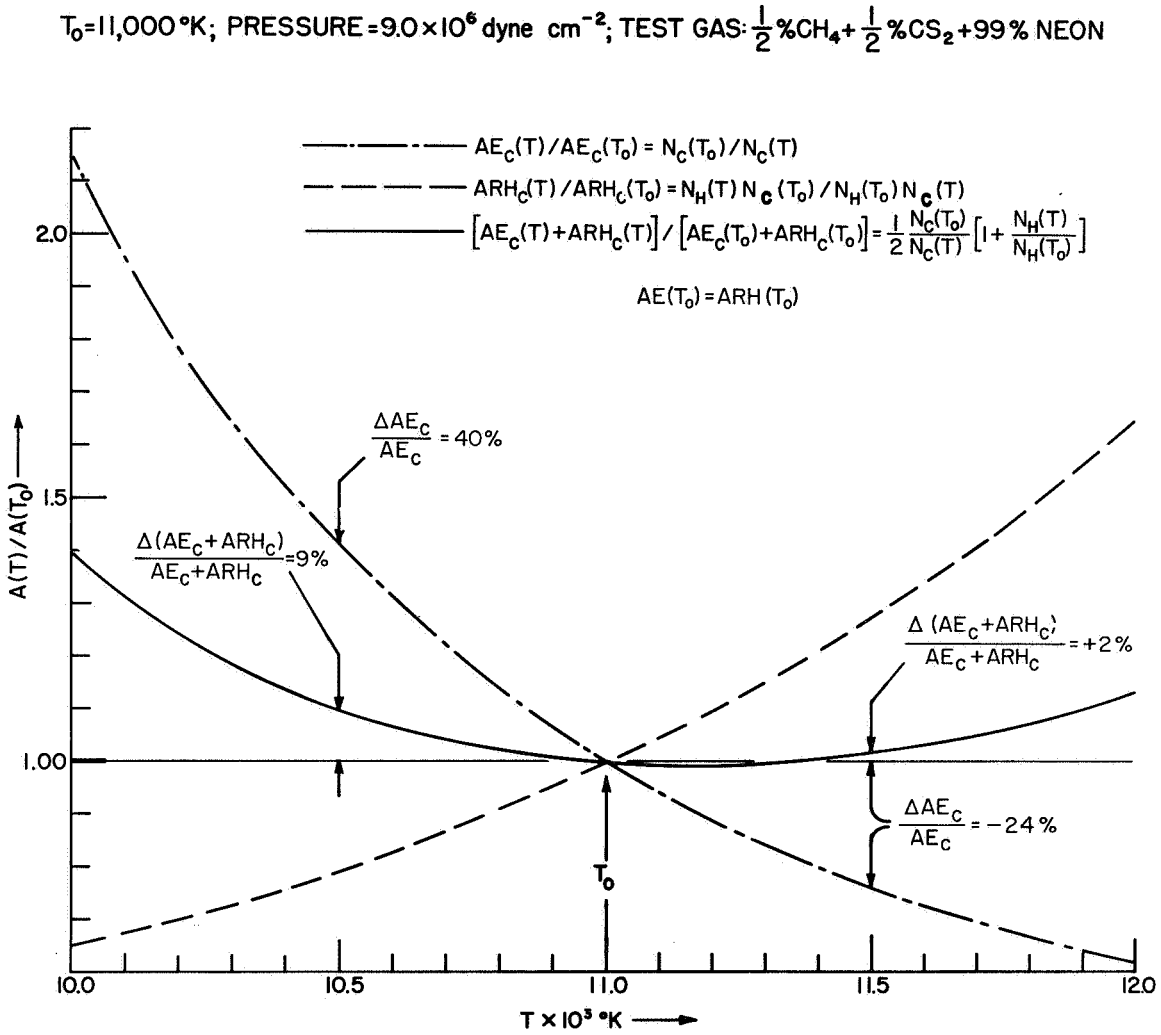


Fig. 6: Relative Thermal Error Propagation in A-Value of CI λ5052 Measured Three Ways: $AE_c$ (Absolute Emission), $ARH_c$ (Trans-Species Relative to $H_\beta$) and ½[$AE_c$ + $ARH_c$] (Thermally Insensitive Method).

If the measured (assumed) temperature is 10,500°K ( -5% error), or is 11,500°K ( +5% error), then the conventional result, $AE_C$ will err by +40% and -24%, respectively. In marked contrast, these temperature errors cause $A(TIB)_C$ to err by only +9% and +2%, respectively.

The <u>range</u> of possible errors for the two results is also strikingly different:

$$-\infty < \frac{AE_C(T)}{AE_C(To)} < +\infty$$

while:

$$1.0 \lesssim \frac{A(TIB)_C(T)}{A(TIB)_C(To)} < +\infty$$

so <u>any</u> error in source temperature can cause $A_C(TIB)_C$ to err only on the high side, i.e., using $A_C(TIB)_C$ one cannot <u>underestimate</u> the true transition probability.

This figure also shows that the TIB method makes less critical, but does not eliminate, the need for reliable temperature determinations. While $\Delta A(TIB)_c/A(TIB)_c \leq \Delta T/T$ for $|T-To|/To \leq 3\%$ , the error in $A(TIB)_c$ does get large when $|T-To|$ gets large since an exponentially increasing term will dominate over an exponentially decreasing term in a sum of the two.

Figure 7 applies the error analysis of Fig. 6 to a pair of hypothetical experiments. In both experiments the true source temperature is 11,000°K, while the hypothetical temperature data (at the top of the figure) form symmetrical distributions. These distributions average 3%

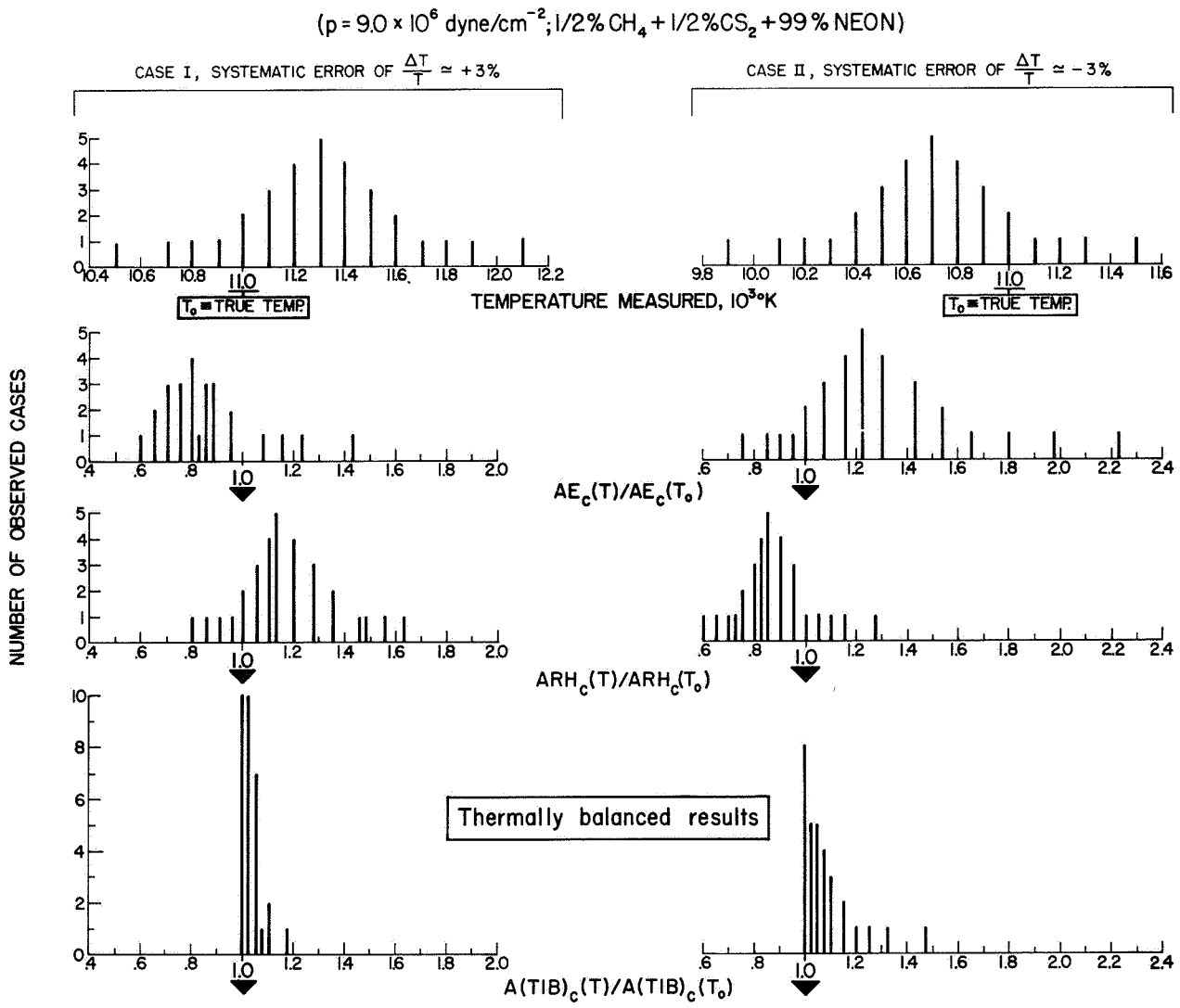


Fig. 7: Thermal Error in Results of Two Hypothetical Experiments Each Measuring the A-Value of CI λ5052 in a Variety of Ways.

too high in Case I (on the left) and 3% too low in Case II (on the right). These synthetic data and Fig. 6 are used to construct distributions of relative (thermal) error in the hypothetical results $AE_c$, $ARH_c$ and $A(TIB)_c$. An experiment conducted in the usual way measures <u>either</u> $AE_c$ <u>or</u> $ARH_c$, but not both, so one would be unaware of the <u>shifts</u> (systematic error) in the averages of the $AE_C(T)/AE_C(T_o)$ or $ARH_C(T)/ARH_C(T_o)$ distributions resulting from the average errors $\Delta\tilde{T}/T_o = \pm 3\%$. The distributions themselves give no clue of <u>shifts</u> since they have sufficient symmetry to pass for Gaussians. If these distributions were treated to standard statistical analysis, RMS deviations of 5% to 10% would be taken as the uncertainty in the averages of the various $AE_c$ and $ARH_c$ distributions. Such tolerances are 2 to 4 times smaller than the real (repeatable) $\pm$ 20% errors in results coming from the $\pm$ 3% systematic errors in the synthetic temperature distribution†.

Evaluation of relative thermal error in the TIB results, $[AE_c(T) + ARH_c(T)]/[AE_c(T_o) + ARH_c(T_o)]$ rests on the interpretation of the highly skewed distributions at the bottom of the figure. Both the reduced scatter in these distributions and their abrupt cut-offs for values $A(TIB)_c(T) < A(TIB)_c(T_o)$ are characteristic of TIB results. The tighter grouping of results is expected from the reduced sensitivity to thermal errors of $A(TIB)_c$. The skewness of the distributions is expected from the essentially parabolic shape of $A(TIB)_c(T)/A(TIB)(T_o)$ as a function of assumed temperature (cf. Fig. 6 ): for cases where the minimum in this curve falls at $T = T_o$, we identify the cut off value in the distribution of TIB results (which should also coincide with

---

†This situation is reminiscent of the literature on line strengths, where disagreements between authors are frequently far in excess of claimed tolerances.

distribution's peak) as the result obtained by use of the true source temperature. Hence, even the reduced scatter in TIB results does not contribute significant uncertainty to the adopted experimental value.

Given this interpretation, the results for $A(TIB)_c$ in both of these hypothetical experiments are seen to be shifted less than -1% by (relative) temperature errors of $\pm$ 3%. This is a twenty-fold reduction in error compared to the conventional ($AE_c$) results.

While the TIB method is intended primarily to minimize propagation of thermal errors, there are additional reasons for preferring it over a conventional emission (AE) measurement. A TIB result has only one half of an AE result's dependence on absolute pressure (or total number density). This is because a TIB result is the average of an AE result, having linear dependence on pressure, with an ARH result, having essentially no dependence on pressure. Furthermore, the TIB result dilutes by one half the linear dependence of AE upon absolute intensity calibrations. That is, ARH measurement requires photometric detectors to be calibrated for change in sensitivity with wavelength. So long as $H_\beta$ and the line studied are separated by only a few hundred Ångstroms, the relative calibrations should have negligible error compared to the absolute intensity calibration required by the AE measurement. With respect to A-values measured the usual (AE) way, the TIB procedure thus halves dependence on two other significant sources of error.

The results $AE_c$, $ARH_c$ and $A(TIB)_c$ from 44 experimental runs using our conventional shock tube are presented in Fig. 8 . To insure the fullest degree of independence between $AE_c$ and $ARH_c$, the absolute

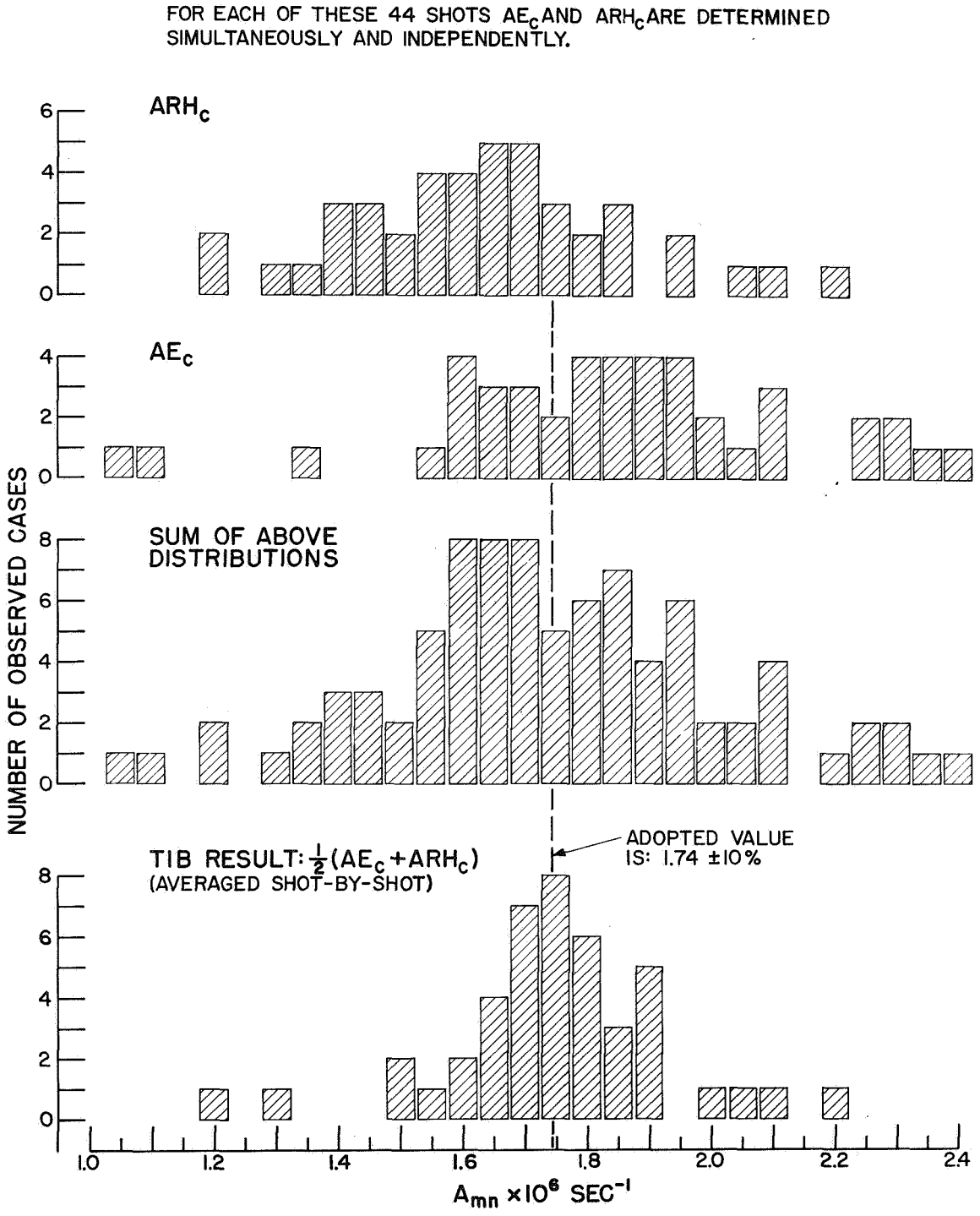


Fig. 8: Current Results for the Transition Probability of CI λ5052: Data From First-Reflected Shocks Using 1%$CH_4$ or ½% $CH_4$ + ½% $CS_2$ Additives.

integrated intensity of CI λ5052 was recorded photoelectrically while the ratio of the integrated intensity of CI λ5052 relative to $H_\beta$ was recorded photographically.

We include in this figure a fourth distribution which is the sum of the $AE_c$ and $ARH_c$ distributions: this is to emphasize that the combined results of two independent experiments, one using $AE_c$ and the other using $ARH_c$, will not be as precise as $A(TIB)_c$ results which utilize on a run-by-run basis, the relationship between the thermal dependences of $AE_c$ and $ARH_c$.

We draw attention to several features in this display. Scatter in the current TIB results is considerably less than in either the current $AE_c$ or $ARH_c$ results. The distribution of the current $AE_c$ results is skewed with respect to the distribution of $ARH_c$ results. The shape of the distribution of current TIB results does not closely resemble that for TIB results in the hypothetical experiments of Fig. 7 : moreover, the reduction in scatter of current TIB results relative to $AE_c$ or $ARH_c$ results is not as pronounced as in the corresponding distributions of Fig. 7 . We comment on each of these (four) observations in turn.

The scatter in the current TIB results is expected to be less than for $AE_c$ or $ARH_c$ results because our measured temperatures contain random error. Even though we average four independent temperature (cf. Chapter VI) determinations, we still are still left with a 1% - 1.5% scatter in our best estimated temperatures. According to Fig. 6 such a scatter in temperature should produce roughly a 7% - 12% scatter in $AE_c$ and $ARH_c$ but not more than 1% scatter in $A(TIB)_c$ . Returning to Fig. 8 we find the spreads in the various distributions do conform quantitatively to these error estimates: RMS scatter in $AE_c$ and $ARH_c$ is

about 15% as opposed to 7% for the TIB results, i.e. 8% greater.

The current results show a 10% discrepancy between the averages of the $AE_c$ and $ARH_c$ distributions. If repeatable errors in temperature were the sole source of systematic error, then this discrepancy could be ascribed (cf. Fig.6 ) to temperatures consistently measured 1% too low. However, other systematic errors, particularly in photometry, (cf. Chapter VI), could be wholly or partially responsible for this discrepancy. In either case, TIB provides the most reasonable measurement: if the error source is temperature, then TIB insures that results will be affected not more than 1%; if the error is in some unspecified variable, TIB has the advantage that it averages two independent results each relying on measured variables in a different way.

There are two reasons why the current TIB results do not cut off abruptly for values less than those where the distribution peaks. While results of the hypothetical experiments of Fig. 7 are subject only to errors in source temperature, and were all "gathered" in the vicinity of a single source temperature, 11,000°K, and at a constant source pressure, the current results are influenced by a variety of errors (cf. Chapters VI and VII), and data were taken over a 2,500°K range of temperatures and a range of pressures varying by a factor of 4. Each source of random error superimposes its own Gaussian distribution onto the idealized results of Fig. 7 , causing them both to broaden and take on values for $A(TIB)_c(T) < A(TIB)_c(T_o)$ . As will be demonstrated in the next section, for different combinations of source pressure and temperature one obtains families of $A_c(TIB)$ curves similar to, but varying in detail from, that shown in Fig. 6 . For this reason one expects that even the idealized experiments, such as those in Fig. 7 , will give results as low as

$A(TIB)_c(T) = .92A(TIB)_c(T_o)$ if conducted over equally wide ranges of source conditions.

The current experiment is not typical in that temperatures were simultaneously measured four independent ways whereas one temperature determination is usually made to suffice. Also the line studied, CI λ5052 , was so faint that photometric noise limited integrated intensity precisions to 10% - 20%, so scatter introduced into $AE_c$ and $ARH_c$ by random photometric errors is as great as scatter originating in random temperature errors. To present a more representative example of how TIB will influence results of a typical experiment, we deduce a new set of A-values from the same data used for Fig. 8 , only now we use the single temperature, $T_{neon}$ , deduced from the integrated intensity of NeI λ5852 rather than the average of four temperatures, as previously. This set of results is presented in Fig. 9 , where TIB is seen to affect approximately a threefold reduction in scatter.

### D. General Applicability of TIB to the Study of Light Elements

So far, we have demonstrated the clear superiority of the TIB method for measuring a particular A-value, CI λ5052 , using a shock tube plasma of prescribed temperature, pressure and composition. We now attempt to show that TIB is a general experimental technique that can be used to advantage in measuring the A-values of most light elements and their ions. In playing off the opposing thermal dependence of various spectral lines, the validity of TIB depends only on whether or not the plasma is in LTE . The method is not restricted to any specific type of thermal source or confined to a particular pressure-temperature domain.

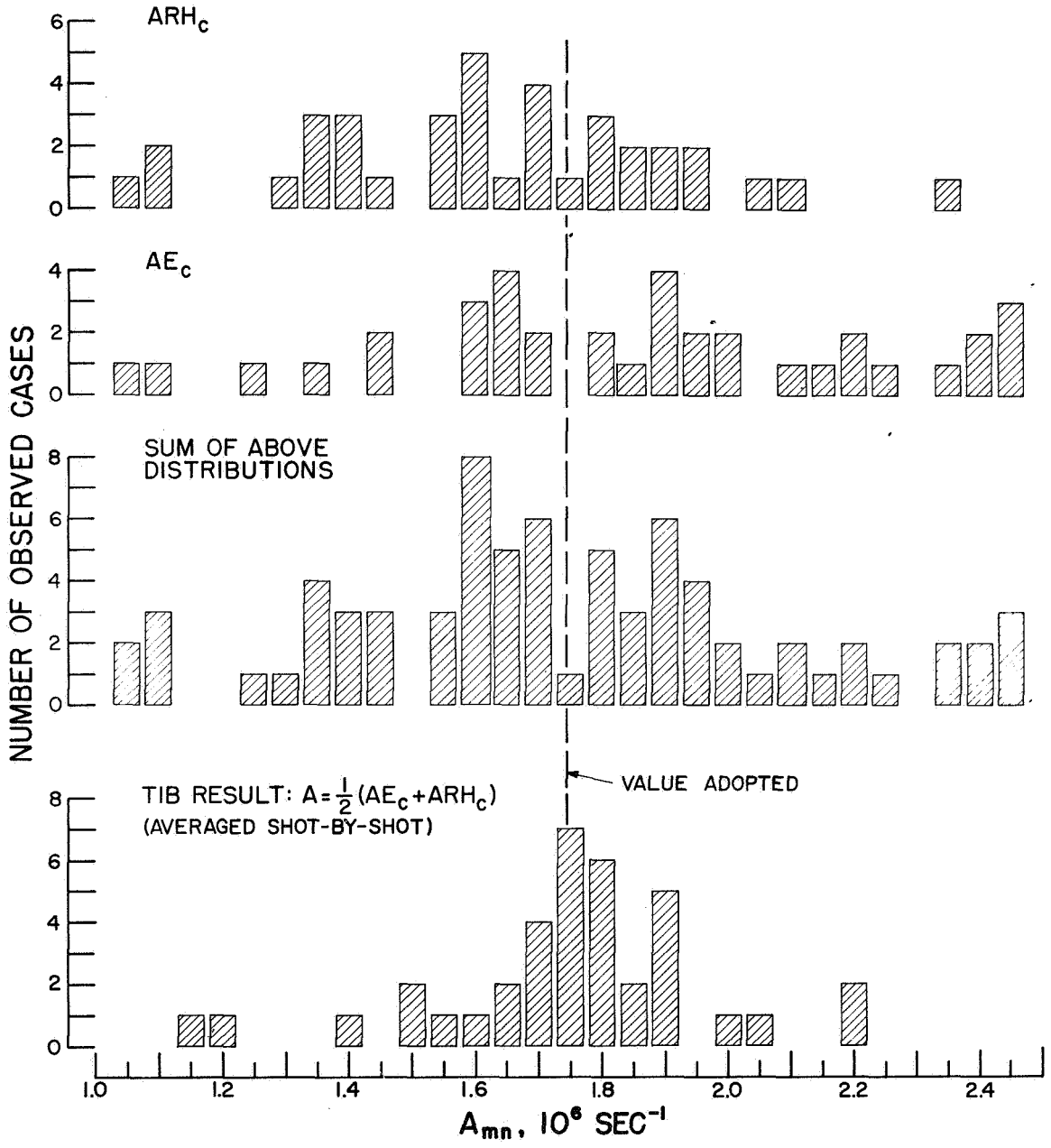


Fig. 9: Reduction in Scatter Due to TIB for an Experiment Employing a Single Means of Temperature Determination: Data for 37 Runs Shown in Figure 8 Re-Evaluated Using $T = T_{neon}$ Rather Than $\tilde{T} = T = \frac{1}{4}(T_{neon} + T_{\alpha} + T_{\beta} + T_{\lambda_{1/2}})$ .

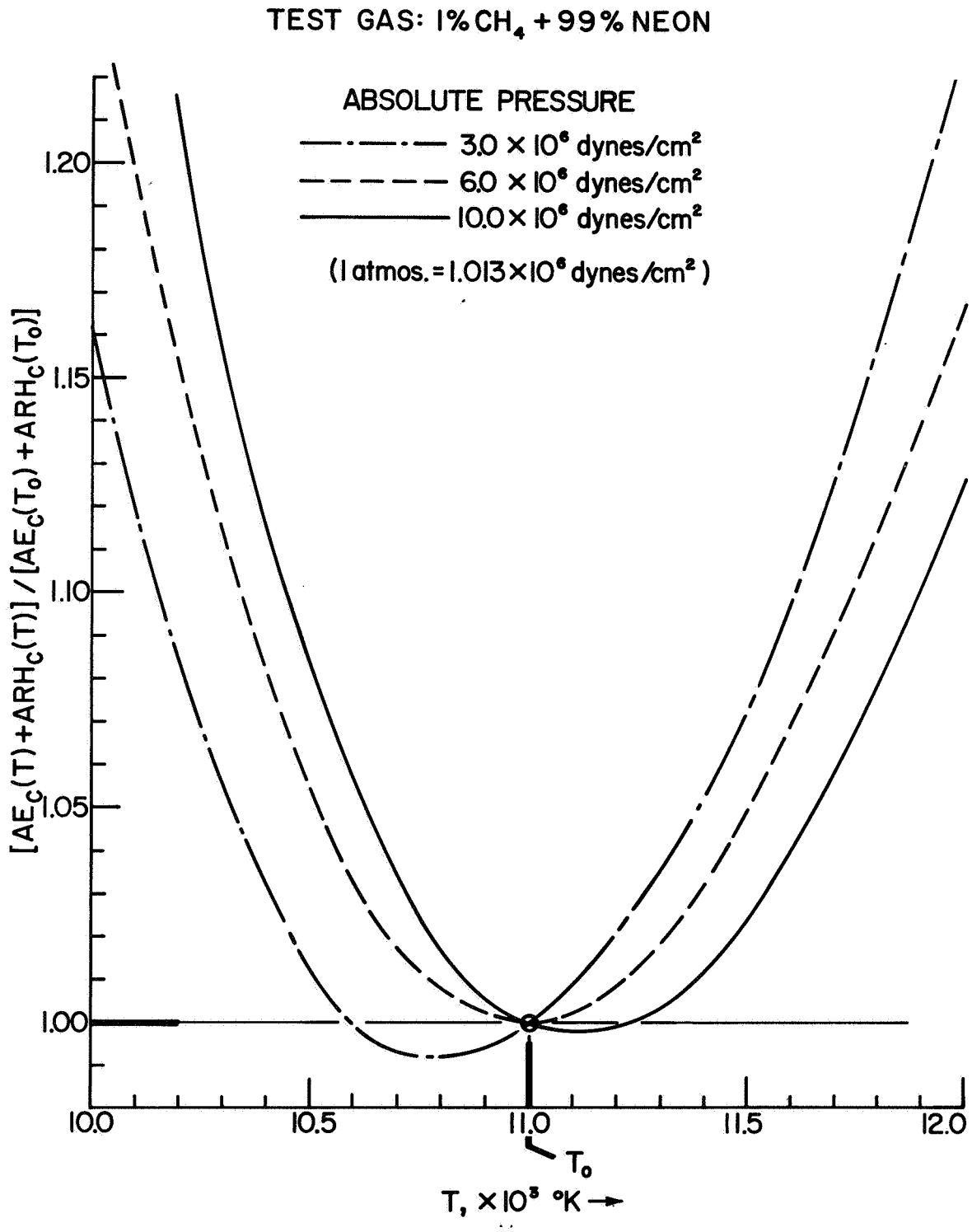


Fig. 10: Dependence of Thermal Balancing, $A(TIB)_C = [AE_C + ARH_C]$, Upon Absolute Plasma Pressure.

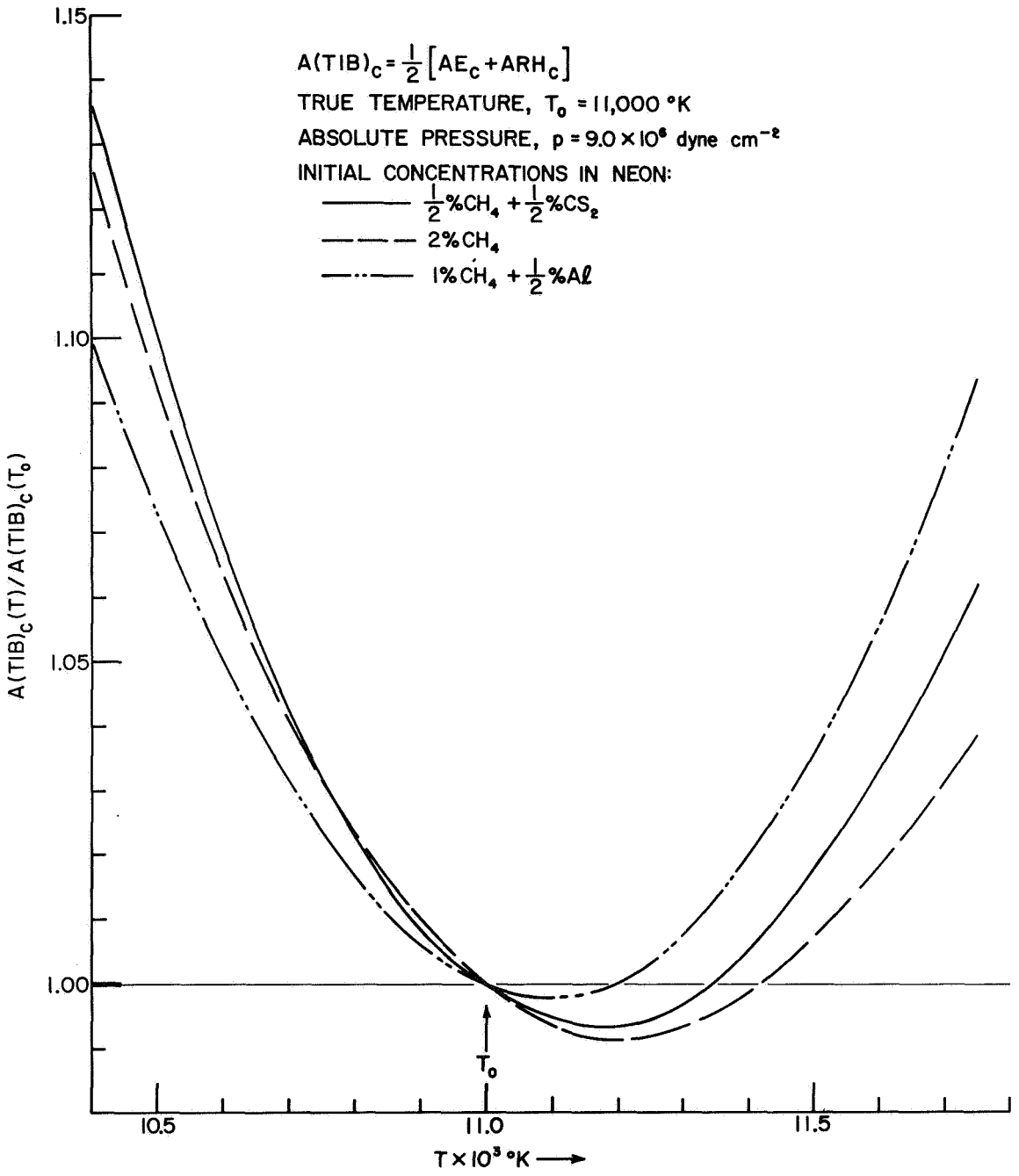


Fig. 11: Dependence of Thermal Balancing on Concentration of Spectroscopic Additive Gas.

Our arguments concerning the general applicability of TIB will be illustrated with concrete examples, most of which were encountered in the present shock tube studies of the light elements. These are presented in the following sequence:

(1) The A-value of CI λ5052 is studied by the same TIB methods used in the introductory example, but with plasmas of varied pressure, composition and temperature.

(2) The A-value of CI λ5052 is studied using the same plasma conditions as in the introductory example, but a variety of TIB techniques are employed.

(3) Using the same plasma as in the introductory example, we apply several TIB techniques to measure the A-value of SI λλ4695.

(4) TIB techniques are applied to the measurement of PII λ5253 , and AℓII λ5593 .

(5) Finally, to show where TIB cannot improve upon simpler methods, we discuss the measurement of SiI λ5948 , SiII λλ6347 and SII λ5453 .

Figure 10 shows that the thermal sensitivity of $A(TIB)_c = \frac{1}{2}[AE_c + ARH_c]$ changes little with factor of 3 changes in absolute source pressure. (Since the source temperature, $T_o$ , is constant, the factor of 3 change in absolute pressure is equivalent to a factor of 3 change in total particle number density.) Because the ordinate in this graph is drawn on an expanded scale, we see some details that were not immediately apparent in Fig. 6 : the minimum in $A(TIB)_c(T)$ does not always occur exactly at $T = T_o$ , and the minimum value of $A(TIB)_c(T)/A(TIB)_c(T_o)$ can be slightly less than unity.

When source temperature and pressure are held constant, the thermal dependence of $A(TIB)_c$ is little changed by varying the spectroscopic additive used in the test gas, as shown in Fig. 11 . For the test gas composed of 1% $CH_4$ and 98.5% neon,we include a relative concentration

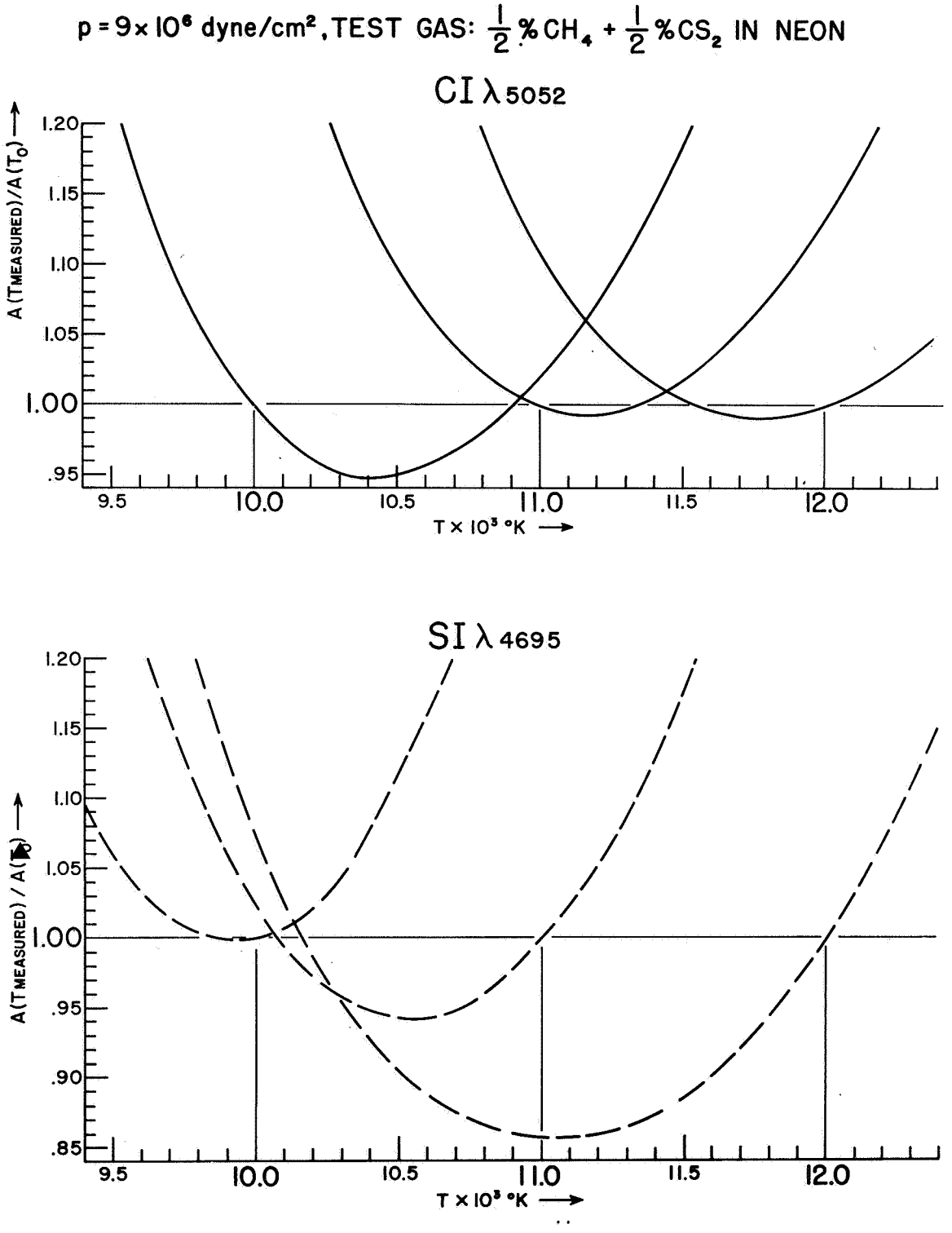


Fig. 12: Dependence of Thermal Balancing on True Source Temperature: Relative Thermal Sensitivity in A(TIB) = (AE+ARH) for CI λ5052 and for SI λλ 4695 at $T_o$ = 10,000°K, 11,000°K and 12,000°K .

of .5% aluminum. The aluminum is included here to show that readily ionized impurities have only small affect on the behavior of $A(TIB)_c$ .

The top half of Fig.12 shows how $A(TIB)_c(T)/A(TIB)_c(T_o)$ varies with $T_o$ when absolute pressure and plasma composition are fixed. Anywhere within the depicted 2000°K range of temperature a relative error of $\pm$ 3% in source temperature will cause less than 5% error in the measured A-value. On closer scrutiny, the figure shows that there is a preferred temperature range for application of TIB . For $T_o$ about midway between $T_o$ = 11,000°K and $T_o$ = 12,000°K A(TIB) will be optimal in two ways: $\left|\frac{\partial}{\partial T} A(TIB)_c\right|$ will remain small over a wider range of $T - T_o$ than elsewhere in the figure, and, the minimal value of $A(TIB)_c(T)/A(TIB)_c(T_o)$ will be 1.00, rather than say, .95, so there will be less ambiguity in interpreting the distribution of experimental results. That is, the low end cut-off in the distribution of results gives the desired A-value precisely.

If $A(TIB)_c = \frac{1}{2}(AE_c + ARH_c)$ does not give a desired insensitivity to errors in temperature, the experimentalist may still be able to obtain thermally insensitive results in one of two ways. If he has the freedom to operate the source over wide ranges of pressure and temperature, he may be able to tailor plasma conditions so that $A(TIB)_c$ does have the desired freedom from thermal errors. However, we have seen that for source temperatures in neighborhood of 1 eV (11,600°K), even quite drastic changes in pressure, in type of additive, or in temperature, have only a minor effect on the thermal sensitivity of $A(TIB)_c$ . This is because at $kT \approx 1$ eV it is Boltzmann equilibrium, rather than Saha equilibrium, which determines the gross thermal dependence of CI λ5052 excited state population densities. So maneuvers to influence $\frac{\partial}{\partial T} A(TIB)_c$ by shifting

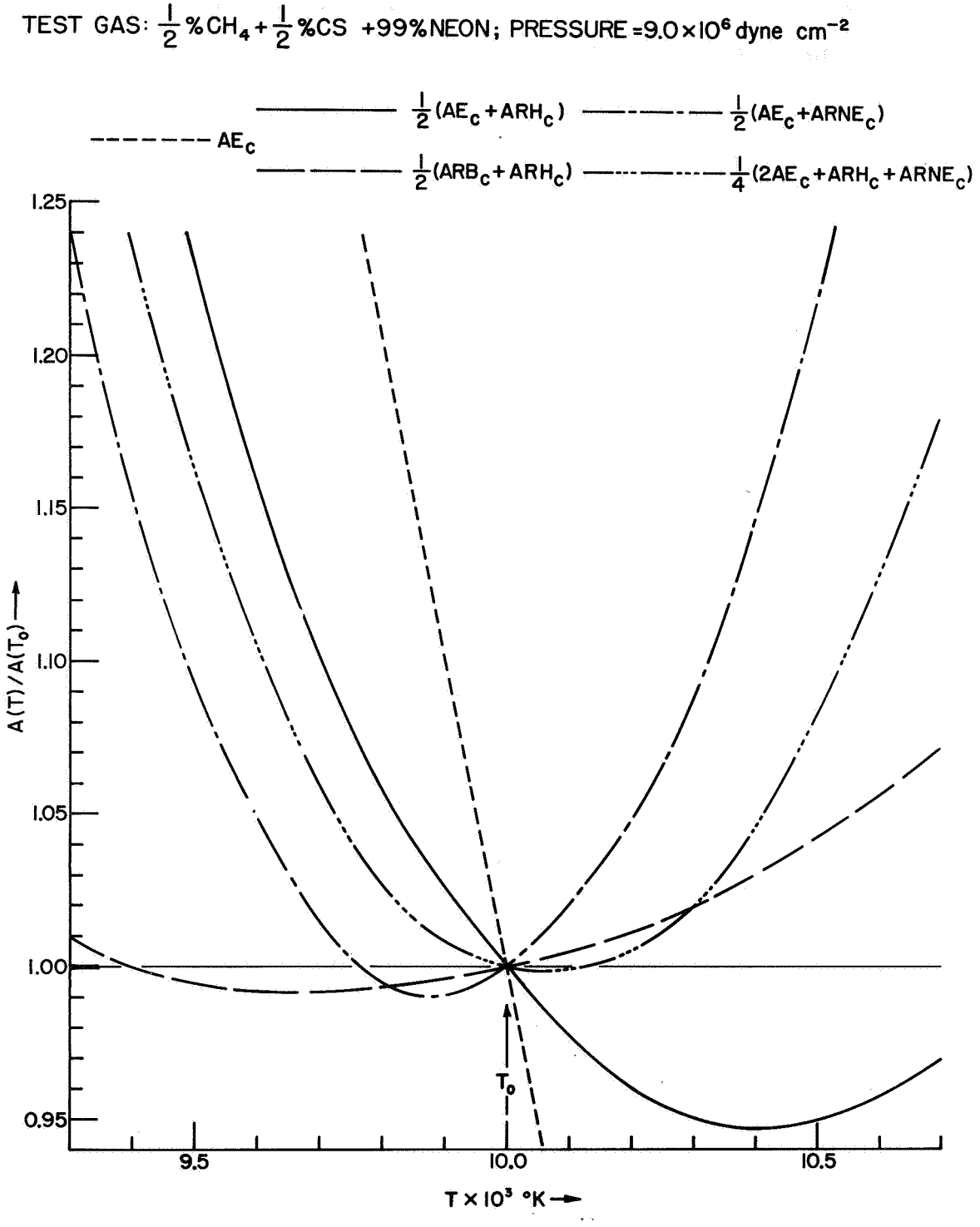


Fig. 13-A: Relative Thermal Sensitivity in the A-Value of CI λ5052 Measured Five Ways, at 10,000°K True Source Temperature ($T_o$).

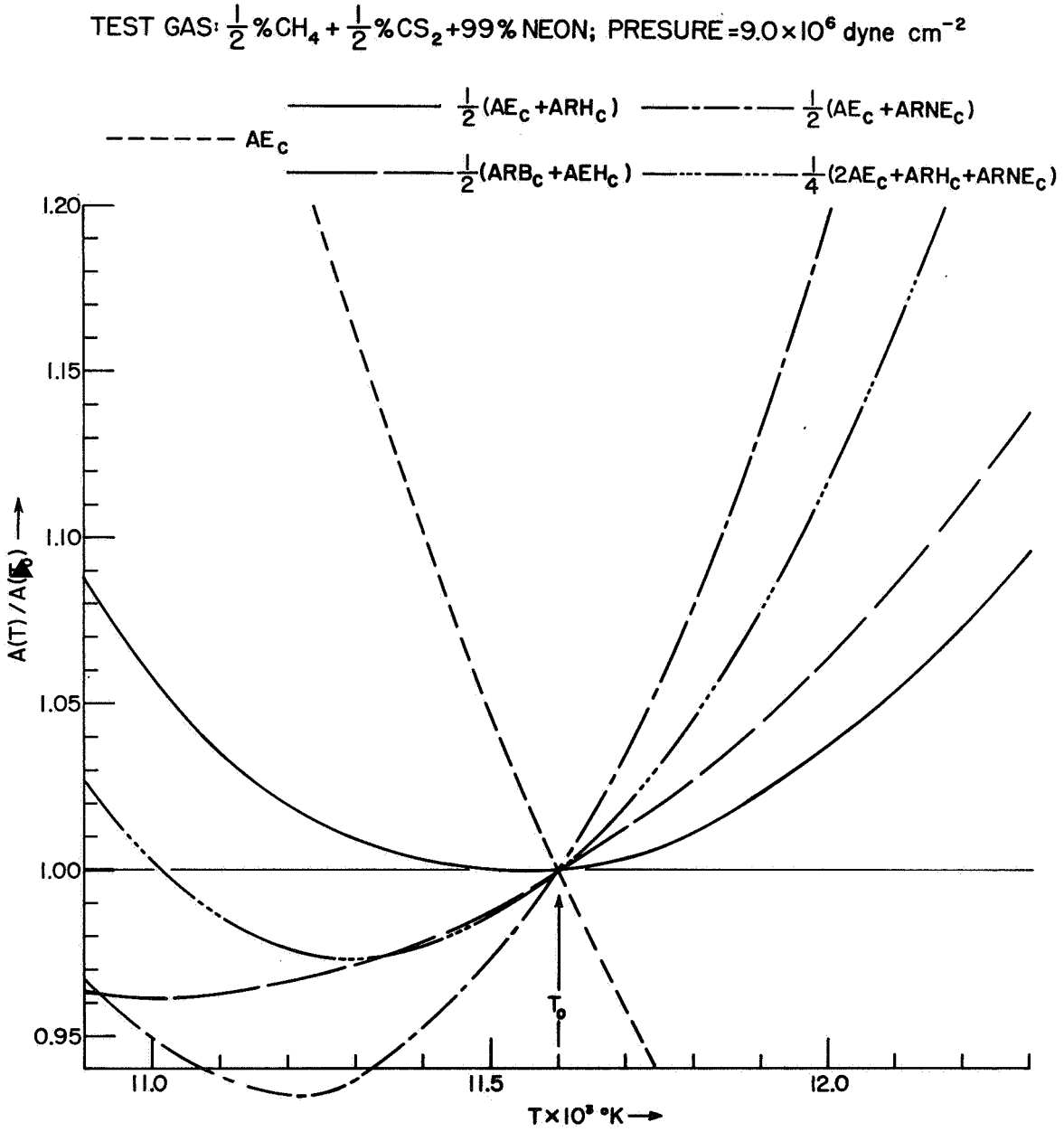


Fig. 13-B: Relative Thermal Sensitivity in the A-Value of CI λ5052 Measured Five Ways, at 11,600°K True Source Temperature ($T_o$) .

Saha equilibrium will usually tax the versatility of most laboratory sources.

The other tactic is to measure the A-value of CI λ5052 by combinations of ways better suited to TIB under normal source conditions than is $\frac{1}{2}[AE_c + ARH_c]$ . Figures 13A and 13B show the relative thermal error propagated into results of three such alternative sets of measurements, (in addition to $\frac{1}{2}[AE_c + ARH_c]$), at the two source temperatures $T_o = 10{,}000°K$ and $T_o = 11{,}600°K$ , respectively.

Two of the A-value determinations introduced here, $ARN_c$ and $ARB_c$ , make use of internal standards other than $H_\beta$ †. $ARN_c$ is the A-value of CI λ5052 deduced from the trans-species relative intensity measurement using NeI λ5852 as the internal standard. Because of the estimated 10% uncertainty in the absolute A-value of this line[13], the TIB result $\frac{1}{2}[AE_c + ARN_c]$ will be inherently uncertain by 5% . $ARB_c$ is the CI λ5052 A-value deduced from a trans-species relative intensity measurement relying on a slit-integrated portion of $H_\alpha$ as the internal standard.

For use as an internal standard the slit-integrated central portion of $H_\alpha$ (whose analytical expression is given by eqn. [17]) offers the advantage that its thermal dependence can be conveniently varied according to the needs of TIB by making use of the laws of radiative

---

†Whenever it is feasible from the standpoint of thermal error propagation, one likes to work with hydrogen Balmer lines as internal standards for a variety of reasons: their A-values are the most precisely known; hydrogen is an almost universal constituent in the volatile compounds used as spectroscopic additive gases so that the relative concentrations of hydrogen and the atom of interest are precisely set by stoicheometric ratios; and from the easily measured $H_\beta$ Stark width one can readily infer plasma temperature from electron density.

transfer. That is, the slit integrated intensity of $H_\alpha$ can be given the slowly varying thermal dependence of the Planck function (at $\lambda = 6562$) if the mean observed optical depth, $\tilde{\tau}$, is made large. At a fixed source temperature $\tilde{\tau}$ can be increased by reducing the slit width, and by using a combination of absolute source pressure and spectroscopic additive concentration designed to increase hydrogen number densities while keeping electron densities low. If, however, TIB requires it, the slit integrated intensity of $H_\alpha$ can be given a stronger thermal dependence by reducing $\tilde{\tau}$. In the limit $\tilde{\tau} \to 0$, however, $H_\beta$ would be a preferable internal standard unless optically thin $H_\alpha$ is completely integrated, since there is considerable uncertainty in the Stark width of $H_\alpha$[56].

The curve $A(TIB)_c = \frac{1}{4}(2AE_c + ARH_c + ARN_c)$, illustrates another TIB option: it often happens that averaging two TIB results, here $\frac{1}{2}[AE_c + ARH_c]$ and $\frac{1}{2}[AE_c + ARN_c]$, will produce results of lesser thermal sensitivity than either of them separately. Whether or not such a composite measurement becomes too tedious depends on whether photographic or photoelectric spectroscopic recording is used.

Returning to Fig.13A, we find that for $T_o = 10{,}000°K$ the five depicted methods of measuring CI $\lambda 5052$ can be ranked in order of decreasing sensitivity to thermal errors as follows: $AE_c$, $\frac{1}{2}[AE_c + ARH_c]$, $\frac{1}{2}[AE_c + ARN_c]$, $\frac{1}{4}[2AE_c + ARH_c + ARN_c]$, and $\frac{1}{2}[ARB_c + ARH_c]$. A similar comparison at $T_o = 11{,}600°K$ (cf. Fig.13B) shows that while $AE_c$ remains the A-value measurement most vulnerable to thermal error, the various TIB methods have shifted quite markedly in their relative thermal sensitivities. We now find that the arrangement, in order of decreasing sensitivity, is: $\frac{1}{2}[AE_c + ARN_c]$, $\frac{1}{2}[ARB_c + ARH_c]$, $\frac{1}{4}[2AE_c + ARH_c + ARN_c]$, and $\frac{1}{2}[AE_c + ARH_c]$.

The example, $A(TIB)_c = \frac{1}{4}[2AE_c + ARH_c + ARN_c]$ quite often leads to speculation regarding the use of a weighted average of two independent A-value determinations to form a TIB result. It might at first appear, for instance, that one could maintain a desired level of thermal insensitivity in the combination of $AE_c$ and $ARH_c$[†] regardless of $T_o$ simply by introducing a weight-factor $\alpha$, such that:

$$A(TIB)_c = \frac{1}{1+\alpha} [AE_c + \alpha\, ARH_c]$$

with $\alpha$ defined by

$$\alpha = - \left. \frac{\frac{\partial AE_c}{\partial T}}{\frac{\partial ARH_c}{\partial T}} \right]_{T_o}$$

Unfortunately, such a procedure is fallacious on two counts. First, the more $\alpha$ departs from unity the more important it becomes that $T_o$ is known precisely. That is, $\alpha$ itself introduces sensitivity to temperature errors. Secondly, setting $\alpha$ greater than unity makes the assertion that $ARH_c$ is a more accurate result than $AE_c$, which may not be at all warranted by the circumstances of the experiment.

We now discuss application of TIB to the measurement of SI λλ4695. The spectroscopic source is the same plasma we have already considered: a test gas initially composed of ½% $CH_4$ + ½% $CS_2$ + 99% neon, at a pressure of $9.0\times10^6$ dyne $cm^{-2}$, and at temperatures between 10,000°K and 12,000°K. While the objectives of TIB, and the basic techniques used to achieve them, remain the same for SI λλ4695 as for CI λ5052, we use this sulfur line to illustrate how TIB is affected when atoms are

---

[†]That is, so long as $\frac{\partial}{\partial T} \ln N_c$ was of opposite sign from $\frac{\partial}{\partial T} \ln\left(\frac{N_c}{NH_\beta}\right)$.

readily ionized. That is, because of the .9 eV difference in their ionization potentials, at $kT \approx 1$ eV the thermal dependences of SI λλ4695 and of CI λ5052 are qualitatively different: while CI λ5052 depends on temperature essentially through a Boltzmann term, the behavior of SI λλ4695 is strongly influenced by Saha equilibrium (cf. Fig.5 ).

The strong influence of Saha equilibrium can complicate a proposed application of TIB -- but in some situations it can also be used to advantage. The bottom half of Fig. 12 shows the thermal sensitivity of $A(TIB)_{SI} = \frac{1}{2}[AE_{SI} + ARH_{SI}]$ at true source temperatures of 10,000°K, 11,000°K and 12,000°K , where

$AE_{SI}$ = A-value of SI λλ4695 measured in absolute emission,

$ARH_{SI}$ = A-value of SI λλ4695 measured relative to $H_\beta$ .

We see that the utility of this TIB measurement rapidly diminishes in going from source temperatures of 10,000°K to 12,000°K. For $T_o$ = 10,000°K the $\frac{A(TIB)_{SI}(T)}{A(TIB)_{SI}(T_o)}$ curve has a minimum value of 1.00 lying within 1% of $T_o$ , so here $A(TIB)_{SI}$ is virtually insensitive to the usual errors in source temperature. At $T_o$ = 11,000°K TIB affords about the same protection to SI λλ4695 as it does to CI λ5052 (in the upper half of the figure) at $T_o$ = 10,000°K. To employ $A(TIB)_{SI}$ at $T_o$ = 12,000°K, however, only defeats the primary purpose of TIB since

$$\left| \frac{\partial A(TIB)_{SI}}{\partial T} \right|_{T_o = 12,000} > \left| \frac{\partial AE_{SI}}{\partial T} \right| .$$

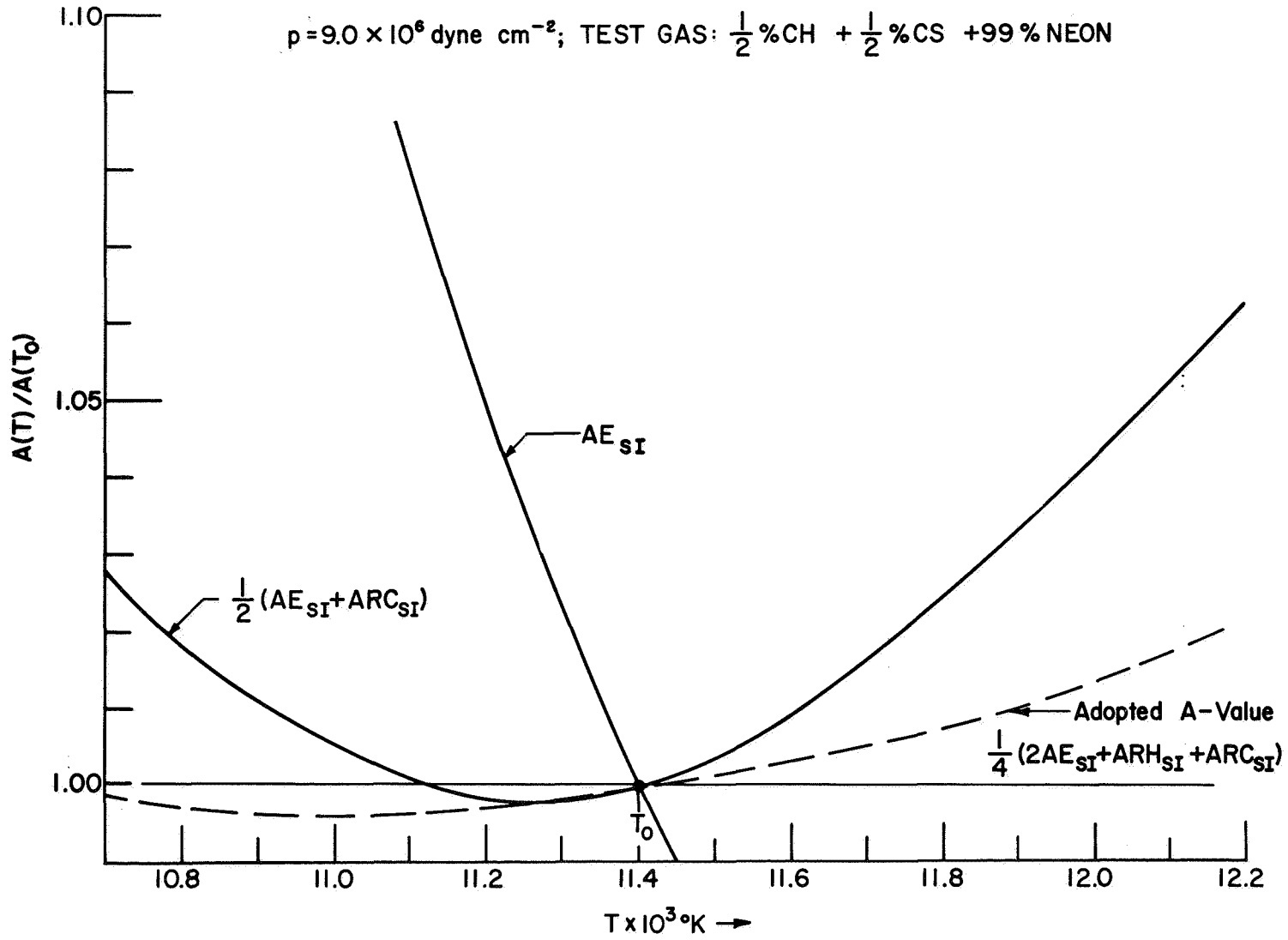


Fig. 14: Thermal Balancing of SI λλ4695 Using the Trans-Species Measurement Relative to CI λ5052 , $ARC_{SI}$ .

If SI λλ4695 is the A-value of primary interest the source should be operated at 10,000°K ; if both SI λλ4695 and CI λ5052 are to be measured simultaneously and with equal accuracy, then a source temperature slightly below 11,000°K should be used.

Because $\frac{\partial}{\partial T}$ $A(TIB)_{SI}$ is quite responsive (unlike $\frac{\partial}{\partial T} A(TIB)_c$) to changes in plasma conditions, the spectroscopist can purposely shift Saha equilibrium to optimize the accuracy of TIB results. For instance, if for the source conditions initially chosen:

$$\left| \frac{\partial}{\partial T} \ln N_{SI\ \lambda\lambda 4695} \right| < \left| \frac{\partial}{\partial T} \ln \left( \frac{N_{SI\ \lambda\lambda 4695}}{N_{H\beta}} \right) \right| ,$$

the inequality can be reduced, or removed, by raising absolute source pressure, increasing the relative sulfur concentration in the test gas, and lowering the source temperature.

One other means of applying TIB to SI λλ4695 is illustrated in Fig. 14 . If the A-value of CI λ5052 is known with a reliability comparable to what we hope to achieve for SI λ4695 (as is the case in the current shock tube studies), then it can be used as the internal standard in a trans-species relative intensity measurement. We denote the SI λλ4695 A-value deduced from this measurement as $ARC_{SI}$ . As Fig. 14 shows, at $T_o$ = 11,400°K the thermal dependence in $A(TIB)_{SI} = \frac{1}{2}[AE_{SI} + ARC_{SI}]$ is far less than in $A(TIB)_{SI} = \frac{1}{2}[AE_{SI} + ARH_{SI}]$.

We pause momentarily to inquire why various $A(TIB)(T)/A(TIB)(T_o)$ curves do not all have the same shape.

Assume that the excited state densities of some line, χ , and $H_\beta$ both have only the thermal dependence found in their respective Boltzmann terms:

$$N_\chi \sim e^{E_\chi/kT} \quad , \quad N_{\chi/NH_\beta} \sim e^{-[E_\chi - E_{H_\beta}]/kT} \quad .$$

Then,

$$\frac{\partial}{\partial T} \; [AE_\chi + ARH_\chi] = \frac{\partial}{\partial T} \; [A(TIB)_\chi] \underset{T=T_o}{=} 0$$

gives

$$E_\chi = E_{H_\beta} - E_\chi$$

while

$$\frac{\frac{1}{2}[AE\ (T) + ARH\ (T)]}{\frac{1}{2}[AE\ (T_o + ARH\ (T_o)]} = \frac{1}{2}[e^{\frac{E}{kT_o}(1-\frac{T_o}{T})} + e^{\frac{E}{kT_o}(1-\frac{T_o}{T})}] \quad .$$

If $(T-T_o)/T_o$ is very small,

$$\frac{\frac{1}{2}[AE\ (T) + ARH\ (T)]}{\frac{1}{2}[AE\ (T_o) + ARH\ (T_o)]} \cong 1 + \frac{1}{2}\left[\frac{E}{kT_o}\right]^2 \left[\frac{T-T_o}{T_o}\right]^2 + \frac{1}{12}\left[\frac{E}{kT_o}\right]^4 \left[\frac{T-T_o}{T_o}\right]^4 + \cdots \quad .$$

So if we neglect Saha equilibrium, and the thermal dependence due to partition functions and the ideal gas law, then curves of $A(TIB)(T)/A(TIB)(T_o)$ will have the following idealized properties: the minimum in the curves will always occur at $T = T_o$ , and the curves will be symmetrical in $(T-T_o)$, and will have a parabolic shape in regions where $\left|\frac{T-T_o}{T_o}\right|$ is small.

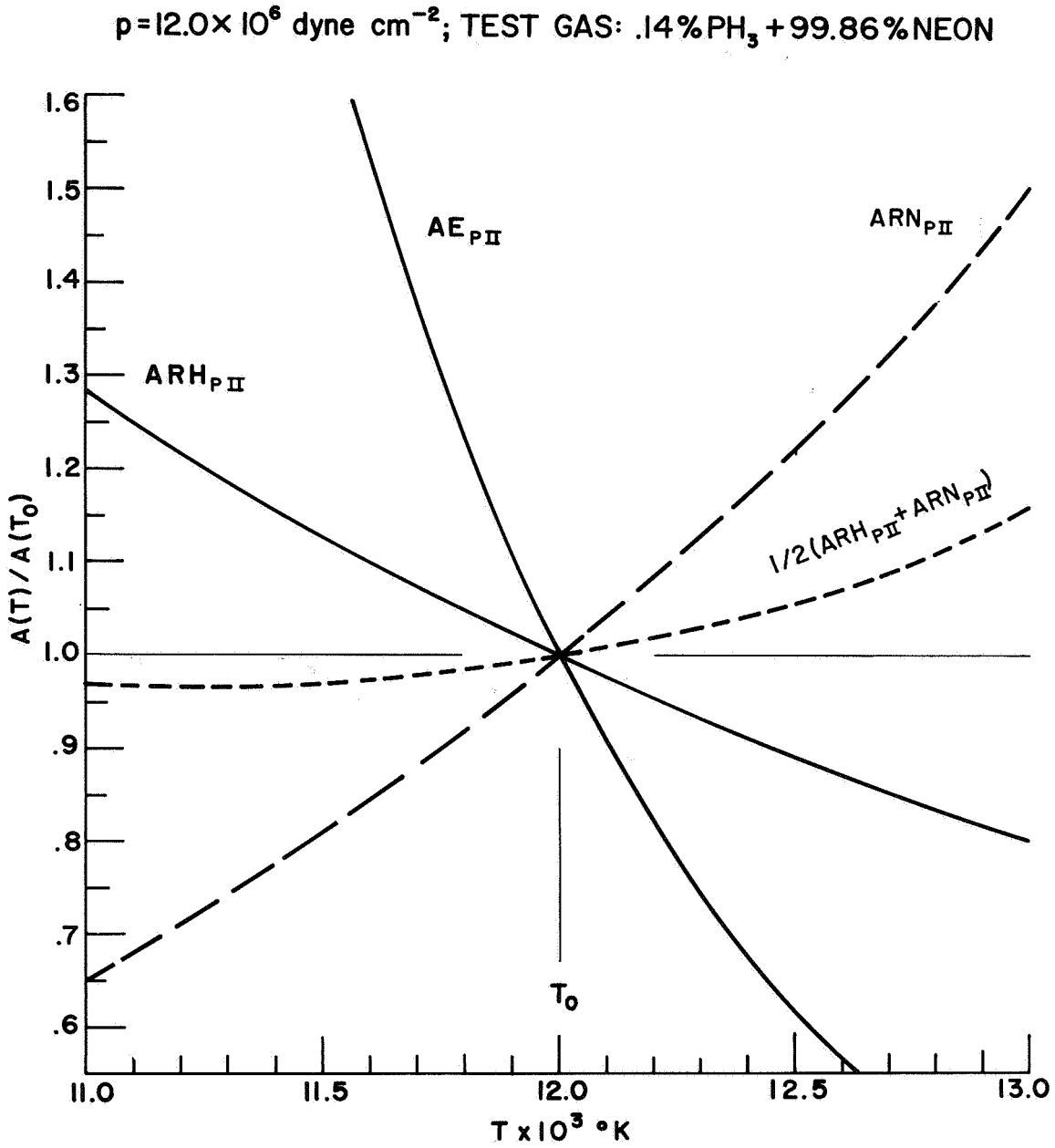


Fig. 15: Relative Thermal Error in the A-Value of PII λ5253 Measured Four Ways.

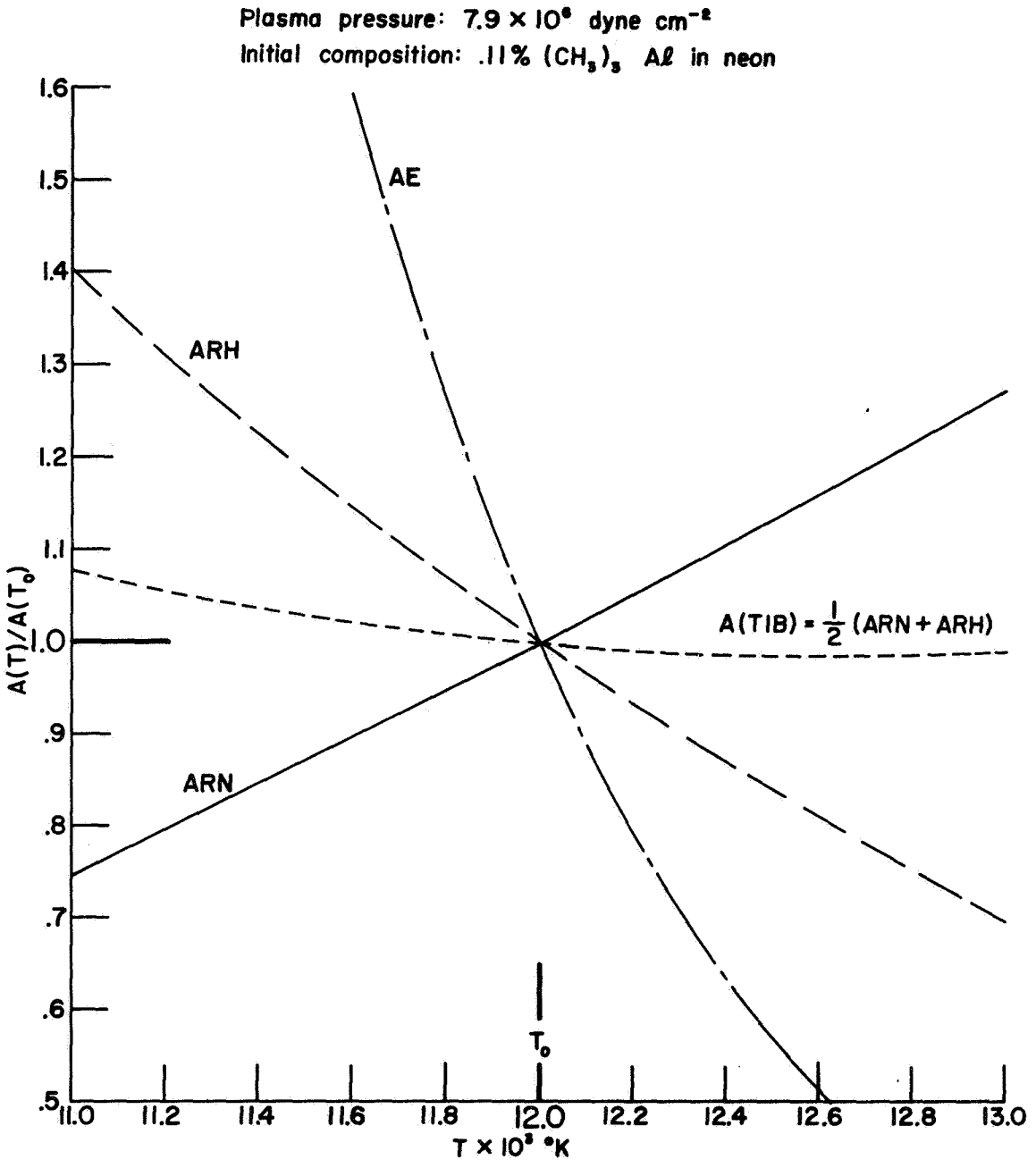


Fig. 16: Relative Thermal Error in the A-Value of AℓII λ5593 Measured Four Ways.

Now consider two applications of TIB <u>which require no absolute intensity measurements</u>:

$$A(TIB)_{PII} = \tfrac{1}{2}[ARH_{PII} + ARN_{PII}]$$

and

$$A(TIB)_{A\ II} = \tfrac{1}{2}[ARH_{A\ell II} + ARN_{A\ell II}] \quad .$$

Here, $ARH_{PII}$ and $ARN_{PII}$ are the A-values of PII $\lambda 5253$ deduced from trans-species relative intensity measurements using $H_\beta$ and NeI $\lambda 5852$, respectively, as absolute internal standards. $ARH_{A\ell II}$ and $ARN_{A\ell II}$ are the A-values of A$\ell$II $\lambda 5593$ deduced in a similar fashion.

The relative error propagaged into $A(TIB)_{PII}$ and $A(TIB)_{A\ell II}$ by temperature errors $(T-T_o)$, as well as specification of plasma conditions, are shown in Figs. 15 and 16, respectively.

It is in the <u>measurement of ion lines such as these</u> where TIB excels the most: not only do the TIB results have two orders of <u>magnitude less thermal dependence</u> than the conventional results $AE_{PII}$, $AE_{A\ell II}$ (cf. Figs. 15 and 16 ), but they are also easier to obtain since <u>no absolute intensity measurements are required</u> (except perhaps for small optical depth corrections). Moreover, the TIB results have essentially <u>no dependence on absolute plasma pressure</u> (or total number densities).

For a number of transitions there is no reason to employ TIB since equal accuracies can be obtained from measurements that are easier to perform. We refer to those ARH measurements which are themselves thermally insensitive, i.e. where there is a convenient pairing of

excitation and ionization energies between $H_\beta$ and the line being studied. One example of such a measurement is ARH for SiII λ6347, shown in Fig. 61. Aside from the well known case of OI λ6157, it is feasible to measure a number of visual or near UV lines of PII, MgII, AℓII, CℓI, OI and NI in this way.

While the A-value of NeI λ5852 (excitation energy = 18.9 ev) is known with only an estimated 10% reliability, as opposed to the 1% for $H_\beta$, overall accuracies not substantially less than 10% should be possible by utilizing thermally insensitive ARN measurements. Fig. 57 shows the thermal sensitivity of $ARN_{SII}$, the A-value of SII λ5453 measured relative to NeI λ5852. Note that these two lines are both strong and narrow, and are separated by only 400Å, so there should not be major problems connected with measurement of their relative intensities.

Other transitions which are exempt from treatment by TIB when source temperatures exceed 9,000°K are those within the (neutral) metals and the most readily ionized light elements. With increasing temperature, ionization depletes the excited states for these transitions as fast as Boltzmann equilibrium populates them; hence the excited state densities have very little net thermal dependence. For these transitions it is the conventional (AE) results which are thermally insensitive, as for example, SiI λ5948 of Fig. 61. Paradoxically, we obtain the poorest accuracies with these lines due to errors in spectroscopic additive partial pressures, absolute plasma pressure and absolute intensity calibration, whereas they should be the most accurate of the conventional (AE) measurements.

## E. Prospects for Extension of TIB to Other Laboratory Sources, Wavelength Regions and Plasma Temperatures

To carry over the illustrated TIB procedures into other spectral regions, or to sources of significantly higher temperatures, requires the adoption of different sets of internal standards. The Paschen and Lyman series come immediately to mind for use in the far infra-red and VUV . The growing body of results from (better) lifetime studies offers many possibilities for internal standards in the UV . The HeI spectrum spans a region from 600Å - 12,000Å with lines whose thermal dependence is just great enough to permit TIB of many singly ionized (and some doubly ionized) light elements whose spectra become bright at 2 eV temperatures.

The application of the TIB procedures carries over directly[†] to anomalous dispersion studies when "hook-displacement" is substituted for "intensity" in the foregoing discussion. A practical hybrid experiment utilizing the best features of both emission and "hook" methods would be to employ anomalous dispersion measurements instead of absolute intensity measurements in obtaining the analog of AE while retaining relative intensity measurements (which for transient sources is virtually synonymous with time resolved photographic recording) for ARH . TIB procedures can be employed with stabilized arcs so long as they are not expected both to remove sensitivity to thermal error and to establish the extent of demixing. That is, TIB is complimentary to, rather than a substitute for, Boldt's[67] procedures for treating the demixing problem in arcs. Discrepancies between AE and ARH results serve warning that some error has been

---

[†]With the exception of ARB, which relies on the laws of radiative transfer.

commited -- but do not specify whether it is in source temperature or assumed demixing ratios.

# CHAPTER IV

# SPECTROSCOPICALLY ORIENTED DESCRIPTION OF THE LUMINOUS SHOCK TUBE

## A. Introduction

In a single firing, the conventional shock tube presents a stationary observer with a series of different plasmas.[27-32,68-72] Some of these persist in the field of view for only fractions of a microsecond, the transit times of sub-millimeter thick, non - LTE relaxation regions behind shock fronts: others persist in essentially steady state for tens or hundreds of microseconds. These longer duration plasmas are slugs of gas several centimeters in length entrained behind incident or reflected shocks. While the transient shock tube emission can be used to study relaxation rates,[28,30,73,74] transition probabilities are studied during periods of steady state emission for which the plasmas have a well defined thermodynamic state.[75]

Given the initial composition of the shock-heated gas, its thermodynamic state can be determined either by "direct" measurement, i.e. a spectroscopic temperature measurement coupled with a transducer measurement of plasma pressure, or by applying hydrodynamic theory to a measured incident shock speed, $S_1$ . Both methods have their drawbacks -- viscous forces and random events at the time shocks are generated cause departures from the one-dimensional shock theory (Rankine-Hugouiot relations), while plasma spectroscopy is susceptible to many systematic errors.

Analysis of source conditions in several previous A-value studies employing shock tubes [28-32] relied primarily on hydrodynamic theory and measured shock speeds, bolstered perhaps by either a single spectroscopic temperature or a transducer-recorded pressure. These investigators were particularly concerned when shock tube hydrodynamic behavior deviated from predictions of the one-dimensional model, and sought, within the framework of hydrodynamics, to infer how seriously the observed deviations would influence the predicted plasma temperatures.

Because the present investigation relies completely upon direct measurement of state variables, we are not seriously concerned with the histories of the plasmas as long as they are homogeneous and in LTE . We did, in fact, perform rudimentary hydrodynamic studies, but for reasons peripheral to the task of obtaining A-values. Before our spectroscopic instrumentation became available, we recorded incident shock speeds and accelerations, reflected shock speeds, and made white light x-t streak photographs to find out if the new shock tube behaved pathologically in any important way.

We found incident shock fronts to be well-formed (not diffuse), the region behind the reflected shock to be homogeneous except for an occasional weak diagonal shock. Incident shock speeds were lower than achieved by other tubes of similar dimensions, but appeared adequate to provide the plasma temperatures required for our emission studies.

Once our apparatus became fully instrumented and we began the spectroscopic data runs, we continued to monitor incident shock speeds† for the following reasons:

---

†The x-t streak photography had to be abandoned when spectrographs displaced the white-light drum camera in the tight confines of our laboratory.

(1) To the extent that hydrodynamically predicted temperatures and pressures are found to agree with direct measurements, we can rely on them for those few data runs where the interpretation of data for direct assessment of temperature or pressure has been rendered unclear by some mishap.

(2) Since much of the earlier shock tube work did rely on hydrodynamic predictions for estimates of plasma pressure and temperature, and since this is still the easiest way to estimate the thermodynamic state of the plasma (i.e., the only experimentally observed quantities are the incident shock speed, $S_1$, and the initial test gas pressure, $p_1$), it is of intrinsic interest to see how well the hydrodynamic predictions $p(S_1)$ and $T(S_1)$ agree with more reliable (redundant) direct measurements. Results of this comparison will to some extent depend on the shock tube's cross-sectional size and shape, and on the type of test gas used. We note, however, that our system is similar to many spectroscopic shock tubes in all these respects.

(3) By establishing an empirical relationship between incident shock speed and the ratio of pressures across the diaphragm prior to breaking, we can employ the Rankine-Hugoniot relations to select initial pressures and compositions to optimize plasma conditions for a particular spectroscopic measurement.

We emphasize that had any, or all, of our hydrodynamic data been omitted, our results for transition probabilities and line widths would not be significantly affected, since shock-predicted thermodynamic quantities were included in the reduction of less than 5% of the data runs.

Section B contains a brief heuristic account of how the shock tube produces a luminous slug of plasma, and correlates shock tube flows with the characteristic luminosities observed in time-resolved spectroscopy. In Section C we compare Rankine-Hugoniot predicted pressures and temperatures for a real test gas with those for an ideal gas. This section also compares Rankine-Hugoniot predicted pressures and temperatures with the results of direct measurements. Section D considers the spectroscopic consequences of boundary layers and weak diagonal waves in our otherwise homogeneous plasmas. Section E examines the performance of the Maryland shock tube in terms of how closely the actual shock speeds approach the theoretical limiting values. It also illustrates how initial conditions can be tailored for approximate optimization of particular line intensities in our shock-heated plasmas.

## B. Shock Tube Operation

The following sketch is intended for the orientation of readers largely unfamiliar with shock tube operation. Numerous quantitative treatments are given in the literature.[68-72,76]

The conventional ("Cold-driver") shock tube is an adiabatic compressor; it relies on a shock wave, rather than a piston, to elevate a small quantity of gas to high temperatures. Its energy source is the pV work performed at the plant which supplies the high pressure driver gas. Its basic elements are two chambers of uniform cross section initially separated by a frangible partition. The longer section (expansion section) is charged with a few hundredths of an atmosphere of the gas to be shock-heated, while the

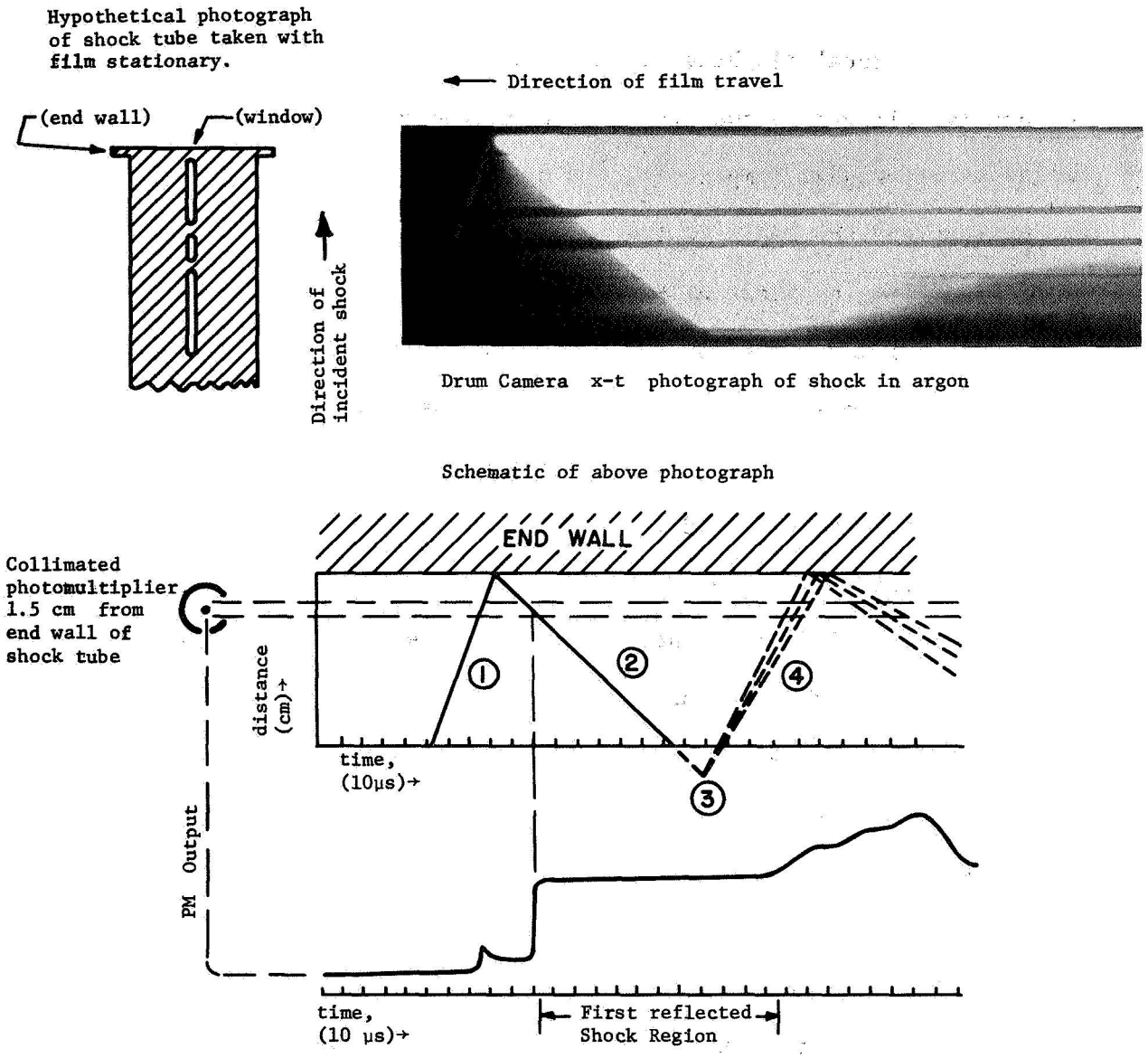


1. Incident shock front, followed by short duration relaxation region.
2. First reflected shock.
3. First reflected shock reflects off hydrogen-argon interface (out of field of view).
4. Multiply reflected waves.

Fig. 17: Schematic Correlation Between Shock Tube Flows and Time-Resolved Spectroscopy Near the End Wall.

shorter (driver) section is pressurized to 10-100 atmosphere with a light (driver) gas. When the partition is suddenly removed (in the present case a metal diaphragm breaks), the discontinuity in static pressure is relieved by two trains of pressure waves, one traveling into the low pressure gas, compressing and heating it, as well as setting it into motion, and the other moving back into the high pressure gas, expanding and cooling it. The train of compressive waves coalesce into a single well-formed shock front of sub-millimeter thickness after traveling 10-30 shock tube diameters (formation distance) downstream from the diaphragm. Entrained behind the shock is the once-compressed slug of test gas, bounded in front by the incident shock wave and behind by an interface with the expanded driver gas.

Figure 17 depicts shock behavior as seen by a stationary observer in the vicinity of the end wall of the shock tube. When the incident shock reaches the end wall it is reflected back into the moving slug of once-compressed plasma, compressing and heating it again. This reflected shock wave also brings the gas virtually to rest (since there can be no gas flow perpendicular to the end wall).

This twice compressed plasma ("first-reflected shock region") is the light source for most of our spectroscopic studies. When viewed 1-2 cm from the end wall, plasma durations are typically 50-150μs , depending on initial gas pressures. During this period the thermodynamic state of the gas is very nearly steady, pressure and temperature typically increasing not more than 4% per 100μsec.

The steady-state plasma is eventually disrupted by multiply reflected shocks (cf. Fig. 17). These are generated when the first reflected

shock wave encounters the driver gas-test gas interface: the driver gas has a much lower molecular weight than the test gas, so the interface presents a discontinuity in sound speeds. Because the interface is not a sharp discontinuity, there is usually a fan of multiple reflected shocks. These compress and heat the plasma still further, but do not produce steady state regions of long duration, as does the first reflected shock.

Shock tube luminosity is finally quenched by the arrival of cooling expansion waves which have been reflected off of the end wall of the driver section.

### C. Hydrodynamic Predictions Compared With Direct Measurements on the Thermodynamic State of Reflected Shocks

An imaginary observer traveling in the reference frame of the shock wave sees gas, in a particular thermodynamic state, entering the wave at some constant velocity and exiting from it at some other constant velocity, and with a changed thermodynamic state. Since the shock wave has essentially zero thickness, it cannot be either a source or a sink for particle mass, momentum or energy: therefore, there is zero net flux of these quantities across the shock wave.

By applying equations for the conservation of these three quantities to shocks propagated in one dimension, employing some basic thermodynamic identities, and performing a considerable amount of algebraic manipulation, one arrives at the Rankine-Hugoniot equations[28-31,68-72,76]. These express the jump-conditions for pressure, temperature, or number density, across a shock in terms of the shock speed (in the laboratory reference frame) and the degrees of freedom of the shocked gas. These equations can be applied

sequentially to relate conditions behind the first reflected shock to the conditions ahead of the incident shock (i.e. the initial state of the test gas).

In Fig.18 we show Rankine-Hugoniot predicted pressures, $p_5(S_1)$ , and temperatures, $T_5(S_1)$ , behind first reflected shocks for a test gas composed of 1% $CH_4$ + 99% neon and initially (before shock heating) at 10 Torr. That is, the figure actually contains two sets of Rankine-Hugoniot predictions: those based on constant specific heats[77] (constant number of degrees of freedom, constant $\gamma = C_p/C_v$ ), shown as dashed curves, and those taking into account real-gas effects (variable specific heat), which are drawn as solid curves. These latter calculations included the effects of molecular dissociation and electronic excitation and ionization. The real gas predictions were made much more tractable by assuming complete molecular dissociation behind reflected shocks: this assumption should be valid to very good approximation[51] since temperatures in this region exceeded 9,000°K. Real-gas Rankine-Hugoniot predictions were obtained using computer codes written by D. Koopman[77] and R. Bengtson.

For a typical shock generated by our equipment, $S_1$ = 3.25 mm/μsec., we note (cf. Fig.18 ) that the inclusion of real gas effects lowers the shock-predicted temperature by 10% and raises the shock-predicted pressure by 15% . The excited state density of $H_\beta$ , $N_{H_\beta}(p_5,T_5)$ , predicted by the real gas calculations is ½ as large as predicted by the ideal gas calculations. This factor of two difference in predicted $H_\beta$ number densities is due almost entirely to the internal degrees of freedom of the 1% $CH_4$ spectroscopic additive gas: the 99% neon carrier gas remains essentially ideal and un-ionized up to temperatures of 12,000°K.

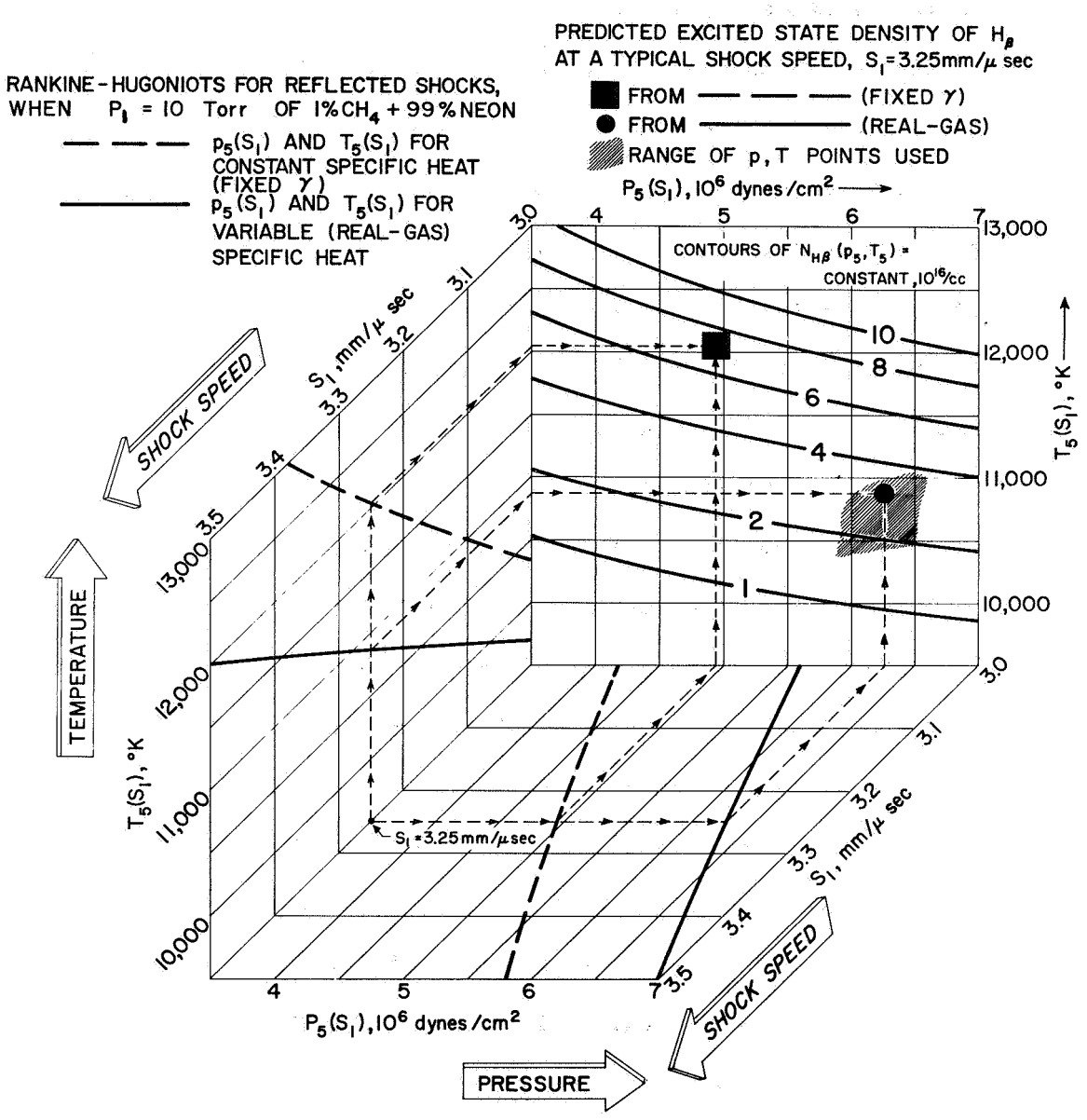


Fig. 18: Rankine-Hugoniot Predictions for a Typical Spectroscopic Variable: The Excited State Density of $H_\beta$ Displayed as a Function of Incident Shock Speed.

The hatched-in area on $N_{H_\beta}(p_5,T_5)$ shows the range of $H_\beta$ excited state densities deduced from direct measurements of temperature and pressure for shocks where $S_1 \cong 3.25$mm/μsec.

Figure 18 also illustrates the precisions in shock speed measurement required when Rankine-Hugoniot equations are employed in quantitative spectroscopic studies. A 3% error in $S_1$ propagates into a 4% temperature error (for real gas predictions), which in turn causes the estimated excited state density of a typical visible line ($H_\beta$) to err by 30% - 50%.

Rankine-Hugoniot (real gas) predicted temperatures and pressures for reflected shocks are compared with directly measured values in Figs. 19 and 20 , respectively. These data are for shocks in 1% $CH_4$ + 99% neon and ½% $CH_4$ + ½% $CS_2$ + 99% neon test gases.

Shock speeds were measured with 1.6 M Hz Potter crystal-regulated chronographs. Shock sensors were either Kistler quartz pressure transducers (rise times of approximately 0.5μsec.) or thin film resistance gauges (rise times of approximately 0.2 sec.) . Time-of-flight test stations were either 30 cm or 60 cm apart, one test station always being located in the same shock tube plane as the optical path used for spectroscopic diagnosis of the plasma. Because the chronographs required 40 volt triggering pulses, while the thin film resistors and quartz pressure transducers supplied only millivolt signals, a multichannel fast-risetime pulse amplifier was constructed using solid state diodes. This circuit added approximately 1.0μsec jitter to the measured shock transit times between stations (the chronographs require a "start" pulse and a "stop" pulse). Moreover, the inherent delay of the amplifier would vary by as much as 1.0μsec from day to day because diode response depended on ambient temperature. Therefore, considering the least count (0.6μsec.) of the chronographs, the

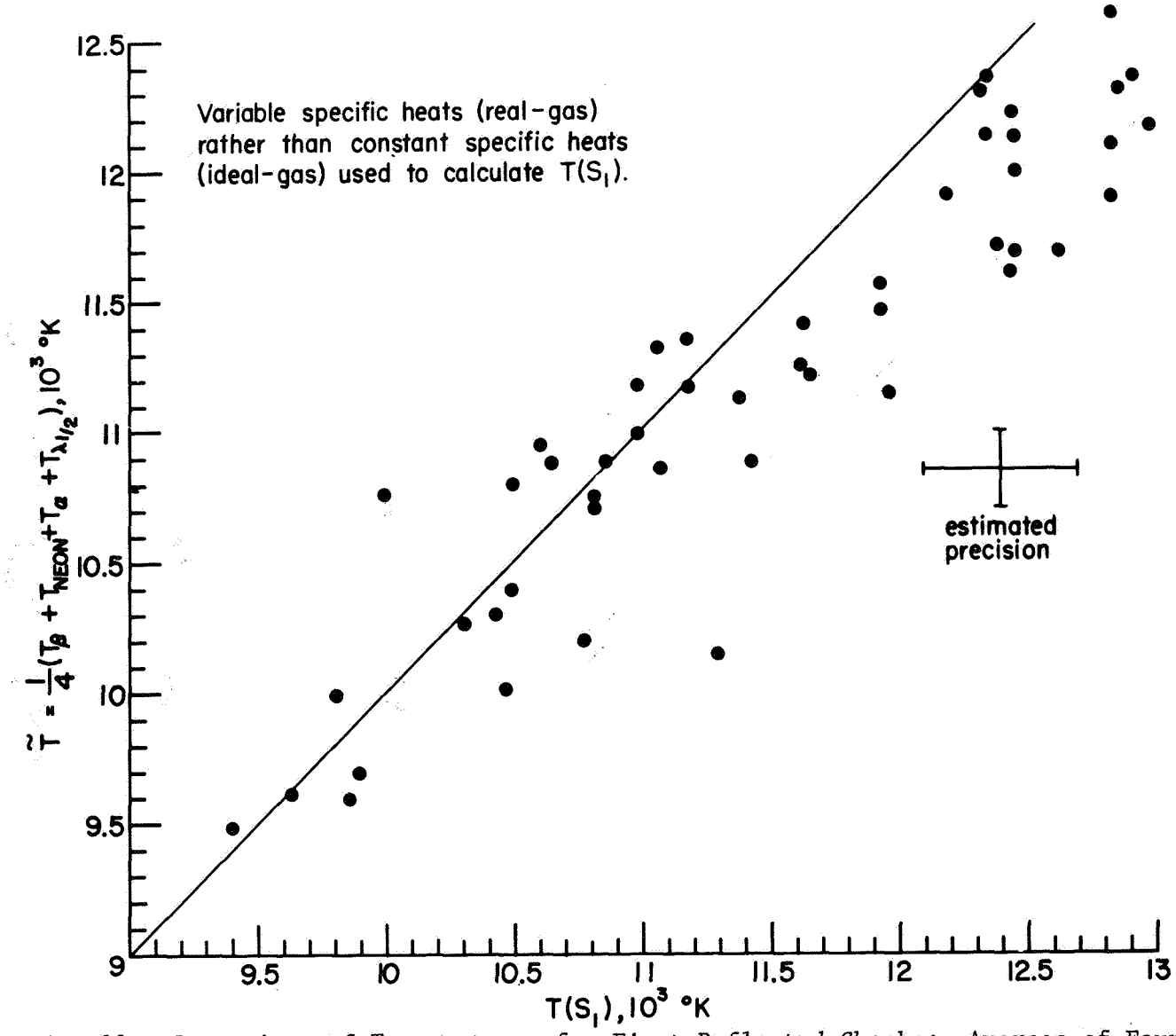


Fig. 19: Comparison of Temperatures for First-Reflected Shocks: Average of Four Independent Direct Determinations, $\tilde{T}$, vs. Rankine-Hugoniot Predictions, $T(S_1)$, Based on Observed Incident Shock Speed.

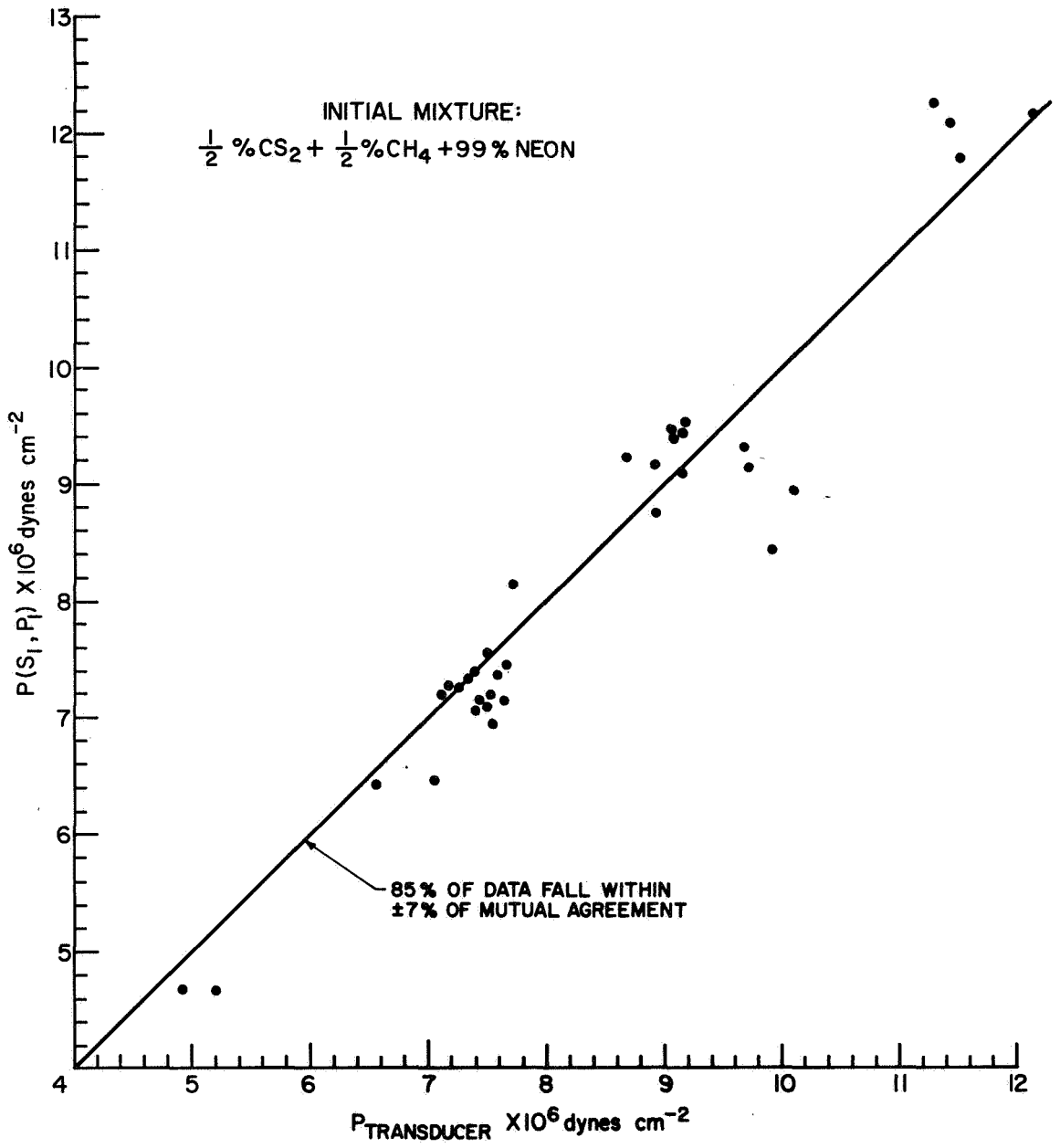


Fig. 20: Measured Pressures Behind First-Reflected Shocks (Quartz Transducers) vs. Pressures Predicted from Rankine-Hugoniot Equations (Including Real Gas Effects) Using Measured Incident Shock Speeds.

jitter in the pulse amplifier and the rise-time of the sensors, we estimate shock speeds were measured with a precision of 2%.

However, the instantaneous shock speed at the position where comparison is made to direct pressure and temperature measurements is generally not the same as the average shock speed between two timing stations spaced 30 cm or 60 cm apart. During preliminary studies, when up to six timing stations (giving five shock speed determinations) were used, we observed shock speeds to be quite dependent on distance from the diaphragm. Velocity profiles were not highly reproducible: successive runs using identical initial conditions might produce shocks that were accelerating, or decelerating, in the vicinity of the test section. We estimate this variation in shock speed causes an additional 1% scatter (random error) in our estimates of local shock speed.

The directly measured temperature, $\tilde{T}$ , in Fig. 19 is the average of four independent, simultaneous temperature determinations (cf. Chapter VII). We estimate $\tilde{T}$ contains less than 1% systematic (repeatable) error and 1% - 2% random error (scatter). Since the first reflected region is generally not strictly a steady-state plasma, we consistently measure $\tilde{T}$ midway through it: temperatures immediately behind the first reflected shock wave will be typically 1% lower than, and temperatures just prior to arrival of multiply reflected shocks will be typically 1% higher than, $\tilde{T}$ . Since the Rankine-Hugoniot theory assumes there will be steady state conditions throughout this region, there is some ambiguity as to whether $\tilde{T}$ , $\tilde{T}$ + 1% or $\hat{T}$ - 1% should be employed for comparison with $T(S_1)$ .

From 9,500°K to 11,000°K, $T(S_1)$ and $\tilde{T}$ agree to within mutual tolerance. Scatter about the agreement line is approximately what is expected from 2% random error in $\tilde{T}$ and 3% - 4% random error in $T(S_1)$ ,

i.e., according to Fig. 18 , a 3% scatter in $S_1$ produces a 3% - 4% scatter in $T(S_1)$ . For $T(S_1)$ between 11,000°K and 13,000°K, however, $\tilde{T}$ is significantly lower than $T(S_1)$ .

We believe this discrepancy at higher temperatures is associated with the fact that lower initial test gas pressures, $p_1$ , are used to generate the hotter shocks. The lower the initial pressures, the greater becomes the influence of boundary layers[28-30,69-72] in determining shock temperatures. Since the Rankine-Hugoniot equations are formulated in one dimension, i.e., neglect boundary layers, $T(S_1)$ is expected to be less valid for our hotter shocks. Also, lower initial pressures lead to lower densities behind the reflected shocks, so readily ionized wall impurities (cf. Chapter VII) will have a greater cooling effect for these shocks than for cooler, denser, shocks.

Comparing $p(S_1,p_1)$ with the pressure measured by a quartz transducer (cf. Chapter VII), Fig. 20 shows 85% of the data fall within 7% of mutual agreement for pressures varying between 3 — $12\times10^6$ dynes $cm^{-2}$. This agreement is well within the 5% - 7% tolerance of the direct pressure measurement and the 4% - 5% tolerance (cf. Fig. 18 ) in $p(S_1,p_1)$ due to the 3% scatter in $S_1$ . Previous authors[28-34,70] have found similar good agreement between directly measured and hydrodynamically predicted pressures, even when hydrodynamically predicted temperatures did not agree well with other data.

## D. Spectroscopic Consequences of Breakdowns in the 1-D Flow Model

The spectroscopist assumes a 1-D flow model because it simplifies radiation transfer calculations and hence the interpretation of emission and absorption data from the luminous shock tube: yet the hydrodynamicist

knows this model describes only the gross features of complicated events. We now show that the spectroscopist's use of the 1-D model causes little sacrifice in accuracy. If a few precautions are taken, the ignored details of shock flows serve only to increase somewhat the scatter in spectroscopic results. We will consider the influence of laminar boundary layers and trailing waves on spectroscopic results obtained from the region behind the first reflected shock.

Real (3-D) flow regions are surrounded by a boundary layer, a thin laminar or turbulent envelope whose thickness is defined to include those portions of the flow where the thermodynamic state differs from the bulk of the plasma. A boundary layer always exists, since the temperature of the gas contacting the tube walls (large specific heat) must assume the wall's temperature, and the condition of "no slip" at the walls establishes a velocity gradient extending into the main flow. The predicted growth of the layer with the time elapsed after passage of the incident shock has been amply confirmed[30,70].

Fortunately, thin boundary layers do not cause significant modulation of non-resonance lines originating in the bulk of the plasma. Throughout the greater portion of the boundary layer the number density of emitters <u>or</u> absorbers of non-resonance lines is very small because in this cooler gas both the upper and lower atomic levels[†] will be thinly populated. If the boundary layer supports a linear temperature gradient between the wall and the bulk of the plasma, then there will be an exponential fall-off in the number density of emitters (absorbers) across the layer. If the full extent of the boundary layer is, say 1 mm,[30-70] then .1 mm away from the

---

[†]For visible lines in light elements values of $E_{up}$ = 11eV, $E_{low}$ = 9eV would be typical.

bulk of the plasma the number density of emitters will have fallen by typically a factor of 3 and of adsorbers by more than a factor of 2. Interactions in this .1 mm region will obviously cause little modulation in an optically thin line originating in a plasma 70 mm deep. For optically thin lines then, the net effect of ignoring the existence of (two) boundary layers 1 mm thick will be to slightly reduce the assumed thickness of emitting plasma along the line of sight $\ell$ , by the relative amount $\ell \frac{70-2}{70} \cong .97$ .

For optically thick lines, the reduction in observed line intensity may be slightly greater since the laws of radiative transfer no longer reduce to the linear approximation. Even here, however, the effective absorbing layer is too thin to cause appreciable error. (For resonance lines the whole extent of the boundary layer comes into play, permitting modulations a factor of $e^{E_{low}/kT} \approx 10^4$ greater than with non-resonance lines of lower state energies $E_{low}$ .)

The expectation of negligible interference from laminar boundary layers rests on the assumption that the layers will be of normal thickness (on the order of 1 mm). In the absence of any direct observations to verify this assumption, four precautions were taken in this investigation:

(1) The optical path was taken 1.5 cm upstream from the end-wall, where the first reflected shock appears within 20μsec. after passage of the incident shock, and where spectroscopic sampling times followed within 50μs after passage of the incident shock. This compromise positioning allowed minimal time for boundary layer growth while still avoiding the region of possible end-wall boundary layers.

(2) The temperature deduced from the optically thick portion of $H_\alpha$ (cf. Chapter VI) is more sensitive to boundary layers than the optically thin lines (i.e., $H_\beta$ and NeI λ5852) used to deduce plasma temperature. Since all three temperatures, $T_\alpha$, $T_\beta$ and $T_{neon}$ , agree to within experimental

tolerance of less than 1%, boundary layers cannot be absorbing more than 3% of the $H_\alpha$ intensity.

(3) Data for the absolute integrated intensity of CI λ5052 was gathered over a range of 5 - $12\times10^6$ dynes $cm^{-2}$ in shock pressure. Since boundary layer growth is accelerated by going to lower shock pressures, the absence (cf. Fig.51 ) of any systematic variation with pressure in the measured A-value of CI λ5052 is an additional confirmation that boundary layer effects are spectroscopically negligible.

(4) The A-value of CI λ5052 deduced from the line's absolute integrated intensity agrees, to within experimental tolerance, (cf. Fig.8 ) with the A-value deduced from the ratio of intensities, CI λ5052 relative to $H_\beta$ . If boundary layers were significantly reabsorbing the energy of CI λ5052, they would absorb proportionately more from the brighter line, $H_\beta$ , so these two measures of the CI λ5052 A-values would diverge with increasing boundary layer absorption if it were significant.

The existence of trailing waves is another basis for objection to the 1-D flow model. Trailing waves are weak shocks produced by non-ideal petaling of diaphragms[†]: they propagate along the tube by diagonal reflection off the walls. In the present experiment diagonal waves were detected in first reflected flows on about 1/4 of the white-light x-t streak photographs made during preliminary shock tube studies. Sometimes they appeared singly, but occasionally whole "fans" were observed. There was no reproducible pattern to the trailing waves.

It is just this lack of reproducibility that over many shots averages out any localized perturbations on the state of the plasma. One thus expects the influence of trailing waves to be restricted to increasing the scatter in results obtained by assuming a homogeneous light source. For more than 90% of the simultaneous state determinations, and a like percentage

---

[†]Prior to opening, a diaphragm assumes a hemispherical shape, so that the first driver gas through the newly opened diaphragm will have some velocity components perpendicular to the tube axis.

of the A-value results, however, the observed is not greater than expected from a-priori estimates of signal-to-noise ratios and reading errors. (We suspect that trailing waves are at least partially responsible for the few anomalous data we obtained,)

In particular, the several simultaneous temperature measurements would respond quite differently to localized hot (or cold) spots along the spectroscopic line of sight. The temperature $T_{neon}$, derived from the optically thin neon $\lambda 5852$, is typically 5 to 10 times more responsive to a localized hot spot than is the temperature $T_{\alpha}$, deduced from the slit-averaged optically thick portion of $H_{\alpha}$ (cf. Chapter VI). Yet, Fig. 43 shows that over a 2,300°K range of temperatures the deviations of $T_{\alpha}$ and $T_{neon}$ from the averaged temperature are not more than 2%.

Moreover, each of 10 - 15 photoelectric channels routinely employed gives a time history of shock tube emission with resolutions of 0.5-5μsec. The typical spectrograph optical path traverses the tube axis in a pencil of rays with mean radius 0.3 mm and mean solid angle $10^{-2}$ steradians, so sampling regions are small enough that photomultipliers can respond to intensity fluctuations localized to thin planar regions perturbed by diagonal waves. For most shocks photoelectric records are similar to those of Fig. 45 ; that is, intensities are constant or slow varying with time. In perhaps 1/4 of the shots small fluctuations, on the order 1/10 - 1/20 of mean signal level, could be detected on all channels simultaneously, and so could not be ascribed to photomultiplier noise. These bona fide fluctuations lasted typically no more than 5 - 7μsec. , (transit time of a diagonal shock across the line of sight), allowing data to be read either earlier or later in time.

## E. Tailoring of Shock Conditions for Optimal Spectroscopic Observations

Although our data indicate that hydrodynamically predicted excited state densities are not accurate enough for quantative spectroscopy, we found the Rankine-Hugoniot relations to be valuable for predicting, approximately, what initial conditions should be employed to optimize the brightness, or the line-to-background intensity ratio, for spectral lines being studied. For example: what combination of driver pressure, $p_4$ , test gas pressure, $p_1$ , and relative concentration of $CH_4$ in neon, $\rho_{CH_4}/\rho_{tot}$ , will give the greatest brightness to CI λ50527?

Given the incident shock speed in terms of these three variables,

$$S_1 = S_1(p_4, p_1, \rho_{CH_4}/\rho_{tot})$$

the Rankine-Hugoniot relations give the excited state density of CI λ5052 in the first reflected shock region, $N_C$ , as

$$N_C = N_C(p_5, T_5, \rho_{CH_4}/\rho_{tot}) = N_C(S_1, \rho_{CH_4}/\rho_{tot})$$

$$N_C = N_C(p_4, p_1, \rho_{CH_4}/\rho_{tot})$$

Since shock speed is monotone-increasing with driver pressure (for constant $p_1$ and $\rho_{CH_4}/\rho_{tot}$), we always use the highest convenient driving pressure, $p_4 = 1000 \pm 100$ psi. Therefore, tailoring plasma conditions to maximize $N_C$ involves selection of an optimal $p_1$ and $\rho_{CH_4}/\rho_{tot}$ .

There are two ways of determining $S_1(p_1, \rho_{CH_4}/\rho_{tot})$†:

---

†We will assume that $P_4$ is as nearly constant as the repeatability of diaphragm breaking pressures (cf. Chapter V) allows.

empirically, and by hydrodynamic predictions. It has long been realized that the hydrodynamic prediction (Taub equation ) is not quantitatively reliable[28-31,70]: it assumes not only 1-D shock tube flows, as do the Rankine Hugoniot equations, but also that the diaphragm separating the test and driver gases is instantaneously removed by some process that neither interferes with the shock tube flows nor requires the expenditure of energy.

Figure 21 presents data for incident shock speeds (measured in the vicinity of the test section) as functions of $p_4/p_1$ , where $p_4$ is approximately constant. Test gases are composed of 1% $CH_4$ + 99% neon and ½% $CH_4$ + ½% $CS_2$ + 99% neon. Predictions of the Taub equation are also shown.

Throughout most of the range $p_4/p_1$= 1,500-10,000, our results fall systematically low with respect to the Taub equation by .06-.10cm/μsec(20-30%). This discrepancy is larger than usually reported by authors using shock tubes of similar dimensions and working pressures: however, we employ unusually thick diaphragms (cf. Chapter V) of soft aluminum, whose expected long opening times are believed to choke-off some of the initial flows during formation of the incident shock.

From the large scatter in $S_1$ at constant $p_4/p_1$ it is obvious that our shock tube plasmas are not reproducible. Shocks in identical test gases and using identical diaphragms may vary in speed by as much as 10% (even when the diaphragms break at identical driving pressure.) The breaking of heavy diaphragms is a highly irreversible process which we do not observe; therefore, we can only infer[78] that the scatter in $S_1$ is due to differences in kinematic behavior of individual diaphragms.

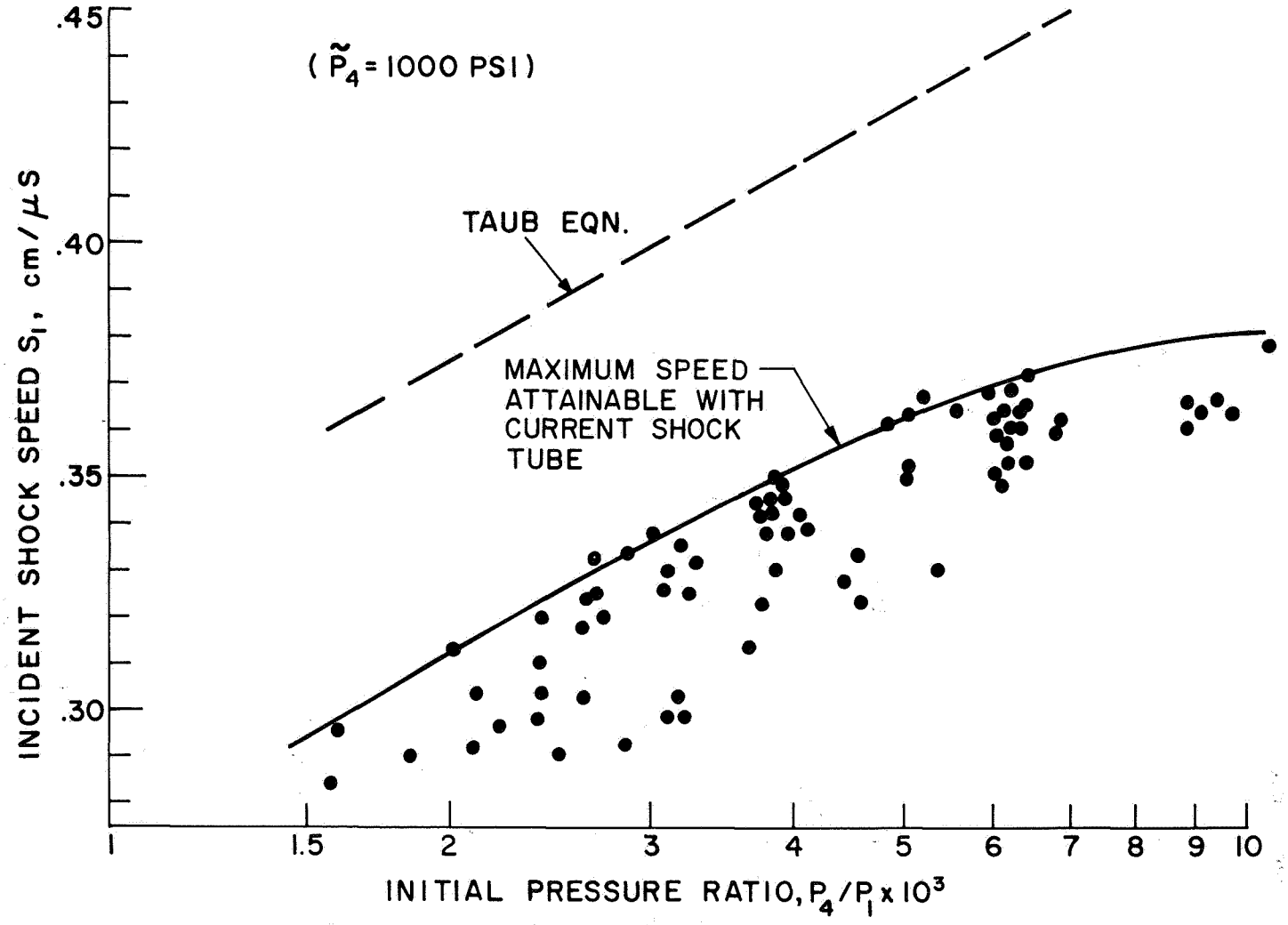


Fig. 21: Measured Incident Shock Speed as Function of Initial Pressure Ratios Across Diaphragm: Hydrogen Driver Gas into Neon + 1% Light Hydrocarbon.

The maximum observed shock speeds form a smooth envelope over the distribution of $S_1$ versus $p_4/p_1$ data in Fig. 21 . We take this set of maximum speeds attainable with our equipment, drawn as a solid curve in the figure, to define $S_1(p_4, p_1)$ for 1% $CH_4$ + 99% neon and ½% $CH_4$ + ½% $CS_2$ + 99% neon test gases. Since $p_4$ varied between 900-1,000 psi for these data, to good approximation:

$$S_1(p_1, p_4) = S_1(p_1)]_{p_4 = 1000 \text{ psi}}$$

Combining real-gas Rankine-Hugoniot equations with the empirical relation $S_1(p_1)]_{p_4}$ , we plot in Fig. 22 the excited state populations of several prominent spectral lines as functions of $p_1$ . We note that for all the lines; $H_\beta$ , CI λ5052, SI λλ4695 and NeI λ5852 , there is a unique initial pressure, $p_1$ , which will give maximum intensity. The lower the excitation energy of a line, the <u>higher</u> the initial pressure (and the <u>lower</u> the reflected shock temperature) required to impart the maximum brightness to the line.

In Fig. 23 we show the excited state density of CI λ5052 as a function of spectroscopic additive gas in a neon carrier with $p_1$ and $p_4$ fixed. We employ an approximate experimental relationship,

$$\frac{\Delta S_1}{S_1} \simeq -6 \times \frac{\Delta\rho(CH_4 + CS_2)}{\rho_{tot}}$$

for the effect of additive gas on shock speed. It is seen that the brightness of CI λ5052 cannot be increased indefinitely simply by enriching the relative carbon concentration in the test gas.

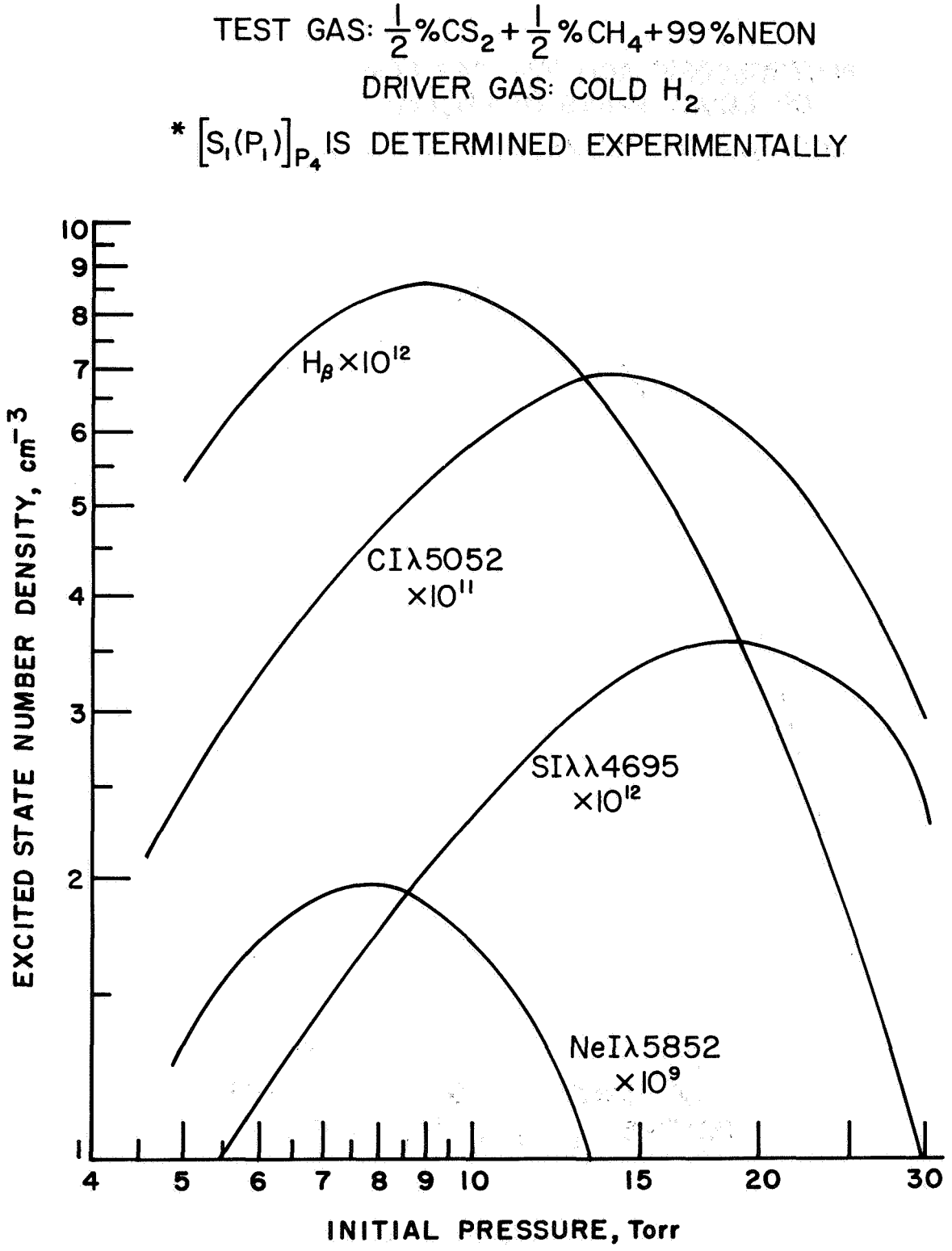


Fig. 22: Maximum Excited State Densities Attainable* With Current Apparatus as Function of Test Gas Initial Pressure.

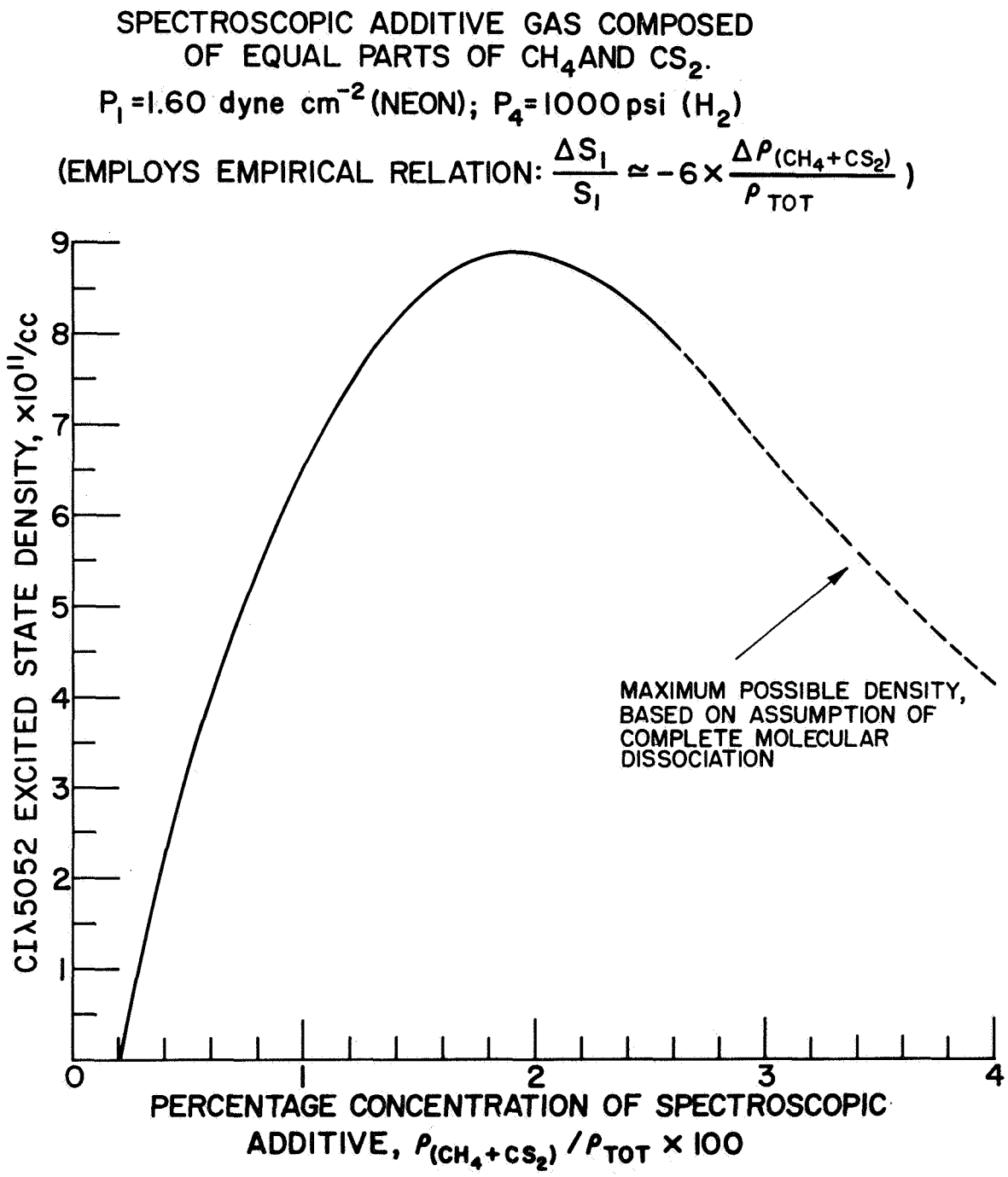


Fig. 23: Maximum Excited State Density of CI λ5052 Attainable With Current Apparatus as Function of Spectroscopic Additive Gas Concentration in Neon Carrier Gas.

# CHAPTER V

# EQUIPMENT

## A. The Shock Tube

1. General description and design considerations. The shock tube is made of mild steel. Various lengths of expansion section have been used between 92" and 150", while the driver section is 48" long. The flow channel has a rectangular cross section of (internal) height 3.64" and width 2.64". Inside corner radii are approximately .010". Interior surfaces are cadmium plated to retard corrosion. Maximum driver pressure is 1800 psi. Two views of the shock tube and associated equipment are given in Fig. 24 and 25.

Before going into details of the shock tube's construction we mention some of the conflicting considerations entering into the design of a conventional (cold driver) shock tube intended for atomic spectroscopy. One must decide between a circular and a rectangular cross section. The rectangular geometry provides a laminar plasma which facilitates the analysis of radiation from an extended source†, and also allows the fitting of plane windows, which are both easier to make than cylindrical windows and do not act as lenses. These advantages are bought dearly--a rectangular shock tube takes twice as long to build, and costs twice as much, as a circular one of comparable size and performance. This is because heavy-walled circular stock is available, but only thin-walled rectangular tubing is currently marketed and this requires external reinforcement to withstand

† Because of the homogeneity of shock tube flows, however, even with a circular cross section there is no need for Abel inversion as with DC arcs.

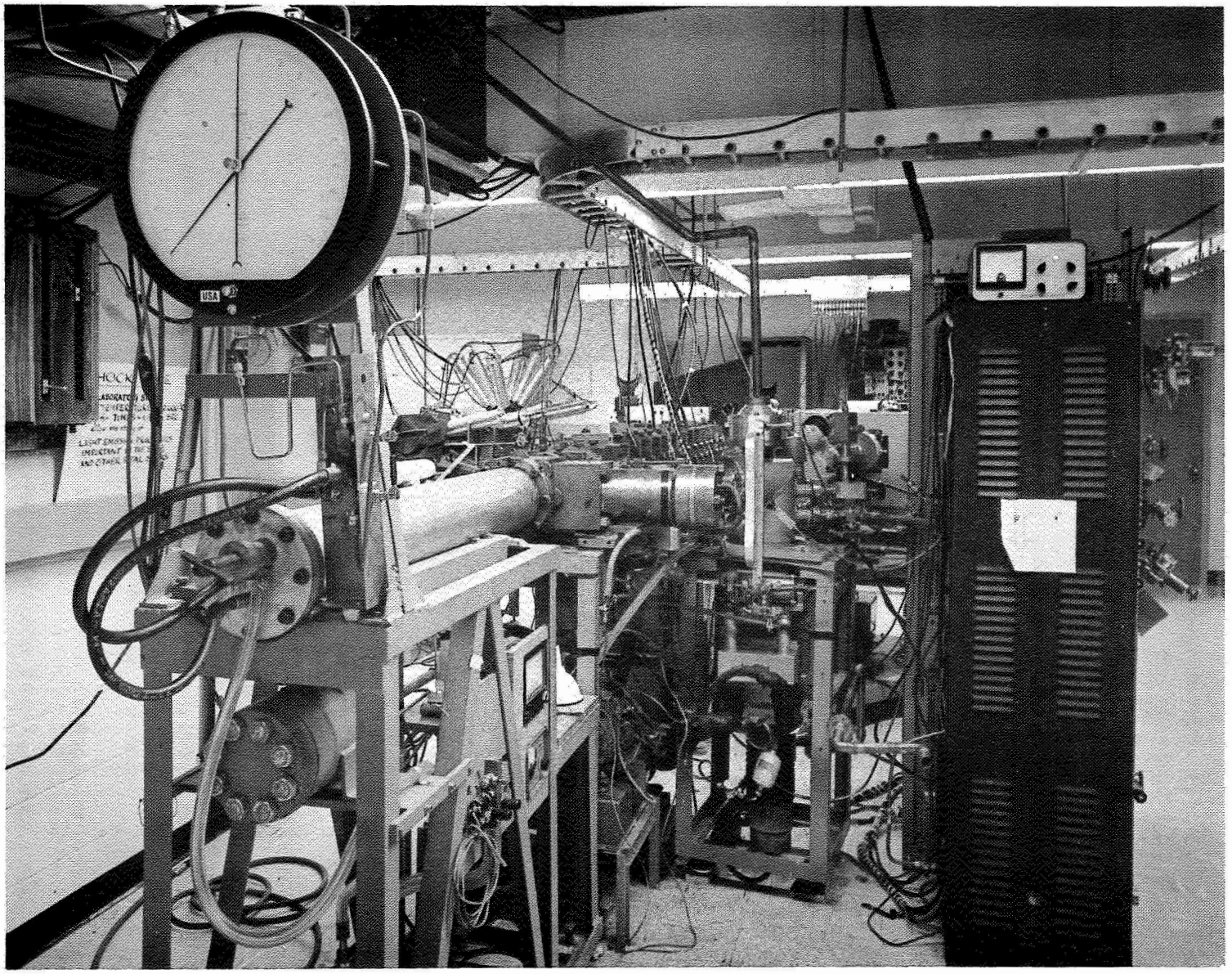


Fig. 24: The Shock Tube, Viewed From the Rear of the Driver Section.

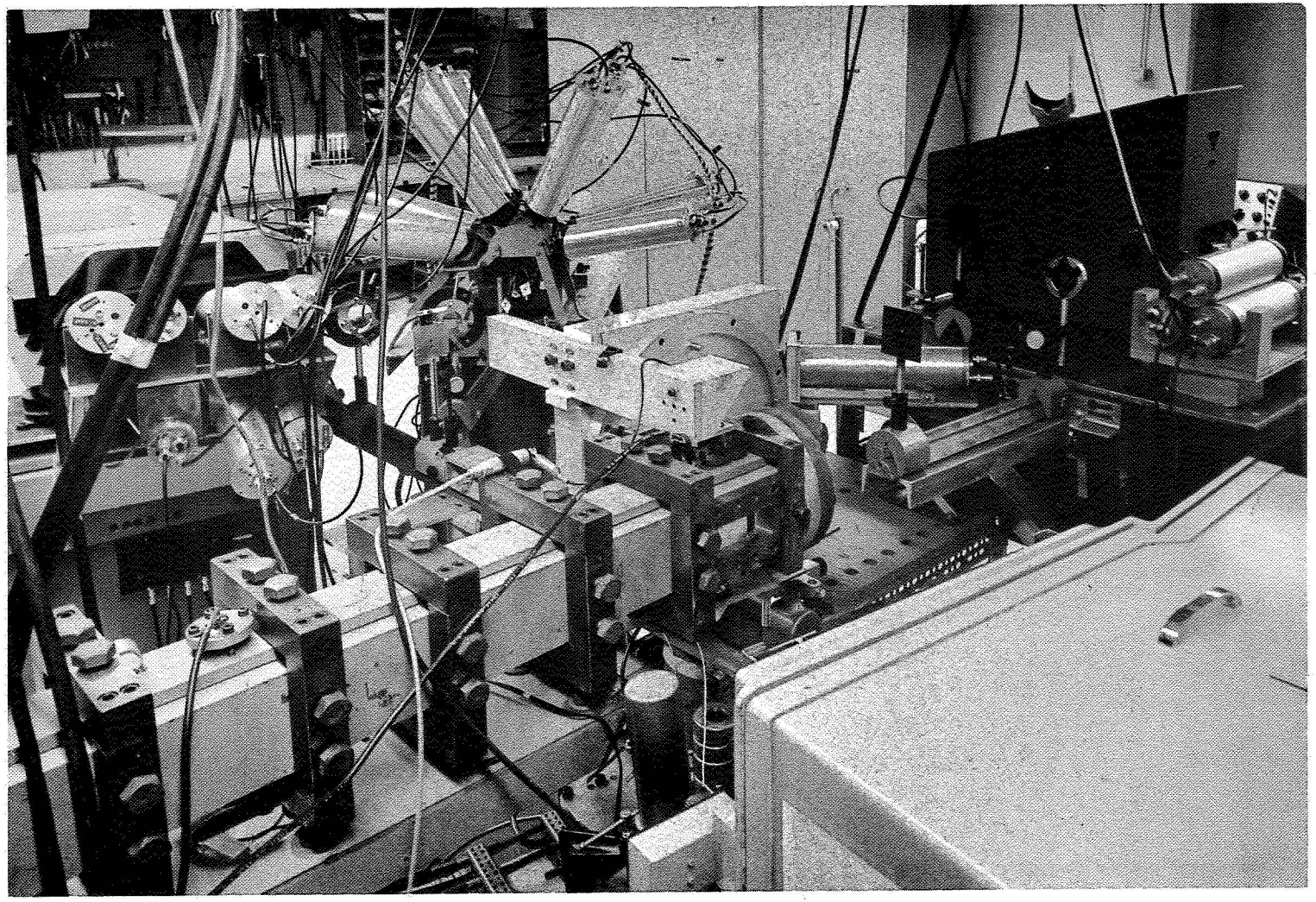

Fig. 25: The Test Section; "SQUID" in Background.

the usual working pressures. Also, construction of flanges and other machining operations can be accomplished by turning (on a lathe) for circular geometries but require milling operations for rectangular geometries. Moreover, circular tubes are far easier to keep clean (there is a small but cumulative build-up of pump oil and spectroscopic additive decomposition products on the walls), because there are no hard-to-reach corners, and because circular tubes can be honed to a high polish and are available in non-porous and non-corrosive materials such as stainless steel.

Choice of the internal dimensions involve a compromise between performance and costs. A large cross section is desirable for both spectroscopic and hydrodynamic reasons. At a given plasma temperature the optical depth of optically thin lines will be proportional to optical path length through the source, and a factor of 2X in optical depth changes the photometric signal to noise ratio by more than two in a line-minus-local-continuum measurement. Moreover, the greater the extent of the source region the less will be relative disruptions in space-averaged quantities caused by local plasma inhomogeneities. A large cross section also improves shock tube hydrodynamic performance. The total volume of boundary layers (at given flow conditions) is proportional to the tube's circumference while total plasma volume is proportional to cross sectional area. Hence, the relative influence of boundary layers upon shock tube flows will diminish inversely with shock tube diameter. Construction and operating costs, however, scale at something like the tube diameter cubed. Doubling the tube diameter means doubling the stress on walls, as well as doubling the wall's perimeter, calling for four times the amount of structural wall material per foot of length. The length of the tube must also increase since it takes a fixed number of tube diameters to establish a well-formed shock.

Shop time also rises because a machinist can cut metal only at a given rate. The volumes of test gas and driver gas needed to produce and maintain a desired plasma will also scale roughly as the tube diameter cubed. The relative lengths of driver and expansion sections is discussed by a number of authors.[69-72]

When a cold driver shock tube is intended for study of the light elements and their ions, the high excitation energies made it especially important not to underdesign the maximum driving pressure. Although increased driving pressures call for heavier construction of both driver and expansion sections (which must withstand terminal static pressures), the extra few hundred degrees of source temperature resulting from an extra few hundred psi driving pressures can often make the difference between barely exciting a desired spectral line to a detectable intensity or enhancing its brightness to useful levels. The present system was designed to the 1800 psi maximum delivery pressure of commercial 200 cubic foot hydrogen cylinders.

2. Construction details. The core of the shock tube is cold-rolled, mild steel tubing, resistance welded with inside flash removed[†]. Wall thickness is 0.180" and mean inside surface finish (measured with a Brush Surface Tester) is .000125". Hydrostatic testing soon made clear the necessity of externally reinforcing this tubing. Under hydrostatic loading the tube swelled in an effort to assume an elliptical cross section; the relative sewlling at the midpoints of the 4" sides was 0.4% at 200 psi, 1.0% at 400 psi, and 4.5% at 600 psi. Cold working at the corners caused rupture at 2600 psi.

---

[†]Supplied by Ryerson Steel or U.S.S.

Different methods of reinforcement were adopted for the driver section, which has no instrument ports, and for the expansion sections where ease of test port installation is a major concern and where static pressures to be withstood are only $\frac{140''}{48''} \approx 1/3$ as great as in the driver.

The expansion sections are reinforced by the use of heavy plates and clamps as shown in Figs. 26 and 27. The tube is sandwiched between ½" bar stock at top and bottom (the 3" faces) and 1" bar stock along the sides (the 4" faces). These plates are forced against the tube by bolts retained in encircling clamps constructed of 1½" bar stock. A torque wrench insures uniform compression. When the clamps are spaced 8" apart, the tube's swelling (measured as before),midway between the clamps is reduced to .13% at 200 psi, .26% at 400 psi and .3% at 600 psi. The tube showed no evidence of elastic hysteresis.

Shock tube flanges are cut from 1" steel plate and a relief groove is milled 1/8" back from all surfaces mating the thin walled tube in order to minimize drawing and oxidation of the latter during welding. Opposing flanges are fitted with taper pins for positive positioning. The test section is terminated by a plug which advances the reflecting plane for incident shocks into the field of view of two pairs of windows used to collect spectroscopic data. The plug is hand-finished to conform closely with the tube's inside surface. Figure 28 shows the union between a flange and the thin-walled rectangular shock tube.

Seven test ports are spaced along the top of the expansion sections. Pressure transducers, thin film resistance gauges[70], ionization gauges, or small windows can be used interchangeably at these sites. One inch diameter holes are cut through the reinforcing bars and the portion of the tube thus exposed is finished-flat with an end mill so it will seal against the O-ring carried in the shoulders of the diagnostic plugs. A one-half

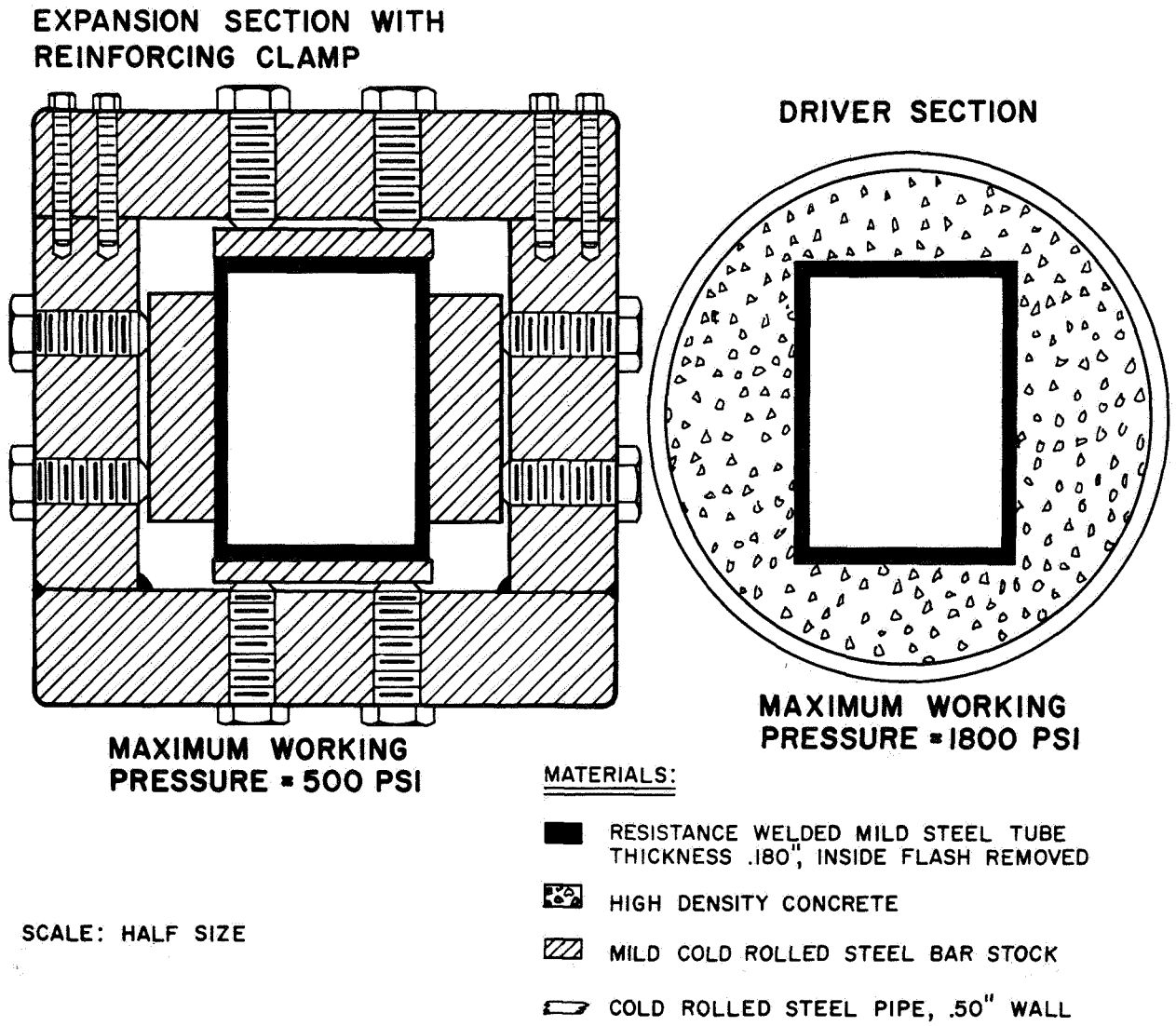


Fig. 26: Schematic Cross Sectional Views of Shock Tube Driver and Expansion Sections.

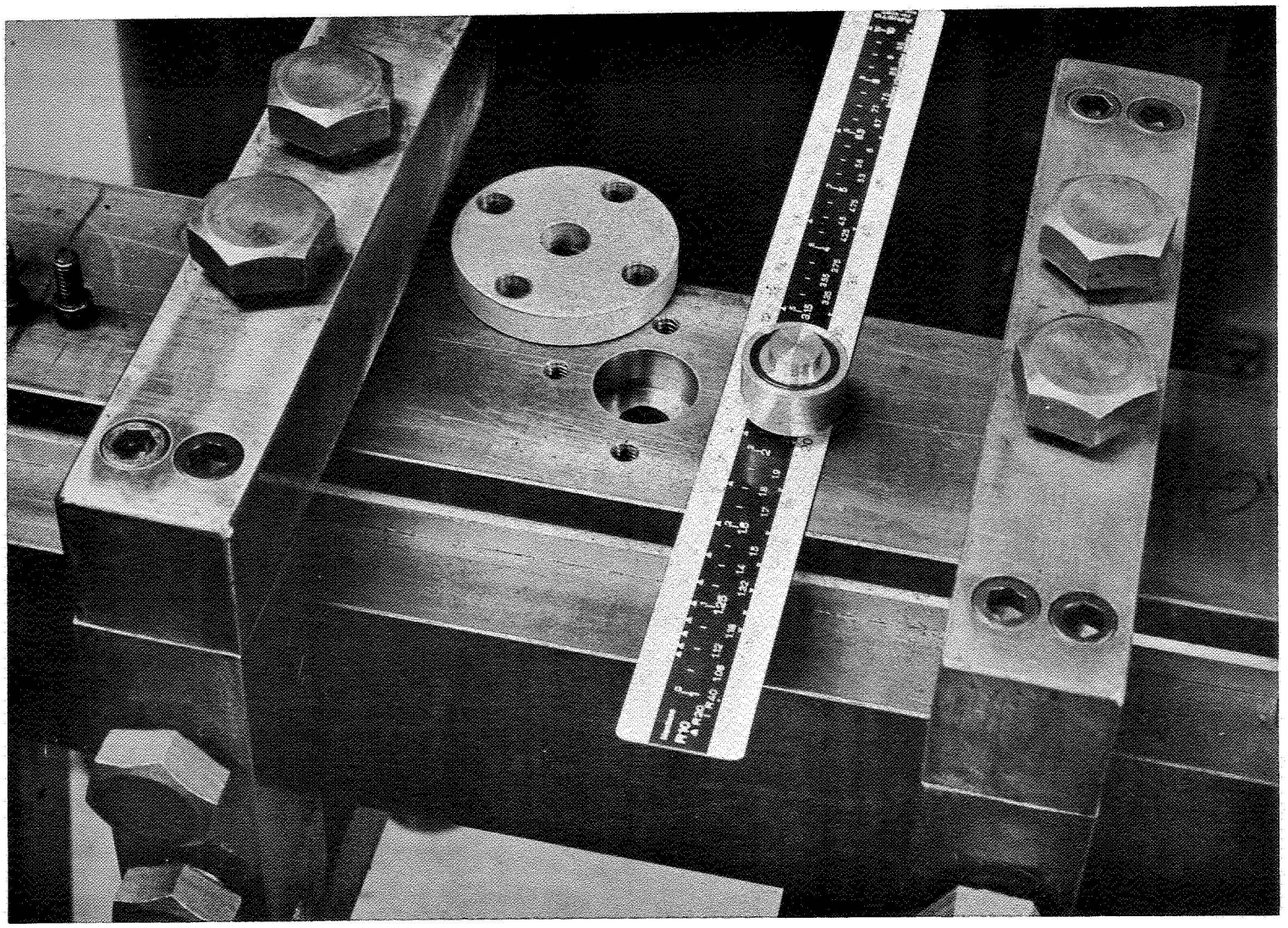

Fig. 27: Dorsal View of Expansion Section, Showing Method of External Reinforcement, a Typical Test Port, and a Blank Diagnostic Plug.

inch hole is then cut through the shock tube wall: the end of the diagnostic plug passes through this hole and fits flush with the tube's flow channel. Hold-downs are anchored in the reinforcing bars by 1/4" Allen bolts. A typical test part site and a blank (dummy) diagnostic plug are shown in Fig. 27.

Spectroscopic viewing is done primarily through two diametrically opposed windows on the sides of the test section, starting 1/32" in front of the end wall and extending 4" upstream from it. Effective window height is 1/2". Two window designs were employed. The first allows the spectroscopic vantage point to be taken anywhere along the window's 4" extent. Two slabs of Pyrex glass optically cemented together, rather than a single machined piece, were used both for ease of construction and safety (on several occasions the inner glass cracked but the outer, thicker glass remained intact). Windows of this design have a life of 20-50 shots before discoloration and abrasion (if not fatiguing) call for their replacement. They have the drawback that great care must be exercised to insure that no portion of the glass actually contacts the steel shock tube walls. Otherwise, the local stress during shock passage will invariably break them. A single layer of Teflon tape on all surfaces abutting the shock tube will relieve critical stresses but progressive erosion of the tape introduces contamination into the shock-heated plasma at the least desirable tube location. Also, a Teflon gasket carrying two O-rings that seal the window relaxes after initial installation and the requisite retightening makes it difficult to position the windows' inner face exactly with reference to the tube's inner walls. A second design has 1/2" by 1/2" windows epoxied into a brass or aluminum

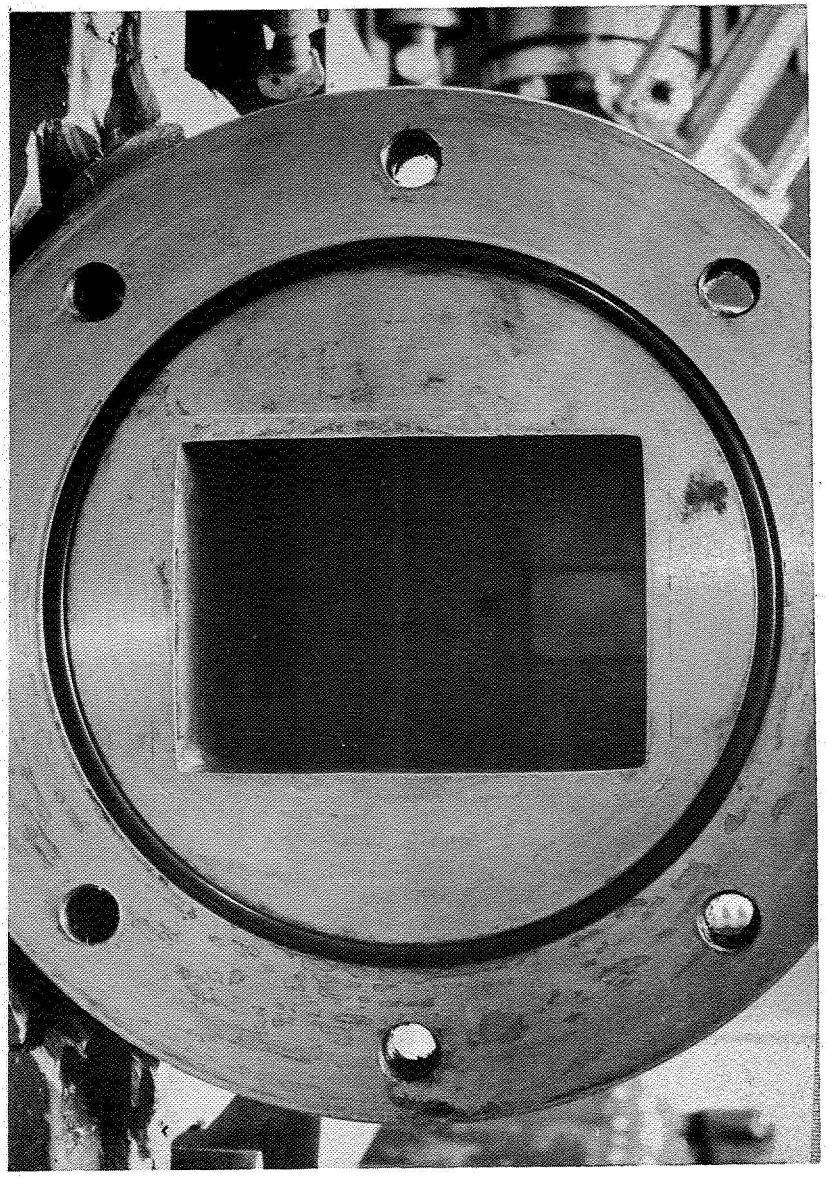

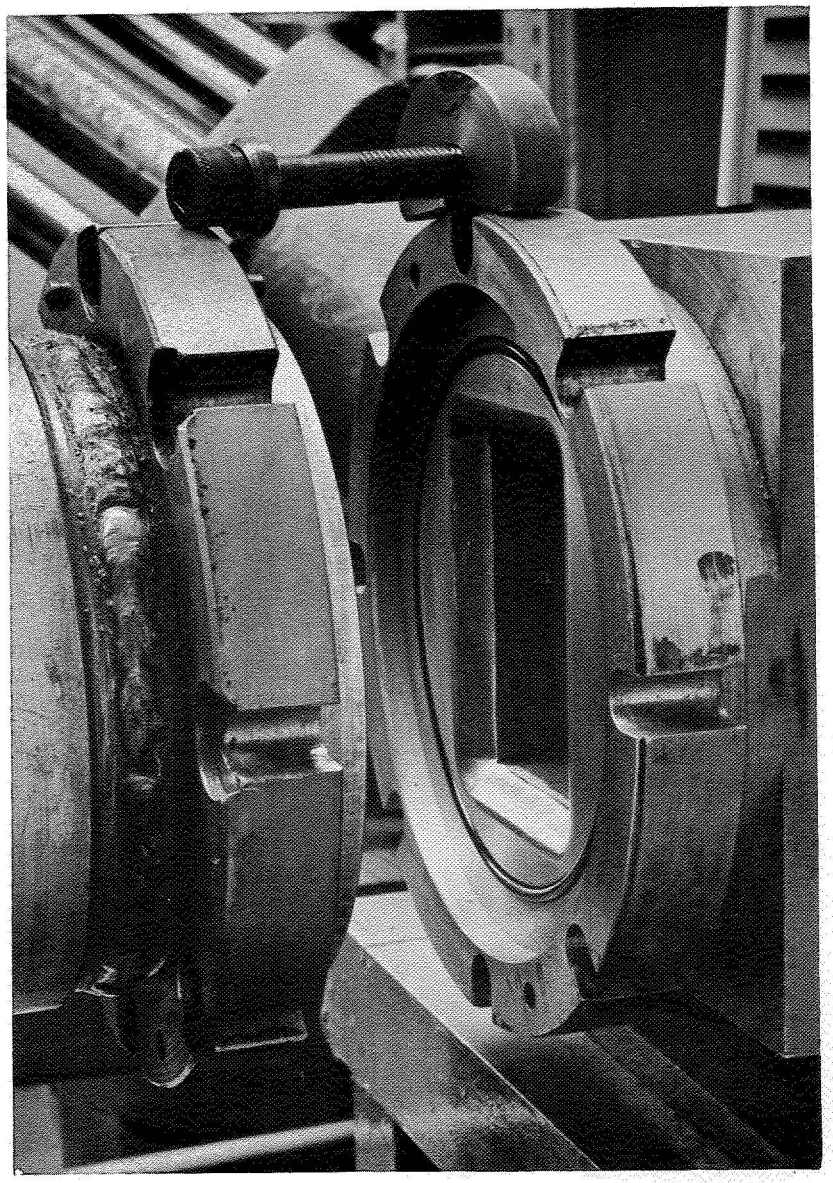

Fig. 28: Face of the Breech Section, Before Installation of Catcher (right), and, Driver Flange, Showing Union of Thin-Walled Tube (left).

"dummy" window which itself carries an O-ring. The problems here are to secure a vacuum tight epoxy seal and to remove the small window for replacement.

The driver section derives its strength from a 5½" ID, 1/2" thick circular pipe set coaxially around the 3" × 4" thin-walled tube. The void between these two cylinders is filled with high density concrete. The University of Maryland Sand and Gravel Institute prepared a high density concrete rated at 2700 psi compressive loading yet having a small aggregate size to promote easy flowing. Because the concrete is not plastic, the 3" × 4" thin-walled tube cannot deform unless there is yield in the heavy outer pipe. (A thin insulating layer of sand should be used wherever the concrete abuts a portion of the pipe to be welded--otherwise steam will evolve and vent through the molten welds). The driver rests on rollers so it may be slid backwards for easy access to diaphragms, which are locked between the driver section and the breech.

The breech holds the diaphragm and serves as the junction between the shock tube and the vacuum system. It is cut from a solid billet of mild steel and its flow channel matches those of the driver and expansion sections. Three concentric ridges .005" high bite into the rims of the diaphragms to prevent their creeping. For positive sealing both the high and low pressure sides of the diaphragm should seat against O-rings since pressurizing the driver strains the driver-to-breech clamping bolts enough to unseat a metal-to-metal seal. Where the 3" × 4" channel meets the (downstream side of the) diaphragm, all corners are broken in 1/4 radii to prevent open diaphragms from shearing off their petals at the roots (cf. Fig.30 ). Diaphragm reloading is speeded by using the clamping arrangement also shown in Fig. 28, which requires the breech bolts to be only slackened, rather than extracted from their nuts, for removal.

The piston valve, shown in longitudinal section in Fig. 32, mounts onto the breech at right angles to the shock tube axis. When the valve is closed, the end of the piston fits flush with the tube's flow channel. An O-ring carried in the piston mates against the side of the breech to provide a high pressure seal. This O-ring sits in an undercut groove so it will not fall out during cycling operations. When the valve is open (piston fully retracted) the valve offers a 4" throughput for rapid vacuum pumping in the molecular pressure regime. The piston rides back and forth on an ajax screw mounted on a thrust bearing. When the valve is open or cycling, two X-shaped O-rings("Quad-rings") on the pistons' OD push against the highly polished bore of the valve to provide vacuum sealing. As a precaution against leakage induced by wear in these O-rings, or scratches in the piston bore, the bonnet of the valve is kept evacuated by a small auxiliary mechanical pump. The bonnet is isolated from the bore of the valve by an O-ring seal about the stem of the ajax screw. Performance of this valve has been very satisfactory--in the course of hundreds of cycles no helium detectable leaks have developed.

3. Diaphragm selection, preparation and performance. Diaphragm OD is 6.5" with an effective load-bearing diameter of approximately 5". X-shaped relief grooves (diagonals of a 3" ×4" rectangle) are made on the downstream face to promote good breaking pressure reproducibility and to discourage the shedding of large fragments. However, without a judicious choice of diaphragm material, these grooves (scribes) accomplish neither objective: with cold-rolled steel, alloyed copper, and tempered aluminum, petal shedding was too frequent. Although annealed mild steel and dead-soft copper diaphragms held together well, their breaking pressures could not be

maintained within satisfactory tolerances†. Dead-soft aluminum (Alcoa #1-S or #11,000) gave good breaking pressure, reproducibility, and petal retention. This material was adopted even though its low tensile strength and high ductility adversely affect shock tube performance and its extreme softness requires the sheet stock to be masked with adhesive paper at the factory to prevent marring during normal handling. The low tensile strength made it necessary to go to diaphragm thicknesses of t = .125" to obtain desired breaking pressures in the range 1000 - 1400 psi. The large masses of the diaphragm petals prevent short opening times and tend to choke off the initial driver gas flows.[31,78] Because of their high ductility the diaphragms bow-out more than 1" before opening: with the flow channel's small dimension being only 2.64", this means that a large component of the initial flows will be wastefully expended in directions normal to the tube walls. These diagonal flow components also generate diagonal waves which can disrupt the homogeneity of the shock tube plasma.[70] Large diaphragm thickness and high ductility are felt to be responsible for the present shock tube's inability to match similar tubes in shock speeds at given initial pressure ratio p4/p1. Figure 29 gives the breaking characteristics for diaphragms of a variety of thicknesses and materials with two different methods of scribe preparation. The "petaling configuration" refers to whether the diaphragm did not open completely ($\theta<75°$, scribe depth too great), opened with petals lying flat against the walls of the breech ($75°<\theta\leq 90°$), or rebounded off the breech walls with sufficient force to end up pointing into the driver ($\theta>180°$). The latter behavior

---

† A cold-driver shock tube is not expected to reproduce shock speeds to better than a few per cent. However, some semblance of reproducibility is necessary for the pretriggering of CRO traces and for the adjustment of CRO gains to give reasonable data displays.

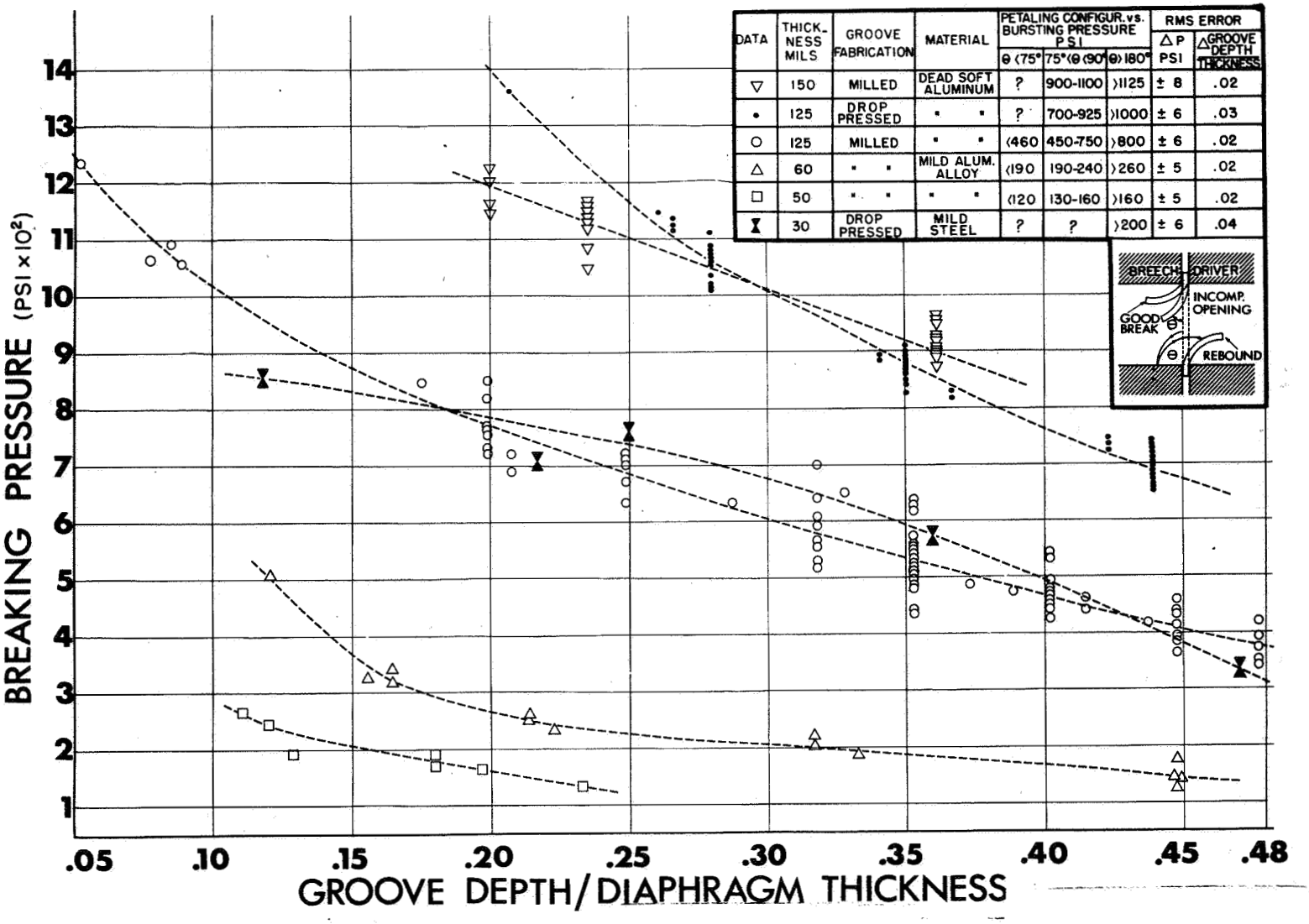


| DATA | THICK-NESS MILS | GROOVE FABRICATION | MATERIAL | PETALING CONFIGUR. vs. BURSTING PRESSURE PSI | | | RMS ERROR | |
|---|---|---|---|---|---|---|---|---|
| | | | | θ <75° | 75°<θ<90° | θ>180° | ΔP PSI | ΔGROOVE DEPTH / THICKNESS |
| ▽ | 150 | MILLED | DEAD SOFT ALUMINUM | ? | 900-1100 | >1125 | ± 8 | .02 |
| • | 125 | DROP PRESSED | " " | ? | 700-925 | >1000 | ± 6 | .03 |
| ○ | 125 | MILLED | " " | <460 | 450-750 | >800 | ± 6 | .02 |
| △ | 60 | " " | MILD ALUM. ALLOY | <190 | 190-240 | >260 | ± 5 | .02 |
| □ | 50 | " " | " " | <120 | 130-160 | >160 | ± 5 | .02 |
| ⧗ | 30 | DROP PRESSED | MILD STEEL | ? | ? | >200 | ± 6 | .04 |

Fig. 29: Diaphragm Breaking Pressures as a Function of (Scribe Depth/Thickness), with Method of Scribing, Material, and Diaphragm Thickness as Parameters.

was subsequently eliminated by installing catching pits in the breech at the points of petal impact. These pits have a maximum depth of ½" and a complex curvature designed to cause maximum deformation in the petals, thereby depriving them of excess kinetic energy. Spent diaphragms, one from before, and the other following, installation of the catcher are shown in Fig. 30.

Both mean breaking pressure (cf. Fig. 29) and scatter in breaking pressure (cf. Fig. 31) depend strongly on the method of making the diaphragm grooves. Initially they were made in a vertical mill using a cutting wheel of 60° included angle. Switching to a die-mounted blade driven by a 6 ton drop-press (drop-forge) gave substantially improved reproducibility, as seen in Fig. 31, higher breaking pressures for a given groove depth and diaphragm thickness (cf. Fig. 29), and also saved many hours of shop time. There are two reasons for the better reproducibility: when the diaphragm blanks are cut from sheet stock stress-relief causes them to buckle slightly, so a mill can not cut to a uniform depth but the die blade forces the diaphragm flat under its impact; also, a gauge block is used to arrest the travel of the die and results in fine tolerances. The reason for the higher breaking pressure is thought to be the work-hardening of material lying directly under the blade.

A rough measure of the spontaneous bursting pressure $p_B$ for unscribed circular diaphragms is:[70]

$$p_B \approx \frac{4tf_{ult}}{D}$$

where t = diaphragm thickness

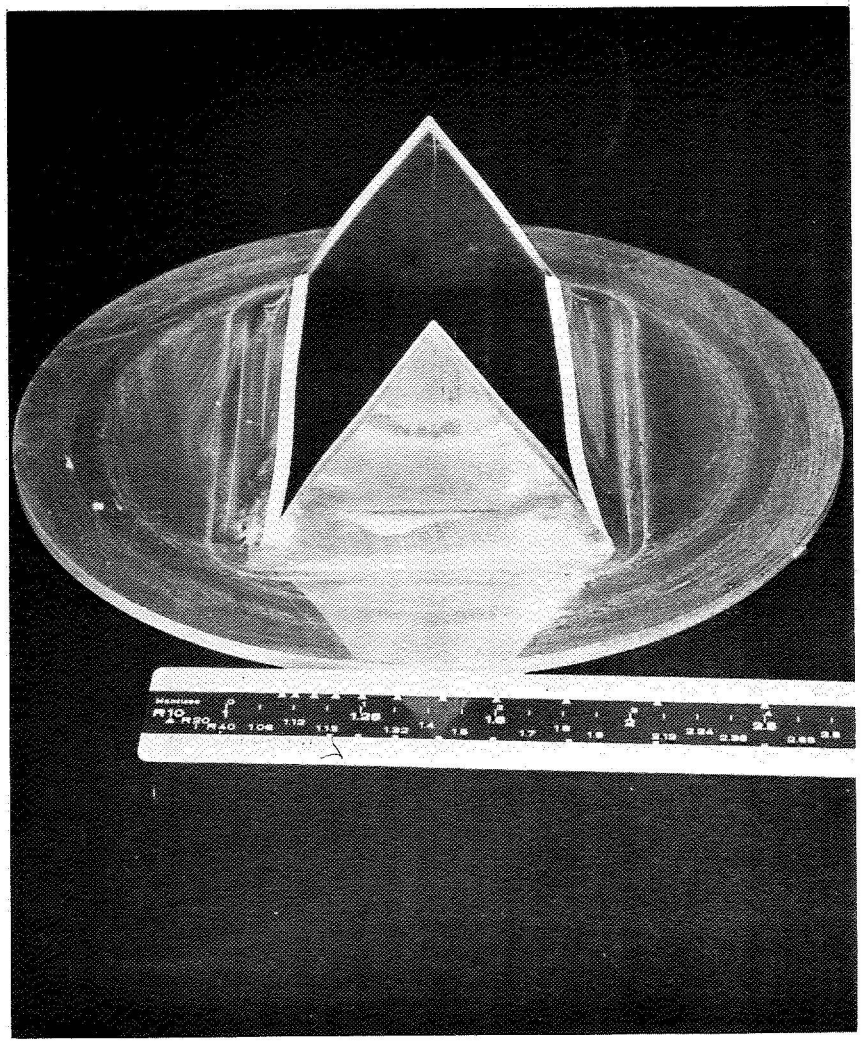

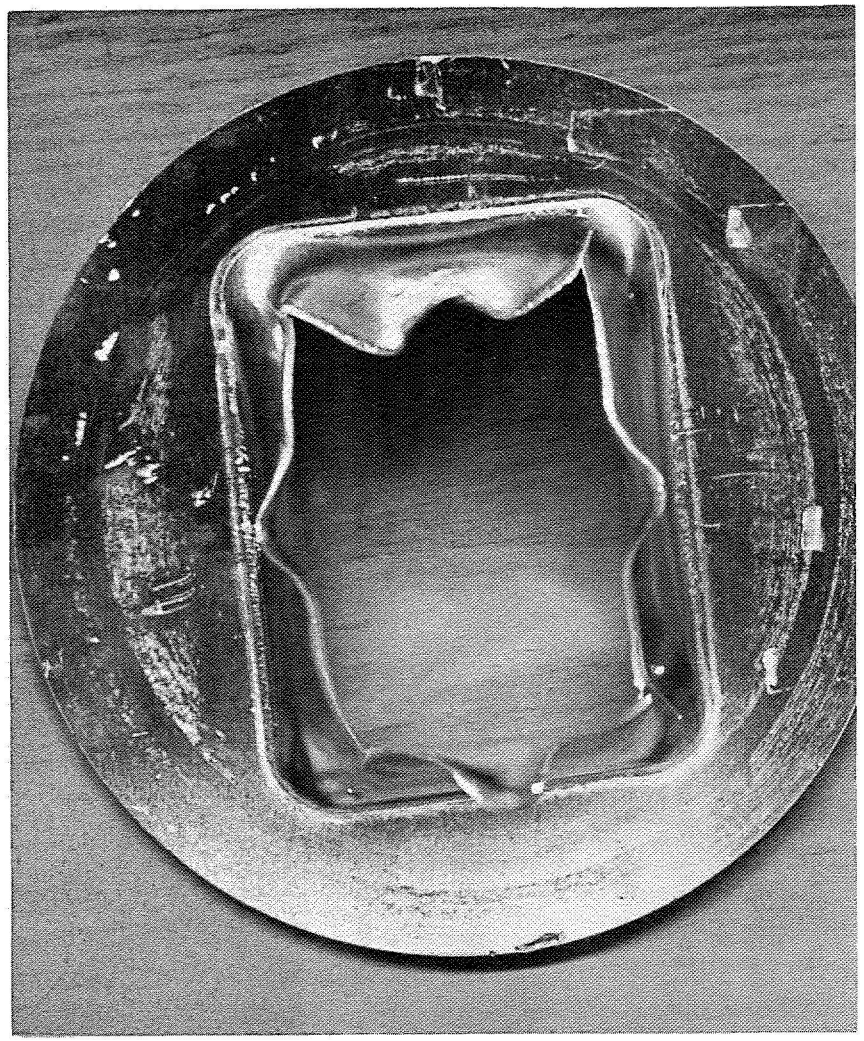

Fig. 30: Spent Diaphragms, Without Catcher Installed (left) and with Catcher installed (right).

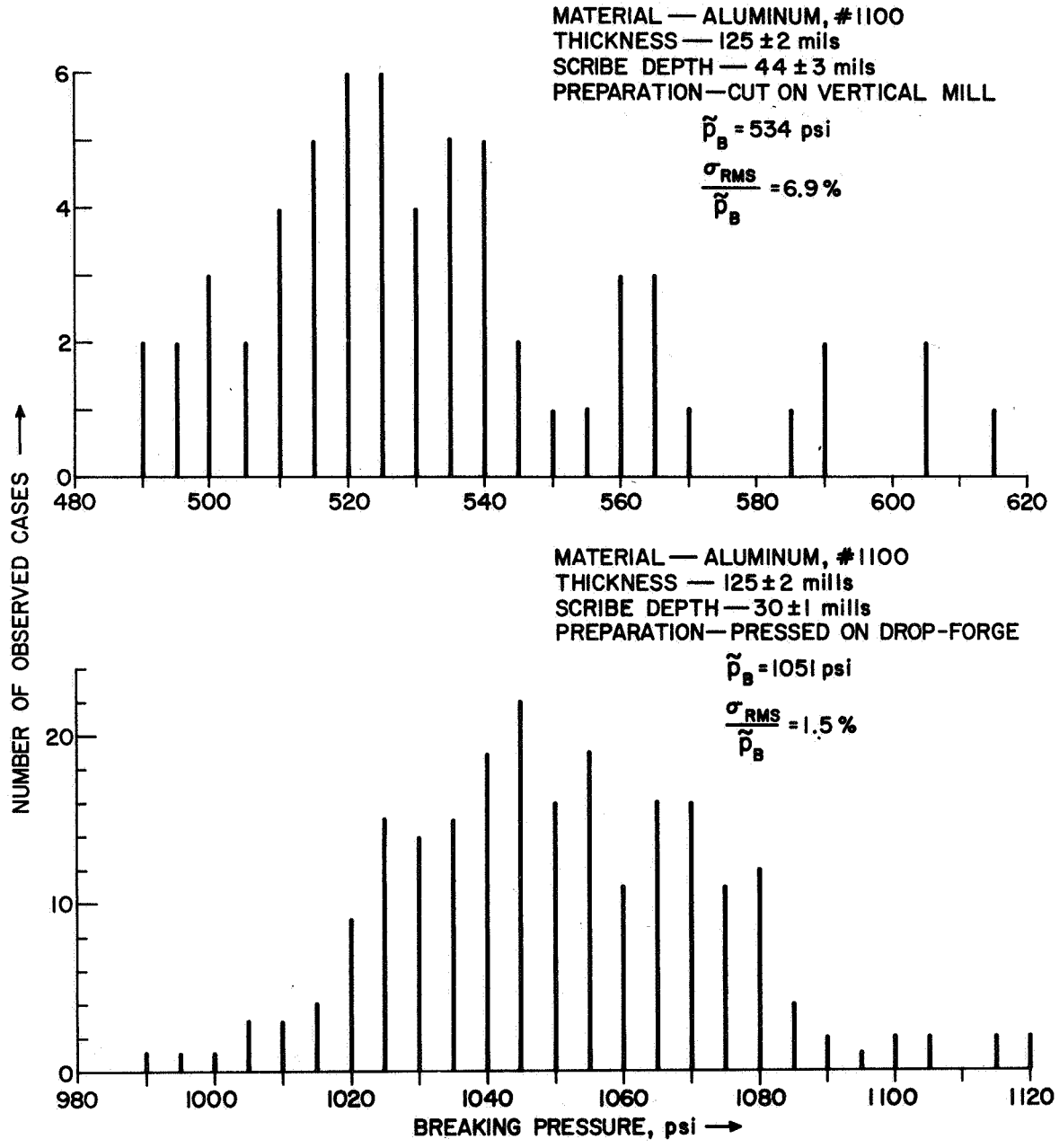


Fig. 31: Reproducability of Breaking Pressure for Two Types of Diaphragm Scribe Preparation.

$f_{ult}$ = ultimate tensile strength

D = unsupported diameter .

The breaking pressure of scribed diaphragms depends on the thickness $(t - d)$ remaining beneath the maximum groove depth $d$, and the local tensile strength of material at that site (which is different than in the bulk of the diaphragm). Moreover, when $d$ becomes a sizeable fraction of $t$, say $\frac{d}{t} > .5$, the stressed diaphragm no longer deforms to assume the shape of a spherical (or in the present case, an elliptical) section, but rather concentrates all the strain at the groove sites giving the stressed diaphragm a prismoidal appearance. A crude model for the breaking phenomena suggested trying to correlate the data of Fig.29 by the relation:

$$p_B \cong \frac{C(t - d)^{3/2}}{Dt^{\frac{1}{2}}}$$

where $C$ is a lumped empirical constant depending on the method of scribe preparation, the cross sectional share of the shock tube, and diaphragm material used. This equation gives the correct functional dependence on $t$ in the limit $d \to 0$, and within the limits $.1 \lesssim \frac{d}{t} \lesssim .5$, fits the data of Fig.29 reasonably well. The utility of this relationship is that once $C$ is established for a particular $p_B$, it enables the operator to prepare a supply of diaphragms giving desired breaking pressures over a factor of 2.

4. <u>Gas delivery and evacuation systems and equipment for handling driver gas</u>. The driver gas (usually hydrogen) is drawn from 200 $ft.^3$ cylinders with 1800 - 2000 psi maximum pressure. Cascading with a three

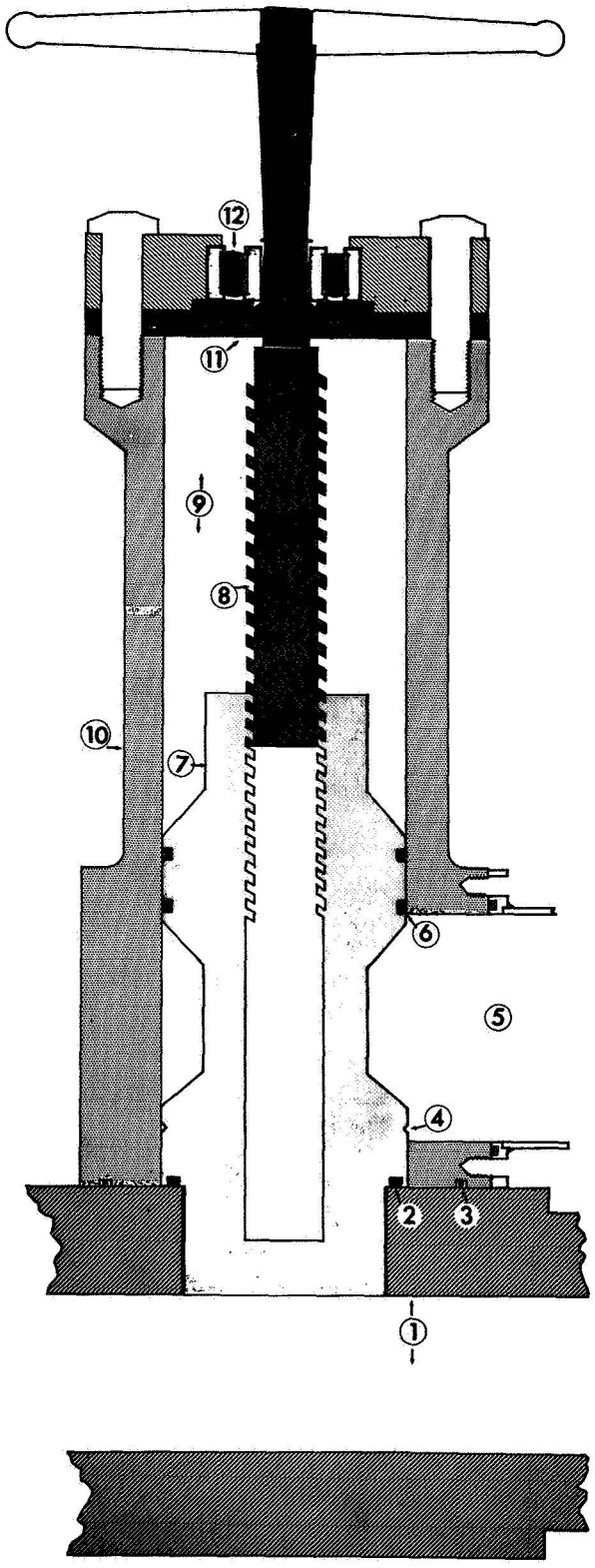


1. Interior of shock tube, short (2.7") dimension.
2. O-ring, groove undercut to prevent unseating during cycling.
3. O-ring: seals body to shock tube breech section.
4. Relief groove.
5. 4" diameter pipe to vacuum system.
6. "Quad-Rings": provide high vacuum seal during cycling.
7. Piston (brass).
8. Ajax screw.
9. Fore-chamber; can be evacuated by an auxilliary pump if leakage develops in "Quad-Rings," 6, or cyclinder bore gets scratched.
10. Body (mild steel).
11. O-ring; seals stem of Ajax screw if 9 is evacuated.
12. Thrust bearing.

Fig. 32: Cut-Away View of 4" Main Valve.

station manifold utilizes the contents of the cylinders down to a few psi gauge pressure. High pressure gas is introduced into the driver through a port in the end flange. High pressure flex hose is used so as not to hamper the mobility of the driver. Pressure is recorded by an 18" , 0 - 2000 psi Heise Bourdon gauge, shock-protected by six feet of .020" ID stainless steel capillary (resistive element) and a small high pressure flask (capacitive element). A 1" bore piston valve mounted on the driver's end flange affords good conductance during preparatory pump-down. After shooting, a quick-opening toggle valve entering a 1/4" exhaust line vents the used hydrogen outside of the building. Hydrogen remaining in the tube at ambient pressure is then removed by an outdoors-vented mechanical pump. A schematic diagram of the shock tube and its gas handling equipment is shown in Fig. 33.

5. <u>The vacuum system</u>. A 15 cubic foot/minute Duo-Seal pump alternately roughs down the system and backs a 4" PMC 720 diffusion pump. Backstreaming, which tends to build up hydrocarbon deposits on the shock tube walls, is reduced by a BC-40 chevron baffle cooled to -30°C by a 1/4 hp compressor working on a mixture of 80% Freon 12 and 20% Freon 22. A liquid nitrogen filled BC-40 baffle added in series to the refrigerated baffle keeps the tube cleaner by stoping backstreaming but does not reduce the pump-down times significantly. A 2½" Kane molecular sieve was placed in the foreline of the mechanical pump to reduce its back flow when roughing against tens of micron pressure. When the system (manifolds, valves, and shock tube expansion sections) was free of leaks detectable on a helium mass spectrograph with sensitivity of $3 \times 10^{-3}$ cubic micro-feet/hour, an ultimate base pressure of $4 \times 10^{-6}$ Torr could be achieved in the test section 24 hours after exposure to atmosphere. This corresponded

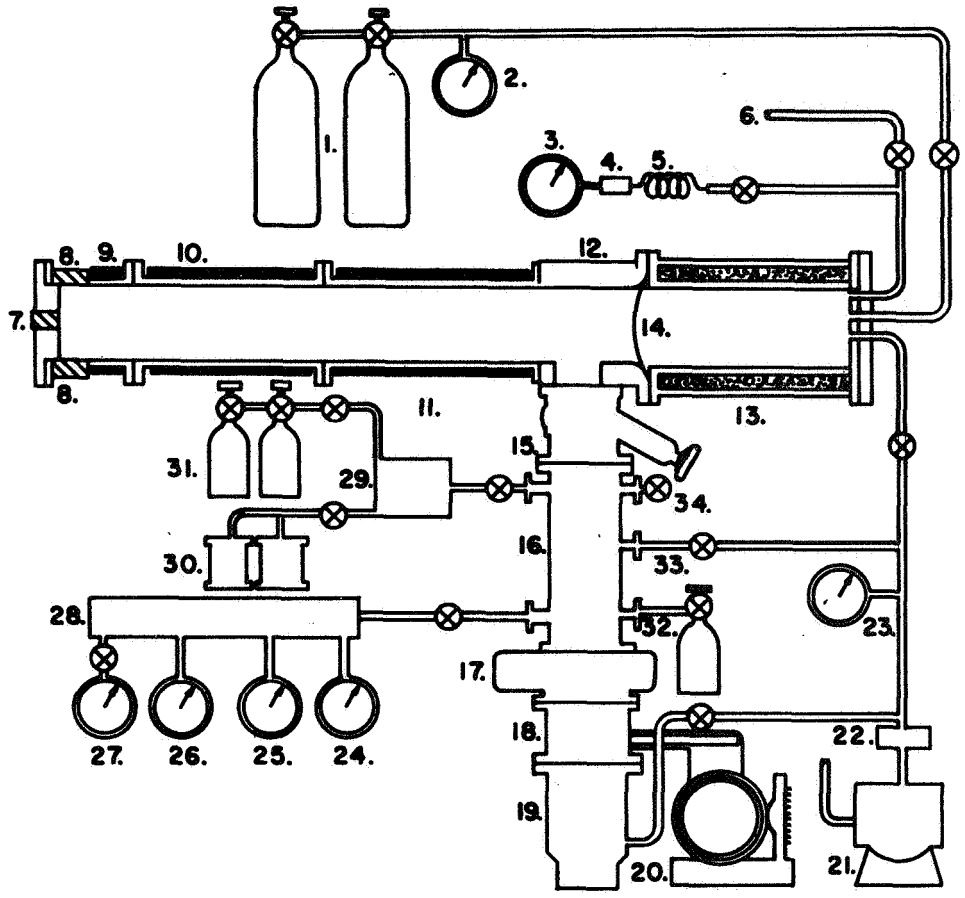


1. 2000psi DRIVER GAS CYLINDERS
2. TANK PRESSURE GAUGE
3. HEISE 0-2000psi DRIVER PRESSURE GAUGE
4. SURGE-TANK GAUGE SHOCK PROTECTION
5. 6' STAINLESS STEEL CAPILLARY TUBE
6. $H_2$ VENT TO OUTDOORS
7. WINDOW FOR AXIAL VIEWING
8. WINDOW FOR LATERAL VIEWING
9. TEST SECTION
10. FIRST EXPANSION CHAMBER
11. SECOND EXPANSION CHAMBER
12. BREECH SECTION
13. DRIVER SECTION
14. DIAPHAGM
15. 4" MAIN VALVE
16. MAIN MANIFOLD
17. VRC 4" GATE VALVE
18. VEECO 4" BAFFLE
19. 4" PMC-721 DIFFUSION PUMP
20. 1/4 hp FREON COMPRESSOR
21. DUO-SEAL 20 CFM PUMP
22. KANE MOLECULAR SIEVE
23. PIRANI FORE-LINE GAUGE
24. 0-20mm DIAPHRAGM GAUGE
25. CVC IONIZATION GAUGE
26. AUTO-VAC PIRANI GAUGE
27. $N_2$-TRAPPED McLEOD GAUGE
28. GAUGE SUB-MANIFOLD
29. MIXING SUB-MANIFOLD
30. STORAGE CYLINDERS
31. CARRIER AND TEST GAS CYLINDERS
32. $N_2$-BACK FILLING STATION
33. ROUGHING PUMP LINE
34. He LEAK-TESTING ACCESS PORT

Fig. 33: Schematic Representation of Shock Tube and Associated Gas Handling Equipment.

to a leak rate of $4 \times 10^{-4}$ Torr/min with pumps blanked off. It was found that backfilling the shock tube with super-dry $N_2$ preparatory to changing diaphragms, reduced pump-down times by factors of 3 - 4 below those required when atmosphere was admitted into the tube. A pop-up relief valve is fitted to the $N_2$ delivery line avoided straining the gate valve and other vacuum components. Most data runs were made after outgassing had subsided to a (virtual) leak rate of approximately $10^{-3}$ Torr/minute: at this level of vacuum the system's cycling rate was 2 - 3 shots/hour.

Several minor catastrophes led to the following safety features: in case of cooling water failure the diffusion pump automatically switched off†; in case of power failure a manual reset is required to start the pumps, eliminating the danger of motor burn-out when hot mechanical pumps "freeze" after a momentary power disruption; standby air bottles are equipped with a system of check valves which continue to supply the pneumatically actuated vacuum valves when the building's air compressor fails. The VRC pneumatically actuated 4" gate valve will automatically isolate the diffusion pump if system pressure exceeds .1 Torr. As a precaution against blowing-up the vacuum system by inadvertent exposure to high pressure (failure to seat the 4" high pressure piston valve), the system is fitted with an aluminum foil pop-out diaphragm to vent the system externally if pressures exceed 40 psi .

To routinely check outgassing rates and to monitor for the inevitable re-appearance of leakage, a multichannel LKB Pirani gauge was used. One channel sampled pressures in an arm of the main manifold

---

† Flow actuated switches supplied by Hayes Manufacturing Co.

situated between the shock tube and vacuum system where conductance to the diffusion pump is the same as from a point midway down the tube. Prior to every run the total (real plus outgassing) leakage in a two-minute period was recorded: if this exceeded $3 \times 10^{-3}$ Torr , the system was allowed additional outgassing time. Leakage that persists regardless of outgassing time is real and the leak source must then be located by a helium leak detector.

Another channel of the LKB gauge is situated on the exhaust line of the forepump to give warning of deteriorating pump oil, burnt-out diffusion pump heaters, broken belt drives, or similar malfunctions. Both channels of the LKB gauge are calibrated against a dry-ice trapped McLeod gauge down to $10^{-5}$ Torr . When the system is periodically overhauled to maintain high vacuum, a CVC ionization gauge monitors pressure down to $5 \times 10^{-7}$ Torr , the base pressure attainable when no helium detectable leaks exist and vacuum pumping has been uninterrupted for several days.

6. Test gas handling equipment. Test gases, typically composed of a 1% spectroscopic additive in a neon "carrier" gas, are introduced through a central manifold containing facilities for mixing, metering and storage.

For quantitative spectroscopy, test and carrier gases are not blended within the shock tube, as this often leads to uncertainty in the partial pressure of spectroscopic additive at the test section. For example, to make 10 Torr of a 1% $CH_4$ in neon mixture, one must first admit 0.1 Torr of $CH_4$ into the system and subsequently add 9.9 Torr of neon. The initial influx neon can sweep methane along with it, thereby enriching the methane concentration at the tube extremities (the test

section). Since there is essentially no convection within the tube, diffusion must be relied upon to re-establish an equilibrium partial pressure of methane throughout the system--but leakage compels the tube to be fired within 1 - 3 minutes after loading the test gas, so there may not be time to equilibrate.

To avoid this problem, test gases are drawn from bottles, either premixed and analyzed commercially in 25 liter or 50 liter quantities, or are previously prepared in the manifold, and then stored, in 10-30 liter† batches, in corrosion-resistant cylinders. All metal ("high purity") regulators were fitted to gas bottles whenever possible as these substantially reduced air contamination. In series with these are several feet of 1/16" OD stainless steel capillary tube terminating in Nupro fine-metering valves. This arrangement allowed for good control of flow rates, permitting shock tube filling times of half a minute. Moreover, the high flow rates within the small bored capillary did not allow constituents to demix†† according to their different thermal velocities at ambient temperature.

Test gas pressures, varying between 4 and 60 Torr, were read on Wallace and Tiernan 8" diaphragm gauges with 0-20 Torr and 0-100 Torr ranges. These have a reading accuracy of better than 1% full scale deflection, and repeated calibration against McLeod gauges showed no detectable elastic hysteresis and no departures from linearity greater than $\mp$ 2% anywhere within their range.

To test for interaction between the shock tube walls and spectroscopic additives of $CH_4$ and $GS_2$, small quantities (0.3Torr)

---

†Twenty liters is adequate for 10-20 runs.

††An operational check (with negative results) for demixing is described in Chapter VII, Section D4.

of these gases were rapidly admitted to the evacuated shock tube and the subsequent pressure changes were recorded: the only changes noted were the expected rise due to leakage. So there is no detectable adsorption of these gases, while if any reactions do occur they preserve the total pressure, which does not seem likely.

## B. Diagnostics

1. Spectrographic instrumentation. Time resolved absolute photometry involved simultaneous use of two spectrographs and a monochromater. Figure 34 shows the deployment of these instruments and the method of recording employed on each: the accompanying table gives approximate apertures, focal lengths, accessible wavelengths, and effective time resolution for each. A more detailed description of the various spectrographs and their respective roles in the investigation will follow an explanation of our unorthodox method of photoelectric image dissection.

Our program of redundant measurement of state variables carried with it the need for multi-channel photoelectric recording. First attempts at multi-channel recording utilized a photoelectric back of conventional design, i.e. employing sets of movable slits in the spectrograph focal plane, each with positionable mirrors to relay light into the appropriate photomultiplier. We were unable to secure satisfactory performance from this system because proper construction proved too challenging, mainly because of exit slit requirements. Slits must have a desired width, be free of wedgness, be aligned with the spectrograph entrance slit to within a few minutes of arc, must have jaws narrow enough to allow for each spectroscopic line-monitoring channel to have a near-background monitoring channel. They must be positioned, reproducibly, to

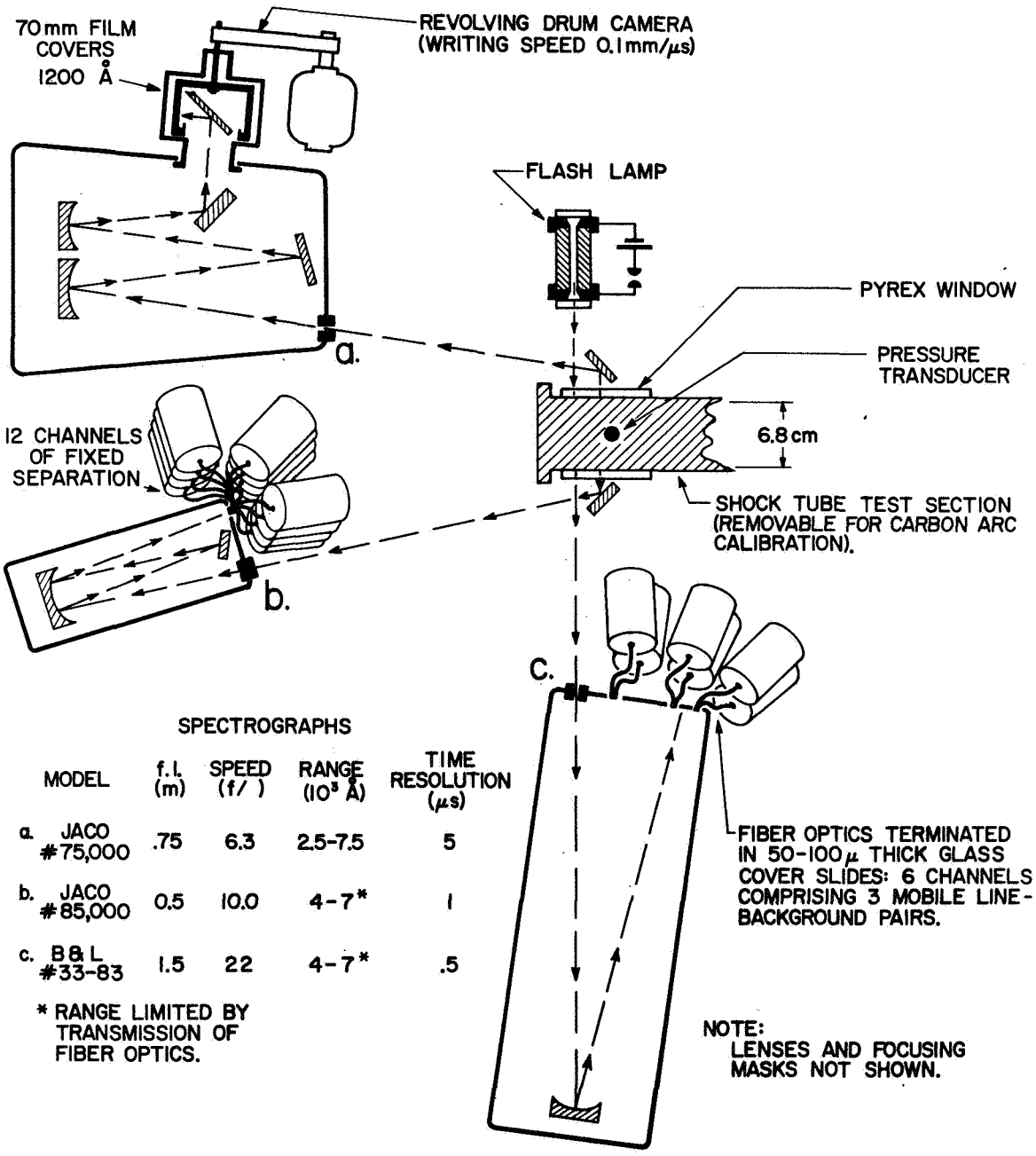


SPECTROGRAPHS

| | MODEL | f.l. (m) | SPEED (f/ ) | RANGE ($10^3$ Å) | TIME RESOLUTION (μs) |
|---|---|---|---|---|---|
| a. | JACO #75,000 | .75 | 6.3 | 2.5-7.5 | 5 |
| b. | JACO #85,000 | 0.5 | 10.0 | 4-7* | 1 |
| c. | B&L #33-83 | 1.5 | 22 | 4-7* | .5 |

* RANGE LIMITED BY TRANSMISSION OF FIBER OPTICS.

Fig. 34: Apparatus for Time-Resolved Spectroscopy of Shock Tube Plasmas.

within 1/5 Å (10μ actual displacement) in the wavelength direction of the focal plane. This wavelength positioning must be accomplished from a site external to the light-tight photomultiplier enclosure. Moreover, the complex array of mirrors in this arrangement made scattered light (cross-talk) difficult to eliminate. Efforts to perfect the conventional photoelectric back were not successful, and it was abandoned when the image dissectors described below become functional only a few weeks after testing of trial models.

In the current method of image dissection light is conveyed to a photomultiplier by internal reflection, first within a microscope cover-glass slide, and then within a fiber-optic bundle. No exit slits are needed: the leading edge of the cover-glass slide, positioned in the spectrograph's focal plane, defines the bandpass destined for a particular photomultiplier. One joins a microscope cover slide and a fiber optic bundle so as to utilize the clean laminar geometry of the former to replace an exit slit while utilizing the flexibility of the latter to circumvent the formidable mechanical difficulties we have already mentioned. A schematic diagram of a "reading-head" containing several photoelectric channels is shown in Fig. 35. To mount a reading-head on a spectrograph, it is first inserted within a hollow cylinder held perpendicular to, and with one end abutting, the focal plane. The cylinder not only protects the fragile assembly of cover-glass slides, but can be rotated around its long axis by a spring-loaded tangent drive, providing easy alignment with the entrance slit. For a monochromater this is the only mounting required. Figure 25 gives an external view of a 12-channel image dissector mounted on a JACO #85,000 monochromater†. Note that each photomultiplier is mounted

---

†Because of its tentacle-like appearance this installation will be referred to as the SQUID or Sequential Image Dissector.

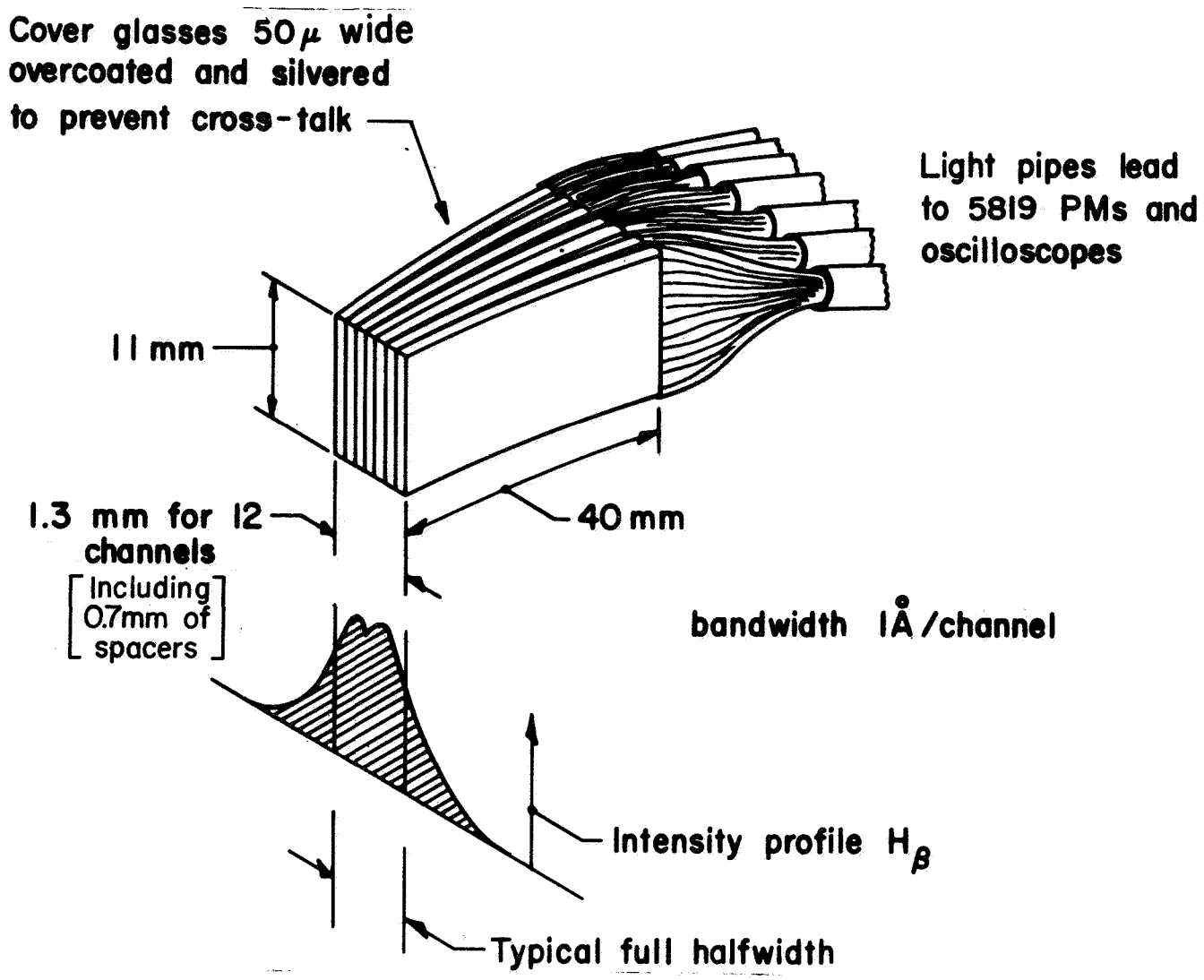


Fig. 35: Schematic Representation of Photoelectric Sequential Image Divider ("SQUID").

in a separate light-tight cylinder, allowing for its individual removal without disturbing the remainder of the installation, and allowing for *in situ* alignment of the reading-head under normal room light. When reading-heads are mounted on a spectrograph, such as the BεL #33-83 the rotating cylinders are themselves mounted in metal blocks which, riding on Teflon pads, can be micrometer-driven along tracks in the wavelength direction of the focal plane.

Cover glass slides are made of optical grade glass, with their two large surfaces ground flat and optically polished. Thickness measured along a single edge seldom varies by more than $\pm$ .4μ ,and because of the high polish of their sides, a cone of light with small solid angle that enters normally at one edge will propagate by total internal reflection to the opposite edge with little attenuation due to scattering off surface imperfections. They can be supplied† cut to desired (rectangular) size for a few dollars an ounce, in thicknesses roughly graded as follows: 55μ $\pm$ 10μ ,85μ $\pm$ 10μ , 125μ $\pm$ 10μ , 145μ $\pm$ 10μ, 180μ $\pm$ 10μ , 200μ $\pm$ 10μ and 250μ $\pm$ 10μ . The majority used in the present work are 11mm × 40mm × 50μ . A given ounce of slides will contain many different thicknesses varying between the stated tolerance limits, so it is necessary to select out samples with the precisely desired thicknesses.

As supplied, the slides' edges are unfinished, carrying the marks of a cutting wheel. Polishing of these edges by a professional optician did not increase the end-on transmittance of the slides, which varied between 50%-70% for light transmitted over the 40mm length.

The 11mm × 50μ edge of a cover glass slide is joined to a 1/8" diameter fiber optic bundle (light pipe) as follows. Select a bundle of

---

†Laboratory Glassware Division, Corning Glass Works, Corning, N.Y.

twice the desired length. At the midpoint remove about 1" of the PVC protective sheath and saturate the exposed fibers with a free flowing epoxy. Then work these into a .5mm deep, 11mm wide groove cut in a 1" square block of Teflon and cap with a flat sheet of Teflon, which is clamped over the groove until the epoxy sets, at which time the 1" length of .5mm × 11mm laminar cross-section is removed from the Teflon mold. When this is cut in half on a glass cutting wheel, and the two laminar edges optically polished, one has two light pipes ready for joining with cover slides. The union is formed by thermoplastic optical cement, worked with a small soldering pen of the type used on microcircuits. By directing a light into the free end (round end) of the light pipe during this operation, and observing the intensity emergent from the cover slide, it is possible to rework portions of the bond where light conductance is poor.

When combining two or more channels to form an image dissector (reading-head), it is necessary to build in a desired spacing between channels and also to guard against possible cross-talk between channels, especially contiguous ones. Phenolic spacers, machined to desired tolerance, effect the desired channel separation, the reading head being clamped together until beads of epoxy, applied along top and bottom, have set. When many channels are used, the flexible cover slides are flared out at their exit ends to make room for the fatter light pipes (cf. Fig. 35 ). Because the large surfaces of the cover slides have an excellent finish, only a negligible percentage of light escapes from one to enter the adjacent one <u>except</u> at points where optical wax has been applied to join light pipes and cover slides. To prevent cross talk, a layer of magnesium fluoride is vacuum-deposited on the large faces (sides) and overcoated with aluminum. If aluminum is applied directly, the internally reflected

light will be greatly attenuated. Freedom from cross-talk is verified when the completed reading-head is swept across a strong, thin spectral line, a channel at a time, and no signal is detected on neighboring channels.

Compared to other methods of multi-channel photoelectric recording the present one has several marked advantages, as well as some serious drawbacks. Its most attractive features are simplicity of manufacture and clean geometry. After spending a few hours learning the handling characteristics of the materials, someone of average dexterity can fabricate a cover glass-light pipe combination in an hour or two[†], while still obtaining good geometry and well-controlled dimensions for the input channel. This makes it practical to custom design reading-heads for specific tasks, such as monitoring a spectral line and its near line-free background, or dissecting a line of broad profile, such as $H_\beta$. Another advantage of cover slides[††] is the dense packing of sampling channels attainable--more than twenty per millimeter.

The several disadvantages to this method of image dissection are: its inherently low overall transmittance, the tendency for transmittance to change with even slight handling of the light pipes. (The need for expensive multi-channel recording is inherent to any image dissector: if a full time history is desired for each channel, then one CRO beam must be allotted each channel, as is the present case--otherwise, sequential

---

[†]This contrasts with the skill and weeks-long effort needed to tease light pipes apart and reassemble them in linear arrays.

[††]Denser spacing is available with use of cellophane "zip-tape" which comes in thinner sheets than cover slides--but handling and light attenuation problems are serious for this material.

sample-and-hold techniques, employing fast zener diode switches, can be used. The overall transmittance of yellow light for a typical 40mm long, 50μ thick cover slide affixed to 12" of light pipe is 10% - 20%, depending on the quality of the junction between them. Transmittance falls off slowly in the red up to 7000Å, but drops to 5% - 10% in the blue-purple region. About 30% - 50% of the incident light is lost in cover slide, while perhaps 50% of what remains is attenuated in the light pipe. Since their attenuation increases exponentially with length, light pipes should be kept as short as possible. A light pipe's transmittance depends upon its configuration which affects angles of incidence for internal reflection within each glass fiber. So, a slight jarring of a light pipe can easily destroy the absolute intensity calibration of a photoelectric channel.

Photoelectric recording was used with the JACO #85,000 monochrometer and the B&L #33-83 spectrograph (cf. Fig. 34). Twelve† RCA #5819 photomultipliers (S-11 spectral response) were employed with the sequential image dissector (SQUID) mounted on the monochrometer. The usual functions of this instrument is to monitor twelve 1.0Å wide segments of the $H_\beta$ profile. For routine data runs, six photomultipliers sampled the spectrum of the B&L spectrograph: these were arranged into three pairs of reading heads, each designed to monitor a particular line and its nearby continuum. Photomultipliers were assigned to the various lines as follows: for CI λ5052 we used RCA #5819's (S-11 spectral response), for NeI λ5852 we used RCA #4459's (S-20 spectral response) and for $H_\alpha$ λ6562 we used EMI 9558-B's (S-20 spectral response).

Photomultiplier circuits were designed to meet the following specifications: dynode capacitors must be large enough that the current

---

†We are indebted to the Maryland State Agency for Surplus Property for making this, and other equipment, available to us at nominal handling costs.

drain during a typical 50 - 150μsec data sampling time does not significantly lower dynode voltages. Anode resistors must be kept small enough that the RC constant of the tube is small compared to the inherent time resolution of the spectrograph, i.e. the mean diameter of the optical path across the shock tube divided by the typical shock speed.

For the measurement of line reversal on $H_\alpha$ (cf. Chapter VI) the PM time response must be small compared to the rise time of the flash lamp.

Time-resolved photographic recording was employed with the 0.75 meter JACO #75,000 spectrograph. A variac regulated Dumore ½ hp motor drove the 5" diameter rotating drum camera up to writing speeds of 0.1mm/μsec. The drum itself was machined from aluminum alloy and dynamically balanced on its Dumore quill. The camera housing is cut from a 7" diameter steel pipe (¼" wall thickness): an earlier rectangular housing, fabricated from $\frac{3}{8}$" aluminum plates would vibrate harmonically when the drum was revolving at high speed.

In the majority of our data runs we used Kodak 2475 (70 mm) film, developed in DK-50 for 6.5 minutes at 75°F. Some spectra of carbon and sulfur were recorded on Kodak 103-F, developed for 3 minutes in D-19 at 75°F.

The effective time resolution of our photographic recording was determined by the height of the slit image in the film plane, i.e., this height divided by the camera's writing speed is the effective time resolution of the film. Typically this was 3-5μsec.

A detailed description of the reversal flash lamp is given by Charatis[31,80].

2. Pressure Transducers give a time-resolved record of pressures behind shocks. We used Kistler #601 quartz transducers coupled with Kister #501 charge amplifiers. The amplifiers are calibrated (cf. Chapter VI) to put out 1.0 mV per psi of shock tube pressure. Time resolutions are 1 - 2μsec. The method of mounting the transducers is critical: their pressure sensitive faces should fit flush with the shock tube walls or else they generate local discontinuities in shock flows and pressures. If the metal-encapsulated transducer is in direct metal-to-metal contact with the shock tube walls, the transducers characteristic 130 kc ringing frequency will be strongly excited. By using the transducer mountings shown in Fig. 36, the ringing is reduced, by factors of 2 - 3 for the "hard" mounting, and 3 - 4 for the "soft" mounting, compared to the ringing obtained when the transducer is mounted directly in the tube walls. Both of these mountings cushion the accelerations at the time of shock passage: the "hard" mounting tends to remain vacuum-tight longer than the "soft" mounting.

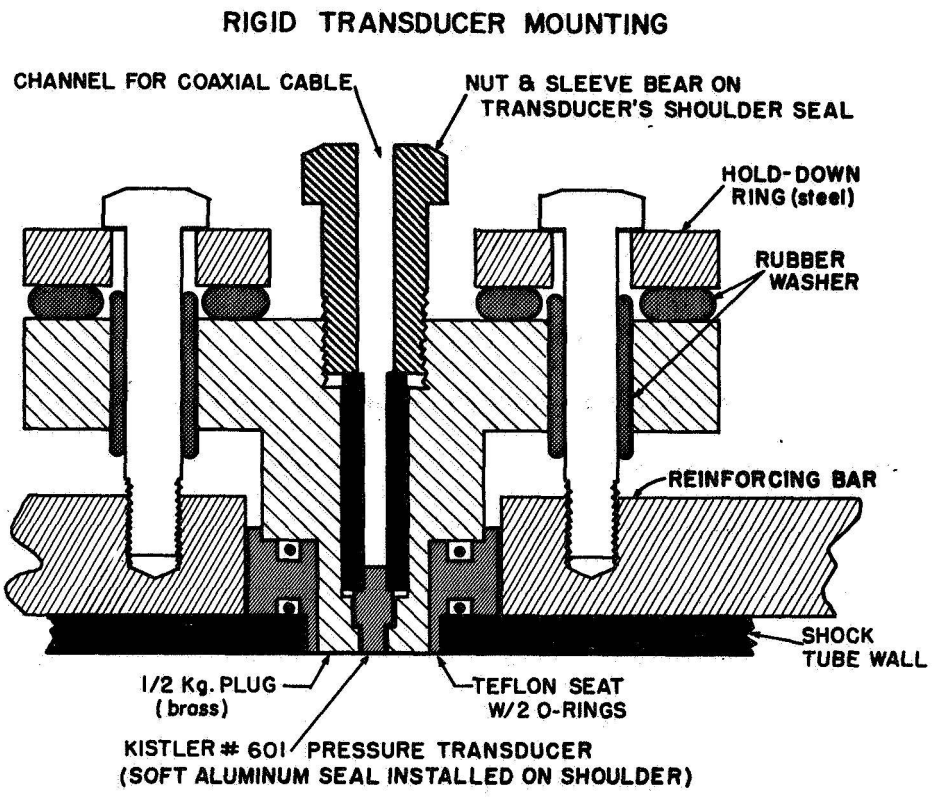


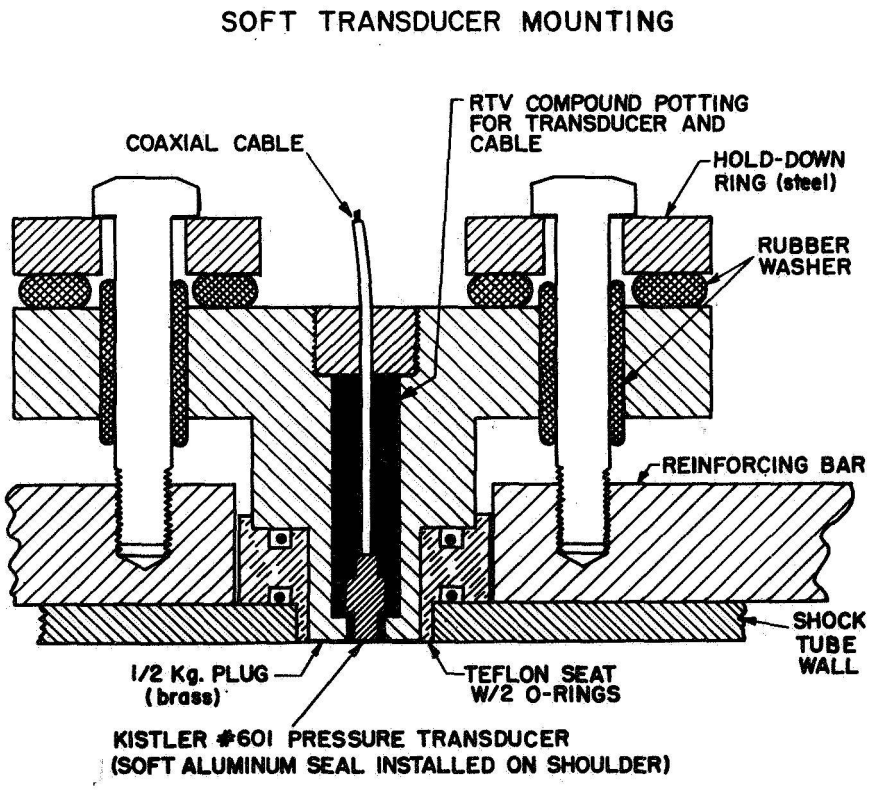


Fig. 36: Two Types of Quartz Transducer Installations Used to Minimize Ringing Amplitudes During Shocks.

# CHAPTER VI

# EXPERIMENTAL METHOD

## A. Introduction

This chapter discusses the experimental techniques used to collect data. We stress that all important variables were measured at least two independent ways: this includes both calibration factors and the data obtained during routine experimental runs.

Absolute intensity calibrations were performed two independent ways; two different photographic emulsions were independently calibrated in relative intensity, and photomultiplier response was routinely checked for linearity *in situ*. Pressure transducers were calibrated both statically and dynamically.

Temperatures behind first reflected shocks were simultaneously measured four independent ways -- and in some cases, six independent ways. Pressures were measured directly with quartz transducers and also deduced from incident shock speeds. The absolute integrated intensity of CI $\lambda 5052$ was simultaneously recorded photographically and photoelectrically.

We feel that this program of redundant measurement, coupled with the TIB methods presented in Chapter III and with the practice of securing data under widely varying plasma conditions, as discussed in Chapter VII, is necessary to guard against large systematic errors in measured A-values.

B. Absolute Photometry

1. Introduction. Photomultipliers were absolutely calibrated two independent ways: first by the well-known method using the chopped emission from a quiecent DC carbon arc crater, as described in Section 1-ii, and then by a new method which adopts as the absolute photometric standard the product $A_\alpha \times L_\alpha(\lambda,Ne)d\lambda$ , where $A_\alpha$ and $L_\alpha(\lambda,Ne)d\lambda$ are, respectively, the transition probability and the shape function of $H_\alpha$ . This new method is described in section I-iii. Photographic emulsions were calibrated by relative intensity comparisons against the carbon arc. The relative intensities were adjusted to absolute values on a shot-to-shot basis by comparison with several absolutely calibrated photoelectric channels in a method described in Section 1-v.

2. Linearity checks. The assumption of linear photomultiplier response is central to the interpretation of our data. We therefore not only bench-tested the response of photomultipliers before installing them, but periodically rechecked them *in situ*. For bench-testing, a General Radio Strobe lamp was used, its repetition rate set allow for recovery of the photomultiplier's dynode capacitors between flashes. The Strobes' discharge cycle is highly reproducible, giving a signal of well-defined half-height duration. By varying the distance between the photomultiplier (henceforth, PM) and the Strobe lamp, the amount of the PM input could easily be controlled. As incident light levels were increased, the onset of saturation was readily detected by an apparant increase in duration of the Strobes' discharge cycle, (i.e. the apparent half-width increased).

Two techniques were used to check PM linearity *in situ*: both required transient sources with brightness surpassing typical shock tube luminosity. The reversal flash lamp (cf. Chapter V) had the requisite

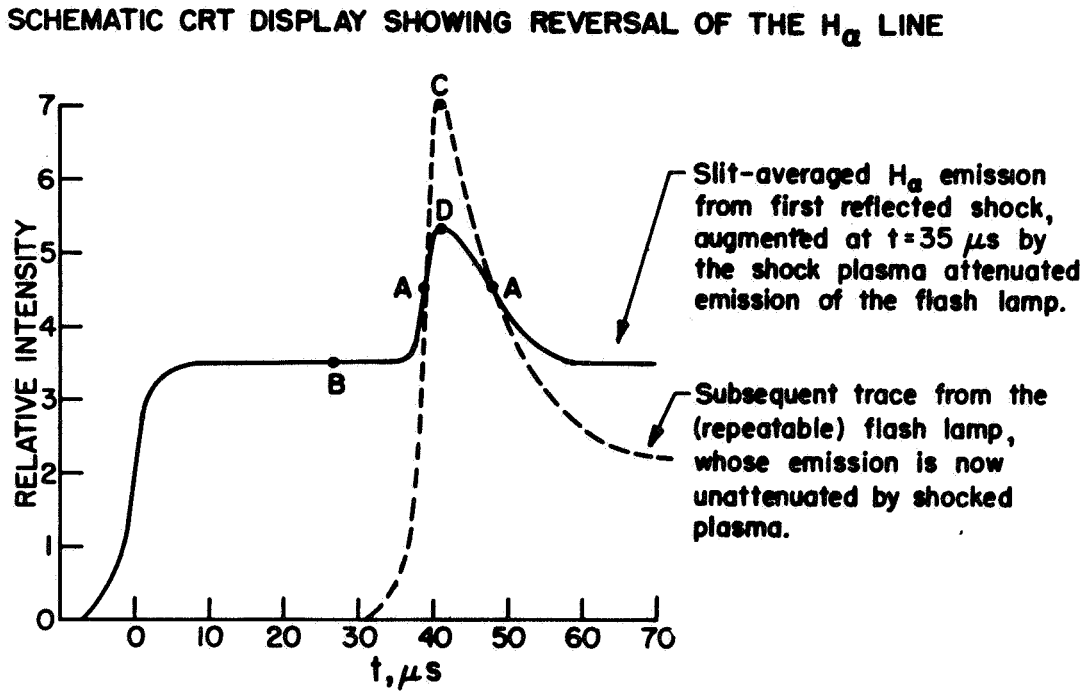


A. These are "reversal points" where $\int I_\nu \, d\nu = \int B_\nu(T) \, d\nu$ . The thermal dependence of points A. is given by curve c. of Figure 4.

B. Shock tube emission of $H_\alpha$ viewed with 2.0Å wide slits. The thermal dependence of point B, for two different mixtures, is given by curves a. and b. of Figure 4.

C. Peak unattenuated intensity of the flash lamp: this is equivalent to grey-body emission from a source several kilodegrees hotter than the shock tube plasma.

D. Peak intensity of flash lamp after attenuation caused by traversing the shock tube in which the central portion of $H_\alpha$ has a high optical depth.

USES OF THIS DISPLAY (assuming that absolute source pressure is known):

(1) The ratio B./A. can be used to convert the relative intensity scale (ordinate) to an absolute intensity scale.

(2) With an absolute intensity scale established, the reversal points A. can be used to measure the source temperature because the Planck function is a unique function of temperature.

(3) (C.-D.)/(C.-A.) vs. B./A. affords an in-situ linearity check upon the photomultiplier since the slit-averaged emission coefficient of the shocked plasma should have the same value whether it is measured in-emission or in adsorbtion.

Fig. 37: Schematic CRT Display Showing Slit-Integrated $H_\alpha$ Intensity and Line Reversal on $H_\alpha$ .

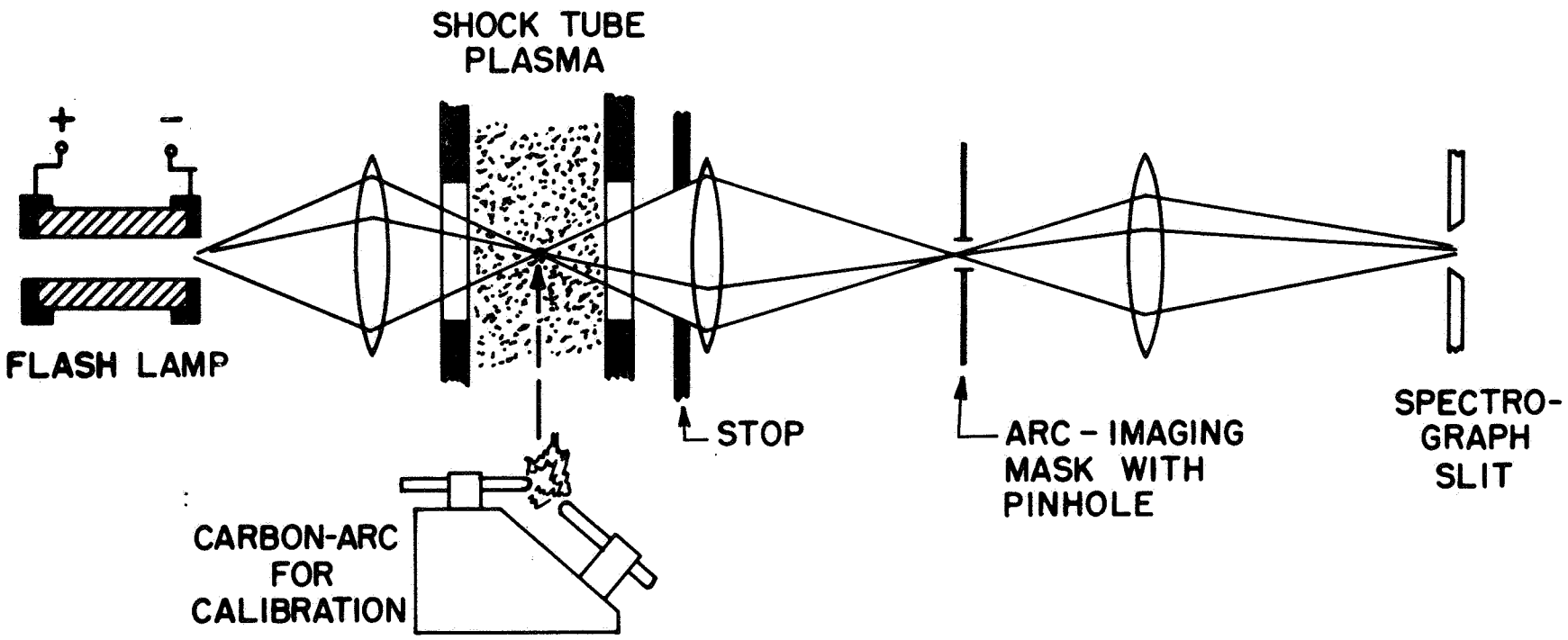


Fig. 38: Optics to Illuminate Spectrograph for Absolute Intensity Calibrations.

brightness and reproducibility (1% - 3%) for this task. A calibrated, fourteen step Kodak neutral density filter was used to modulate the flash lamp intensity: thus PM input signal levels are made to span, in known increments, the range encountered during routine data runs.

The second in situ linearity check is based on the laws of radiative transfer and is performed during regular data runs. A spectrograph-mounted PM views the steady state shock tube plasma, first in emission, and then in absorption against the hotter grey body emission of the flash lamp: the values of the mean shock tube optical depth, $\tilde{\tau}$ , deduced from the emission and absorption observations will agree only if the PM is operating linearly.

Because the subject of this and the following section is the interaction between radiation from a hot transient plasma (a flash lamp discharge) with a cooler, steady state plasma, (the shock tube plasma) we should make clear precisely how the spectrograph is illuminated. Radiation should be collected from the cooler (shock tube) plasma from within only that cone of rays defined by the radiation from the hotter (flash lamp) plasma. Therefore, we use the arrangement of lenses and stops depicted in Fig. 38 : the circular stop on the lens defines the required cone of rays emerging from the shock tube[†].

The solid curve in Fig. 37 represents the output of a PM monitoring the central 2Å of $H_\alpha$ during a typical data run. Within a few μsec after passage of the reflected shock front, intensity rises to the steady state level denoted by point B , where it remains for the duration of the first

---

[†]The focusing mask and pinhole are used when calibrating the system against a carbon arc. When the arc is placed in the optical path, it is imaged on this mask where the pinhole selects out the desired radiation of the anode crater "hot spot."

reflected shock, or until the flash lamp is discharged[†]. The expression for the slit-integrated intensity of $H_\alpha$ during this time is given by eqn. [17] . For brevity we introduce the notation:

$$\int_{-1\text{Å}}^{+1\text{Å}} I_\alpha(\lambda)d\lambda = B_{\lambda_o}(T_{ST}) \int_{-1\text{Å}}^{+1\text{Å}} (1-e^{-\tau})d\lambda = I_{ST} = IB \quad \text{of Fig. 37}$$

where $T_{ST}$ is the temperature of the shock tube plasma and $\tau$ is the optical depth: both are independent of time within the depicted 70 μsec period.

The dashed curve, peaking at point C , represents emission from the discharged flash lamp observed in the absence of any attenuating shock tube plasmas. The spectrum of this radiation is featureless (grey-body), so it can be described over limited wavelengths by a Planck function[††]

$$I_{FL}(t) = 2\text{Å}\cdot B_\lambda(T_{FL}(t)) \quad .$$

This defines the black body temperature (at $\lambda$) of the flash lamp. The flash lamp duration is a few μsec, so $T_{FL}(t)$ is a rapidly varying function of time.

Sychronizing the flash lamp to fire when a shock heated plasma lies between it and the PM produces the observed intensity curve, BADA . At any time the observed intensity is composed of the shock tube emission

---

[†]Figure 34 shows the experimental arrangement: the $H_\alpha$ channel is in the B&L spectrograph, and the flash lamp radiation passes through the shock tube.

[††]The flash lamp radiation could be described instead by some grey-body temperature $T' > T_{FL}$ so that $E_\lambda(T')B_\lambda(T') = B_\lambda(T_{FL})$ and the forthcoming analysis would not in any way be affected.

$I_{ST}$ plus the shock tube-attenuated flash lamp intensity:

$$I(t)_{total} = B_\lambda(T_{ST}) \int_{-1\text{Å}}^{+1\text{Å}} [1-e^{-\tau}]d\lambda + B_\lambda(T_{FL}(t)) \int_{-1\text{Å}}^{+1\text{Å}} e^{-\tau}d\lambda \quad .$$

The points "A" where the full and dashed curves cross† identify the Planck function intensity, $B_\lambda(T_{ST})$ , of the shock tube plasma. That is, the condition

$$I(t)_{total} - I_{FL}(t) = 0$$

is satisfied (for finite $\tau$ ) by the condition:

$$B_\lambda(T_{ST}) - B_\lambda(T_{FL}(t)) = 0$$

or, equivalently, is satisfied for times $t'$ when

$$T_{FL}(t') = T_{ST} \quad .$$

Therefore, at points "A" (times t') ;

$$IA = B_\lambda(T_{FL}(t')) = B_\lambda(T_{ST}) \quad .$$

To perform the <u>in-situ</u> linearity check one overdetermines $\int_{-1\text{Å}}^{1\text{Å}} [1-e^{-\tau}]d\lambda$ through use of the three intensities IC, ID and IB , picked-off

---

†These are the "reversal points," so named because spectral features of the shock tube plasma, such as $H_\alpha$ , are passing from a condition where they observed in emission against the time-increasing local background (from the flash lamp) to the condition where they are observed in absorbtion.[31]

$$IC - ID = I_{FL} - I_{total}$$

$$= B(T_{FL}) - B(T_{ST}) \int_{-1\mathring{A}}^{+1\mathring{A}} [1-e^{-\tau}]d\lambda$$

and

$$IC - IA = B_\lambda(T_{FL}) - B_\lambda(T_{ST}) \quad .$$

Combining the above equations:

$$\frac{IC - ID}{IC - IA} = \frac{IB}{IA} = [2\mathring{A}]^{-1} \int_{-1\mathring{A}}^{+1\mathring{A}} [1-e^{-\tau}]d\lambda \equiv \tilde{\varepsilon} \quad . \qquad [22]$$

Since IC > ID > IB , these overdeterminant conditions will be self-consistent only when the photomultiplier is operating linearly. Note that linearity is checked at the signal levels and durations of interest for recording shock tube data. (From IB we will deduce the temperature $T_\alpha$ and from IA , the temperature $T_{rev}$ , as explained in the next section.)

Before going on to consider a new method for <u>in situ</u> absolute intensity calibration based on Fig. 37 , we direct attention to the CRT tracing reproduced in Fig. 45 . The points on the real trace (Fig.45 ) analogous to points A, B, C and D of the schematic (Fig. 37) can readily be identified. In practice, the flash lamp signal can be superimposed on the subsequent flash lamp-plus-shock tube signal so that points "C", and "D" coincide to a fraction of 1 μsec in the CRT sweep direction. We mention again that flash lamp peak intensities are reproducable to 1% - 3%[†], because it is this reproducability which allows us to make use of sequential traces of $I_{FL}$ and $I_{total}$ .

---

[†]Similar, or better, reproducability is claimed for the commercial Garton[81] type of flash lamp.

3. Absolute intensity calibration using the A-value and shape Function of $H_\alpha$ as absolute standards. By using the reversal flash lamp and the laws of radiative transfer we obtain an absolute intensity calibration (at 6563Å) which refers to the A-value and shape function of $H_\alpha$ as the ultimate standards of spectral irradiance. Results of this procedure will be compared with extensive carbon arc calibrations in Section B-5.

Returning to Fig. 37 , let us identify the signal for the slit-integrated intensity of $H_\alpha$ , as coming from a plasma of known composition and pressure: ½% $CH_4$ + ½% $CS_2$ + 99% neon at $p = 9.0\times10^6$ dyne $cm^{-3}$. If the source temperature is unknown, then IB , which is recorded as a relative intensity in arbitrary units in Fig. 37 ,is associated with an absolute intensity (in units of carbon arc intensity) lying somewhere along the curve "C" in Fig. 4 . That is:

$$\beta IB = \int_{\frac{ws}{2}}^{\frac{ws}{2}} I_\alpha(\lambda)d\lambda \qquad [23]$$

where $\beta$ is the unknown scaling factor necessary to establish the absolute sensitivity of the detector, i.e. $\beta$ absolutely calibrates the detector. We recall from the discussion concerning eqn.[17],that for a given pressure and plasma composition, the right hand side of eqn. [23] is a unique function of plasma temperature only. Therefore, IB in units of absolute intensity is a function of the two unknowns, $\beta$ and T .

Figure 37 also depicts the signal level (relative intensity in arbitrary units) for reversal $IA = \frac{1}{\beta} B_\lambda(T_{ST})\cdot ws$.Since the Planck function at the wavelength 6563Å is a function of T only (which is also depicted in Fig. 4 ), IA is a second observed variable that is a function of the two unknowns $\beta$ and T .

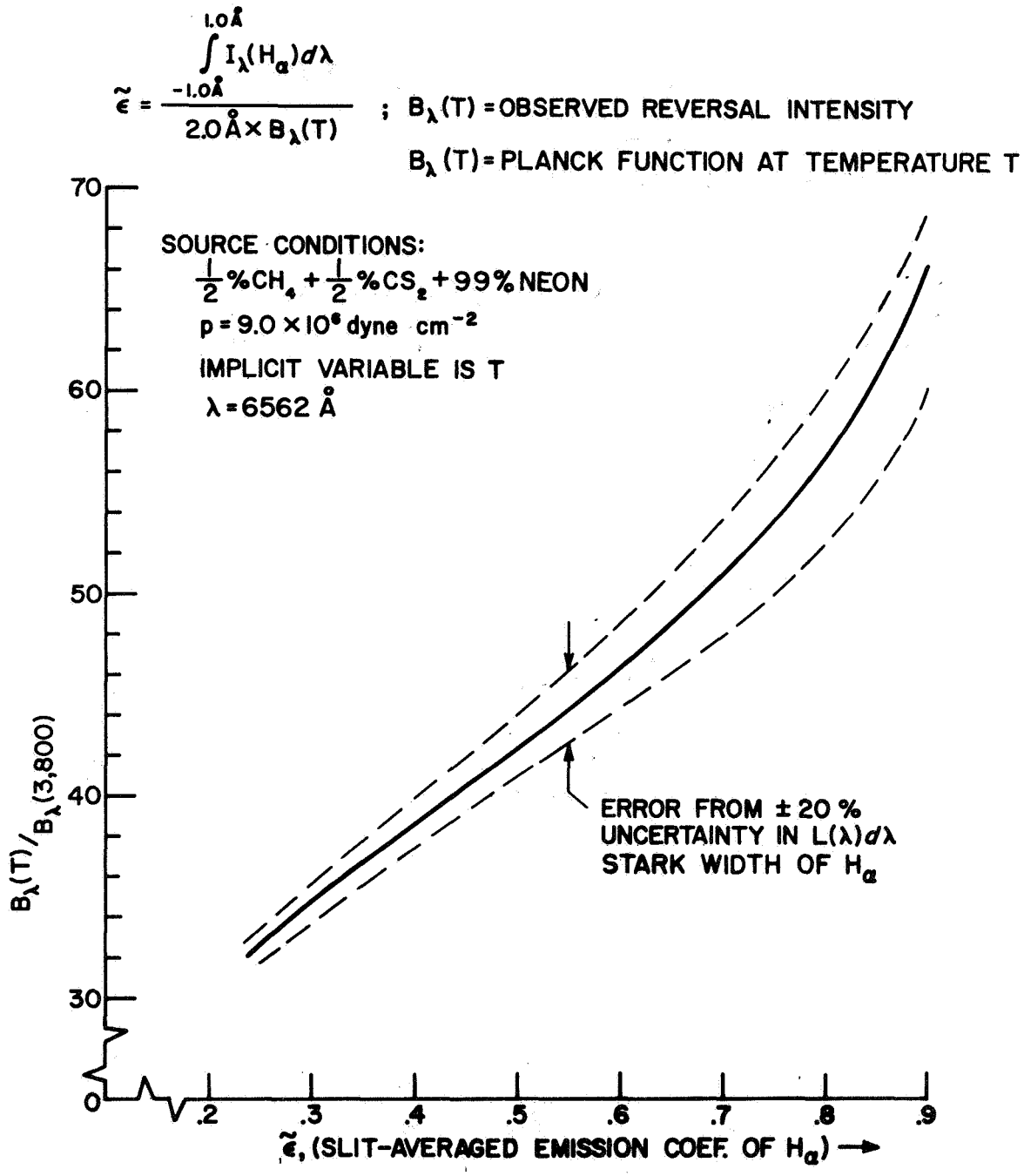


Fig. 39: Absolute intensity Calibration Using $H_\alpha$ as Internal Standard: Reversal Intensity vs. Slit Averaged $H_\alpha$ intensity/Reversal Intensity.

So, between $IA(\beta,T)$ and $IB(\beta,T)$ we can simultaneously solve for both† $\beta$ and $T$. Since the immediate interest here is to determine $\beta$, we parameterize the simultaneous equations to give the graphical solution shown in Fig. 39. Explicitly,

$$\frac{IB(\beta,T)}{IA(\beta,T)} = \frac{\beta}{\beta}\,\frac{B_\lambda(T)}{B_\lambda(T)}\,(ws)^{-1}\int_{-\frac{ws}{2}}^{\frac{ws}{2}}[1-e^{-\tau}]d\lambda = \tilde{\varepsilon}(T) \quad .$$

That is, the ratio of the two intensities, IA and IB, observed on the same uncalibrated detector, is a unique function of plasma temperature.

Because both $B_\lambda(T)$ and $\tilde{\varepsilon}(T)$ are unique functions of temperature, we can express the Planck function in terms of $\tilde{\varepsilon}$:

$$B_\lambda(\tilde{\varepsilon}) = B_\lambda\left(\tilde{\varepsilon}\left(\frac{IB}{IA}\right)\right) = \beta IB\left(\frac{IB}{IA}\right) \quad . \qquad [24]$$

This equation yields the desired absolute intensity calibration: the Planck function associated with the intensity IB, observed with an uncalibrated detector, is a unique function of the intensity ratio IB/IA.

In Fig. 39 † $B_\lambda(\tilde{\varepsilon})$ is expressed in units of carbon arc intensity at 6563Å. As an illustrative example, we apply this figure to absolutely calibrate the intensities shown in the schematic CRT trace of Fig. 37. We find

$$\frac{IB}{IA} = \frac{3.55}{4.55} = .78$$

---

†In the usual procedure, comparison against the carbon arc determines $\beta$, so that the reversal intensity $B_\lambda(T_{ST})$ can be used to determine source temperature. This is the well known "reversal-temperature" [31,71,80-85]

††The vertical error bars in Fig. 39 are the images of the error bars in Fig. 4; they represent the uncertainty in the shape of $H_\alpha$ as a function of electron density.

for which Fig. 39 gives:

$$\frac{B_\lambda(\tilde{\varepsilon})}{B_\lambda(3{,}800°K)} = 56.0 \pm 3.5 = \beta IA \quad .$$

Having established the calibration factor, $\beta$ , we can find the source temperature with the aid of Fig. 4 . Using $B_\lambda(T) = 56 \pm 3.5$ we obtain $T = 11{,}600°K + 330°K$ . (This temperature is equivalent to the "reversal temperature"[31,71,80,82-85] that would be obtained when $\beta$ is determined from comparison with the carbon arc). We might also use

$$\beta IB \int_{-\frac{ws}{2}}^{\frac{ws}{2}} I_\alpha(\lambda)d\lambda = 43.7 \pm 3.5$$

to obtain

$$T = 11{,}600°K \pm 200°K \quad .$$

(We call this temperature $T_\alpha$ and will discuss it further in Section C.)

So long as $.4 < \tilde{\varepsilon} < .8$ , the internal calibration method is accurate to 6% - 8%, which is sufficient to give source temperature with a 2% - 3% accuracy at $T = 11{,}000°K$. If current studies[86] on the shape of $H_\alpha$ as a function of electron density are successful in reducing the present 20% uncertainty[87] down to a level comparable with that of $H_\beta$ , (for $10^{16} < Ne < 10^{17}$ this is currently $\pm$ 5%), then the accuracies available from this interval calibration will become $\pm$ 2% for the absolute intensity and $\pm$ .6% for plasma temperature.

Even with the currently realizable accuracies, this new method of calibration has several distinct advantages that recommend it for use at least to verify carbon arc calibrations (at $\lambda = 6563\text{Å}$), if not to replace them. Among the advantages of the new calibration are the following:

(1) It is performed <u>in situ</u>, so there are no questions about duplicating optical paths (lens positions, source positions, window transmissions) for calibrations and data runs as there are with carbon arc.

(2) It calibrates detectors at the same signal levels and signal durations that are encountered in taking data from bright transient plasmas, rather than at the far lower signal levels, and longer durations, available from the chopped carbon arc.

(3) For light sources where re-absorption in boundary layers is pronounced, the new calibration leads to more accurate emission studies since the ratio $\frac{IB}{IA}$, and hence $B_\lambda(IB/IA)$, will be less affected by re-absorbtion than is $B_\lambda(T)$ or IA by itself-

(4) The internal calibration is obtained at no extra expense when one performs a conventional reversal temperature measurement at $H_\alpha$.

(5) Internal calibration, unlike the carbon arc calibration,[88] can be performed in the IR or the UV[†] if the spectra in these regions contain a line for which the uncertainty in the product of A-value and Stark broadening parameter is not greater than 20%, and for which peak optical depths greater than .4 can be obtained.

---

[†]Unfortunately, the internal calibration can seldom be employed with T-tube plasmas whose durations are usually not long compared to flash lamp durations.

We emphasize that since the internal calibration is applied at a single wavelength, one must still use a carbon arc (or tungsten filament lamp) to transfer the calibration to other wavelengths: relative calibrations, however, are far less prone to error than absolute intensity calibrations.

4. Absolute intensity calibrations using the carbon arc. Photomultipliers were absolutely calibrated against the carbon arc in the conventional way. We followed the usual prescriptions[88-91] for electrode outgassing, advancing to "hissing points," etc. The imaging screen and pinhole for selecting radiation from the desired anode "hot-spot" were shown in Fig. 38. A toothed chopping wheel passed the beam intermittently so as to prevent drain on the PM dynode capacitors.

Some of our earlier calibrations used the published carbon arc irradiance values of Null and Lozier.[91] The newer findings of Hattenburg and Kostkowski[88] were adopted in time to be used in calibrating most of our data runs.

We had difficulty obtaining the ideal "quiescently burning arc of maximum brightness." Optimal ballast resistance would change from day to day; indeed, sometimes one could burn through several pairs of electrodes without ever achieving a quiescent state. Adding a low pass filter (capacitance 2000 μf and inductance 40 h ) to the motor generator circuit made the arc less susceptible to diurnal changes, but did not guarantee reproducibility. Wandering of the "hot spot" also complicated the calibration — the arc can burn quiescently, drawing a steady recommended current (which was constantly monitored) and still the emission reaching the PM tubes would fluctuate as the hot-spot's image skirted the pinhole. Wandering of the arc column,

together with our rather poor current stabilization[†], introduced scatter into our calibration voltages. There is some ambiguity concerning how a distribution of calibration voltages is to be interpreted: to adopt the average voltage for a particular calibration ignores the fact that both major sources of scatter, wandering of the arc column and current fluctuations, tend to lower signal levels. A major uncertainty in our carbon arc calibrations therefore arises in the estimation of the amount that arc wandering and current fluctuations have systematically lowered calibration voltages.

This uncertainty, folded in with scatter from photomultiplier noise and reading error, varied typically between 5% and 10% depending on the particular PM tube, being calibrated, the wavelength being calibrated, and how cooperative the arc was on that particular day. Taking into account the possible failure of the calibration optical path exactly to duplicate the optical path used during the data runs[††], we estimate our absolute intensity calibrations against the carbon arc were reliable to 8% - 15%.

The six photoelectric channels on the 1.5 meter B&L spectrograph (which monitor the lines CI λ5052, NeI λ5852, $H_\alpha$ and their nearly continua) were calibrated simultaneously, as were the twelve SQUID channels. Simultaneous carbon arc sampling was accomplished by means of a common trigger pulse to single-sweep the oscilloscopes for all channels. The purpose of simultaneous sampling is to make the calibrations of the various channels, relative to each other, independent of arc instability.

---

[†]When a new motor generator replaced the "converted" arc welder as our DC power supply, current stability improved markedly -- but this arrived too late to be much of a help.

[††]Digital voltmeters were used to check the PM high voltage supplies for long term drift. This was found to be negligible.

Another factor which complicates absolute intensity calibrations using the carbon arc is the decline of shock tube window transmission with use. With every firing of the shock tube, the windows become progressively more pitted (by minute diaphragm fragments) and opaque (decomposition residues from test gases become imbedded in the glass).

The reproducibility of the flash lamp (over tens of discharges) allows us to continually monitor window transmissions. We therefore can relate the window transmissions at the time of one set of carbon arc runs to the transmissions when later carbon arc runs are made, and can also adjust calibration voltages to compensate for lowering of window transmissions during data runs (i.e., between carbon arc calibrations). To ascertain the loss in window transmission we note the apparent drop-off of peak flash lamp intensity when it is discharged subsequent to each shock tube run. Because there is no corresponding decrease in peak intensity when the flash lamp is fired repetively with no intervening shock tube runs, we know the flash lamp intensity itself is not progressively falling-off. Plotting the observed peak intensity as a function of number of window exposures to shock tube plasmas, we find window transmission falls-off on the average by 0.42% per experiment.

5. <u>Comparison of absolute intensity calibrations from the Carbon arc with the new internal method</u>. Having discussed the conventional carbon arc calibrations and the internal calibrations utilizing $H_\alpha$, we now compare them. For each shock tube run providing a reversal intensity IA (in arbitrary units) the absolute intensity,

$$B_\lambda(T_{ST}) = \frac{1}{\beta} IA$$

can be computed using either the calibration factor $\beta \equiv \beta(ca)$ , from the carbon arc calibration, or the calibration factor $\beta = \beta(\frac{IB}{IA})$ deduced from internal calibration of <u>that particular</u> run. In Fig. 40 we plot

$$B_\lambda(T_{ST}) = [\beta(\frac{IB}{IA})]^{-1} IA$$

against

$$B_\lambda(T_{ST}) = [\beta(ca)]^{-1}$$

both variables normalized to units of carbon arc intensity at $\lambda = 6563\text{Å}$ . The results for the 24 runs depicted are not expected to fall along a smooth curve because $(\frac{IB}{IA})$ is specific to each particular shock tube run where IB is observed with $\pm$ 4% precision and IA (the reversal points) with 8% precision. Fully 85% of the data are within $\pm$ 10% of the mutual agreement, which is well inside the <u>a priori</u> estimated tolerances of $\pm$ 8% for $[\beta(\frac{IB}{IA})]_{avg.}$ and the $\pm$ 5% - 15% for $\beta(ca)$ .

On closer examination of Fig. 40 one can detect that the average $[\beta(\frac{IB}{IA})]^{-1}$ is something like 6% greater than $\beta(ca)$ . The source of the discrepancy could not be established. We therefore adopted the average of the two methods as the most reliable absolute intensity at our disposal. (Because of the scatter in $\beta(\frac{IB}{IA})$ we took the average from the 24 dipicted data runs.) This makes our adopted $\beta$ for the $H_\alpha$ line channel about 3% larger than $\beta(ca)$ . The same 3% adjustment was then applied to the other photoelectric channels which were calibrated using the carbon arc only.

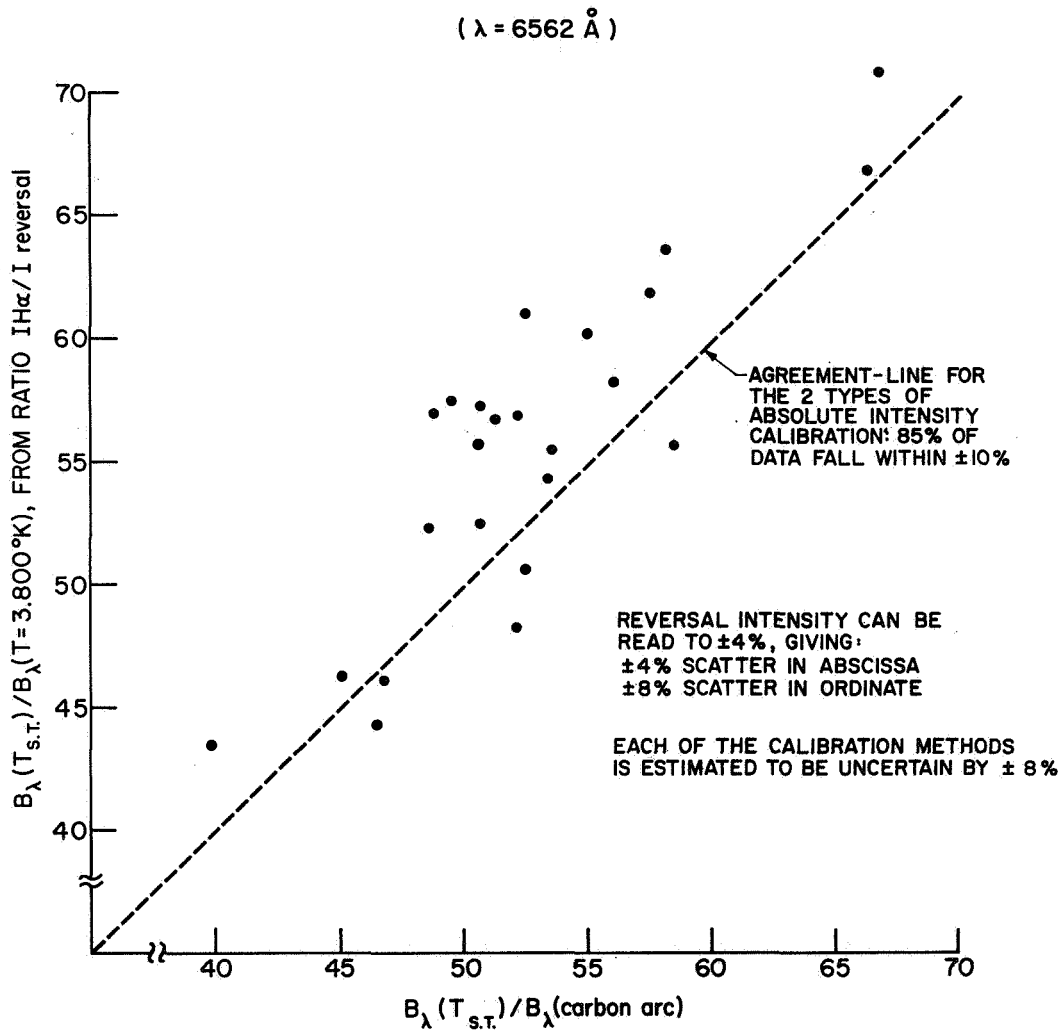


Fig. 40: Comparison of Independent Absolute Intensity Calibrations: Reversal Intensities (In Units of Carbon Arc Intensity) Calibrated by Slit-Averaged Emission Coefficient of $H_\alpha$ vs. Values Calibrated by Direct Comparison Against the Carbon Arc.

6. Calibration of photographic emulsions. Absolute calibration of photographic emulsions consisted of two distinct phases: relative intensity calibration using the carbon arc, and fitting of the relative intensities to an absolute scale, on a shot-by-shot basis, via comparison with several absolutely calibrated photomultipliers. The same procedures were used to calibrate both the Kodak #2475 and Kodak #103-F emulsions. More than 90% of the data runs employed #2475 because it is 2-3 times faster than #103-F. When scanned with a Jaco #2310 densitometer, both emulsions had equivalent grain.

The Seidel-curves[92,93] $-\log(\frac{T}{1-T})$ versus log(intensity), with T the specular transmission, were constructed for different wavelengths using an EG&G xenon flash lamp and a Kodak 14 step neutral density filter. After photoelectrically verifying the lamp's reproducibility, we exposed emulsions to single discharges viewed through a range of density steps. Because durations of the lamp discharge approximated exposure times in the data runs, there was no chance of reciprocity failure. For transmissions of less than 3% (densities greater than 1.5), the Seidel curves became unreliable because film blackening become a very weak function of exposure.

The carbon arc was used to determine the change of emulsion sensitivity with wavelength[†]. Spectrograph slits were opened fully (8Å bandpass) so that reasonable densities could be obtained for short exposure times approaching those of the data runs. For relative carbon arc irradiance as a function of wavelength we used the values of Hattenburg and Kostkowski[88].

The above relative calibrations relate photographically recorded intensities at all points in a spectrum... An absolute intensity calibration

---

[†]The carbon arc is not bright enough to provide the range of log(intensity) we require to construct Seidel curves.

at any wavelength thus converts the entire recorded spectrum to an absolute scale. We apply absolute calibrations, or rather, we transfer absolute photoelectric calibrations, at 6-10 different wavelengths.

This is done on a routine shot-by-shot basis during the data runs. We thus avoid any critical dependence of absolute film sensitivity upon such hard to regulate factors[29,93] as exact developer temperature, precise method of agitation, and ambient humidity. The photoelectric SQUID channels are allocated for this purpose, being placed on the red half of $H_\beta$. Because intensity varies by at least half an order of magnitude between the peak and wings of the H profile, this positioning insures that at least some of the PM channels will correspond to useful film densities (i.e. densities neither on the foot nor the shoulder of the Seidel curve) regardless of the plasma conditions. Both the photographic and photoelectric records are time resolved. Both contain easily recognized time-markers such as the arrival of the first reflected and multiply reflected shocks, and are therefore easily sychronized with each other.

Figure [41] presents the data from a particular first reflected shock plasma: the absolute intensities deduced from eight SQUID channels are represented by vertical bars, each with a height

$$R = \frac{I_{\tilde{\lambda}}}{B_{\tilde{\lambda}}(T = 3{,}800°K)} ,$$

where $I_{\tilde{\lambda}}$ is the slit averaged intensity for the pertinent 1Å segment of $H_\beta$ and $B_\lambda(T = 3{,}800°K)$ is the carbon arc intensity averages over the same 1Å bandpass (the width of the bars in the figure are accordingly 1Å wide). The superimposed half-profile of $H_\beta$ is the simultaneously recorded photographic relative intensity, $I_{rel}(\lambda)$, scaled by the factor $\alpha$,

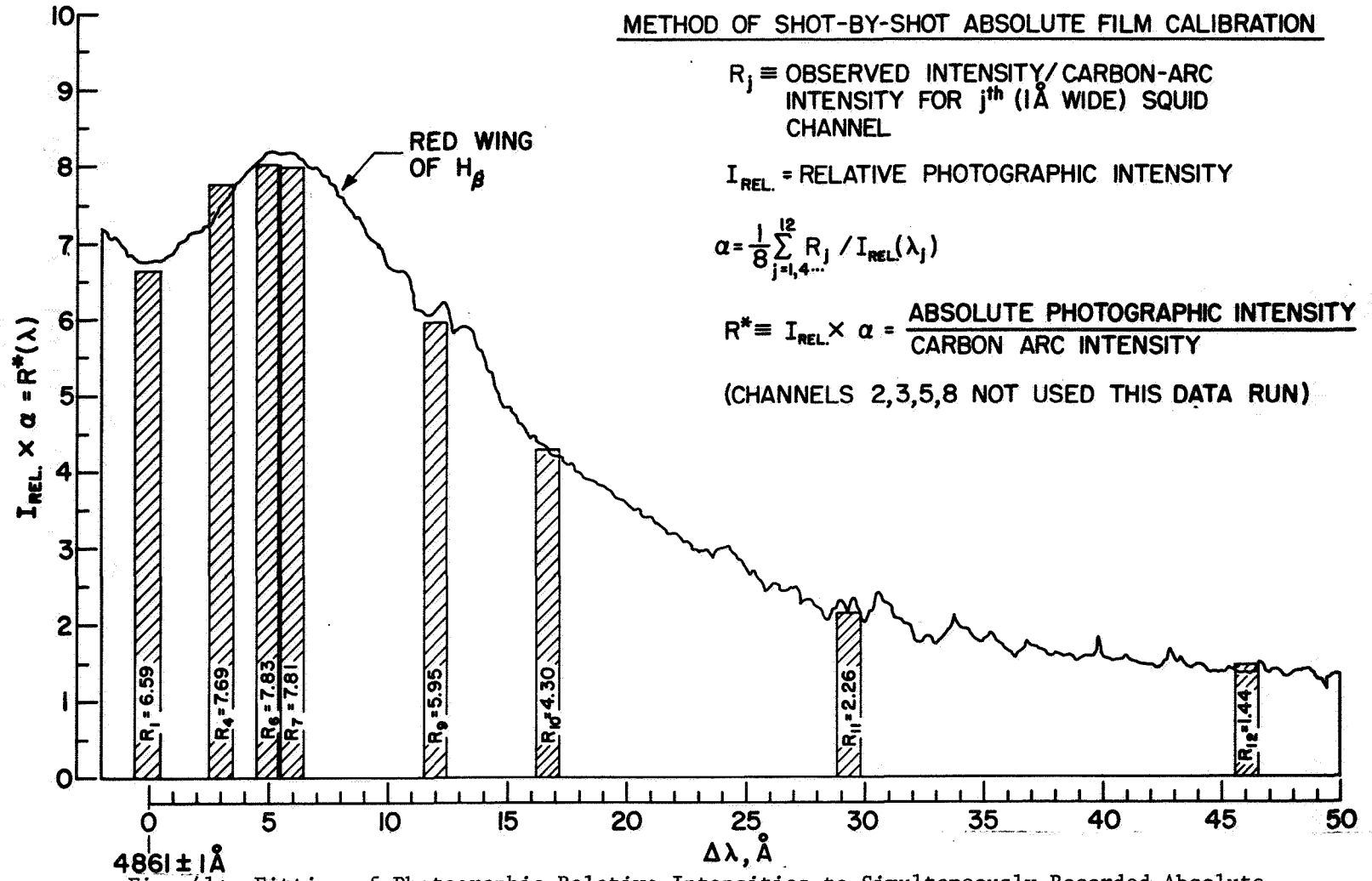


Fig. 41: Fitting of Photographic Relative Intensities to Simultaneously Recorded Absolute Intensities of 8 Photoelectric ("SQUID") Channels.

$$\alpha = \frac{1}{8} \sum_{j=1,4\ldots}^{12} R_j/I_{rel}(\lambda_j)$$

where $\lambda_j$ is the mean wavelength monitored by the j-th 1.0Å wide SQUID channel. (Only 8 of the 12 SQUID channels were used on this shot.) We henceforth use the notation

$$R^*(\lambda) = \alpha \times I_{rel}(\lambda)$$

to denote the absolute photographic intensity in units of local carbon arc intensity.

Data from the run depicted in Fig. 41 gives a somewhat better than usual agreement between photoelectric $R_j$ values and $R^*(\lambda_j)$ values. More typically $R_j/R^*(\lambda_j) = 1.0 \pm 6\%$ on the central portions of $H_\beta$, and $R_j/R^*(\lambda_j) = 1.0 \pm 15\%$ on the wings (channels 11 and 12), so that $\alpha$ can be fitted to eight channels with a 3% - 4% precision. To check on the accuracy of the transfer from absolute photoelectric to absolute photographic intensities, we compare the $\alpha$ values for different exposures made on the same piece of film†. Apart from minor variations in the emulsion sensitivity or the local development, we expect all portions of the same film to have the same absolute sensitivity, i.e., $\alpha$ should be constant for all exposures on the same 18" piece of film. We find for three data runs sharing the same film that the three $\alpha$-values will usually agree to within 5% - 10% with their average. However, comparing the average $\alpha$-value of two different films, we typically find a 10% - 20% disagreement: so this shot-by-shot calibration technique reduces scatter in absolute photographic photometry by a factor of two.

---

†Because film loading, unloading and developing is tedius, it is advantageous to use a single 18" length of drum camera film to make three successive exposures -- overlapping of two time resolved spectra occurs only once in 20 runs recorded in this way.

Figure 41 also checks on the validity of our $\log(I_{rel})$ versus $-\log(\frac{T}{1-T})$ calibrations at 4861Å : the change in film sensitivity between $\lambda = 4861$Å (corresponding to SQUID channel #1) and $\lambda = 4907$Å (corresponding to SQUID channel #12) is only a few percent, while the plasma brightness at these two wavelengths typically differ by factors of 3 to 10, depending on shock conditions. By neglecting the small change in film sensitivity over 46Å then, comparing $R^*(\lambda_j)$ against $R_j$ for all 8 channels amounts to checking the relative photographic intensities against the relative photoelectric intensities at a fixed wavelength.

We implicitly perform another check on our Seidel curves when we measure relative line intensities within the same multiplet using a wide range of source temperatures. If two lines arise from the same excited state and are optically thin, the ratio of their integrated intensities should be independent of source conditions. Varying source temperature scales both line intensities exponentially. If, for example, the two lines belong to an SII multiplet, and one is, say, three times brighter than the other, one then expects the ratio of their intensities to behave as follows:

$$\left.\frac{9}{3}\right]_{T = 10{,}000°K} \cong \left.\frac{27}{9}\right]_{T = 10{,}500°K} \cong \left.\frac{63}{21}\right]_{T = 11{,}000°K} \cong \left.\frac{135}{45}\right]_{T = 11{,}500°K}$$

Therefore, relative intensities will not be independent of temperature if an erroneous $\log I_{rel}$ versus $-\log(\frac{T}{1-T})$ curve is used.

As an additional self consistency check on both $\log I_{rel}$ versus $-\log(\frac{T}{1-T})$ and the change of emulsion sensitivity with wavelength, we measured the same spectra ( CI, SI and SII in the region $4600\text{Å} \lesssim \lambda \lesssim 5700\text{Å}$) using independently calibrated #2475 and 103-F emulsions. Relative A-values deduced

from both sets of data runs agreed within expected tolerances. Moreover, the average of 15 runs using #2475 gave the A-value of $H_\beta(\lambda = 4861\text{Å})$ relative to $H_\gamma(\lambda = 4340\text{Å})$ correct to 9% (difficulty in discriminating $H_\gamma$ wings from the local continuum may be partially responsible for the 9% discrepancy.)

7. <u>Simultaneous photographic and photoelectric measurement of CI λ5052 integrated intensity</u>. In our data runs the absolute integrated intensity of CI λ5052 was simultaneously measured two independent ways; by time resolved photography and also photoelectrically. Because peak optical depths of CI λ5052 never exceeded .03 - .04, optical depth corrections could be neglected, making reduction of the photographic integrated intensities a matter of simply measuring the area contained within the line profile. The width of the spectrograph slit, or its relation to the lines halfwidth, need not be known with this type of recording. We denote the profile's area as $R_c^*$ when it is measured in units of $(I_{rel} \times \alpha) \times 2.0\text{Å}$. This form is convenient for computation since $R_c^*$ is the integrated intensity of CI λ5052 relative to $B_\lambda(T = 3800°K) \times 2.0\text{Å}$. The factor 2.0 is used to make $R_c^*$ directly comparable with $R_c$, the absolute integrated intensity of CI λ5052 photoelectrically recorded using a 2.0Å bandpass.

The photoelectrically recorded CI λ5052 absolute intensity was measured using a 2.0Å bandpass. Depending on plasma electron densities, between 40% and 70% of the lines total energy was slit-integrated within this bandpass. Because Doppler broadening is insignificant compared to Stark broadening for this line, its shape is essentially Lorentzian. We apply eqn. [21] to correct for the wing intensity not viewed by the PM. To estimate the (full) Stark halfwidth, $\Delta\lambda_S$, we use (cf. eqn. [13]) measured

electron densities and experimentally determined (cf. Chapter VII) Stark broadening parameters. We define $R_C$ as:

$$R_C = \left[ R_{C_{L+B}} - R_{C_B} \right] \left[ \frac{2}{\pi} \tan^{-1} \left( \frac{2.0\text{Å}}{\Delta\lambda_S} \right) \right]^{-1} \qquad [25]$$

where $R_{C_{L+B}}$ is the ratio of observed intensity at 5052Å to the carbon arc intensity at 5052Å , both viewed with the same 2Å bandpass.

Bridges[25] mentions a second wing correction that should normally be used: the wings of CI λ5052 extend out far enough to contribute to $R_{C_B}$ at 5079Å , thus making $R_C$ (slightly) too small. However, CI λ5052 is itself situated on the wings of CI λλ5041, so $R_{C_{L+B}}$ is slightly too large. The relative intensities of CI λ5052 and CI λλ5041 , causes these two small corrections approximately to cancel.

Comparison between $R_C$ and $R_C^*$ data is made in Fig.42 . The scatter in these data conform to our previous estimates of 15% - 25% precisions for the photographic recording and ± 10% - 20% precisions for the photoelectric recording. We must anticipate that our results for the CI λ5052 A-value, which depend linearly upon either $R_C$ or $R_C^*$ , will contain at least as much relative scatter -- a contention that is borne out by Fig. 8 .

Besides the scatter in $R_C$ versus $R_C^*$ , for which we can account, there is the systematic discrepancy,

$$\tilde{R}_C \simeq 1.07\ \tilde{R}_C^* \quad ,$$

whose source we do not know. Systematic errors in $R_C$ can arise from incorrect absolute intensity calibration, or improper exit slit alignment,

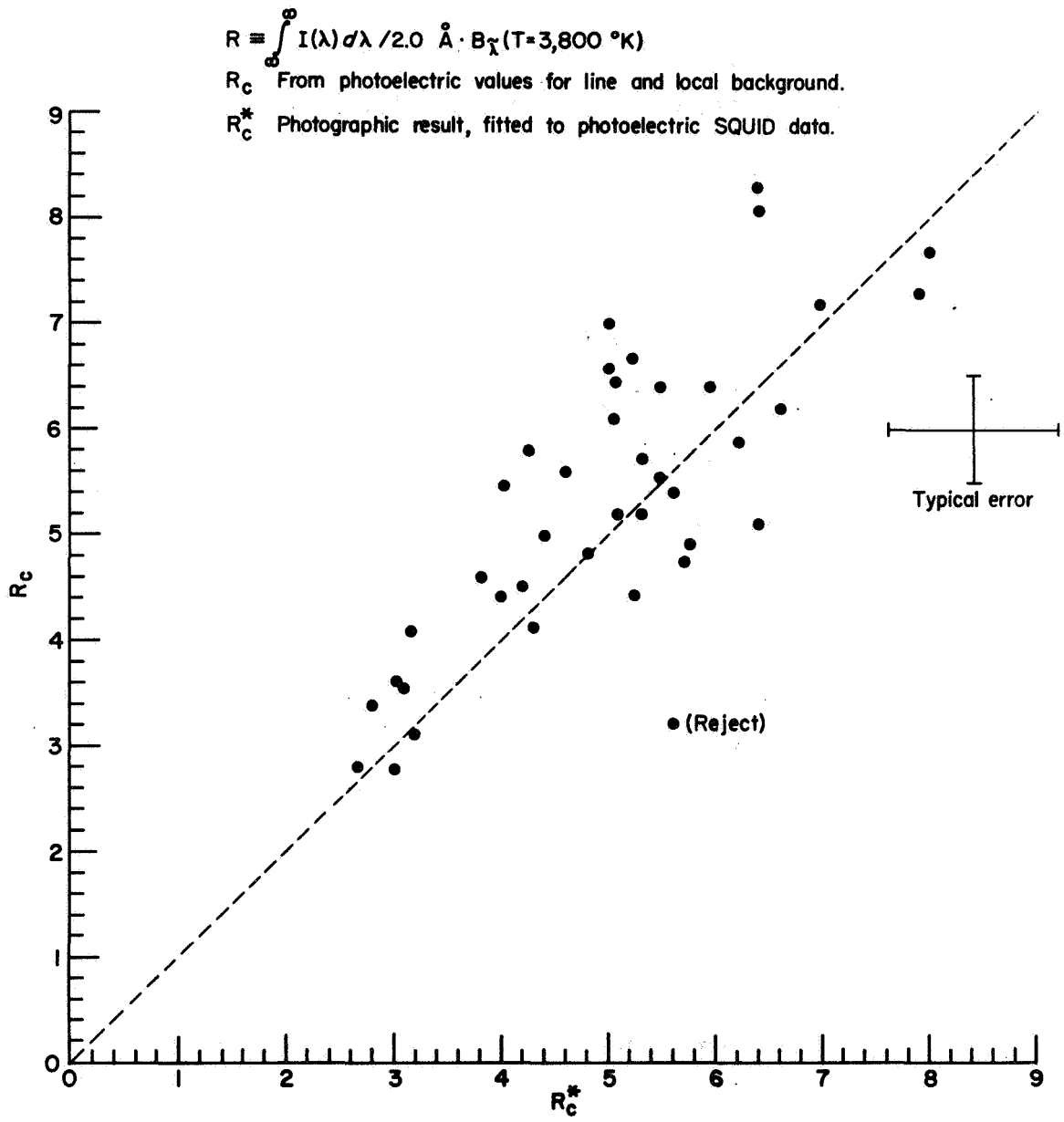


Fig. 42: Comparison of Simultaneous Measurements of Integrated Absolute intensity of CI λ5052 : Wing-Corrected Photoelectric Recording vs. "SQUID" Calibrated Photographic Recording.

while $R_C^*$ is susceptible to errors in the interpretation of CI λ5052 profiles and incorrect absolute calibration factors α . We estimate $R_C$ and $R_C^*$ have roughly equivalent accuracy. The 7% level of agreement between $\tilde{R}_C$ and $\tilde{R}_C^*$ is well within experimental tolerance. We use $\frac{1}{2}(R_C+R_C^*)$ as the best-estimated absolute intensity for each of the 39 runs where both $R_C$ and $R_C^*$ are available.

8. Method of recording absolute integrated intensities of $H_\alpha$, NeI λ5852 , $H_\beta$ and lines studied for A-values. With the exception of CI λ5052 all integrated absolute integrated intensities were routinely measured a single way, either photoelectrically or photographically.

Neon I λ5852 was measured using photoelectric line and background channels on the B&L one meter spectrograph. Because the 2Å entrance slits are more than ten times wider than typical full halfwidths, wing corrections amounted to only a few percent. Using Griems value[7] for the λ5852 Stark broadening parameter and the NBS value[13] of $.719\times10^8 sec^{-1}$ for its transition probability, we followed the methods outlined in Chapter II to compute optical depth corrections: at temperatures less than 12,000°K, self-absorption amounted to less than 10% of observed intensities.

The 2Å wide central portion of $H_\alpha$ was measured photoelectrically and interpreted via the methods outlined in Chapter II. When slit-averaged optical depths exceeded 0.5, local background contributions to the slit-integrated intensity were negligible, as seen from the detailed portion of curve "C" in Fig. 4 . For lower mean optical depths, local background intensities, $I_B$ , (monitored by the photoelectric channel at λ = 6592Å ) were taken into account in forming

$$\int_{-1Å}^{1Å} I_\alpha(\lambda)d\lambda = \frac{I(\alpha)}{L+B} - \frac{I(\alpha)}{B} .$$

The integrated intensity of $H_\beta$ was taken in a manner analogous to $R_C^*$, except that for $H_\beta$ optical depth corrections were routinely applied, as explained in Chapter II. For this purpose we used $T_{neon}$ or $T_\alpha$ (cf. next section) for the approximate temperature. The SQUID channels provide the absolute photographic intensity per wavelength interval necessary for the optical depth correction.

Integrated absolute intensities of all other lines (for example, SiI λ5948, SiII λλ5056, PII λ5053) were measured as R* values, with optical depth corrections applied for cases where peak optical depths exceed .05.

## C. Temperature Measurements

1. Introduction. Temperature was simultaneously measured four independent ways in the typical data run, using the following observations: absolute integrated intensity of (optically thin) $H_\beta$, the absolute integrated intensity (usually optically thin) of NeI λ5852, the partially integrated optically thick portion of $H_\alpha$, and the halfwidth of $H_\beta$. In perhaps 40% of the runs two additional temperatures, $T_{S_1}$ deduced from the incident shock speed, and $T_{rev}$, a line-reversal temperature, were also measured. These were not routinely used in reduction of the A-values for reasons discussed below.

Each of the measured temperatures has its own susceptibility to systematic errors (cf. Table I ). Because of their widely disparate dependence on absolute intensities, source pressure and source composition, the four temperatures cannot agree unless they are free from significant systematic errors. While some set of hypothetical systematic errors could perhaps be arranged to make these four temperatures agree at some single

Table I . COMPARISON OF ERROR PROPAGATION AND SCATTER FOR DIFFERENT METHODS OF OBTAINING PLASMA TEMPERATURE*

| Temperature | Scatter† for 37 shocks °K | Relative error (%) in temperature determinations due to +10% errors in the following measured variables. | | | |
|---|---|---|---|---|---|
| | | absolute plasma pressure | absolute integrated line intensity | initial partial pressure of additive gases | effective plasma thickness |
| $T_\alpha$ | 70 | + 2.5 | + 2.8 | + 2.5 | + 2.5 |
| $T_\beta$ | 118 | + 1.0 | + 1.0 | + 1.0 | + .0 |
| $T_{neon}$ | 90 | + .4 | + .4 | .0 | + .4 |
| $T_{\lambda\frac{1}{2}}$ | 220 | + .9 | .0 | + .9 | .0 |

*For a shock tube plasma of initial composition ½% $CH_4$ + ½% $CS_2$ + 99% neon , at mean pressure $9.0\times10^6$ dyne $cm^{-2}$ and mean temperature 11,600°K .

†For the $i^{\underline{th}}$ shock we take $\tilde{T}_i = \frac{1}{4}(T_{\alpha_i} + T_{\beta_i} + T_{neon_i} + T_{\lambda\frac{1}{2}})$ and define

"scatter" = $\frac{1}{37} \sum_{i=1}^{37} |T_i - \tilde{T}_i|$ for the 37 data plotted in Figure 43.

spurious value, a spurious agreement cannot be maintained over a 2500°K range of source temperature, for with different test gases, or with widely varying pressures. If the four redundant measurements have roughly equivalent precisions then their average is statistically twice as reliable as any one of them alone.

Figure 43 may convey the impression that mutual agreement between the redundant temperature determinations inevitably follows when reasonable care is exercised in making the individual measurements. Our experience indicates that to achieve mutual agreement on the first attempts (i.e. to start out with a system free of systematic errors) would require very good luck as well. The shots represented by the data in Fig.43 were preceded by an equal number of preliminary runs in which there were significant disagreements between the various temperatures.

The first and largest disagreement noticed in the preliminary data runs was that the temperature deduced from $H_\alpha$ , $T_\alpha$ , was falling between 5% and 10% lower than the average of the other temperatures. Repeated recalibrations against the carbon arc did not alter this pattern, while signal levels were far below the saturation levels established in prior bench testing of the photomultipliers. However, a slight difference was noted between the shapes of flash lamp discharges recorded by the $H_\alpha$ line and by $H_\alpha$ background channels. This was puzzling in view of the previously established local greyness of the flash lamp spectrum. Subjecting the $H_\alpha$ channel to the <u>in situ</u> linearity check, outlined in Section B, showed the $H_\alpha$ photomultiplier to be saturating at 1/4 the previously required signal levels. Replacing the faulty photomultiplier caused $T_\alpha$ to group with the other temperatures.

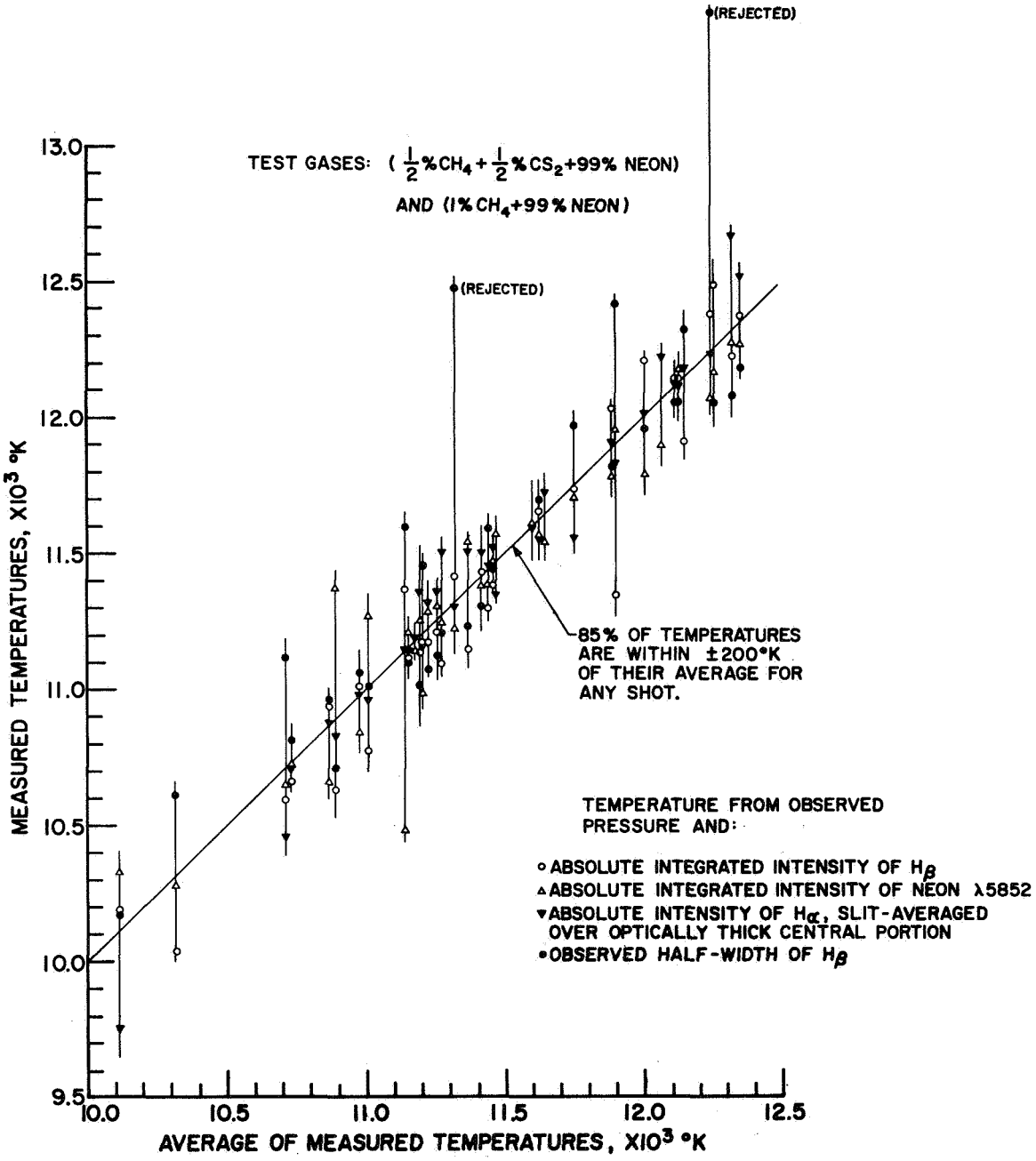


Fig. 43: Comparison of Four Simultaneous Temperature Measurements in First-Reflected Shocks.

On numerous occasions, optical parts were inadvertently moved out of alignment -- having the effect of spoiling the absolute calibration of a spectrograph. If it had not been for our redundant temperature measurements, serious errors could easily have escaped immediate detection.

Redundant temperature measurements also test the validity of our assumptions concerning LTE and source homogeneity, as discussed in Section G of this chapter and Chapter IV, respectively.

2. Measurement of $T_{neon}$. $T_{neon}$ is the temperature solved for when eqn. [1] is applied to the line NeI λ5852 and the NBS value[13] $.719\times10^{8}\,sec^{-1}$ is used for the NeI λ5852 transition probability. The 1.5 meter B&L spectrograph, with its slit opened to a 2.0Å bandpass, was used to measure $R_{neon_{L+Bk}}$ and $R_{neon_{Bk}}$. Because the entrance slit width is 5 to 10 times greater than the typical NeI λ5852 full halfwidth, no wing corrections were necessary. Although optical depth corrections were applied to ($R_{neon_{Bk}}$ - $R_{neon_{Bk}}$) when $T > 12{,}000°K$, this correction was only marginally significant since in no cases did the correction to $T_{neon}$ amount to more than + 1%.

Because of its 18.9 ev excitation energy, the intensity of NeI λ5852 is very sensitive to changes in the (space-averaged) source temperature: a 1% change in T will produce a 25% change in $R_{neon_L} = (R_{neon_{L+Bk}} - R_{neon_{Bk}})$. Conversely, $T_{neon}$ is relatively insensitive to errors in the measured variables p, and the absolute intensity, $R_{neon_L}$, as Table shows.

We found two disadvantages with $T_{neon}$. It is unreliable below 10,000°K where the difference between $R_{neon_{L+Bk}}$ and $R_{neon_{Bk}}$ is strongly affected by noise. A purely operational problem is the difficulty in maintaining a good CRO display of $R_{neon_{L+Bk}}$ when faced with shock tube non-reproducibility. Typical ± 3% variations in source temperature can reduce the trace height to a few mm or throw it off scale.

3. Measurement of $T_{\lambda_{1/2}}$. The temperature $T_{\lambda_{1/2}}$ is deduced from observed pressure and the halfwidth of $H_\beta$. Using the Stark broadening predictions of Griem[56] to obtain the plasma electron density, we then employ the coupled Saha-Boltzmann equations and measured pressure to deduce $T_{\lambda_{1/2}}$.

For our typical shock tube plasmas a 5% error in the $H_\beta$ halfwidth causes a 4% error in $T_{\lambda_{1/2}}$, so particular care should be taken in measuring this variable. Because our photographic scans usually extended several hundred Ångstroms on either side of $H_\beta$, it was not difficult to distinguish the lines' wings from the local continuum unless $H_\beta$ was very broad ($Ne \sim 10^{17} cm^{-3}$). The halfwidth was usually taken to be simply the width of the $H_\beta$ profile at half maximum intensity, with the maximum intensity interpreted as the average of the red and blue peak intensities. Although better precisions were possible by multi-point fitting of the observed profiles to theoretically predicted shapes, as was done for a few data runs, this procedure proved too time consuming for routine use. Before reading the halfwidths, the $H_\beta$ profiles were treated to the point-by-point optical depth correction outlined in Chapter II: this correction reduced the apparent halfwidths by 1% - 4%. Corrections for the instrument profile were also routinely applied. However, the normal bandpass was 1.0Å, so these latter corrections seldom reduced the apparent $H_\beta$ halfwidths by more than 2%.

Scatter (random error) in our measured halfwidths varied between 5% and 10%, depending on the type of plasma studied. For shocks where $Ne > 10^{17} cm^{-3}$ precisions dropped to perhaps 15%, because the $H_\beta$ profiles became very diffuse, while for a few shots where $T > 12{,}000°K$ and

$Ne < 4 \times 10^{16} cm^{-3}$ , precisions also fell to 15% because the central portions of the $H_\beta$ profile became so bright that they produced emulsions too dense for accurate reduction to intensities.

We are aware of no sources of systematic error. Interference from superimposed lines should not be a problem, since lines strong enough to discriminate from grain were recognized in our wavelength resolved recordings. While weak, broad, recombination features might escape detection, temperatures deduced from the $H_\beta$ halfwidth agreed with the other three independent temperatures equally well in all test gases whose composition was precisely known.

In reducing the $H_\beta$ halfwidths to electron densities, we interpolated Griem's [56] tables for both electron density and temperature.

An obvious advantage of $T_{\lambda_{1/2}}$ to the current work is its freedom from reliance on absolute intensity calibrations (except for small optical depth corrections), so with respect to this important source of error it is qualitatively different from our other measured temperatures. Moreover, $T_{\lambda_{1/2}}$ is obtained at practically no extra expense when $T_\beta$ (described below) is measured.

Two disadvantages of $T_{\lambda_{1/2}}$ are the poor precision in measuring $\lambda_{1/2}$ (cf. Table I ), and the sensitivity of plasma electron densities to readily ionized wall contaminants whose (small) concentrations are difficult to estimate accurately.

4. <u>Measurement of</u> $T_\beta$ . Using the area under the optical depth-corrected absolute intensity profile of $H_\beta$ , together with the measured pressure and known A-value of $H_\beta$ , eqn. [1] can be solved for temperature. We refer to this temperature as $T_\beta$ .

Errors in the absolute integrated intensity of $H_\beta$ can arise from problems in delineating the $H_\beta$ profile or from errors in the absolute film calibration. We have already discussed these two error sources separately: typical precision for the integrated absolute $H_\beta$ intensity is 10%. We therefore expect (cf. Table I ) at least a 1% scatter in $T_\beta$ . The impurity levels of hydrogen (from wall contaminants) are too small to significantly affect $T_\beta$(cf. Section F). Scatter is measured pressures (cf. Section D) typically contributes less than 0.5% scatter to $T_\beta$ .

5. Measurement of $T_\alpha$ . Given the partially slit-integrated absolute intensity of $H_\alpha$ and the plasma pressure, eqn. [7] can be solved for temperature. An illustrative example of this procedure was given in Section B following the discussion of the in situ intensity calibration.

Although they both utilize the known A-values of Balmer lines, $T_\alpha$ and $T_\beta$ have quite different functional dependence on observed variables (cf. Table I ). This difference stems from the disparate peak optical depths of the two lines rather than from the small difference in their excitation energies . Under our normal plasma conditions the peak optical depths of $H_\alpha$ are 0.5 - 3.0 while peak optical depths of $H_\beta$ are 0.04 - 0.20. So the portion of $H_\alpha$ we monitor is nearly a black body and does not share the strong thermal dependence of $H_\beta$ .

Unlike the other temperatures we measure, which depend on space-averaged quantities throughout the depth of the source, $T_\alpha$ depends primarily on conditions in portions of the plasma nearest the detector. Therefore, reproducible macroscopic temperature gradients along the line of sight would cause $T_\alpha$ to differ systematically from $T_{neon}$ , $T_\beta$ or $T_{\lambda_{1/2}}$ .

$T_\alpha$ is our most precise temperature determination (cf. Table I ). The two reasons why $T_\alpha$ is precise are that the central portion of $H_\alpha$ is very bright, so signal-to-noise ratios are excellent; and $T_\alpha$ has only a slight dependence on measured pressures. The accuracy of $T_\alpha$ , however, is not felt to be superior to the other measured temperatures because $T_\alpha$ is particularly sensitive to error in absolute intensity calibrations (cf. Table I ) and also because of the uncertainty in the Stark broadening of $H_\alpha$ .

6. Comparison of the redundant temperature measurements. In Fig. 43 we show temperature data for 37 shock tube runs employing ½% $CH_4$ + ½% $CS_2$ + 99% neon or 1% $CH_4$ + 99% neon. For each of these runs we plot the four redundant temperature determinations, $T_{neon}$ , $T_{\lambda_{1/2}}$ , $T_\beta$ and $T_\alpha$ against their average, $\tilde{T}$ . (In a few runs only three of the four temperatures were available.)

Over the depicted temperature range, 10,100°K ~ 13,300°K, none of the four types of temperature measurement show a significant systematic disagreement with $\tilde{T}$ . The diverse functional dependence of these four temperatures upon several experimental variables is shown in the last four columns of Table I . We interpret this persistent agreement between four independent measurements to indicate that $\tilde{T}$ does not contain more than 1% systematic (repeatable) error.

Approximately 85% of all temperature determinations fall within ± 200°K of $\tilde{T}$ . We therefore estimate that the random error (scatter) in $\tilde{T}$ for a particular run is between 1% ~ 1.5%. Precisions are better in the range 11,200 ≤ $\tilde{T}$ ≤ 11,700°K than at lower temperatures, where poorer signal-to-noise ratios are the rule, or at higher temperatures, where film densities sometimes get undesirably large and where low initial test gas pressures (needed to obtain

strong shocks) are less conducive to steady shock tube flows. Temperature data for other test gases are similar to those of Fig. 43 except that most runs in $SiH_4$ were too cool (typically 9,500°K) to give reliable $T_{neon}$ data.

The two anomalous $T_{\lambda_{1/2}}$ temperatures shown in the figure were rejected on statistical grounds. Thorough re-examination of the data for these two runs failed to disclose reading errors or physically plausible reasons why these two data should depart so markedly from $\tilde{T}$ .

The four redundant temperature measurements are not equally precise. The second column of Table I gives the quantity:

$$\left[ \sum_{j=1}^{37} \left( \frac{T_{j,i} - \tilde{T}_j}{\tilde{T}_j} \right)^2 \Big/ 36 \right]^{1/2} \qquad i = \alpha, \lambda_{1/2} , \text{ etc.}$$

computed for the 37 shots depicted in Fig. 43 . This method of specifying precision ranks the temperature measurements, in order of decreasing precision, as $T_\alpha$ , $T_{neon}$ , $T_\beta$ , and $T_{\lambda_{1/2}}$ .

7. <u>Reversal temperature and shock speed temperature</u>. Although incident shock speed, $S_1$ , was recorded for 50% of our data runs and the reversal intensity at $H_\alpha$ was recorded for perhaps 40% of our shock tube firings, the two temperatures, $T_{S_1}$ and $T_{rev}$ , deduced from these data were not routinely used for the reduction of A-values, i.e., were not routinely used in forming $\tilde{T}$ .

The reliability of $T_{S_1}$ hinges not only on the assumption of LTE , as do $T_{neon}$ , $T_\alpha$ , $T_\beta$ and $T_{\lambda_{1/2}}$ , but also on the more questionable assumption (cf. Chapter IV) that shock tube hydrodynamics can be <u>accurately</u> described by a one-dimensional model. While the systematic disagreement

and large scatter in $T_{S_1}$ versus $\tilde{T}$ shown in Fig. 19 do not recommend the inclusions of $T_{S_1}$ in $\tilde{T}$, the fact that the disagreement between our four spectroscopic temperatures and this hydrodynamic temperature is typically not greater than 5% is additional evidence that boundary layers do not grossly distort the laminar geometry.

Those occasions on which $T_{rev}$ was available (i.e., the flash lamp was functioning properly) almost always coincided with plasma conditions giving $1.5 \leq \tau_{eff} \leq 3.0$, so that the reversal intensity differed little from the slit-averaged emission of $H_\alpha$. To include both $T_\alpha$ and $T_{rev}$ in $\tilde{T}$ for these runs would therefore weight essentially the same temperature measurement twice with respect to $T_{neon}$, $T_\beta$ and $T_{\lambda 1/2}$. While this double weighting might not make $T$ less reliable, there is no <u>a priori</u> reason to believe it improves it. We were therefore content to employ the reversal intensities solely for the internal intensity calibrations discussed in Section B.

To forestall objections to our later use of $T = 1/4(T_{neon} + T_\alpha + T_\beta + T_{\lambda 1/2})$ for computing $\lambda 1/2(P,\tilde{T})$ and $A_{mn}(P,\tilde{T})$ of $H_\beta$ : it is realized that $\tilde{T}$ is not linearly independent from $T_\lambda$ and $T_\beta$. However, computation of $\lambda 1/2(P,\tilde{T}')$ and $A_{mn}(P,\tilde{T}'')$, where $\tilde{T}' \equiv 1/3(T_{neon} + T_\alpha + T_\beta)$ and $\tilde{T}''$ $1/3(T_{neon} + T_\alpha + T_{\lambda 1/2})$, would have effectively tripled an already large number of calculations. Since $\tilde{T}$ hardly ever differs from $\tilde{T}'$ or $\tilde{T}''$ by as much as 1% in a usual data run, it was felt this additional labor was unwarranted.

D. Pressure Measurements

1. Calibration. The quartz transducer and charge amplifier were calibrated (mV/psi) three different ways. These calibrations agreed mutually to ± 5%. One calibration was supplied by the manufacturer. The second was a statistic calibration against a dead weight tester. The third was a dynamic calibration using two small chambers maintained at a few psi differential pressure and separated by a cellophane diaphragm: the transducer registered the change in pressure when a plunger opened the diaphragm.

For the data runs a single transducer was mounted on the top wall of the shock tube in the same plane viewed by the spectrographs. To verify whether the pressure measured side-on at this location was the same as in the bulk of the plasma, a number of preliminary† trials simultaneously employed a second (similarly calibrated) transducer mounted in the center of the end wall. To within mutual tolerance (± 7%) both of these transducers recorded identical pressures when read at the same time with respect to arrival of the reflected shocks.

2. Measurements behind the reflected shock. Use of transducers to measure shock tube pressures is complicated by two types of interference. One is modulation of the desired transducer outputs by the characteristic 130 kHz ringing of the piezoelectric quartz crystal. A judicious choice of transducer mounting, as discussed in Chapter V, Section B , can reduce excitation of this ringing by as much as a factor of 3 . The ringing amplitude can be reduced a further factor of 2 by using a Kistler

---

†The two transducers could be used simultaneously only during preliminary runs employing an end flange without the plug used to advance the reflecting plane into view of the windows. It was discovered (too late to effectively remedy) that the apparently solid steel end wall plug was full of minute fissures. These frustrated attempts to make a vacuum-tight installation of an end wall transducer for use during regular data runs.

tuned interference filter in series with the charge amplifier output. The residual ringing then causes no more than a few percent ambiguity in the interpretation of the pressure record, as can be judged from the typical CRO trace given in Fig. 45.

A second interference arises because the transducer responds to plasma electron density as well as pressure. At high electron densities recorded pressures apparently decay linearly with time -- the higher the electron density, the greater the apparent decay rate. At $Ne = 5\times10^{16}/cc$ the relative decay rate is approximately 10% per 50μs . The mechanism by which the electron density influences the metal-encapsulated crystal is not clear. The apparent pressure decay is definitely instrumental in origin: for shocks in pure argon or kyrpton, where electron densities exceed $2\times10^{17}/cc$ , the observed pressures appear to decrease rapidly,and soon go strongly <u>negative</u>. For the usual shocks neither temperatures nor electron densities decay with time. Moreover, shocks in pure neon, or in any test gas where electron densities are very low (say $Ne \ll 2\times10^{16}cm^{-3}$) , do <u>not</u> exhibit this apparent fall-off of pressure with time. On the contrary, observation of more than 50 shocks in pure neon covering a range of 3 in shock pressure, showed that for the duration of the first reflected shock, pressures either remained constant or else showed a (relative) increase of a few percent per 50μs .

To circumvent interference from the transducer's sensitivity to plasma electron densities we routinely measure pressures at the instant of arrival of the first reflected shock before there is time for the apparent pressure decay to set in. In practice, this means we measure pressure throughout the duration of the first reflected shock in order to average-out interference from ringing and then extrapolate the best-fit smooth pressure record (of

negative slope in time) backwards in time to the arrival of the first reflected shock. Depending on plasma electron densities, this procedure imposes a + 5% to + 15% correction onto the pressures actually read at the spectroscopic sampling times 20μs to 40μs after arrival of the first reflected shock.

It is recalled that these pressure measurements generally agree to better than 10% (cf. Fig. 20 ) with the pressures deduced from the local shock speeds, $S_1$ , and the real-gas Rankine Hugoniot relations. We feel this agreement very nearly amounts to an agreement between two "direct" pressure measurements by independent means, since $p(S_1)$ is the one thermodynamic variable for which investigators consistently report good agreement between Rankine Hugoniot predictions and "directly" measured data.

## E. Redundant Measurement of Electron Density

Plasma electron densities were routinely deduced two independent ways: by applying Griem's Stark broadening theory for Balmer lines to our observed $H_\beta$ halfwidths, and by applying the Saha-Boltzmann equations to our measured pressure and temperature. We denote these two estimates of electron density as $Ne_\lambda$ and $Ne(p,\tilde{T})$ , respectively.

Were it not for the impurities boiled off the walls, our plasmas would be closed thermodynamic systems and would be over-determined by the three state variables $p,\tilde{T}$ and $Ne_\lambda$ . If we assume that only the impurity concentrations of aluminum are not effectively known (cf. Section F), then these three thermodynamic variables are just sufficient to determine the state of our plasmas. That is, systematic discrepancies between $Ne(\lambda_{\frac{1}{2}}$ of $H_\beta)$ and $Ne(p,\tilde{T})$ should allow us to deduce the unknown aluminum concentration.

Figure 44 compares $Ne_\lambda$ and $Ne(p,\tilde{T})$ for 56 first reflected and multiply reflected shocks. Data for multiply reflected shocks are generally less precise because it is more difficult to measure the half-widths of the broad $H_\beta$ profiles in these plasmas, and also, because multiply reflected shocks are not as homogeneous as the first reflected shocks. The depicted $Ne(p,\tilde{T})$ values were computed on the assumption of zero concentrations of aluminum. The approximate hydrogen and carbon impurity levels deduced by methods discussed in Section F, were included in calculating $Ne(p,\tilde{T})$ .

Approximately 85% of the $Ne(p,\tilde{T})$ and $Ne_\lambda$ data are within 15% of mutual agreement. Our a priori estimates of random error in a single $Ne(p,\tilde{T})$ and a single $Ne_\lambda$ determination are $\pm$ 8% and $\pm$ 12%, respectively.

There is a 3% systematic discrepancy between $Ne_\lambda$ and $Ne(p,\tilde{T})$, i.e.,

$$\left[\frac{Ne_\lambda}{Ne(p,\tilde{T})}\right]_{avg.} = 1.03$$

with

$$\frac{\sigma}{\sqrt{56}} = .02 \quad .$$

This discrepancy, of only marginal statistical significance, is in the direction $(Ne_\lambda > Ne(p,\tilde{T}))$ expected if aluminum impurity concentrations are greater than zero. However, this small discrepancy might easily be accounted for by the uncertainty in Griem's broadening parameters[56] for $H_\beta$ (which are not claimed to be reliable to better than 3%) or, by a systematic temperature error of 1%.

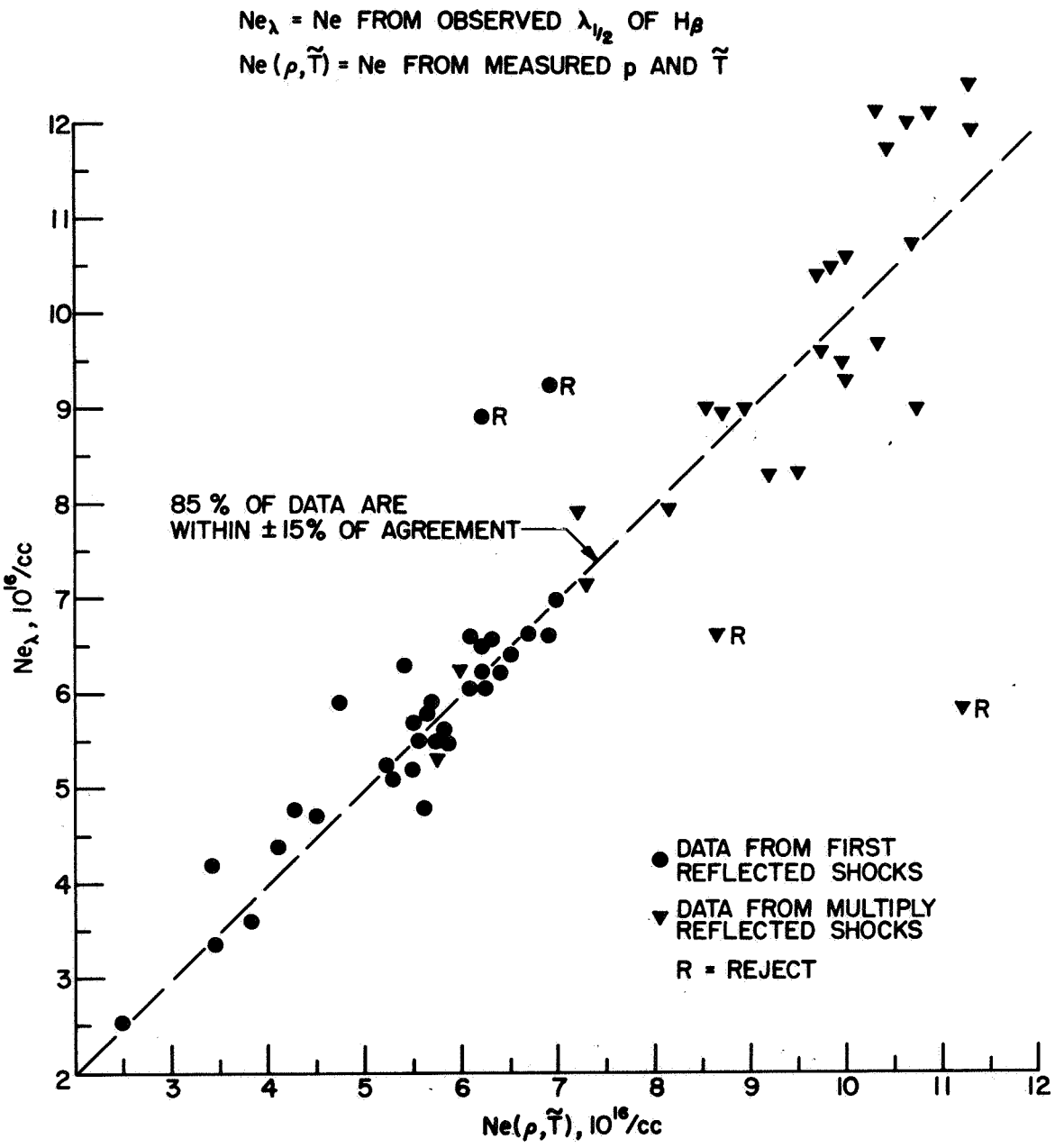


Fig. 44: Comparison of Electron Densities Deduced From the $H_\beta$ Halfwidth with Electron Densities Computed From Measured Temperatures and Pressure.

## F. Methods for Deducing Concentrations of Plasma Impurities

Two kinds of impurity were always present on the shock tube walls: the finely powdered debris deposited by opening diaphragms, and hydrocarbons deposited by the backstreaming of our pumps.

We used the following techniques to assess the amount of hydrogen that boils off the walls during our typical shock tube runs. Shocks were made in Research Grade pure neon, or mixtures of neon and argon. The absolute intensity of either $H_\beta$ or $H_\alpha$ was measured along with the plasma pressure, $T_{neon}$ and $T_{\lambda_{1/2}}$. From these data and the known A-value of $H_\beta$ (or $H_\alpha$) we deduced the hydrogen number densities. This was done for a variety of plasma conditions, temperatures varying between 10,500°K and 12,500°K and pressures varying over 7 - $20\times10^6$ dyne $cm^{-2}$. For all these runs the hydrogen number densities deduced for first-reflected shocks remained constant to within a factor of 2: the mean hydrogen impurity concentration corresponded to 3% of the hydrogen present in a typical shock using ½% $CH_4$ + ½% $CS_2$ + 99% neon test gases. A few shocks were also made using 2% $O_2$ + 98% neon test gases to obtain hydrogen impurity levels by relative intensity measurements against OI lines of known A-values[94]. These runs confirmed the hydrogen impurity concentrations deduced in the earlier runs. We routinely included the mean hydrogen impurity concentration in all our thermodynamic calculations.

We could not directly assess the impurity concentrations of carbon because the visible CI lines are too weak. The fact that no CI lines were detectable in shocks using neon and argon mixtures does enable us to say that carbon impurity concentrations do not exceed 5% of the carbon concentrations found in the usual data runs employing ½% $CH_4$ + ½% $CS_2$ + 99% neon

test gases. By reasoning that the relative carbon to hydrogen content of a heavy hydrocarbon is less than 0.5, we deduce that the usual carbon impurity concentration amounts to less than 3% of the carbon normally present in a data run using ½% $CH_4$ + ½% $CS_2$ + 99% neon test gases.

As an operational check on our estimate of carbon impurity concentrations, we plotted (cf. Chapter VII) the measured A-value of CI λ5052 as a function of carbon additive gas (1% $CH_4$ or ½% $CH_4$ + ½% $CS_2$) initial partial pressure and found no correlation.

Impurity concentrations of sulfur, phosphorus and silicon were assumed to be zero, since all of these elements have strong visible ion lines which could not be detected in hot (T > 12,000°K) shocks in pure neon.

Although a damp cloth smeared across the shock tube walls would invariably pick up aluminum dust, we estimate that typical aluminum impurity concentrations in first reflected shocks were less than 0.01% molal. The two AℓI resonance lines, λ3961.5 and λ3944.0 , were observed in emission or absorption at different times during a typical shock tube run. However, their behavior during a typical shock tube run indicated that much of the observed intensity of these lines originated in the thin boundary layer so they could not be used to assess aluminum concentrations in the bulk of the plasma. Therefore, to estimate the stated upper limit of aluminum impurity concentrations we relied on the strong AℓII line, λ5593 . Knowing our detection threshold, the plasma temperature, and the A-value for this line (cf. Chapter VII) the fact that it was never detected in hot shocks (T >~12,000°K) in neon or neon plus argon test gases, allowed us to deduce an upper limit for the aluminum impurity level.

Moreover, aluminum impurity concentrations exceeding 0.01% molal, would be expected to cause $[Ne_\lambda/Ne(p,\tilde{T})]_{avg.}$ to exceed 1.03 (recall conclusion of Section E, above).

## G. Observations Supporting the Assumption of LTE

Our data are reduced to A-values under the assumption that shock tube plasmas are in a state of LTE. The temperatures and electron densities of our shocks easily meet the theoretical criteria[7,9,29,95-98] for plasmas to be collision dominated (LTE). We now list some experimental evidence to show that our light source is behaving in conformity with the assumption of LTE.

A few μsec after arrival of the first reflected shock, all spectral line intensities will relax to values that either remain constant for the 50 - 100μs duration of the first reflected shock region, or they will all increase slowly, as qausi-constant rates, during this period[†]. Both of these types of time dependence support the assumption of LTE . Shocks that produce time independent intensity for one line do so for all lines regardless of excitation energy or stage of ionization. Hence, there is no long-term equilibration to deep-lying atomic levels. When shocks produce lines that vary slowly with time, it is observed that the intensities of various lines increase at relative rates corresponding to the temperature derivatives of the relevant Saha-Boltzmann equations. That is, by assuming a linear relationship between temperature and time the Saha-Boltzmann equations correctly predict the relative rates of change in excited state populations between lines varying by a factor of 5 in $\frac{\partial I}{\partial t}$ .

Figure 43 also tests the assumption of LTE . In particular, $T_{\lambda_{1/2}}$ does not depend so critically on LTE as does $T_{neon}$ . Griem's theory for Stark broadening of Balmer lines[56] depends on the translational temperatures

---

[†]Both types of behavior can be observed, successively, in shocks generated under identical conditions--so we ascribe the difference between constant intensity shocks and slow-varying intensity shocks to the non-reproducible details of shock formation.

of electrons and ions and the reduction of $Ne_\lambda$ to $T_\lambda$ depends on Saha equilibrium rather than Saha-Boltzmann equilibrium. So the agreement between $T_{neon}$, derived from the population of the 18.9 eV neon line λ5852, and $T_{\lambda_{1/2}}$ over a 2,000°K range of temperature strongly supports the assumption of LTE.

As a final argument in behalf of LTE we refer to Fig. 5. Our results for the A-value of CI λ5052 show no systematic dependence on on electron density over the range $3 - 7\times10^{16}\,cm^{-3}$, so we conclude the plasmas are collision dominated throughout this range.

H. Sample Data From a Typical Shock Tube Run

The CRT traces in Fig. 45 are typical of the raw photoelectric data obtained with 1% $CH_4$ + 99% neon test gases. Approximately 30 sec after arrival of the reflected shock front the plasma temperature is 11,400°K and pressure is $9.6\times10^6$ dyne $cm^{-2}$.

In addition to the data shown in Fig. 45; the pressure transducer output, the CI λ5052 line and background channels, the NeI λ5852 line and background channels, the $H_\alpha$ line and background† channels, and 3 of the 12 SQUID channels monitoring $H_\beta$, we routinely obtain the following data (not shown): the signals from 3 to 9 other SQUID channels on the wings of $H_\beta$, a time resolved spectrogram covering 1100Å (similar to Figs. 53 and 59) and the readout of 1 or 2 chronographs timing the shock speed.

The time dependence of the depicted data is approximately average for shocks into test gases with initial pressures 10-12 Torr: for initial pressures greater than 20 Torr, spectral intensities are essentially time independent throughout the first reflected shock.

---

†We monitor the background of $H_\alpha$ because the low optical depths allow us to check flash lamp repeatability.

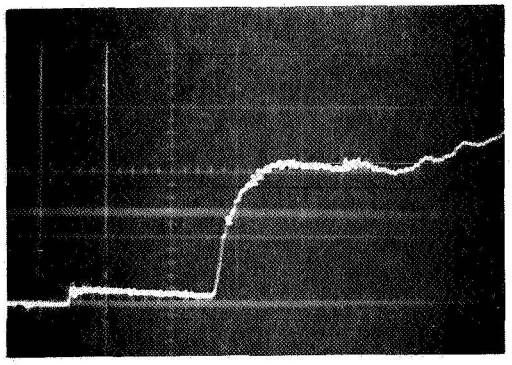

Pressure channels,

gain: 0.05 V/cm.

sweep speed: 20 μs/cm .

CRT trace includes pressure of incident and first reflected shocks.

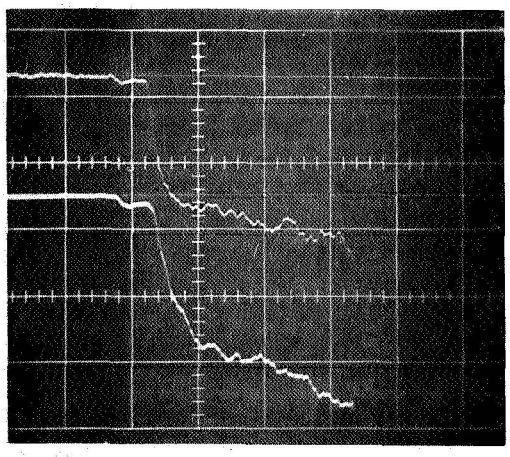

Carbon line (5052Å) channel. (inverted)

gain: 0.01 V/cm.

Carbon background (5079) Channel, (inverted)

gain: 0.005 V/cm.

sweep speeds: 20 μs/cm .

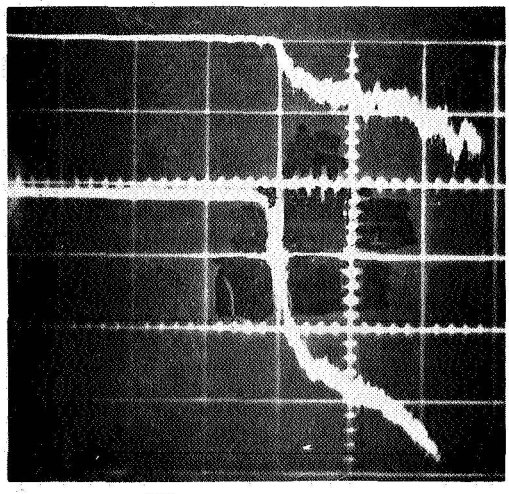

Time →

Neon background (5867Å) Channel (inverted)

gain: 0.02 V/cm.

Neon line (5852Å) channel, (inverted)

gain: 0.20 V/cm.

sweep speeds: 20 μs/cm.

Fig. 45: Typical Data From One Shock Tube Firing.

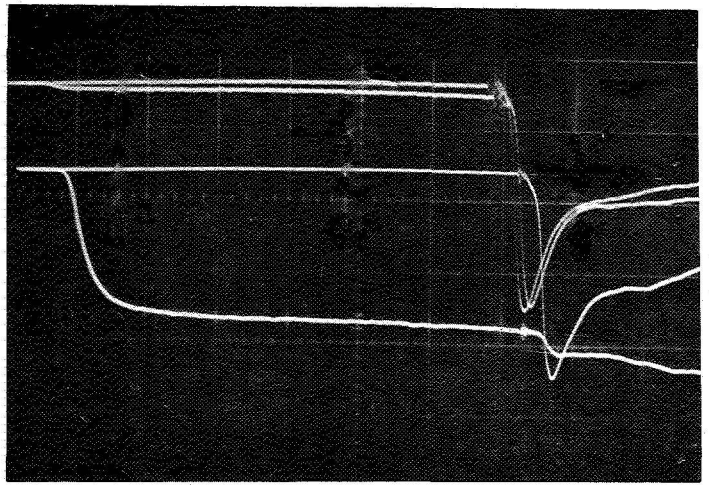

Time →

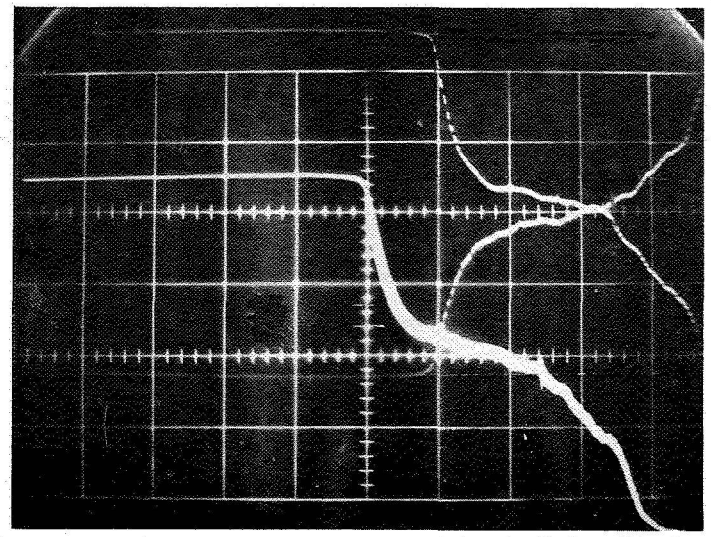

Fig: 45: Typical Data From One Shock Tube Firing. (concluded)

$H_\alpha$ wing (6587Å) channel (inverted).
gain: 1.0 V/cm .

$H_\alpha$ line channel (inverted).
gain: 0.5 V/cm .

Sweep speeds: 10 μs/cm .

For each channel there are two superimposed CRT traces:

Flash lamp + shock tube
and
Flash lamp alone .

$H_\beta$ (SQUID) channels.

#1. (inverted).

gain: 1.0 V/cm .

#6.,

gain: 1.0 V/cm .

#2. (inverted),

gain: 0.5 V/cm .

Sweep speeds: 20 μs/cm .

Fig. 45: concluded.

# CHAPTER VII

# RESULTS

## A. Introduction

The scope of the current transition probability measurements is summarized in Table II. The relative amount of effort devoted to the different elements is reflected in the number of runs made, the wavelengths covered, the range of conditions produced in the shock tube, the variety of test gases used, and in the number of methods (e.g. AE, ARH, etc.) employed. The motives behind this division of effort were already mentioned in Chapter I. As for its consequences: there is a general correlation between the accuracy of results for each element and how exhaustively it was measured. In Table III the transitions studied are listed according to wavelength, and are classified as to whether they are blended or isolated and whether their Stark widths and shifts are also studied.

Results are presented an element at a time. While all results were obtained on the same apparatus, shared the same experimental methods (described in Chapter VI), and adhered to the thermally insensitive approaches described in Chapter III, each element posed a unique set of problems. Therefore, details of the measurements vary from element to element.

In assessing the possibilities for repeatable error in our results for each element we rely upon the agreement obtained between redundant measurements of thermodynamic state and photometric variables, and on the consistency of results gathered over widely varying source conditions--rather than upon comparisons with previous experimental or theoretical work.

Table II. SCOPE OF RESULTS FOR A-VALUES

| Atom | Photographic scan (Å) (No. of runs Δ) | Line measured absolutely (Å) (No. determinations) | Methods used (No. of runs) | Additive gases | Temperature range (°K) | Pressure range ($10^6$ dyne/cm$^2$) |
|---|---|---|---|---|---|---|
| CI | 4600-5700 (54)<br>4000-5100 (12)<br>5700-6800 ( 4) | 5052.1 (44)<br>† | AE (54)<br>ARH (44)<br>ARB (35)<br>ARN (20)* | 1% $CH_4$<br>[.5% $CH_4$ + .5% $CS_2$] | 9,500-13,000 | 5-20 |
| OI | 4600-5700 ( 2)<br>5200-6300 ( 3) | λλ5436.1 ( 3)<br>Δ | Relative to OIλ6157 | 2.0% $O_2$ | 11,000-12,000 | 9-25 |
| NeI | 4750-5900 (12)<br>5200-6300 ( 7) | 5852.5 (19) | Relative to $H_\beta$ | Pure neon<br>.2% $CH_4$<br>.14% $PH_3$<br>.11% $(CH_3)_3A\ell$ | 12,000-13,000 | 5-15 |
| AℓII | 4800-5900 ( 3) | 5593.2 ( 3) | ARH ( 3) | .11% $(CH_3)_3A\ell$ | 12,000-12,800 | 9-20 |
| SiI | 4850-5950 ( 9)<br>5300-6400 ( 2)<br>4570-5700 ( 1) | 5948.5 (10) | AE ( 8)<br>ARH ( 7)* | .21% $SiH_4$<br>1.0% $SiHC\ell_3$ | 8,600-10,000 | 13-40 |
| SiII | 4850-5950 ( 9)<br>5300-6400 ( 2)<br>4570-5700 ( 1) | 5056.0<br>5056.3 } (10) | ARH ( 9)<br>AE ( 7)* | .21% $SiH_4$<br>1.0% $SiHC\ell_3$ | 8,600-10,000 | 13-40 |
| PI | 4800-5900 ( 3)<br>4600-5700 ( 1)<br>5300-6400 ( 2) | 5477.7 ( 5) | AE ( 5)<br>ARH ( 4)* | .14% $PH_3$ | 9,500-13,000 | 9-40 |
| PII | 4800-5900 ( 3)<br>4600-5700 ( 1)<br>5300-6400 ( 2) | 5253.5 ( 5) | ARH ( 5)<br>ARN ( 1)<br>AE ( 3)* | .14% $PH_3$ | 8,500-13,000 | 9-40 |
| SI | 4600-5700 (26)<br>4000-5100 ( 3)<br>5700-6800 ( 3) | λλ4695<br>† (30) | AE (30)<br>ARH (30)<br>ARC (23) | [.5% $CH_4$ + .5% $CS_2$]<br>[.25% $CH_4$ + .75% $CS_2$] | 9,500-12,500 | 8-20 |
| SII | 4600-5700 (26)<br>4000-5100 ( 3)<br>5700-6800 ( 3) | 5453.6 (18) | ARH (12)<br>ARN (16)<br>AE ( 5)* | [.5% $CH_4$ + .5% $CS_2$]<br>[.25% $CH_4$ + .75% $CS_2$] | 9,500-12,500 | 8-20 |
| CℓI | 4570-5700 ( 1) | 4601.0 ( 1) | ARH ( 1) | 1.0% $SiHC\ell_3$ | 10,000 | 10 |

Δ For relative (intra-atomic) $A_{mn}$ - values, each "run" really presented at least two independent shock regimes since results were obtained from multiply, as well as first, reflected shock flows.

† For $C_I$ and $S_I$ only TIB results are counted as independent determinations.

* Supplementary method used to check for self-consistency: precision not comparable with other method(s) used.

Table III. TRANSITION PROBABILITIES STUDIED, ARRANGED BY WAVELENGTH

| | λ(Å) | | λ(Å) | | λ(Å) | | λ(Å) | | λ(Å) |
|---|---|---|---|---|---|---|---|---|---|
| CI | 4064.2*§ | | 5330.8§† | | 6347.1 | | 6041.9*§ | | 5646.9§ |
| | 4064.2*§ | | 5341.1§† | | 6371.3 | | 6046.0*§ | | 5564.9† |
| | 4065.1*§ | | 5343.3§† | PI | 5015.8 | | 6052.7*§ | | 5578.8 |
| | 4231.3 | | 5400.6 | | 5061.9 | | 6743.6§† | | 5606.1† |
| | 4268.9 | | 5562.8 | | 5079.3 | | 6748.8§† | | 5616.6 |
| | 4352.1* | | 5656.7 | | 5098.2§ | | 6757.2§† | | 5645.6* |
| | 4371.3 | | 5764.4† | | 5100.9§ | SII | 3963.1 | | 5659.9† |
| | 4762.4§ | | 5820.2† | | 5109.6 | | 4028.8 | | 5664.7 |
| | 4762.4§ | | 5852.5 | | 5149.4§ | | 4142.3 | | 5819.2 |
| | 4766.6§ | | 5881.9 | | 5154.8§ | | 4145.1 | CaI | 4601.0† |
| | 4771.7§ | | 5944.8 | | 5162.2§ | | 4153.1 | | |
| | 4775.8§ | | 6143.1 | | 5345.8 | | 4174.0 | | |
| | 4812.8*§ | | 6163.6 | | 5458.3 | | 4193.5* | | |
| | 4817.3*§ | | 6217.3 | | 5477.7 | | 4278. | | |
| | 4826.7*§ | | 6266.5 | | 5514.7§† | | 4294.5 | | |
| | 4932.0† | | 6598.9 | | 5517.0§† | | 4431.0* | | |
| | 5039.0§ | AlII | 5593.2† | | 5546.9 | | 4463.5 | | |
| | 5039.0§ | SiI | 4772.7 | | 5905.0 | | 4483.4 | | |
| | 5041.6§ | | 4782.9 | PII | 4602.1 | | 4486.6 | | |
| | 5044.0§ | | 4792.2§ | | 4658.3 | | 4524.6§ | | |
| | 5049.6§ | | 4792.3§ | | 4927.0 | | 4524.9§ | | |
| | 5052.1† | | 5006.0† | | 4943.4† | | 4648.1* | | |
| | 5380.2† | | 5493.2 | | 4954.3 | | 4656.7 | | |
| | 5793.5§ | | 5517.5 | | 4969.6 | | 4668.5* | | |
| | 5801.1§ | | 5622.2 | | 5152.2* | | 4716.2 | | |
| | 5805.7§ | | 5645.7† | | 5191.4† | | 4779.1* | | |
| | 6587.8 | | 5665.6† | | 5253.5† | | 4792.0 | | |
| OI | 4772.5*§ | | 5684.5† | | 5296.1 | | 4815.5† | | |
| | 4772.9*§ | | 5690.5† | | 5316.1† | | 4917.1 | | |
| | 4773.8*§ | | 5701.1† | | 5316.1 | | 4924.0§ | | |
| | 4801.8*§ | | 5708.4† | | 5344.7 | | 4925.3§ | | |
| | 4802.2*§ | | 5747.6 | | 5378.1 | | 4942.4 | | |
| | 4803.0*§ | | 5753.6 | | 5386.9† | | 4991.9 | | |
| | 4967.4§ | | 5754.3§ | | 5409.7† | | 5009.5† | | |
| | 4967.9§ | | 5763.0 | | 5425.9† | | 5014.0† | | |
| | 4968.8§ | | 5772.2 | | 5450.7 | | 5027.1† | | |
| | 5018.8§ | | 5780.4 | | 5483.6 | | 5032.4† | | |
| | 5019.3§ | | 5993.1 | | 5499.7† | | 5103.3† | | |
| | 5020.1§ | | 5797.9 | | 5507.1 | | 5142.3 | | |
| | 5329.0§† | | 5859.2* | | 5541.2 | | 5201.0§ | | |
| | 5329.6§† | | 5873.7 | | 5583.3 | | 5201.3§ | | |
| | 5330.7§† | | 5948.5† | | 5588.2 | | 5212.6† | | |
| | 5435.2§† | | 6125.0§ | | 5727.7 | | 5320.7† | | |
| | 5435.8§† | | 6131.6§ | SI | 4154.2§ | | 5345.6† | | |
| | 5436.8§† | | 6131.8§ | | 4411.3 | | 5428.6† | | |
| | 6046.3§† | | 6142.4§ | | 4694.1§† | | 5432.7† | | |
| | 6046.5§† | | 6145.0§ | | 4695.5§† | | 5453.6† | | |
| | 6046.5§† | | 6155.0§ | | 4696.3§† | | 5466.5* | | |
| NeI | 4704.4§ | | 6237.3§ | | 5278.1§† | | 5473.6† | | |
| | 4708.9§ | | 6244.5§ | | 5278.7§† | | 5509.6† | | |
| | 4710.0§ | | 6254.2§ | | 5279.0§† | | 5518.7* | | |
| | 4712.1§ | | 6254.8§ | | 5498.2*§ | | 5526.2 | | |
| | 4715.3§ | SiII | 5041.0† | | 5501.1*§ | | 5536.7 | | |
| | 4953.0 | | 5056.0§ | | 5507.0*§ | | 5556.0 | | |
| | 5037.8 | | 5056.3§ | | 5696.6*§ | | 5639.9§ | | |
| | 5144.9§ | | 5957.6 | | 5700.2*§ | | 5640.3§ | | |
| | 5145.0§ | | 5978.9† | | 5706.6*§ | | 5645.6§ | | |

*Upper limit estimate

§Observed as a blended line

†Stark width and shift also measured

†Stark width also measured

There have been relatively few previous experimental studies of the lines we measure, so we utilize all comparison data that is available. We quote the tolerances assigned to their results by the authors themselves: in most cases these are probable error (PE) estimates, although a few authors give only the uncertainty due to scatter (random error). When the same transition has been studied by two or more workers, differences between results typically exceed claimed tolerances. Moreover, disagreements between two experiments is generally of the same order as their mutual disagreement with Coulomb approximations. For example, this level of disagreement is approximately a factor of 1.8 for the visible lines of CI and SI .

The strongest lines in the spectra of CI , SiI , NeI , PI and SI are in the UV or near IR , while the A-values we measure seldom exceed $1\times10^{6}\,\mathrm{sec}^{-1}$ . Hence, the radial matrix elements in the Coulomb approximations for these lines are very small and inherently unreliable[14-16].

We could not meaningfully test our relative A-values for agreement with the J - file sum rules[99-102]. With the exception of SII , our results did not encompass the majority of transitions for a complete array, or else predicted radial matrix elements of different multiplets in the array differed by large factors, so that uncertainty in radial wave functions is large enough to obscure the behavior of angular wave functions which the sum rule is intended to test.

We did compare our results for 4s - 4p transitions in SII with the J - file sum rule and found disagreements far greater than

could be accounted for by experimental errors: apparently this array is subject to strong configuration interaction.

## B. Estimation of Experimental Errors

Tolerances stated in the tables are 80% confidence estimates of total error. They represent the RMS combination of uncertainty due to scatter (random error) with the uncertainty compounded from upper limit estimates of possible systematic errors.

For each atom (ion) studied, the one line designated as being "measured absolutely" has the smallest tolerance. This is because such lines are the strongest isolated ones studied, are the lines most carefully checked for self-consistency, and are usually measured the maximum number of times for that atom. The range of tolerance for these lines runs from $\pm$ 10% for CI λ5052 to $\pm$ 35% for SiI λ5948. Scatter is responsible for only a small fraction of these total tolerances regardless of whether results are based on 44 independent determinations as for CI λ5052 , or only on 5 determinations, as for PI λ5477.

Since all other transitions of an element (in the same ionization stage) were measured relative to one of these "absolutely measured" lines,, they generally warrant larger tolerances (15% - 45%) because of such factors as low signal-to-noise ratios, difficulties in the interpretation of diffuse or partially merged lines, and uncertainty in relative film sensitivity between widely spaced wavelengths. In a

few cases we lacked a sufficient number of determinations to make a good statistical statement.

The compendium of error sources given below includes only the more important errors discussed in the dissertation.

Possible Sources of Systematic Error:

Improper performance or interpretation of absolute and relative photometric calibrations against the carbon arc.

Uncertainty in the Stark broadening parameters for $H\alpha$ , affecting the *in situ* method of absolute intensity calibration.

Uncertainty attached to the wing corrections and curves of growth for slit-integrated lines.

Failure to make (a small) correction to effective path length in recognition of finite boundary layer thickness.

Incorrect interpretation of photographic profiles with respect to assignment of baselines or the influence of weak interfering lines.

Uncertainty in the transition probability of NeI $\lambda 5852$ , used as an internal standard.

The uncertainty in the theoretical Stark width of $H\beta$ , which influences our calculation of plasma electron densities.

Astigmatism in recording of CRT traces and departures from linear gain for large CRT deflections.

Pressure calibration errors or departures from linear gain of transducers.

Error in the molal concentration of spectroscopic additive (e.g. $SiH_4$ , $PH_3$) in neon carrier mixes stored for long periods.

Uncertainty regarding the (small) amount of readily ionized wall-impurities (e.g. Al , Ca , Cd ) entering the plasma.

Uncertainty in the approximate estimates for the (small) concentrations of H, C, S, Si, Aℓ, O, and P injected into plasmas from wall impurities.

Error from any of these possible sources cannot exceed known limits without causing statistically significant discrepancies between our sets of redundant measurements. If we assume all possible systematic errors to be present at their highest undetectable levels, then their net effect on the typical A-value determination can be lumped into <u>repeatable</u> (relative) uncertainties of:

$$\Delta I_{abs.} \leq \pm 8\%$$

$$\Delta I_{rel.} \leq \pm 2\% \text{ per } 100\text{Å}$$

$$\Delta p_{total} \leq \pm 6\%$$

$$\Delta T \leq \pm 1\%$$

$$\Delta pp_{\substack{of \\ additive}} \leq \begin{array}{l} \pm 5\% \text{ for C, S, C}\ell \text{ and O} \\ \pm 20\% \text{ for Si and P} \\ \pm 35\% \text{ for A}\ell \end{array}$$

The uncertainty in a result, $\Delta_S A$, due to systematic errors, is taken to be:

$$\Delta_S A = \left[ \sum_j \left( \frac{\partial A}{\partial X_j} \Delta X_j \right)^2 \right]^{1/2}$$

where $\Delta X_j = \Delta I_{abs}, \Delta I_{rel}, ---, \Delta_{pp}$ of additive.

Sources of Random Error (Scatter):

Photographic noise from grain, local fog levels, and emulsion inhomogeneities.

Noise-in-signal affecting photomultiplier outputs.

Error involved in reading CRO traces.

Localized, transient inhomogeneities in the source plasma caused by weak (non-reproducible) diagonal shocks.

Interference due to the ringing of the pressure transducer.

Random error from these sources will be superimposed on whatever systematic (repeatable) errors are present. The (relative) effect of random errors on a typical <u>single</u> experimental run may be lumped as follows:

$\Delta\tilde{T} = \pm 1\%$

$\Delta p_{total} = \pm 8\%$

$\Delta \int_{-\infty}^{\infty} I(\lambda)d\lambda = \pm 10\%$ for strong lines, e.g. SiII λ5056 ;

$= \pm 20\%$ for lines of moderate strength, e.g., CI λ5052 ,

$= \pm 40\%$ for the weaker lines measured, e.g. SI λλ5790 .

The <u>a priori</u> estimated random error $\Delta_r A$ in a <u>single</u> A-value determination is:

$$\Delta_r A = \left[ \sum_i \left( \frac{\partial A}{\partial Xi} \Delta Xi \right)^2 \right]^{1/2}$$

where $\Delta Xi = \Delta\tilde{T}$ , $\Delta p$ total , $\Delta \int_{-\infty}^{\infty} I(\lambda)\, d\lambda$ .

These <u>a priori</u> estimates of random error generally tally quite well with the actual scatter in results. That is:

$$\Delta_r A \simeq 1.28\ \sigma(A)$$

where $\sigma(A)$ is the RMS deviation (variance) in the distribution of results, and the factor 1.28 makes the r.h.s. of the equation the 80% confidence limit for a hypothetical Gaussian distribution.

Whenever n , the number of determinations, is greater than six, we also plot the distribution of results, as in Figs. 8 , 46, and 50, to see if the limited sample does resemble a Gaussian, and to take the value $\tilde{A} \pm \Delta' A$ within which 80% of the data falls. The contribution of random errors, $\Delta_r \tilde{A}$ , to the result is then taken to be the <u>larger</u> of $\frac{\Delta' A}{\sqrt{n}}$ , $\frac{\Delta A}{\sqrt{n}}$ .

The stated tolerances are the expressions:

$$\left[ (\Delta_s A)^2 + (\Delta_r \tilde{A})^2 \right]^{1/2} .$$

C. Monitor on Overall Accuracy:
Measured Hβ Transition Probability

A direct check on experimental error consists in measuring a transition probability whose value is already well known. Candidates for such measurement in the visible include Hβ and several OI and NI lines. Due to the combination of low A-values and high excitation energies the desired NI lines could not be excited to useful brightness using $N_2$ as a spectroscopic additive. Multiplet (10) of OI was obtained with good brightness, but only a few runs were made using test gases including oxygen. Even if many data were available for this blended OI multiplet, it would still be preferable to measure the A-value of Hβ because the thermal dependence of OI multiplet (10) is identical† to Hβ ; however, the Hβ transition probability is known to ± 1% while that of OI λλ6157 has estimated reliability of only ± 10%.[13,104] By process of elimination, then, we were led to "measure" the A-value of Hβ , the comments of Chapter VI, Section C-7 notwithstanding.

---

†Excitation and ionization energies coincide to better than 0.1 eV.

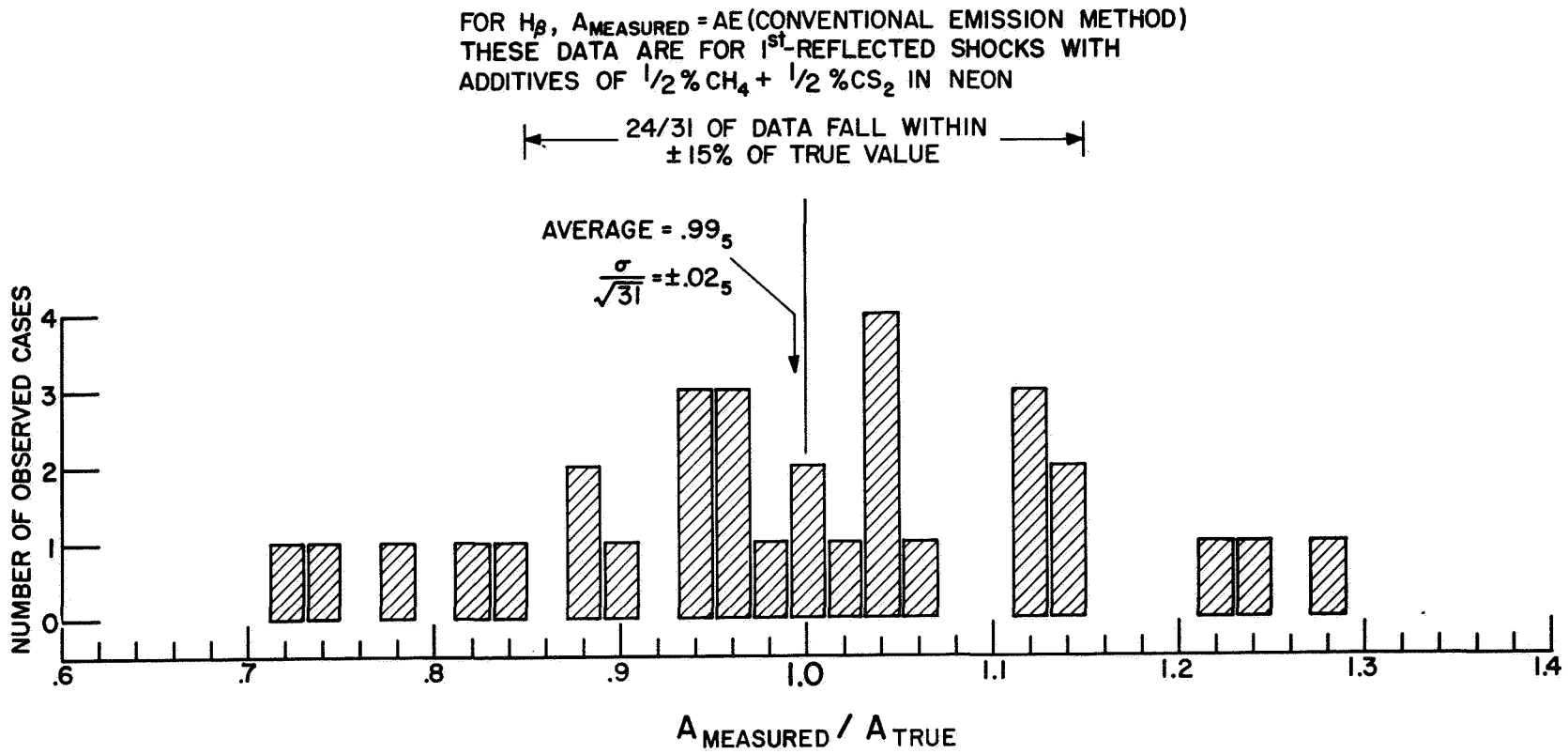


Fig. 46: Monitor for Overall Experimental Accuracy: A-Value of $H_\beta$ Measured Simulteneously with Data for A-Values of CI , SI and SII .

The measurement was performed by the conventional emission (AE) method, during the same runs used to determine CI , SI and SII A-values. A histogram of results is given in Fig.46 . The 1% agreement of AE with the known A-value, $8.42\times10^6$ $sec^{-1}$, is to some extent fortuitous: from the spread in this Gaussian distribution we would have taken the 80% confidence limit to be $\pm$ 3.1%. Moreover, systematic errors amounting to $\pm$ 10% can enter this determination.

D. Transition Probabilities for CI

1. Introduction. The visible lines of CI are inherently weak in spectra from laboratory sources. Their faintness stems from a combination of small A-values (typically $\lesssim 10^6$ $sec^{-1}$) with excitation energies (10-11 ev) that fall close to the CI ionization limit. A Grotrian diagram for visible CI lines studied is given in Fig.48 . A densitometer tracing, Fig 48 shows the typical grain noise in the integrated intensities of the three strongest visible CI lines; λ5052, λ5380, λλ4770, when using a 1% $CH_4$ additive. Even when operating our shock tube at temperatures and pressures selected to optimize CI line brightness, we seldom obtained peak optical depths for the strongest CI line (λ = 5052Å) exceeding .03 at T = 11,600°K. With slit integrated intensities of CI λ5052 only a few times brighter than the carbon arc crater, signal-to-noise ratios allowed precisions of typically 15% - 25% for photographic recording and 10% - 20% for photoelectric recording. Since a large scatter can effectively mask systematic errors, the faintness of the line proved a major obstacle in the study of CI λ5052 where, as already stated, we are striving for our greatest accuracy. Forty-four data runs were made, not only for the sake of reliable statistics for

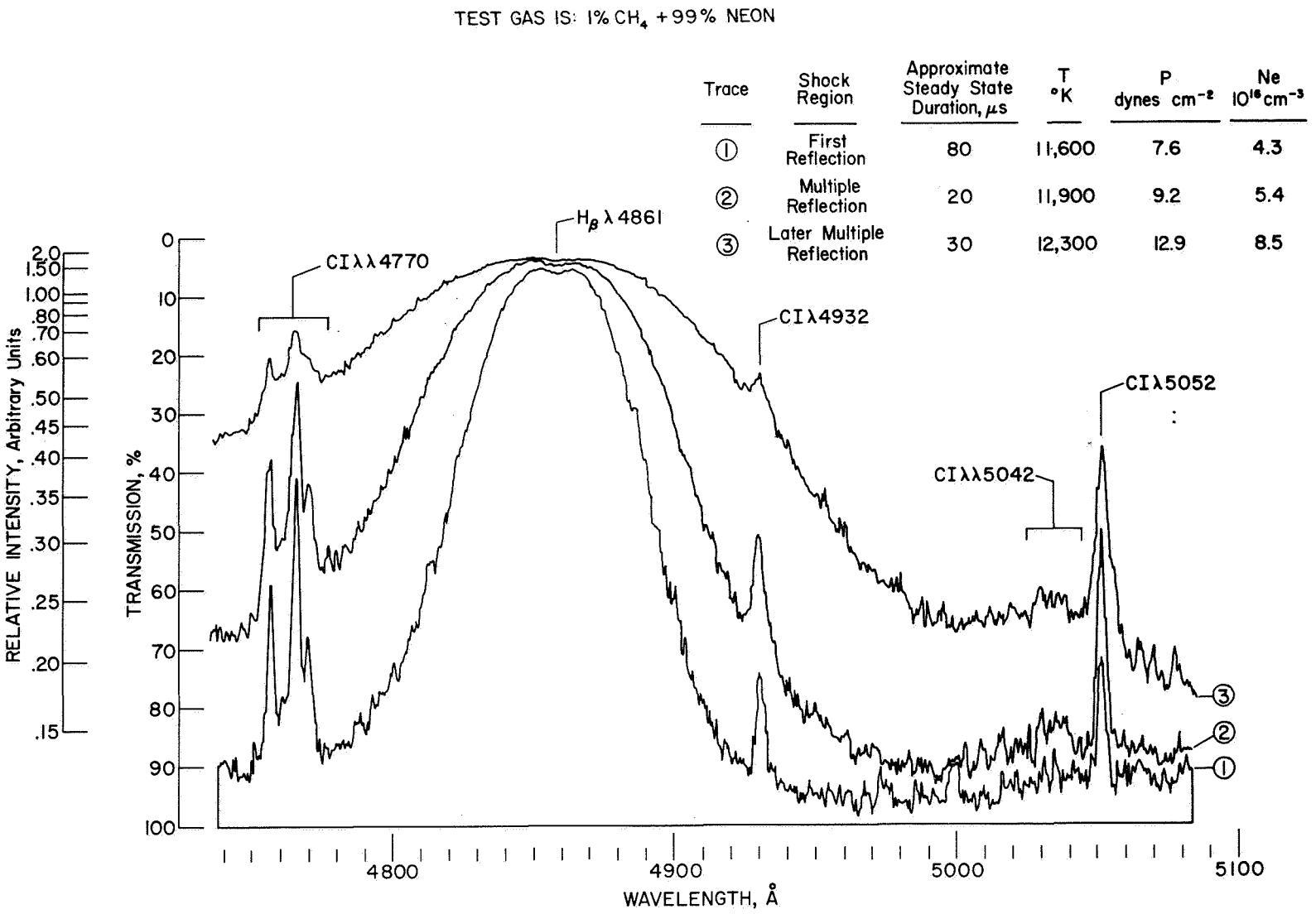


Fig. 47: Densitometer Tracings, 4750Å - 5100Å, for Three Successive Steady State Regions Recorded During a Single Shock Tube Firing.

A-value results, but also to obtain a desired level of significance in the comparisons between redundant thermodynamic and photometric variables. Figure 48 is a Grotrian diagram of the CI lines we measured.

No CII lines were detected. Even in the multiply reflected regions of our strongest shocks ($T \gtrsim 13{,}000°K$, $p \gtrsim 8\times10^6$ dyne $cm^{-2}$) using 1% $CH_4$ test gases, the CII multiplet $\lambda\lambda4267$ was indistinguishable from local emulsion grain. Calculations based on the Coulomb approximation show that despite a multiplet g A-value of $14\times2.46\times10^8$ $sec^{-1}$, signal levels are expected to fall below our detection threshold because of the high (22.86 ev) excitation energies involved.

2. Selection, Execution and Reduction of Data Runs. Of the 44 data runs for the study of CI, 17 used test gases of 1% $CH_4$ in neon and 27 used test gases of .5% $CH_4$ + .5% $CS_2$ in neon. Methane was selected for a spectroscopic additive because it contains only carbon (subject for study) and hydrogen (for plasma diagnosis), is stable (will not break down or polymerize) under our normal operating conditions and is a gas at STP. Methane was considered preferable to other light hydrocarbons (pentane, ethane, etc.) because it has less of a tendency to deposit carbon on shock tube walls and windows after each run. Carbon bisulfide enabled us to study CI, SI, and SII simultaneously, since there is no significant interference between lines of these species.

Initial test gas pressures of 20 Torr, 14 Torr and 9 Torr were selected to give (at driving pressures of 1100 ± 100 psi) plasma temperatures grouping about 10,800°K, 11,300°K and 12,100°K. The distribution of achieved temperatures, seen in Fig. 43 reflect the non-reproducibility of the shock tube. This figure also shows that most data runs were made

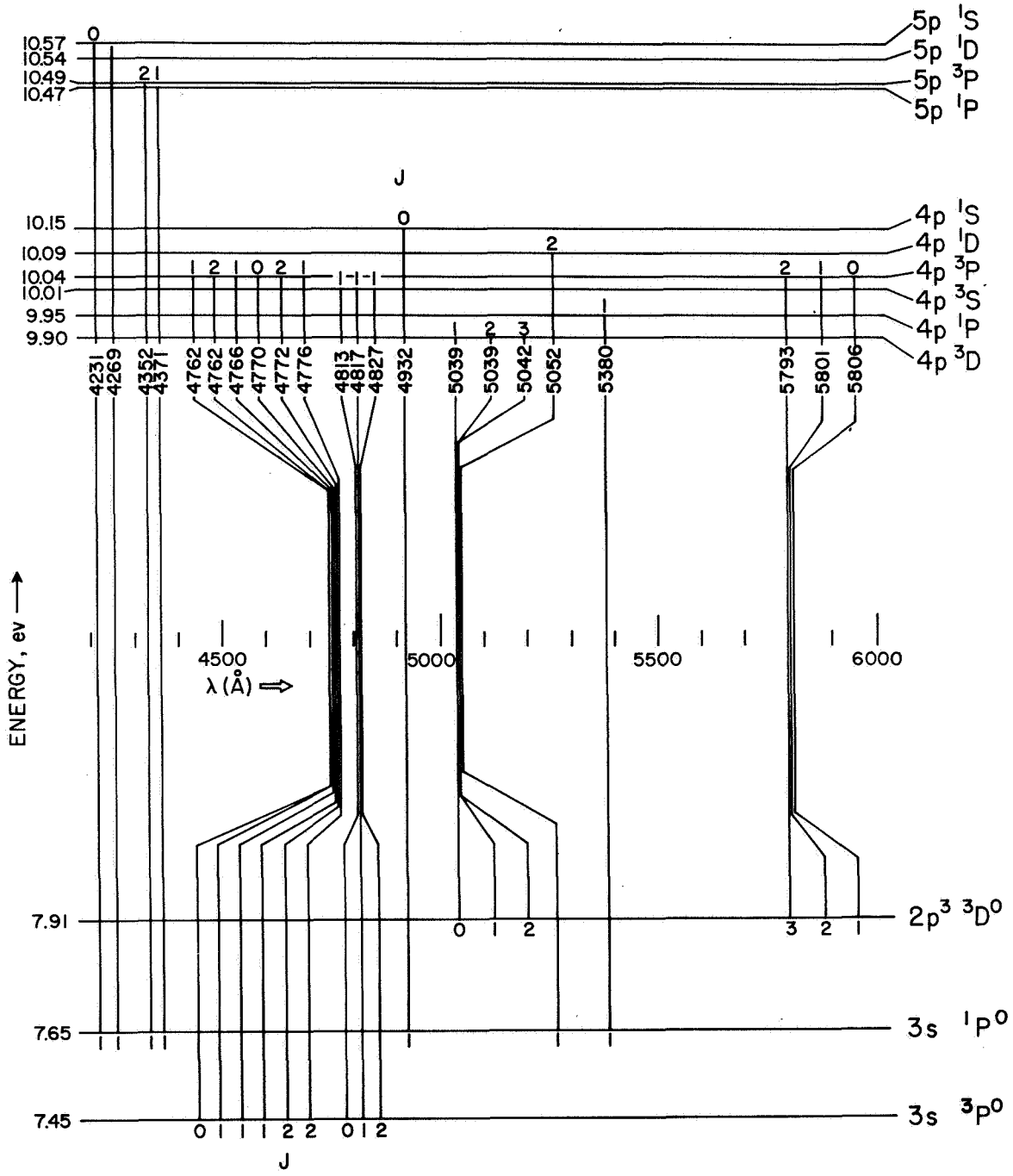


Fig. 48: Grotrian Diagram for CI Lines Currently Studied.

in the vicinity of 11,300°K to acquire good statistics for one set of plasma conditions.

Selection of λ5052 as the CI line to be absolutely measured (all other CI lines are measured relative to it) was based on the following considerations: λ5052 is the strongest† isolated line in the visible spectrum of CI , and it also lies close enough to $H_\beta(\lambda = 4861)$ to insure good relative photographic intensities for calculation of $ARH_C$ . The corellation between line brightness and resulting A-value precision for weak lines can be appreciated with the aid of Fig.49 : if the hatched-in area, representing the range of photographically recorded peak CI λ5052 intensities, is shifted to transmissions 17% - 20% higher, as it would be for the next brightest isolated CI line, λ5380, precisions would typically be lowered by a factor of 1.5-2. In refering to CI λ5052 as "isolated," we implicitly neglect interference from the blended multiplet CI λλ5041 . Because it is relatively weak, the wings of this multiplet cause no significant loss of accuracy in the assignment of base-lines for CI λ5052 so long as entrance slit widths are less than 3Å , as they are for both photographic and photoelectric recording in the current data runs.

In reducing data for λ5052, we follow the methods discussed in Chapters VI and III, here briefly recapitulated in a footnote††.

---

†While the merged CI multiplet 4770 is both stronger and closer to $H_\beta$ than λ5052, its photoelectric measurement requires (integrating) entrance slits more than 15Å wide. However, such wide entrance slits would greatly reduce precisions in $T_\alpha$ and $T_{neon}$ obtained from $H_\alpha$ and NeI λ5852 photoelectric channels which are on the same spectrograph.

††Source temperature is taken to be the unweighted average of however many of $T_\alpha$, $T_\beta$, $T_{neon}$ and $T_{\lambda\frac{1}{2}}$ are available for a particular run. Source pressure is that read from the quartz transducer, except for the few cases when CRO recording problems made it unavailable: then, shock speed-predicted pressures $p(S_1)$ were used, relying for justification upon the good previous agreement between $p(S_1)$ and p from the transducer shown in Fig. 20 . Impurity

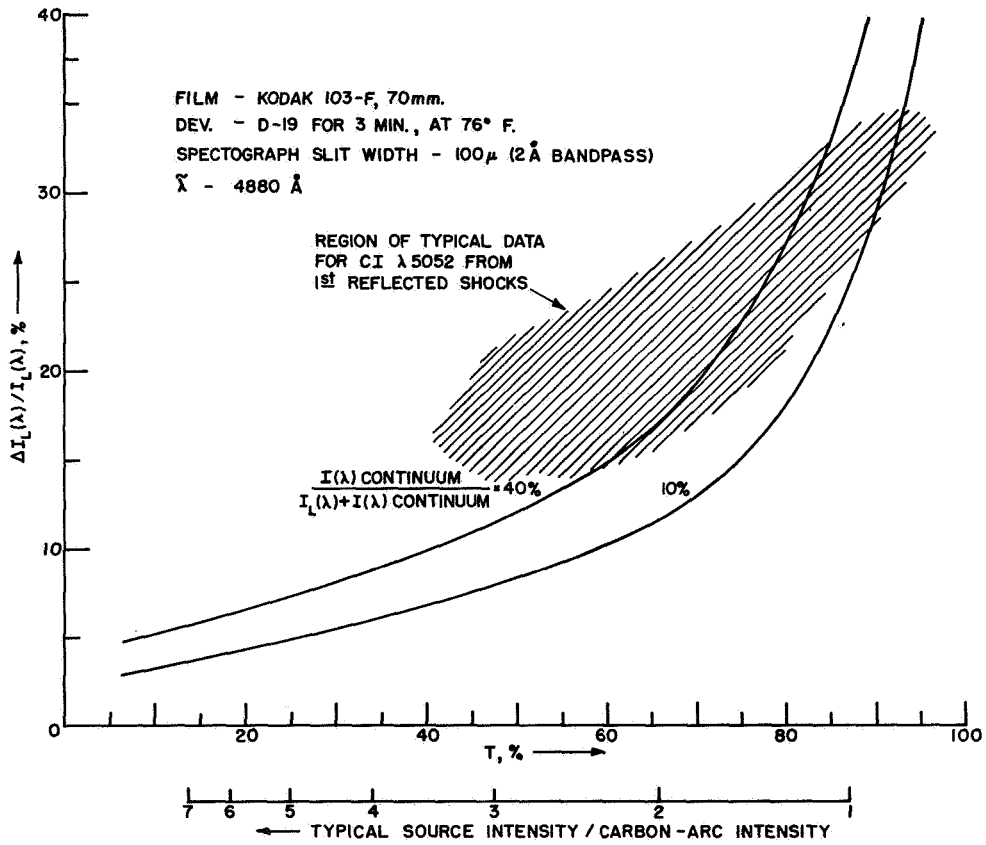


Fig. 49: Uncertainty in Line Intensity, $\Delta I_L(\lambda)/I_L(\lambda)$ , Arising from Emulsion Grain, Shown as a Function of Specular Transmission.

From amongst the four independent measurements of $A_{mn}$ for CI λ5052: $AE_C$, $ARNE_C$, $ARB_C$ and $ARH_C$, it is possible to construct several thermally insensitive averaged results. For instance, in Chapter III we showed the small implicit thermal dependence of the following combinations:

$$A_C = \tfrac{1}{2}(AE_C + ARH_C)$$

$$A_C = \tfrac{1}{2}(ARB_C + ARH_C)$$

$$A_C = \tfrac{1}{2}(ARN_C + AE_C)$$

$$A_C = \tfrac{1}{4}(ARN_C + ARH_C + 2\,AE_C) \quad .$$

Not all of these combinations are used in arriving at our final result. $ARN_C$ was used (only occasionally) for self-consistency comparisons. This is because photoelectrically measured integrated line intensities for Ne λ5852 had a large scatter[†††] (directly attributable to low signal-to noise ratios), and also because it is not desirable to use

---

††(cont.)
levels of hydrogen and carbon (from wall contaminants) were deduced from intensities of $H_\alpha$ and $H_\beta$, during runs in pure neon, neon plus a few percent orgon, and neon plus a few percent oxygen, where source temperatures were approximately known.

The two redundant measurements of the CI λ5052 integrated absolute intensity were employed as follows: the slit-integrated photoelectric value ($R_C$ of Fig. 42 ) was averaged with the photographic - SQUID calibrated value ($R_C^*$ of Fig. 44 ) for computation of the emission A-value ($AE_C$), and also for computing the A-values $ARN_C$ and $ARB_C$ measured relative to NeI λ5852 and $H_\alpha$, respectively. To compute the A-value relative to $H_\beta$, $ARH_C$, the ratio of λ5052 to $H_\beta$ photographic relative intensities was used.

†††
This scatter does not invalidate use of the line to obtain $T_{neon}$ since source temperature is a very weak function of neon line intensity.

the NeI λ5852 A-value for a ± 10% internal standard when $H_\beta$ provides a ± 1% internal standard and comparable or better thermal balancing with our plasma temperatures.

The reason for not employing $ARB_C$ in calculating final results is more subtle: $ARB_C$ and $AE_C$ are not sufficiently independent, either in thermal dependence or method of observation, to warrant inclusion of <u>both</u> $ARB_C$ and $AE_C$ in the reduction of final results. That is, both $AE_C$ and $ARB_C$ are linearly dependent on the same $(\frac{1}{2}R_C + \frac{1}{2}R_C^*)$ integrated intensity of CI λ5052. Since the uncertainty in a TIB result arising from temperature errors of ± 1% is small compared to the error in $\frac{1}{2}(R_C + R_C^*)$, <u>either</u> $AE_C$ or $ARB_C$ can be used with equivalent accuracy. We chose $AE_C$ rather than $ARB_C$ because it is available for a larger percentage of the data runs, and adopt $A\ (TIB)_C \equiv \frac{1}{2}(AE_C + ARH_C)$ for our TIB result. Distributions of $AE_C$, $ARH_C$ and $A\ (TIB)_C$ values from 44 data runs are given in Fig. 8 . The distribution formed by combining the $AE_C$ and $ARH_C$ distributions, without recognizing any shot-by-shot relationship between these two independent results, is included to bring out by comparison against the $A\ (TIB)_C$ distributions how thermal insensitivity is responsible for a tighter grouping. The shape of the $A\ (TIB)_C$ distribution, the displacement of $AE_C$ with respect to $ARH_C$, and the selection of the adopted $1.74\times10^6 sec^{-1}$, which is <u>not</u> the arithmetic <u>mean</u> of our $A(TIB)_C$ results, were discussed in Chapter III.

To obtain other CI transition probabilities relative to CI λ5052 , we use relative photographic intensities and equation . Data were collected from both first reflected and multiply reflected shock regions in an effort to obtain the most reliable statistics for the relative intensity ratios, which have standard deviations as high as ± 40%

| λ(Å) | $\tilde{A}_{REL.}$ | SCATTER | | TOTAL $A_{REL.}$ TOLERANCE | $A_{REL.}$, NBS COMPILATION |
|---|---|---|---|---|---|
| | | σ(RMS) | $\sigma/\sqrt{n}$ | | |
| 5380 | $.99_0$ | $.1_0$ | 2% | ±8% | $.94_1$ |
| 4932 | $2.01_5$ | $.3_3$ | 3% | ±10% | $2.70_5$ |
| MLT.(6) 4770 | $.80_0$ | $.1_6$ | 3% | 16% | $.94_1$ |

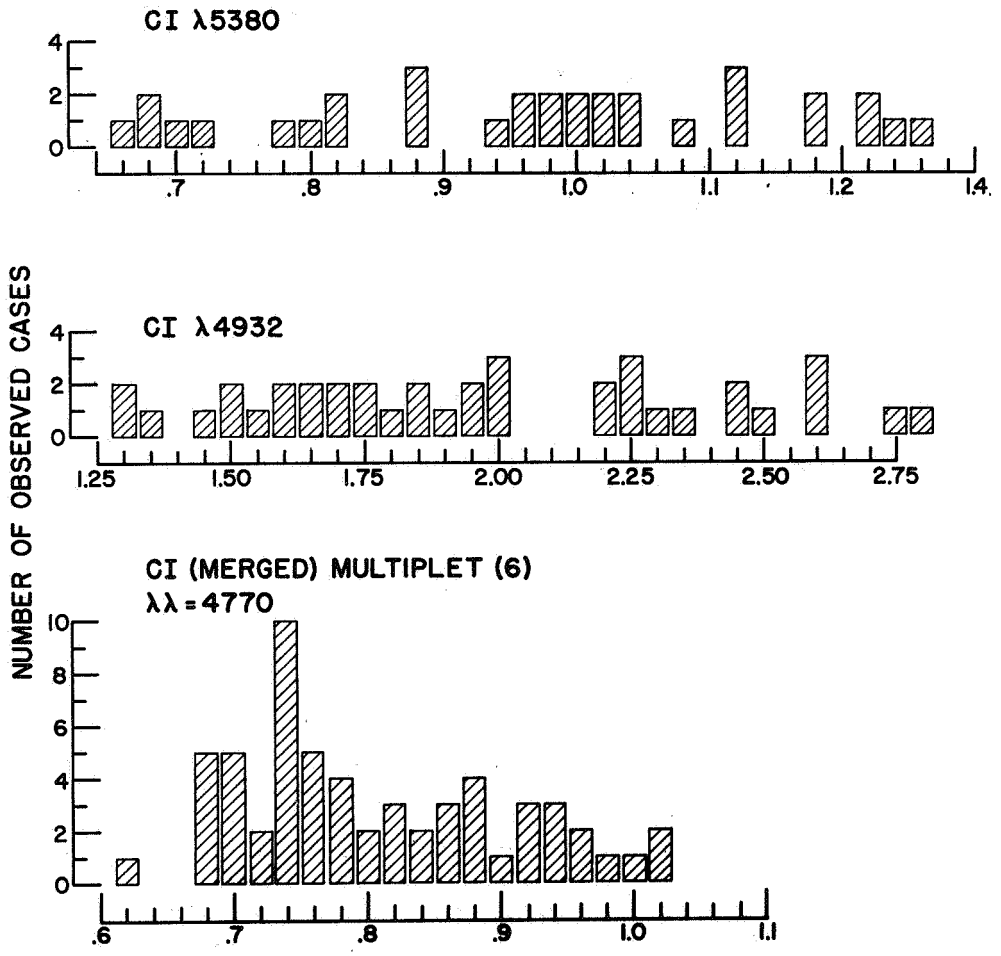


Fig: 50: Results for Some CI A-Values Measured Relative to CI λ5052 .

for the weaker lines measured. Lack of spatial homogeniety in multiple reflected flows causes no problem here, since most visible CI lines come from upper levels within .5 ev of CI λ5052.

The distributions of results for λ5380, λ4932 and λλ4770, relative to λ5052, are given in Fig. 50 . The RMS deviations, $\sigma$ , in these distributions are not excessive in light of the photographic noise problem just discussed. However, $\sigma/\sqrt{n}$ , with n the number of determinations, is not a particulary useful index of the uncertainty in the averages of these distributions since they hardly resemble Gaussians. For λ5380 and λ4932 there is no apparent tendency for the distributions to peak at a central value, while the distribution for λλ4770 does peak but is not symmetrical. We do not understand why these distributions are not normal -- but these weak, grainy profiles afford ample opportunity for systematic, as well as random, reading errors.

3. Results. Measured CI transition probabilities are listed in Table IV as the Einstein coefficient for spontaneous emission, $A_{mn}$ , in $10^6$ inverse seconds. We also list $\log_{10}gf$ where g is the degeneracy (2J + 1) of the lower level of f the absorption oscillator strength. Unless otherwise stated, terms, J-values and "multiplet numbers" are of from Mrs. (Moore) Sitterley's[105] well-known astrophysical compilation. Wavelengths are in Ångstroms. The A-value of CI λλ5041 has a 35% tolerance because its faintness and diffuse shape make it difficult to distinguish from the continuum. Ambiguity in the result is agravated by the predicted presence of a recombination peak underlying this merged multiplet.

Individual lines of multiplet (6) could not be resolved for data runs using .5% $CH_4$ + .5% $CS_2$ test gases. The high source temperatures needed to give good brightness to these lines also lead to strong ionization of

Table IV. TRANSITION PROBABILITIES FOR CI†

| Multiplet | Transition (n, lower)(m, upper) | $J_n-J_m$ | λ(Å) | Amn $10^6 sec^{-1}$ | $\log_{10}gf$ | Tolerance | Remarks |
|---|---|---|---|---|---|---|---|
| 4 | 3s $^3P$ - 4p $^3D$ | 2-3 | 5041.6 | | | | |
| | | 1-2 | 5039.0 | | | | |
| | | 0-1 | 5039.0 | .20 | -1.917 | ± 25% | (1) |
| | | 2-2 | 5049.6 | | | | |
| | | 1-1 | 5044.0 | | | | |
| 5 | 3s $^3P^\circ$ - 4p $^3S$ | 2-1 | 4826.7 | .21 | -2.657 | 25% | (2) |
| | | 1-1 | 4817.3 | .13 | -2.866 | 35% | |
| | | 0-1 | 4812.8 | < .10 | <-2.982 | --- | |
| 6 | 3s $^3P^\circ$ - 4p $^3p$ | 2-2 | 4771.7 | | | | |
| | | 1-1 | 4766.6 | | | | |
| | | 2-1 | 4775.8 | | | | |
| | | 1-0 | 4770.0 | 1.39 | -1.370 | 20% | (3) |
| | | 1-2 | 4762.4 | | | | |
| | | 0-1 | 4762.4 | | | | |
| 7 | 3s $^3P^\circ$ - 5p $^3D$ | 2-3? | 4065.1 | | | | |
| | | 1-2? | 4064.2 | < .04 | <-2.828 | --- | (2) |
| | | 0-1? | 4064.2 | | | | |
| 11 | 3s $^1P^\circ$ - 4p $^1P$ | 1-1 | 5380.2 | 1.72 | -1.650 | 15% | |
| 12 | 3s $^1P^\circ$ - 4p $^1D$ | 1-2 | 5052.1 | 1.74 | -1.478 | 10% | (4) |
| 13 | 3s $^1P^\circ$ - 4p $^1S$ | 1-0 | 4932.0 | 3.51 | -1.893 | 15% | |
| 14 | 3s $^1P^\circ$ - 5p $^1P$ | 1-1 | 4371.3 | .59 | -2.295 | 30% | (5) |
| 15 | 3s $^1P^\circ$ - 5p $^3D$ | 1-2? | 4352.1 | < .17 | -2.617 | --- | (2) |
| 16 | 3s $^1P^\circ$ - 5p $^1D$ | 1-2 | 4268.9 | .23 | -2.503 | 25% | |
| 17 | 3s $^1P^\circ$ - 5p $^1S$ | 1-0 | 4231.3 | .60 | -2.792 | 35% | (5) |
| 18 | $2p^3$ $^3D^\circ$ - 4p $^3P$ | 3-2 | 5793.5 | | | | |
| | | 2-1 | 5801.1 | .35 | -1.799 | 35% | (5) |
| | | 1-0 | 5805.7 | | | | |
| 22 | 3p $^1P$ - 4d $^1P^\circ$ | 1-1 | 6587.8 | 1.3 | -1.608 | 40% | (5) |

†Listed multiplets are effectively complete.

Remarks: (1) The large tolerance assigned these merged lines stems both from their weakness and from their diffuse appearance, which might mask blending with a predicted CI recombination feature. (2) When lines are detectable, but have marginal signal-to-noise ratios, the grainy profiles are interpreted to contain the maximum conceivable energy. (3) For a small percentage of the data, members of this multiplet could be partially resolved: to within the error limits of these observations LS coupling described the relative line strengths with the multiplet. (4) This transition was measured absolutely: all other CI transitions were measured relative to it. (5) A large tolerance attaches to these results both because the lines are weak and because relatively few films were exposed at these wavelengths.

sulfur, so Stark broadening blends the multiplet. However, a few runs in 1% $CH_4$ test gases gave electron densities not greater than $3\times10^{16}$/cc and still yielded good brightness in these lines. Under these conditions individual lines, or pairs of lines, could be resolved. To within $\pm$ 10% for the stronger lines in the multiplet, and $\pm$ 25% for the weaker ones, the relative intensities were in agreement with LS coupling predictions.

4. Check for systematic error: invariance of results with changing experimental parameters. Measured A-values should not reflect changes in experimental conditions. We now check our CI $\lambda$5052 results to see if they show any significant dependence upon source temperature T, pressure p, electron density Ne, or initial partial pressure of carbon additive. We also check for possible demixing of pre-mixed test gases and for long term variations in the apparatus.

Figure 51 shows D vs. T, D vs. p and D vs. Ne, where D is a measured CI $\lambda$5052 A-value normalized against our adopted result, $1.74\times10^6$ $sec^{-1}$. We cannot discern any significant systematic variation of D over the given ranges of T, p, or Ne. The statement $\frac{\partial D}{\partial Ne} \simeq 0$ is by no means trivial, since it indicates the following:

(i) There is no systematic error in the wing correction of CI $\lambda$5052.

(ii) There is no systematic error from readily ionized wall containments, since their relative influence on Saha equilibrium would diminish with increasing Ne.

(iii) The source plasma is behaving consistently with the assumption of L.T.E. -- that is, since free electrons

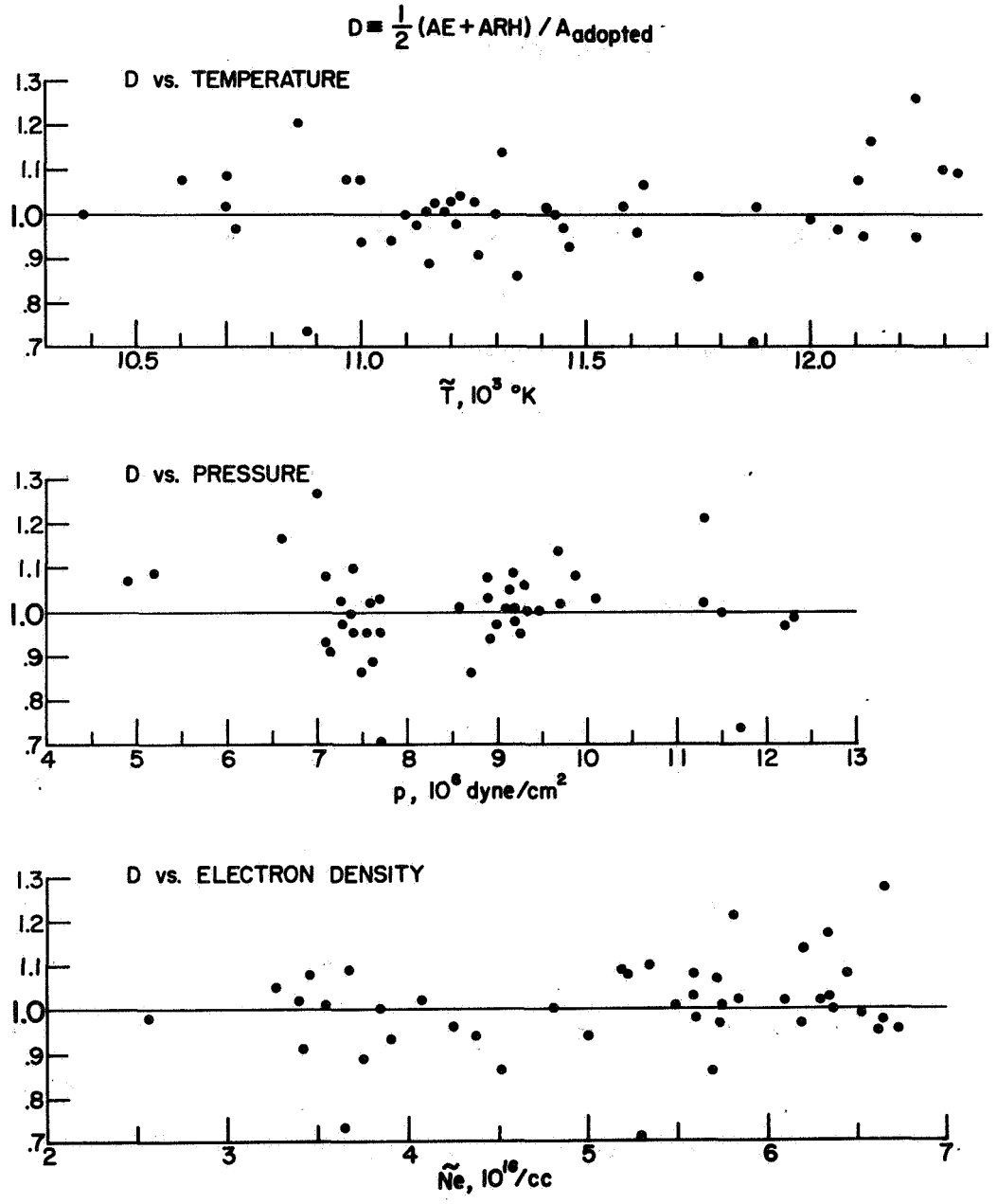


Fig. 51: Testing A-Value of CI λ5052 Results for Possible Systematic Dependance Upon Measured Thermodynamic Variables.

establish L.T.E. , a system not in L.T.E. at low electron densities should give different results from those collected at three times greater electron densities where a thermodynamic description is more valid.

In Fig. 52 different plotting points are used to distinguish between .5% $CH_4$ + .5% $CS_2$ and 1% $CH_4$ test gases. From the invariance of D under changes in partial pressure (and species) of carbon additive, we infer that our test gas compositions have neither been enriched by carbon-carrying wall contaminants (in excess of estimated impurity levels) nor have been depleted of carbon additive by adsorption or reactions prior to shock-heating. D is plotted against the order of drawing a charge of test gas from a pre-mixed batch to check for possible demixing during metering operations. That is, if significant demixing occurs at the metering valve, or in the delivery lines then that portion of a batch remaining in the storage cylinder will be enriched (or depleted) in its spectroscopic additive concentration by each succeeding run, so that runs made when the premixed batch is fresh will give lower (or higher) A-values than later runs using the same premixed batch. The plot of D versus the long term ordering of runs may be regarded as a check upon the stability of calibrated detectors. The final 10 runs do appear to group about 5% lower than preceding runs -- but in view of expected scatter this trend is of only marginal statistical significance. Its cause can be chance, some (unknown) change in the apparatus, <u>or</u> a poorly prepared test gas, since all ten runs used the same batch of pre-mixed 1% $CH_4$ in neon. There is no clear justification for rejecting them: but had they been rejected, adopted A-value would be

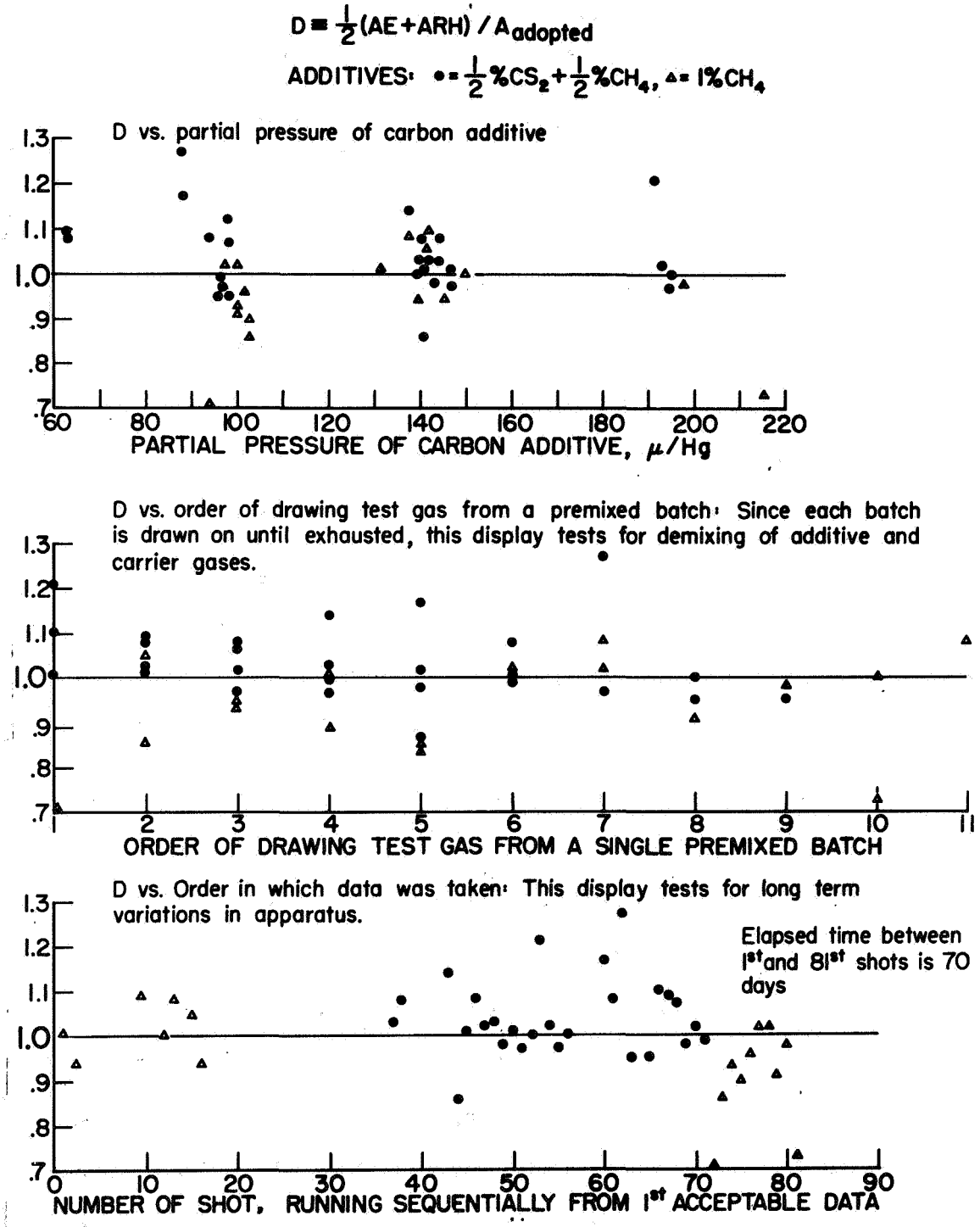


Fig. 52: Testing A-Value of CI λ5052 Results for Possible Systematic Dependance Upon Operational Variables.

shifted by no more than 1% or 2%, since the net effect of their rejection would be to eliminate the "tail" on the left side of the $A_C$(TIB) distribution shown in Fig. 8 †. From the plot of D against run number it is also noted that almost one half the final 81 runs were not used to find $A(TIB)_C$. Some of these runs were made in test gases without carbon additives, for instance to find carbon impurity levels, or to produce high level continua for in situ comparisons of the intensity calibrations for different photoelectric channels. Other runs were rendered useless by accidents in the developing of films, poor synchronization between oscilliscope sweeps and available test times, and, in a few cases, because carbon lines were not bright enough to measure.

5. Comparison between present CI results and the literature. Table V compares the present CI results with those of five previous investigations, (listed in chronological order), the predictions of the Coulomb approximation[103], and the values adopted in the NBS compilation.[13] The cited experiments employed the conventional emission (AE) method, with the exception of Doherty's[29] work which used "trans-species" relative measurement (ARH) against $H_\beta$. Thermal sources used are identified in the table. Most values given in the NBS compilation represent the results of Richter[106] normalized by a factor of 1.30 to conform with Coulomb approximations: multiplets (5) and (16) were taken from Foster[107], with a normalization factor of 1.40 applied to agree with Coulomb approximations; multiplet (14) is a Coulomb approximation. The Coulomb approximations in the last column were calculated for us by Oertel[103] using computer coded hydrogenic wave functions. When radial matrix elements are in the vicinity of a zero (cancellation) these predictions are often significantly different from those interpolated

---

†As was discussed in Chapter III, those portions of $A(TIB)_C$ distributions to the left of peak values only weakly affect selection of the adopted A-value.

TABLE V . Comparison of measured CI transition probabilities with literature values.

| Multiplet | λ(Å) | Transition probabilities $A_{mn}$ ($10^6$ sec$^{-1}$) | | | | | | | | |
|---|---|---|---|---|---|---|---|---|---|---|
| | | This experiment § | NBS adopted (1966), Ref. 13 | Experimental Average‡ | Foster (1962), Ref. [107]+ | Foster (1962), Ref. [108]+ | Doherty (1961), Ref. [29]§ | Richter (1958), Ref. [106]o | Maecker (1953), Ref. [109]o | Coulomb approx.† |
| (4) | 5041* | .20±25% | .39±50% | .27 | .134±13% | .209±7% | --- | .30±30% | .15±14% | 1.55 |
| (5) | 4826.7 | .21±25% | .47±50% | --- | .34±12% | --- | --- | --- | --- | .24 |
| | 4817.3 | .13±35% | .28±50% | | --- | --- | --- | --- | --- | .14 |
| | 4812.8 | <.10 --- | .097±50% | --- | --- | --- | --- | --- | --- | .05 |
| (6) | 4770* | 1.39±20% | 1.6±50% | 1.24 | .95±2% | 1.26±8% | 1.8±20% | 1.20±25% | .52±14% | 1.34 |
| (7) | 4064* | <.04 --- | --- | --- | --- | --- | --- | --- | --- | .12 |
| (11) | 5380.2 | 1.72±15% | 1.6±50% | 1.48 | 1.15±6% | 1.20±9% | 2.75±20% | 1.25±20% | .71±19% | 2.24 |
| (12) | 5052.1 | 1.74±10% | 1.7±50% | 1.74 | 1.27±4% | 1.61±8% | 4.20±20% | 1.30±25% | .86±13% | 1.94 |
| (13) | 4932.0 | 3.51±15% | 4.6±50% | 4.07 | 3.40±6% | 4.63±5% | 8.6±20% | 3.50±20% | 1.5±14% | 5.22 |
| (14) | 4371.3 | .59±30% | .97±50% | --- | .4 --- | --- | --- | --- | --- | 1.21 |
| (15) | 4352.1 | <.17--- | --- | --- | --- | --- | --- | --- | --- | --- |
| (16) | 4268.9 | .23±25% | .32±50% | --- | .23±8% | --- | --- | --- | --- | .41 |
| (17) | 4231.3 | .60±35% | --- | --- | --- | --- | --- | --- | --- | 1.70 |
| (18) | 5800* | .35±35% | .39±50% | .36 | --- | --- | --- | .30±30% | .17±16% | .30 Δ |
| (22) | 6587.8 | 1.3 ±40% | 2.4 ±50% | --- | --- | --- | --- | --- | --- | 2.52 |

*Blended multiplet
†Refined calculation by Oertel (private communication), see Ref. [103]
ΔAuthor's estimates from B. & D. (1949) tables
‡Normalized to current result for $C_I$ λ5052.

Cited experiments performed in emission, with sources:
oWall-stabilized arc
+Vortex-stabilized arc
§Conventional shock tube

Additional calculations for $C_I$ λ5052,

2.50-Author's estimates from B. & D. (1949) tables

in the B & D (1949) tables.[15]

For a comparison based on the strongest lines: λλ4770, λ5380.2, λ5052.1, and λ4932.0, the current results are found to average 21% higher than Richters' results, 7% less than the NBS estimates, 34% larger than the earlier of Foster's investigations, 4% larger than the average of all previous experiments and 15% less than Oertel's Coulomb approximation. It has been suggested[13] that Maecker's[109] results were strongly influenced by demixing. Doherty's[29] results for carbon average a factor of two larger than other literature values, but his results for neon average a factor of two smaller. Since both elements were measured relative to $H_\beta$, both discrepancies would result[†] if his source temperatures, deduced from incident shock speeds, were 10% too high.

While elaborate precautions were taken to insure a reliable absolute A-value for CI λ5052, our results for other CI lines relative to λ5052 are based on quite conventional relative intensity measurements. All but the weakest CI lines we measure originate in upper levels between 9.9 and 10.2 eV, so relative A-values depend essentially upon relative intensities. There is no obvious reason to correlate the reliability of an author's relative A-values with the reliability of his absolute scale. Comparison of the relative A-values of the different investigators does not offer clear statistical grounds (cf. Table V) for favoring certain results or rejecting others.

For the sake of argument we suppose all authors measured relative A-values with equivalent accuracy and regard the average of their results to be the most reliable set available. Normalized to the current

---

[†]Figure 5 can be used to verify this assertion.

result for CI λ5052, this set of A-values appears in the fifth column of Table V . Current results agree with this set about as well as they do with NBS estimates: in both cases agreement is within our stated tolerances except for λ4932.

E. SI And SII Transition Probabilities

1. Introduction. The spectrum of SI has few visible lines, with those strong enough for us to measure with reasonable precision (say, those with $A_{mn} > 10^5 sec^{-1}$) confined to the three multiplets λλ4695, λλ5278, and λλ6752, all of which are blended in our spectra. The appearance of λλ4695 and λλ5278 in Fig. 53 is typical of first reflected shocks using .5% $CH_4$ + .5% $CS_2$ additives. The Grotian diagram for these lines is Fig. 54 .

In contrast, SII has a rich visible spectrum. Because A-values are of order $10^8$ $sec^{-1}$, many SII lines, including several intercombination lines, appear with good brightness when source temperatures exceed 11,000°K. Fig. 53 shows the typical SII spectrum from a multiply reflected shock in neon containing .5% $CS_2$ + .5% $CH_4$ . Less than 10% of the lines are blended.

2. Design, execution, and reduction of data runs. Twenty-seven of the thirty-one shocks used to study sulfur employed .5% $CH_4$ + 5% $CS_2$ test gases, permitting simultaneous study of CI , SI , and SII . A single drum camera recording covering the range 4600Å - 5700Å contains nearly all strongest visible lines of these three spectra. Four additional runs used .25% $CH_4$ + 75% $CS_2$ test gases. The pressure-temperature regime is given in Table II . Measurement of thermodynamic variables was discussed in the section on CI .

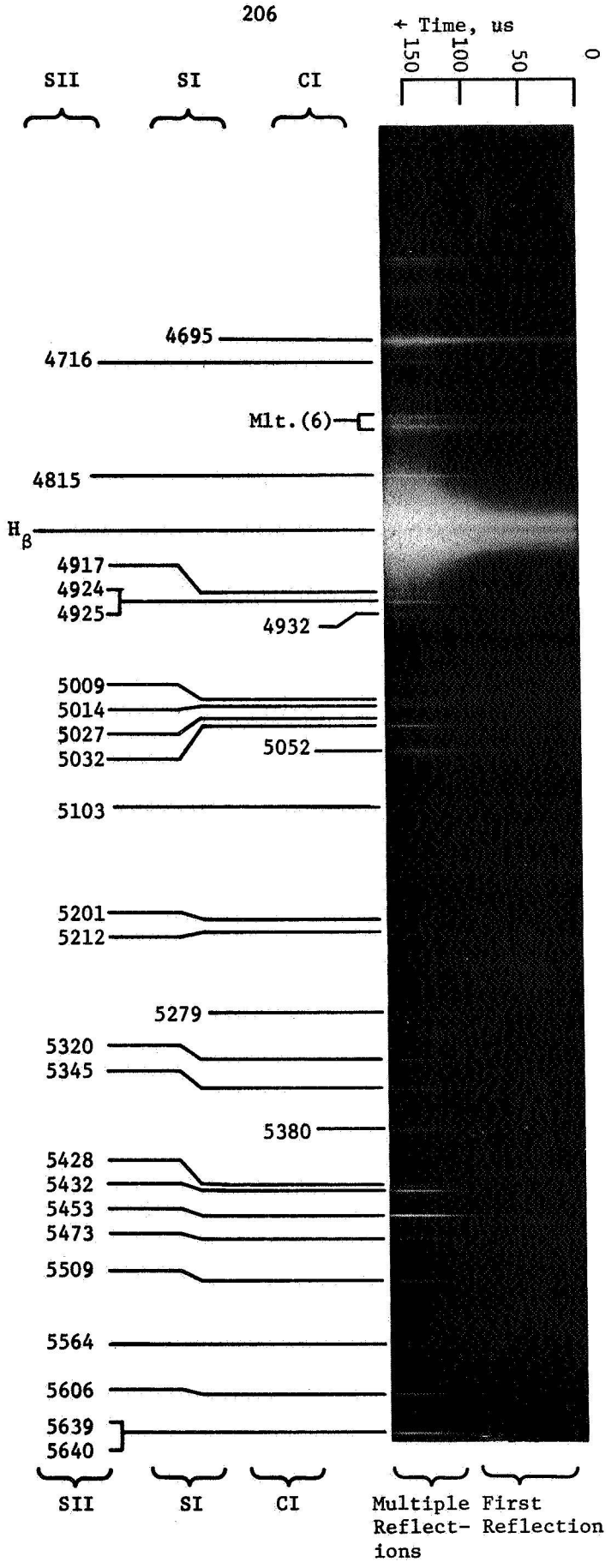


Fig. 53: Time-Resolved Spectrogram of Shock in ½% $CH_4$ + ½% $CS_2$ + 99% Neon .

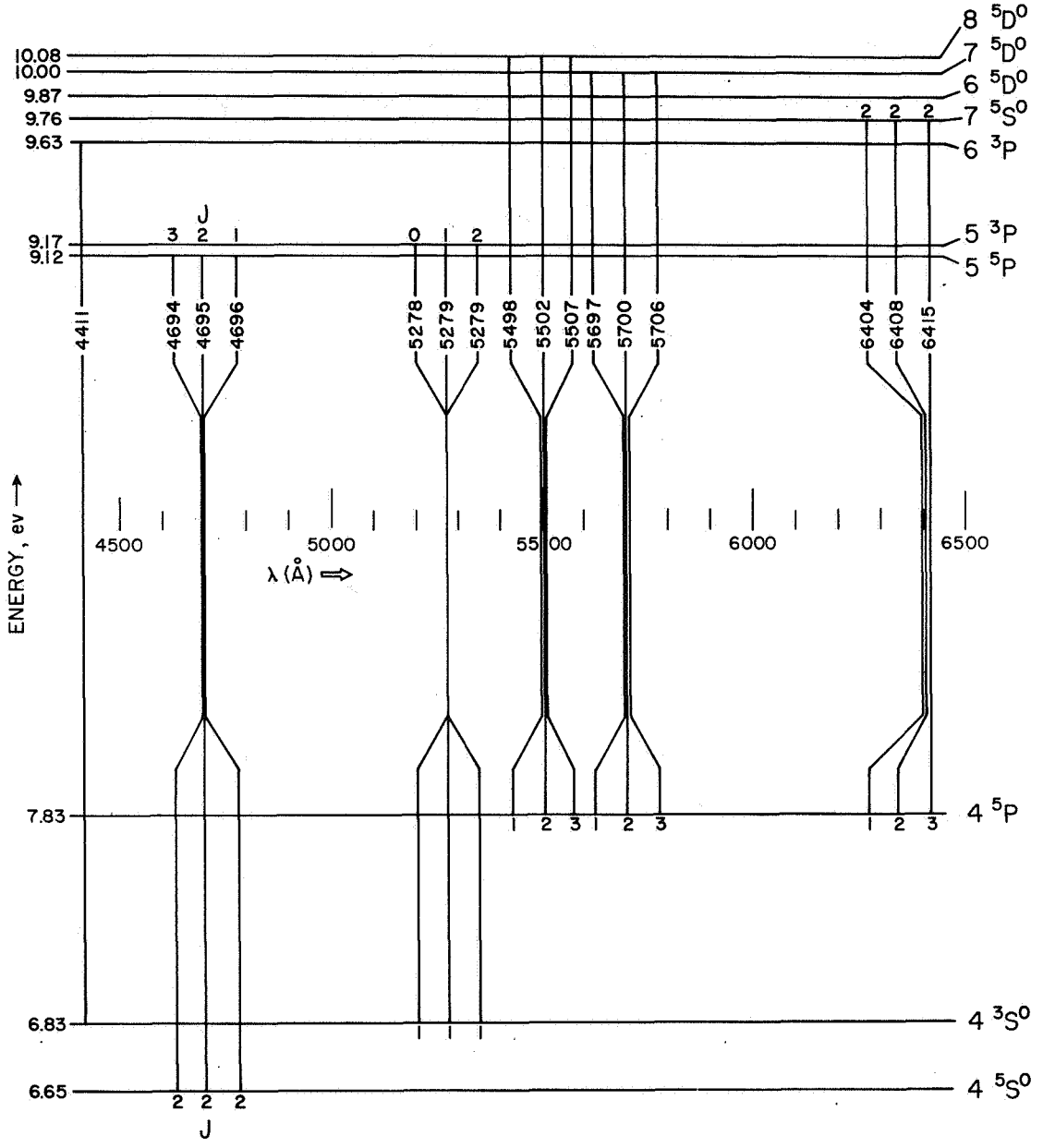


Fig. 54: Grotrian Diagram For SI Lines Currently Studied.

A zero impurity concentration of sulfur (from wall contaminants) was assumed because no SII lines were detected in pure neon plasmas at 13,000°K.

The blended multiplet λλ4695 was selected to be the absolutely measured "line" for SI because its proximity to $H_\beta$ and its greater brightness offer better chances for an accurate A-value determination than do other SI features between 4600Å and 6700Å. Unlike CI λ5052, whose absolute integrated intensity was measured two independent ways ($R_c$ and $R_C^*$), λλ4695 relies entirely on $R_S^*$, that is, the photographic intensity in arbitrary units scaled to absolute intensity by fitting to several absolutely calibrated photoelectric (SQUID) channels. Since the SQUID scans the red half of $H_\beta$, any systematic errors in relative photographic intensity as a function of wavelength carry over directly into the absolute integrated line intensities measured anywhere but at 4850 - 4900Å. For this reason proximity to $H_\beta$ is important, both when a transition probability is measured relative to $H_\beta$ (an ARB - value) and when it is measured in absolute emission (an AE - value).

In Chapter III we showed that $A(TIB)_S = \frac{1}{2}\cdot(AE_S + ARH_S)$ is less sensitive to thermal error in the region 9,500°K < T < 11,600°K than either $AE_S$ or $ARH_S$ alone, while for T > 11,600°K $AE_S$ has the least thermal sensitivity. Because many of the data runs were made at temperatures around 11,600°K (cf. Fig. 43 ) where neither $AE_S$ nor $\frac{1}{2}(AE_S + ARH_S)$ affords the desired degree of freedom from thermal errors, the transition probability for SI λλ4695 was taken to be:

$$A(TIB)_S \equiv \frac{1}{4}(2AE_S + ARH_S + ARC_S)$$

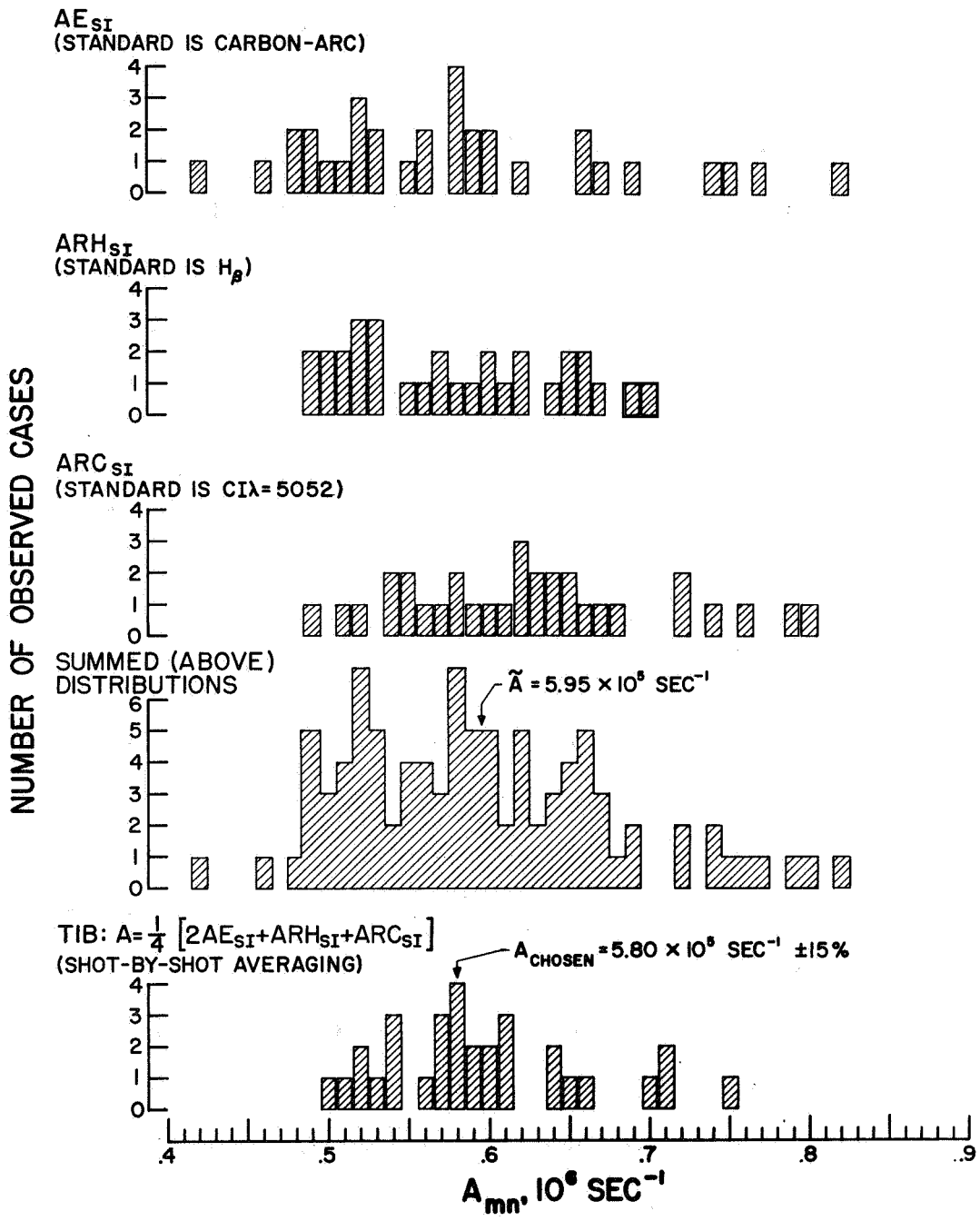


Fig. 55: Results for the Absolute A-Value of the Blended SI Multiplet, λλ4695 .

where $ARC_S$ is the SI λλ4695 transition probability measured relative to the CI λ5052 transition probability. We use our adopted value, $1.74\times10^6$ $sec^{-1}$ for CI λ5052. Although $ARC_S$ thus inherits the ± 10% tolerance of the new internal standard, CI λ5052, we feel this is compensated for by the thermal insensitivity of $\frac{1}{2}(ARC_S + AE_S)$, shown in Fig. 14. Lest it be suggested that the A-values of SI λλ4695 and CI λ5052 are not independent because they are measured simultaneously, we recall that 17 data runs used 1% $CH_4$ additives (no sulfur present), and that Fig. 52 showed $\tilde{D}$ for these runs agree to within 5% with the $\tilde{D}$ for 27 runs using .5% $CH_4$ + .5% $CS_2$ additive.

$AE_S$, $ARH_S$, $ARC_S$ and $A(TIB)_S$ values for 31 runs are displayed in Fig. 55. Here, as with CI λ5052, the TIB combination of independent A-value determinations gives a tighter distribution than do any of component determinations ($AE_S$, etc.) by themselves. The peak of the $A_S(TIB)$ distribution cannot be so easily identified here as for $A_C(TIB)$ (cf. Fig. 8), so we assign to the adopted value of $.58\times10^6$ $sec^{-1}$ a ± 15% tolerance rather than the ± 10% assigned to CI λ5052. There appears to be no significant systematic difference between the averages of the $AE_S$, $ARH_S$, $ARC_S$ results.

The absolutely measured SII transition is λ5453.8. This brightest of isolated SII lines was strong enough to measure in more than half of the first reflected shocks, and did not become optically thick in multiply reflected shock regions. The relative (to λ5453) A-values of 44 other SII lines were measured almost exclusively in multiply reflected shocks because the extra 500°K to 1000°K in these regions enchanced line intensities by factors of 3 - 4 with respect to first reflected shock regions, where they were usually too faint to measure well.

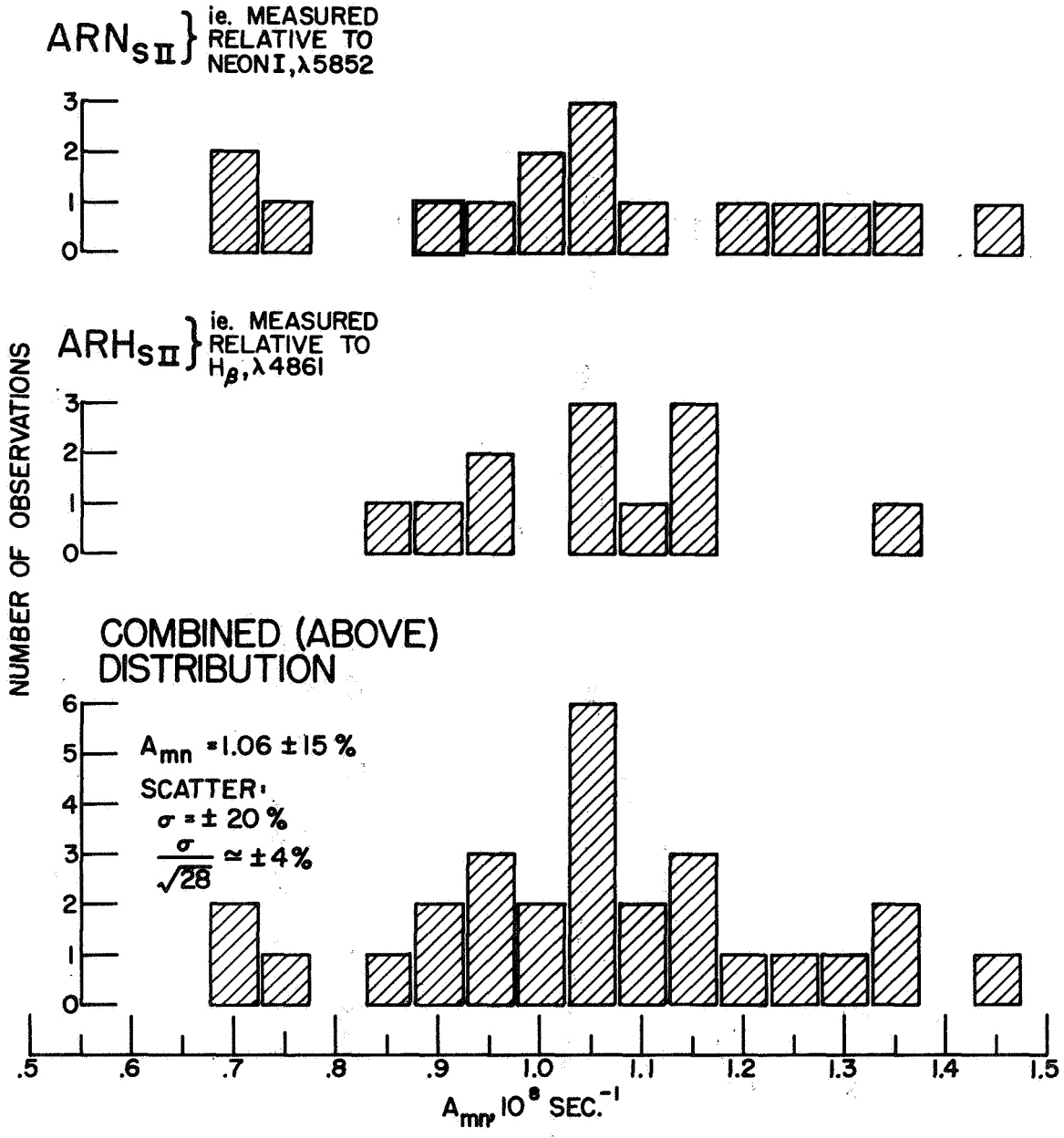


Fig. 56: Results for the Absolute A-Value of SII λ5453 .

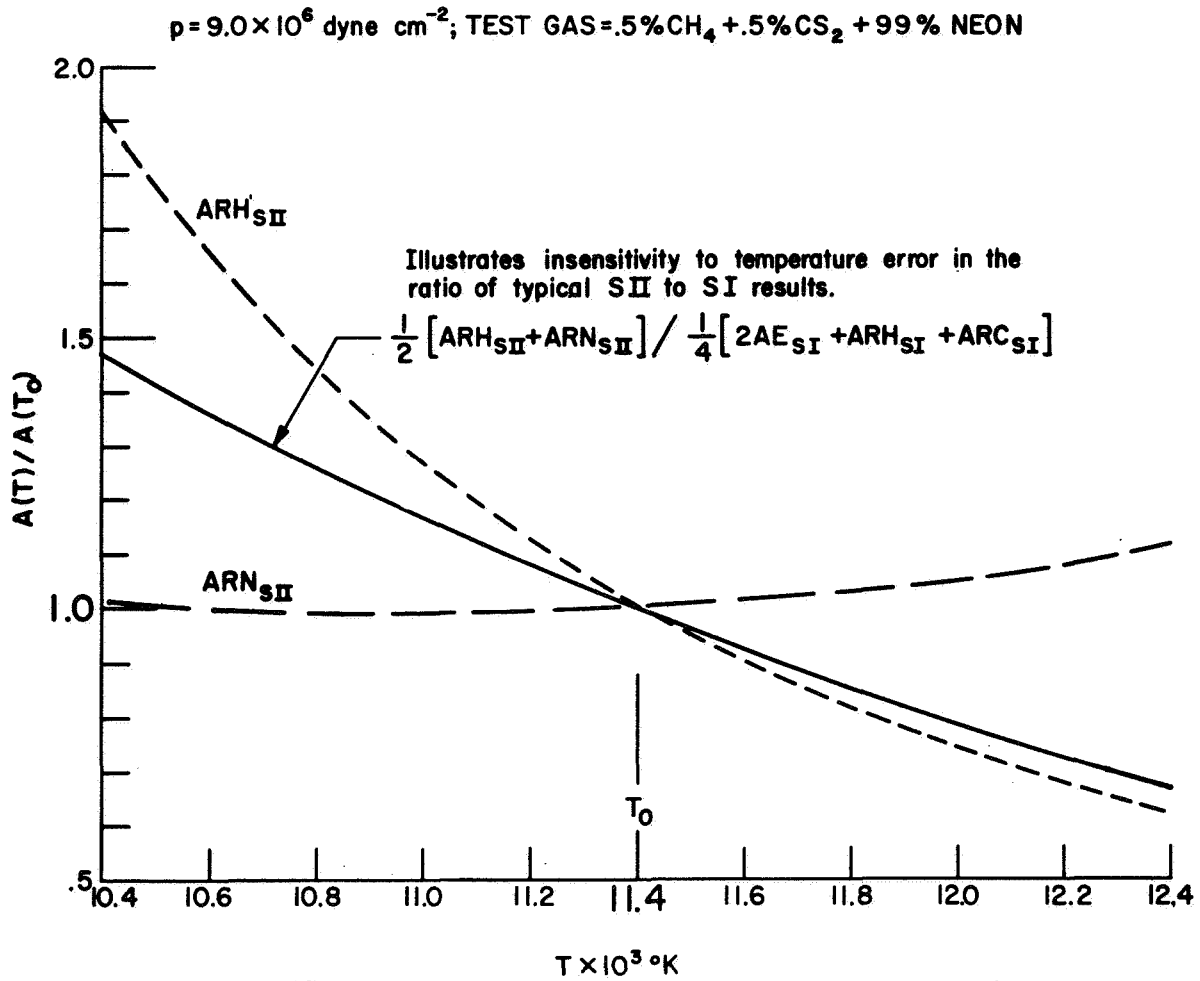


Fig. 57: Relative Thermal Error in the A-Value of SII 5453 Measured Two Ways, and, Relative Thermal Error in the Ratio of TIB Results for SII λ5453 Relative to TIB Results for SI λλ4695 .

In Chapter III we suggested two ways to measure the SII λ5453 absolute A-value:

$ARN_{SII}$ = A-value of SII λ5453 measured relative to NeI λ5852 ,

$ARH_{SII}$ = A-value of SII λ5453 measured relative to $H_\beta$ .

Relative errors propagated into these results as a function of temperature error is given in Fig. 57 . Both methods should have equivalent accuracy: $\frac{\partial}{\partial T} |\log ARN_S|$ is less than $\frac{\partial}{\partial T} |\log ARH_S|$ , but the A-values of $H_\beta$ and Ne λ5852 are good to ± 1% and ± 10%, respectively. Results from 16 determinations of $ARN_{SII}$ and 13 determinations of $ARH_{SII}$ are shown in Fig. 56 . Since we see no reason to favor either of these trans-species relative measurements, we adopt the average of all determinations, $1.06\times10^8$ $sec^{-1}$, as giving the most reliable result.

3. Results. Current results for 8 blended SI multiplets and 45 isolated visual lines of SII are presented in Tables VI and VIII, respectively.

4. Checks for internal consistency. The mutual agreement (cf. Fig. 55 ) between the three sets of results for SI λλ4695, $AE_S$ , $ARH_S$ , $ARC_S$ can be regarded as a mutual agreement between results of three independent experiments. Although they rely on simultaneously observed data, each of these three results has its own distinct thermal dependence and derives from a different combination of photometric variables. In particular, $AE_S$ depends upon absolute concentrations and absolute intensities

Table VI TRANSITION PROBABILITIES

FOR MERGED† SI MULTIPLETS

| Multiplet | Transition (n, lower)(m, upper) | λ(Å)** | Amn* $10^6 sec^{-1}$ | $\log_{10} gf$ | Tolerance | Remarks |
|---|---|---|---|---|---|---|
| 2 | $4\ ^5S^\circ - 5\ ^5P$ | 4695 | .58 | -1.541 | ± 15% | (1) |
| 4 | $4\ ^3S^\circ - 5\ ^3P$ | 5278 | .33 | -1.906 | 20% | |
| 5 | $4\ ^3S^\circ - 6\ ^3P$ | 4411 | <.04 | <-2.98 | --- | |
| •• | $4s\ ^3S^\circ - 4p\ ^3P$ | 4154 | .18 | -2.378 | 45% | (2) |
| 8 | $4\ ^5P - 5\ ^5D^\circ$ | 6752 | 6.0 | .0108 | 35% | (3) |
| 10 | $4\ ^5P - 6\ ^5D^\circ$ | 6049 | <.18 | <-1.56 | --- | |
| 11 | $4\ ^5P - 7\ ^5D^\circ$ | 5701 | <.07 | <-2.07 | --- | |
| 12 | $4\ ^5P - 8\ ^5D^\circ$ | 5503 | <.04 | <-2.34 | --- | |

†Range of electron densities; $5 < Ne < 12 \times 10^{16}/cc$ .

**Approximate wavelength of peak intensity.

*For merged multiplets: $A_{mn} = \sum_J g_J A_J/(2L + 1)(2S + 1)$ .

•• Multiplet given by Frerichs (1933).

Remarks: (1) This multiplet measured absolutely; other SI multiplets measured relative to it. (2) Several lines of SII are superimposed on this multiplet, their interference being approximately compensated for. (3) This is a strong, well-defined feature, the accuracy of the A-value being degraded (to ± 35%) because only two observations were made.

Table VII. COMPARISON OF MEASURED SI TRANSITION PROBABILITIES WITH LITERATURE VALUES.

| Multiplet | λλ(Å) | Transition probability for blended multiplets, $10^6 sec^{-1}$ | | | | |
|---|---|---|---|---|---|---|
| | | This experiment | Bridges *et al.* (1967), Ref.[25] | Foster (1967), Ref.[26] | Coulomb approximation | NBS adopted (1968), Ref.[13] |
| (2) | 4695 | .58 ± 15% | 1.03 ± 30% | .583 ± 4% | 2.01°<br>1.22°† | .78 |
| (4) | 5279 | .33 ± 20% | .54 ± 30% | .350 ± 4% | .88°° | .38 |
| (5) | 4411 | <.04 -- | --- | --- | --- | --- |
| † | 4154 | .18 ± 45% | --- | .796 ± 4% | --- | --- |
| (8) | 6752 | 6.0 ± 35% | 11.0 ± 35% | --- | 7.5* | 7.9 |
| (10) | 6409 | <.18 -- | --- | --- | --- | --- |
| (11) | 5701 | <.07 -- | --- | --- | --- | --- |
| (12) | 5503 | <.04 -- | --- | --- | --- | --- |

†Multiplet identified by Frerichs, (1933), Ref. [131].

°† Calculation by Oertel (private communication): see Ref.[103].

°° Estimate by Goldberg *et al.* (1960), Ref. [3].

* Author's estimates from Bates and Damgaard (1949) tables.

Table VIII. TRANSITION PROBABILITIES FOR SII

| Multiplet | Transition (n, lower)(m, upper) | $J_n$-$J_m$ | λ(Å) | Amn $10^8 sec^{-1}$ | $log_{10}gf$ | Tolerance | Remarks |
|---|---|---|---|---|---|---|---|
| 1* | 3s $3p^4$ $^2P$ - 4p $^2S°$ | 1½-½ | 5027.1 | .30 | - .643 | ± 20% | |
| | | ½-½ | 5142.3 | .25 | - .703 | 25% | |
| 6* | 4s $^4P$ - 4p $^4D°$ | 2½-3½ | 5453.6 | 1.06 | + .578 | 15% | (1) |
| | | 1½-2½ | 5432.7 | .84 | + .348 | 15% | |
| | | ½-1½ | 5428.6 | .50 | - .054 | 15% | |
| | | 2½-2½ | 5564.9 | .23 | - .193 | 20% | |
| | | 1½-1½ | 5509.6 | .57 | + .016 | 15% | |
| | | ½-½ | 5473.6 | 1.11 | - .001 | 15% | |
| | | 2½-1½ | 5645.6 | .17 | - .488 | 30% | |
| | | 1½-½ | 5556.0 | .28 | - .587 | 35% | |
| 7* | 4s $^4P$ - 4p $^4P°$ | 2½-2½ | 5032.4 | .69 | + .196 | 20% | |
| | | 1½-1½ | 4991.9 | .29 | - .363 | 20% | |
| | | ½-½ | 4942.4 | .22 | - .793 | 25% | |
| | | 2½-1½ | 5103.3 | .44 | - .163 | 20% | |
| | | 1½-½ | 5009.5 | .73 | - .260 | 20% | |
| | | 1½-2½ | 4924.0 } | .29 | + .023 | 20% | |
| | | ½-½ | 4925.3 } | | | | |
| 8 | 4s $^4P$ - 4p $^2DP$ | 2½-2½ | 4779.1 | <.06 | <- .909 | --- | |
| 9* | 4s $^4P$ - 4p $^4S°$ | 2½-1½ | 4815.5 | .78 | + .035 | 20% | |
| | | 1½-1½ | 4716.2 | .26 | - .460 | 20% | |
| | | ½-1½ | 4656.7 | .16 | - .682 | 35% | |
| 10* | 4s $^4P$ - 4p $^2P°$ | ½-1½ | 4193.5 | <.11 | <- .936 | --- | |
| 11 | 3d $^4F$ - 4p $^4D°$ | 4½-3½ | 5606.1 | .38 | + .156 | 20% | |
| | | 3½-2½ | 5640.3 | .39 | + .047 | 30% | |
| | | 2½-1½ | 5659.9 | .45 | - .063 | 20% | |
| | | 1½-½ | 5664.7 | .52 | - .301 | 20% | |
| | | 3½-3½ | 5526.2 | .11 | - .395 | 25% | |
| | | 2½-2½ | 5578.8 | .10 | - .553 | 20% | |
| | | 1½-1½ | 5616.8 | .11 | - .682 | 35% | |
| | | 1½-2½ | 5536.7 | .09 | - .605 | 30% | |
| | | 2½-3½? | 5466.5 | .02 | -1.145 | --- | |
| 14 | 4s $^2P$ - 4p $^2D°$ | 1½-1½ | 5819.2 | .11 | - .651 | 40% | |
| | | ½-1½ | 5646.9 | .57 | + .037 | 40% | |
| | | 1½-2½ | 5639.9 | .68 | + .289 | 40% | |
| 15 | 4s $^2P$ - 4p $^2P°$ | 1½-1½ | 5014.0 | .72 | + .036 | 20% | |
| | | ½-½ | 4917.1 | .42 | - .516 | 25% | |

(Table Continued)

*Measurement secured for all members of multiplet.

Remarks: (1) this transition measured absolutely: other SII transitions are measured relative to it.

Table VIII. (continued)

| Multiplet | Transition (n, lower)(m, upper) | $J_n-J_m$ | λ(Å) | Amn $10^8 sec^{-1}$ | $log_{10}gf$ | Tolerance | Remarks |
|---|---|---|---|---|---|---|---|
| 32 | $3d\ ^2P - 4p'\ ^2D°$ | 1½-½ | 4431.0 | <.10 | <- .75 | ---- | (4) |
| 36 | $3d\ ^2D - 4p'\ ^2D°$ | 2½-2½ | 4668.5 | <.20 | <- .41 | ---- | (4) |
| | | 1½-1½ | 4648.1 | <.30 | <- .41 | ---- | (4) |
| 38* | $4s'\ ^2D - 4p'\ ^2F°$ | 2½-3½ | 5320.7 | 1.05 | + .552 | ± 15% | |
| | | 1½-2½ | 5345.6 | 1.12 | + .459 | 15% | |
| 39 | $4s'\ ^2D - 4p'\ ^2D°$ | 2½-2½ | 5212.6 | .96 | + .370 | 20% | |
| | | 1½-1½ | 5201.0 } | .76 | + .091 | 20% | |
| | | 2½-1½ | 5201.3 } | | | | |
| 40 | $4s'\ ^2D - 4p'\ ^2F°$ | 2½-1½ | 4524.9 } | 1.04 | + .106 | 30% | |
| | | 1½-1½ | 4524.6 } | | | | |
| 43 | $4p\ ^4D° - 5s\ ^4P$ | 3½-2½ | 4463.5 | .74 | + .123 | 45% | |
| | | 2½-1½ | 4483.4 | .42 | - .296 | 45% | |
| | | 1½-½ | 4486.6 | .90 | - .265 | 45% | |
| 44 | $4p\ ^4D° - 4d\ ^4F$ | 2½-3½ | 4153.1 | 1.27 | + .418 | 40% | |
| | | ½-1½ | 4142.3 | .65 | - .173 | 40% | |
| | | 1½-2½ | 4145.1 | .70 | + .035 | 40% | |
| 45 | $4p\ ^4D° - 4d\ ^4D$ | 1½-1½ | 3963.1 | 1.05 | - .006 | 40% | |
| | | 3½-3½ | 4028.8 | .31 | - .220 | 40% | |
| 46 | $4p\ ^4P° - 5s\ ^4P$ | 2½-2½ | 4792.0 | 1.08 | + .348 | 30% | |
| 49 | $4p\ ^4P° - 4d\ ^4D$ | 2½-3½ | 4294.5 | .31 | - .164 | 40% | |
| | | ½-½ | 4278.5 | .67 | - .435 | 40% | |
| 61 | $4p\ ^2P° - 5s\ ^2P$ | ½-½ | 5518.7 | <2.6 | <+ .376 | --- | (4) |
| 64 | $4p'\ ^2F° = 4d'\ ^2F$ | 2½-3½ | 4174.0 | 2.9 | .783 | 40% | |

*Measurement secured for all members of multiplet.

Remarks: (4) Upper limit estimates are given for lines which are detectable but not measurable to better than ±50 tolerance.

while $ARH_S$ and $ARC_S$ depend on relative concentrations and relative intensities.

The two sets of independent results for SII λ5453, $ARN_{SII}$ and $ARH_{SII}$, also agree to within mutual tolerances (cf. Fig.56 ). While both of these results are deduced from relative intensity measurements and rely on relative concentrations, they have quite different dependence on source temperature (cf. Fig.57 ).

Results from the 4 runs employing .25% $CH_4$ + .75% $CS_2$ + 99% neon test gases agreed to within joint tolerance with the results from the 31 runs employing .5% $CH_4$ + .5% $CS_2$ + 99% neon test gases.

Because $CS_2$ is an organic solvent, we were concerned that it might be adsorbed onto the thin film of hydrocarbon residue on the shock tube walls prior to firing. Even though partial pressures of $CS_2$ admitted to the tube were much less than $CS_2$ vapor pressures at ambient temperature, we decided to check our results for evidence of $CS_2$ adsorption.

In Fig.58 the independent variable is the ratio of actual initial partial pressure of $CS_2$ to the initial partial pressure of $CS_2$ based on the assumption of no adsorption of $CS_2$ subsequent to filling the shock tube: i.e., if ½ of the $CS_2$ is actually adsorbed, the value of this ratio is 0.5. For test gases composed of .5% $CH_4$ + .5% $CS_2$ (assumed) + 99% neon, two pairs of results would change in opposite directions if adsorption occured: the ratio of the two SI λλ4695 A-values, $ARC_S/ARH_S$ would increase with adsorption while the ratio of electron density deduced from the $H_\beta$ halfwidth to the electron density deduced from Saha equilibrium and measured pressure and temperature, $Ne(\lambda_{\frac{1}{2}} \text{ of } H_\beta)/Ne(p,\tilde{T})$ , would decrease.

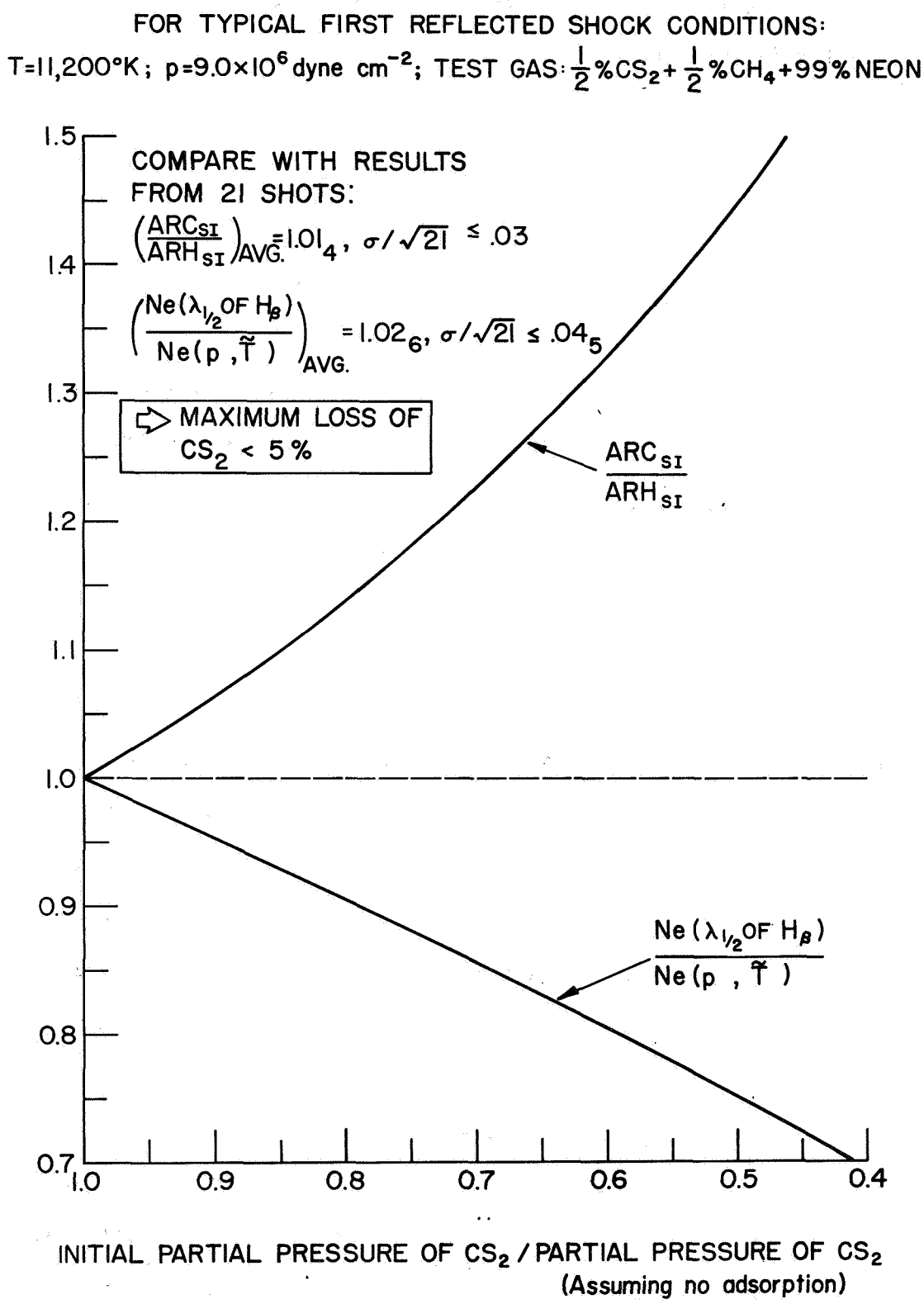


Fig. 58: Discrepancies that Would Result From Unrecognized Loss (Adsorption) of $CS_2$ .

Using results from 21 runs where all four of these results were available, we find:

$$[ARC_S/ARH_S]_{avg} = 1.01_4 \pm .03$$

$$[Ne(\lambda_{\frac{1}{2}} \text{ of } H_\beta)/Ne(p,\tilde{T})] = 1.02_6 \pm 045 \ .$$

Fitting these averaged results to Fig. 58 , we obtain in both cases that not more than 5% $CS_2$ could have been lost through adsorption.

5. <u>Comparison of current SI and SII results with literature values</u>. Current results for SI are compared in Table VII with various predictions from the hydrogenic model and with results from two previous investigations[25,26].

With the exception of λλ4154, there is a better than 10% mutual agreement in relative A-values between all three experiments. If Foster's value for λλ4154 were correct, this multiplet would appear comparable in strength to λλ4695 , whereas we observe it to be scarcely 1/5 as strong. The origin of this discrepancy is obscure: several SII lines are superimposed on λλ4154 , but they are too weak to substantially change its A-value even if all their intensities were attributed to the underlying SI multiplet.

In absolute value, our results average a factor of .6 less than Bridges', thus slightly exceeding mutually claimed tolerances. We are within 3% of agreement with Foster for λλ4695 . A substantial fraction of Bridges' 30% tolerance is intended to cover uncertainty in the extent $SO_2$ is demixed in his wall-stabilized arc. Had he assumed no demixing,

his SI results would agree to within 5% with those of Foster and the present study. Foster relied on the turbulence in his vortex-stabilized arc to prevent demixing of $SO_2$ $C\ell_2$ -- but arc column wobble introduced uncertainty into his absolute intensity measurements. To guard against large systematic errors he therefore measured four OI lines† as a rough control on his results: these OI transition probabilities average about 15% high with respect to values adopted by Wiese[13] et al.

As Bridges points out, the Coulomb approximation is not expected to be particularly reliable for the SI configurations involved. For λλ4695 and λλ5279 the Coulomb approximation is, in fact, particularly unreliable because the radial matrix elements nearly cancel. This places critical dependence on details of the assumed radial wave functions. Cancellation is much less pronounced for SI λλ6752 : for this multiplet the current result falls 16% below the Coulomb prediction, $7.6\times10^6$ $sec^{-1}$ , while Bridges' result is a factor of 40% too large.

Current results for SII absolute transition probabilities are compared with Coulomb approximations, the NBS adopted values and the sole previous experimental study (Bridges and Wiese)[25] in Table IX .

For 15 out of the 16 lines common to both experiments there is agreement to well within joint tolerances. For λ5453, the most accurately measured line in both studies, the absolute A-values agree to 6%, while 12 out of 16 determinations agree to 20% or better.

Both sets of results average a factor of 1.3 higher than Coulomb predictions. Bridges points out on the one hand that these SII

---

†Foster's source temperatures were deduced from the absolute intensities of several CℓI lines. For the A-values of these lines he used the straight mean of his own previous results with those of Hey. These average A-values agree to within a few per cent of those obtained recently by Bengtson[51] in his extensive study of the halogens.

Table IX. COMPARISON OF MEASURED S II TRANSITION PROBABILITIES WITH LITERATURE VALUES.

| Multi-plet | λ(Å) | $A_{mn}$, $10^8 sec^{-1}$ | | |
|---|---|---|---|---|
| | | This experiment | Bridges et al. (1967), Ref.[25] | Coulomb approx. |
| ( 1) | 5027.1 | .30 ± 40% | .36 ± 40% | |
| | 5142.5 | .25 ± 40% | --- | |
| ( 6) | 5453.61 | 1.06 ± 15% | 1.00 ± 35% | .78† |
| | 5432.7 | .84 ± 15% | .78 ± 35% | .55† |
| | 5428.6 | .50 ± 15% | .50 ± 35% | .33† |
| | 5564.9 | .23 ± 20% | .20 ± 35% | .22† |
| | 5509.6 | .57 ± 15% | .46 ± 45% | .40† |
| | 5473.6 | 1.11 ± 15% | .86 ± 35% | .64† |
| | 5645.6 | .17 ± 30% | --- | .036† |
| | 5556.0 | .28 ± 35% | --- | .12† |
| ( 7) | 5032.4 | .69 ± 20% | .87 ± 35% | .69 |
| | 4991.9 | .29 ± 20% | --- | --- |
| | 4942.4 | .22 ± 25% | --- | --- |
| | 5103.3 | .44 ± 20% | --- | --- |
| | 5009.5 | .73 ± 20% | --- | --- |
| | 4924.0<br>4925.3 | .29 ± 20% | --- | --- |
| ( 8) | 4779.1 | <.06 -- | --- | --- |
| ( 9) | 4815.5 | .78 ± 20% | .94 ± 35% | .57 |
| | 4716.2 | .26 ± 20% | .34 ± 35% | .40 |
| | 4656.7 | .16 ± 35% | --- | |
| (10) | 4193.5 | <.11 -- | --- | --- |
| (11) | 5606.1 | .38 ± 20% | .40 ± 35% | .19 |
| | 5659.9 | .45 ± 20% | .43 ± 45% | .16 |
| | 5664.7 | .52 ± 20% | .48 ± 35% | .20 |
| | 5526.2 | .11 ± 25% | --- | --- |
| | 5578.8 | .10 ± 20% | --- | --- |
| | 5616.6 | .11 ± 35% | --- | --- |
| | 5536.7 | .09 ± 30% | --- | --- |
| | 5466.5 | <.02 -- | --- | --- |
| | 5640.3 | .39 ± 30% | --- | --- |
| (14) | 5646.9 | .57 ± 40% | --- | --- |
| | 5639.9 | .58 ± 40% | --- | --- |
| | 5819.2 | .11 ± 40% | .12 ± 40% | .16 |
| (15) | 5014.0 | .72 ± 20% | --- | --- |
| | 4917.1 | .42 ± 20% | --- | --- |
| (32) | 4431.0 | <.10 -- | --- | --- |
| (33) | 4668.5 | <.20 -- | --- | --- |
| | 4648.1 | <.30 -- | --- | --- |
| (38) | 5320.7 | 1.05 ± 15% | 1.16 ± 35% | .85 |
| | 5345.6 | 1.12 ± 15% | 1.15 ± 35% | .78 |
| (39) | 5212.6 | .96 ± 20% | --- | --- |
| | 5201.0<br>5201.3 | .76 ± 20% | --- | --- |
| (40) | 4524.9<br>4526.6 | 1.0 ± 30% | --- | --- |
| (43) | 4463.5 | .74 ± 45% | --- | --- |
| | 4483.4 | .42 ± 45% | --- | --- |
| | 4486.6 | .90 ± 45% | --- | --- |
| (44) | 4153.1 | 1.27 ± 40% | --- | --- |
| | 4142.3 | .65 ± 40% | --- | --- |
| | 4145.1 | .70 ± 40% | --- | --- |
| (45) | 3963.1 | 1.05 ± 40% | --- | --- |
| | 4028.8 | .31 ± 40% | --- | --- |
| (46) | 4792.0 | 1.08 ± 30% | --- | --- |
| (49) | 4294.5 | .31 ± 40% | --- | --- |
| | 4278.5 | .67 ± 40% | --- | --- |
| (61) | 5518.7 | <2.6 -- | --- | --- |
| (64) | 4174.0 | 2.9 ± 40% | --- | --- |

†Calculation by Oertel (private communication), see Ref [103].

transitions should be regarded as only "moderately excited" (so Coulomb predictions should, by the general criteria,[15] be only "moderately" reliable); yet on the other hand he points out that for the same classes of transitions in OII (analogous optical electron configurations) theoretical and experimental results generally agree to within 25%.

Measured relative strengths for some lines of the 4s-4p transition array are compared with LS coupling predictions and Garstang's[110] intermediate coupling predictions in Table X . In this display, adopted from Bridges and Wiese, all data are normalized to the Coulomb approximation line strength for SII λ5453.8. Our results follow roughly the same pattern recognized by Bridges: lines of multiplet (6) appear to obey intermediate coupling more closely than LS coupling, while the other multiplets show no discernible conformity to either type of coupling.

We now consider the dilemma posed by our 6% agreement with Bridges' SII results and our factor of .6 disagreement with SI results. Error in source temperature and error in total sulfur (SI + SII) number density must work in concert to produce this pattern of agreement and disagreement. Error confined to the total number density of sulfur can only scale the A-values of SI and SII at essentially the same rates. Since SII lines have more than ten times the thermal sensitivity of SI lines (cf. Fig. 5 ), only the A-values of SII will be appreciably affected by temperature errors of a few per cent. Since it is the SII results which agree, and the SI results which disagree, temperature errors alone cannot be at fault. (The excellent agreement of SI relative A-values and SII relative A-values obviously rules out relative intensities as the source of error.)

Consider the susceptibility of the <u>two experiments to combined error in temperature and sulfur concentration</u>. In Bridges' arc, thermal

Table X. COMPARISON OF MEASURED SII LINE STRENGTHS TO STRENGTHS PREDICTED BY LS COUPLING AND INTERMEDIATE COUPLING†.

| Multiplet | λ(Å) | This experiment | Bridges and Wiese | Intermediate coupling* | LS coupling |
|---|---|---|---|---|---|
| (6) | 5453.8 | 50.2 -- | 50.2 | 50.2 | 50.2 |
| | 5432.8 | 29.5 ± 5% | 29.0 | 29.2 | 26.1 |
| | 5428.6 | 11.7 ± 5% | 12.4 | 11.9 | 10.3 |
| | 5564.9 | 8.7 ± 12% | 8.0 | 8.1 | 11.3 |
| | 5509.7 | 13.7 ± 8% | 11.7 | 12.2 | 13.3 |
| | 5473.6 | 13.1 ± 9% | 10.8 | 10.7 | 10.3 |
| (7) | 5032.4 | 19.2 ± 12% | 25.6 | 29.0 | 26.3 |
| (9) | 4815.5 | 12.8 ± 15% | 16.3 | 7.3 | 12.4 |
| | 4716.2 | 4.0 ± 15% | 5.5 | 10.2 | 8.2 |
| (14) | 5819.2 | 3.1 ± 35% | 3.6 | 2.8 | 4.5 |
| (38) | 5320.7 | 46.0 ± 7% | 53.9 | 50.2 | 50.2 |
| | 5345.7 | 37.6 ± 7% | 40.9 | 32.9 | 35.1 |

† This table adopted from Bridges and Wiese, Ref.[25], to include current results. Strengths are normalized to the Coulomb predicted value for λ5453.8.

* Intermediate coupling calculations are by Garstang, Ref. [110].

gradients cause demixing of the $SO_2$ additive; therefore the sulfur/oxygen ratio, $\gamma$ , at a given arc radius had to be experimentally determined. From observed $H_\beta$ halfwidths electron density was deduced. This is a function of $\gamma$ and T . Intensities, $I_o$ , of several OI lines of known A-values were measured absolutely -- these also are functions of $\alpha$ and T . $I_o(\gamma,T)$ and $N_e(\gamma,T)$ were then solved simultaneously for the two unknowns $\alpha$ and T , giving:

$$\gamma = 2.3 \pm 30\%$$

$$T = 11{,}360°K \pm 100°K \quad .$$

If $\gamma$ was in reality 30% greater and T was really 150°K less, then the A-values deduced for SI would be about 30% too high while those for SII would remain essentially unchanged. So here is at least one feasible set of coupled temperature and concentration errors which could account for the discrepancy in the ratio of SI to SII transition probabilities.

To similarly scrutinize the current experiment, we begin by refering to Figs. 57 and 5 . The first of these shows that if T were really 11,200°K , rather than an assumed† 11,400°K , then the ratio of SI λ5453 to SI λλ4695 A-values, $ARN_{SII}/A(TIB)_{SI}$ , would be in error by only 9%. Figure 5 shows that had we employed the conventional emission (AE) measurements for <u>both</u> SI λλ4695 and SII λ5453 , as did Bridges, rather than thermally insensitive measurements, then the ratio of SII to SI A-values would have been 35% too high. So in the current work,

---

†We here assume a larger temperature error for this work than for Bridges' simply to make a stronger case -- claimed accuracies in temperature for the two experiments are equivalent.

small errors in temperature cannot produce large shifts in SII results relative to those of SI . There is no possibility for demixing of our plasmas, but an analogous uncertainty in sulfur density can arise from error in the initial partial pressure of $CS_2$ in our test gases. Figure 58 and the discussion pertinent to it indicated our partial pressures of $CS_2$ should be accurate to better than 5% . However, even if this error were ten times greater, the relative densities of SI to SII would shift only a few per cent in maintaining Saha equilibrium:

$$\left.\frac{\partial \frac{NSI}{NSII}}{\partial (NSI + NSII)}\right]_{T = 11,400°K} \approx 0 \quad .$$

So in the current work, neither temperature error alone, nor sulfur number density error alone, nor any combination of the two, can appreciably shift the A-values of SII with respect to SI .

F. Transition Probabilities for SiI and SiII

1. Introduction. Our results for SiI and SiII differ from our results for CI , SI and SII in two respects: accuracies for SiI and SiII were markedly reduced by a set of unfavorable circumstances (discussed in Section 2), and these results run lower than predicted values by large, consistent factors.

Figure 59 shows the silicon spectra obtained when 40 Torr of .2% $SiH_4$ in neon is shock-heated. Even at the relatively low 9,800°K temperature of this plasma the ion lines are easier to measure than the neutrals because of their greater brightness and less diffuse shapes. Excited state densities for several SiI and SiII lines are plotted as functions of temperature in Fig. 60 .

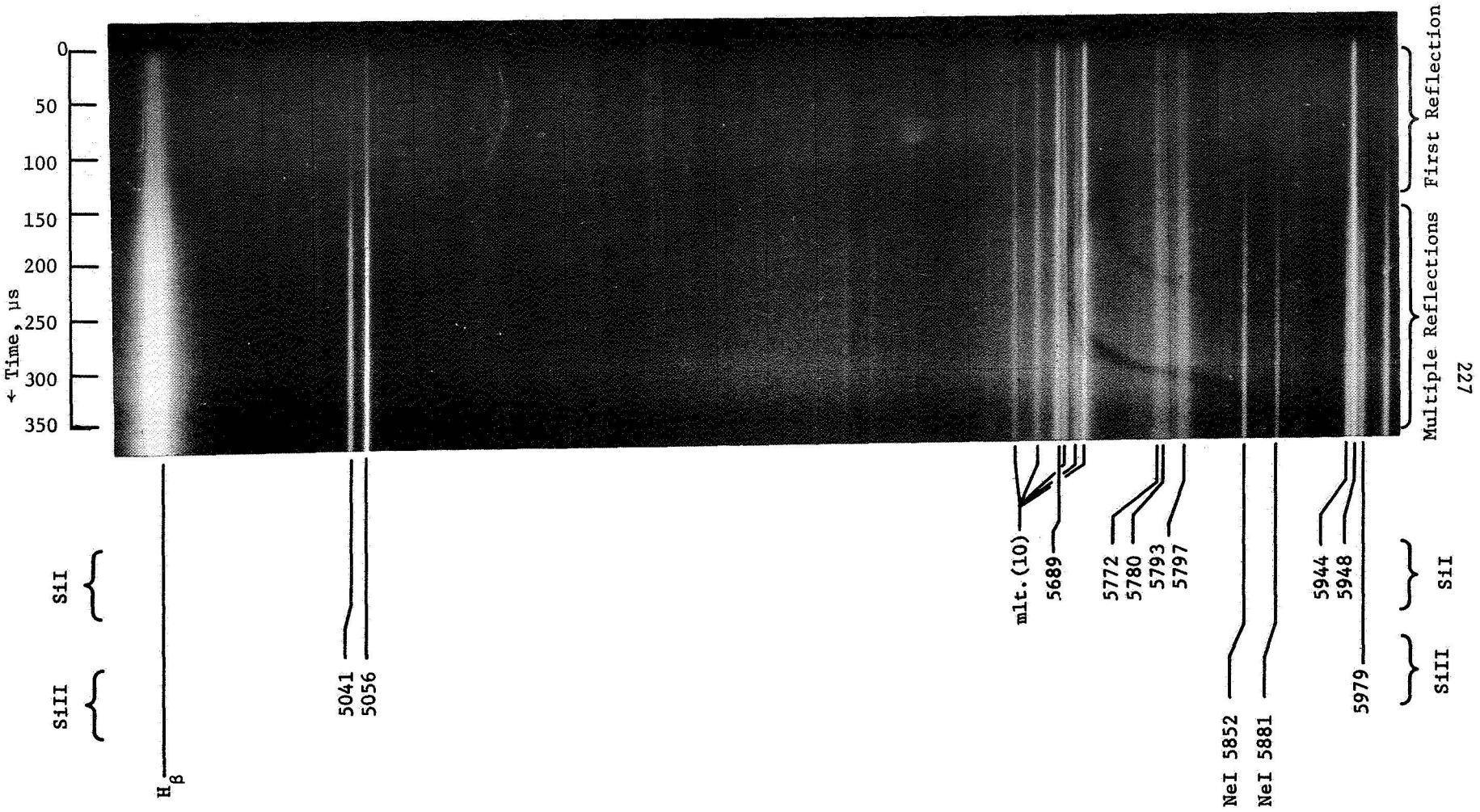


Fig. 59: Time-Resolved Spectrogram of Shock in 0.21% $SiH_4$ + 99.79% Neon.

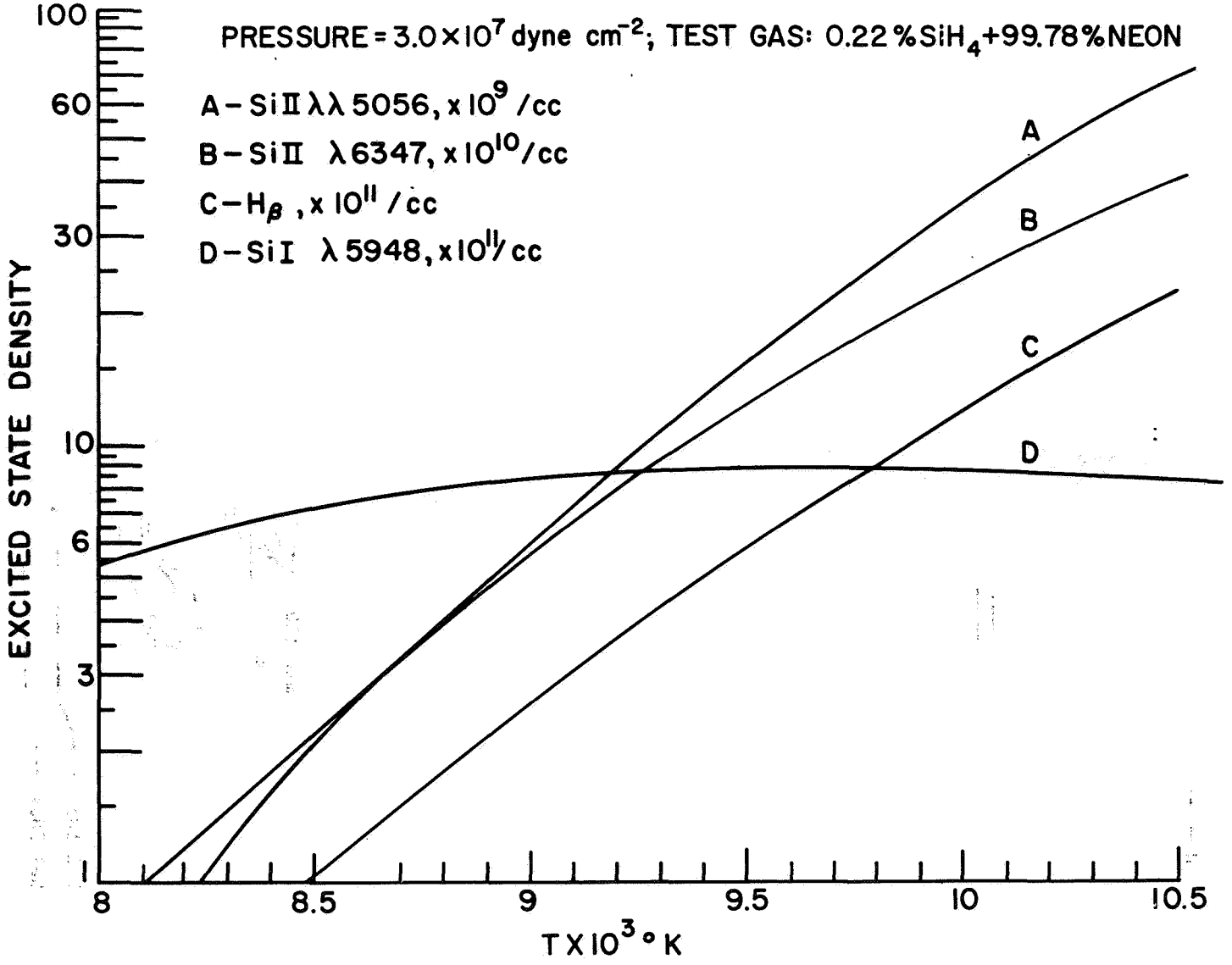


Fig. 60: Excited State Densities of Some Visible Silicon Lines as Functions of Temperature.

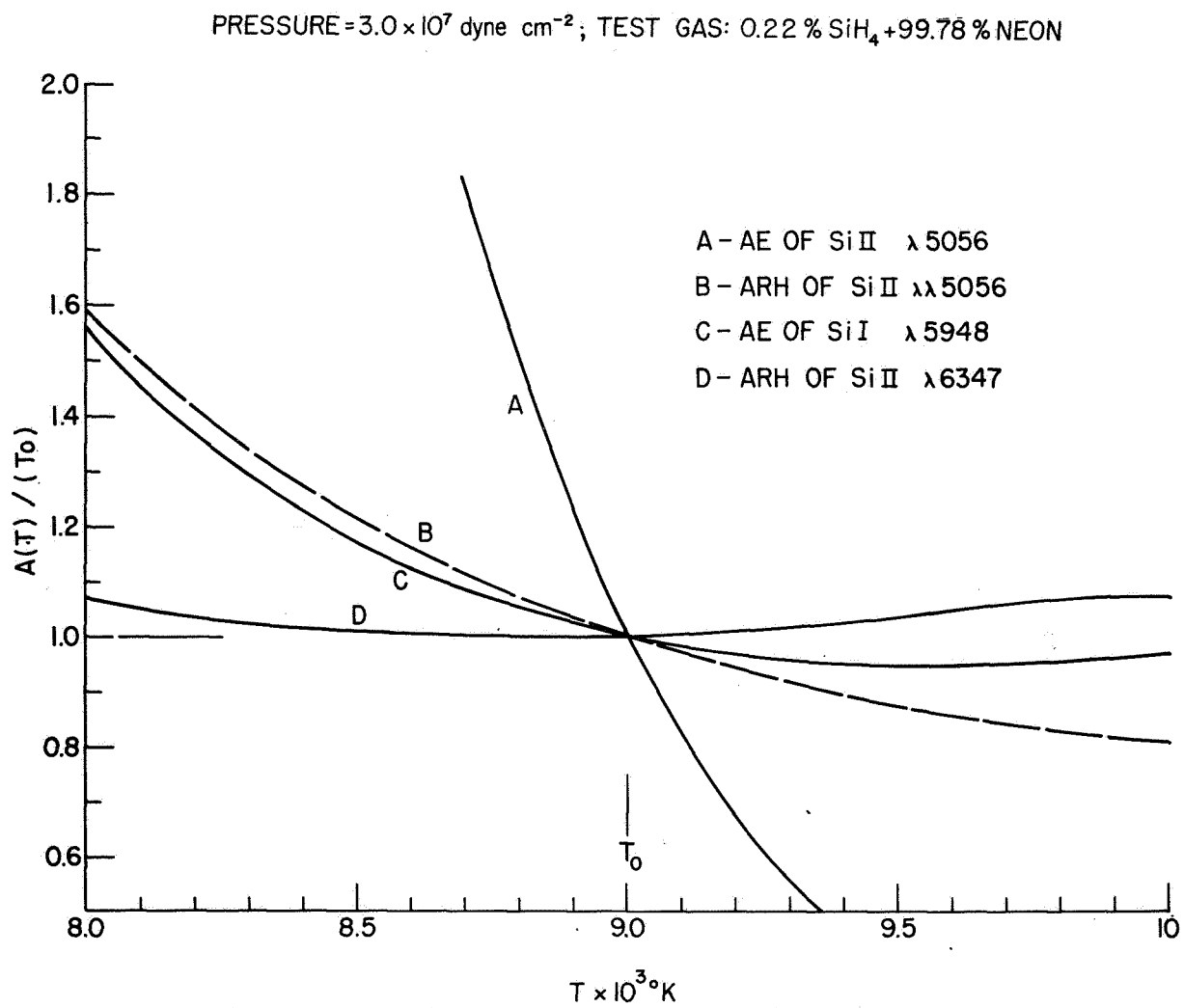


Fig. 61: Relative Thermal Error Propagated into AE of SiI λ5948 , ARH of SiII λ6347, and AE , ARH of SiII λλ5056 at True Source Temperature ($T_o$) of 9,000°K .

2. Selection of methods, experimental problems, and reduction of data. The "absolutely measured" line for SiI is λ5948 and for SiII we use the merged pair of lines λλ5041 . These were selected by the same criteria applied in selecting SI λλ4695 and SII λ5253 for the sulfur measurements.

Figure 61 shows the relative thermal error propagation in the measured A-values of SiI λ5948 , SiII λλ5056 and SiII λ6347 for our typical shock tube plasmas. As previously, AE is an A-value measured in absolute emission and ARH is an A-value measured relative to $H_\beta$ .

Silane was chosen as the usual spectroscopic additive because it contains no more than the desired constituents†, silicon and hydrogen, and does not hydrolyze as readily as volatile silicon/chlorine/hydrogen compounds. Because pure silane burns spontaneously in air, it was judged preferable to order a premixed dilute test gas consisting of 1/3% silane in neon. This was supplied with an infra-red analysis†† certifying the silane concentration to be .33% molal.

Most data runs employed this test gas at 40-45Torr initial pressure. Plasma temperatures behind first reflected shocks varied between 9,500°K and 10,000°K. It was necessary to go to these high initial pressures to bring the SiI lines up to reasonable brightness because silane concentrations are small and SiI readily ionizes, while the lines themselves have small A-values (typically $10^6 sec^{-1}$) and large halfwidths.

However, these high initial pressures hampered our ability to determine plasma temperature. For temperatures less than 10,000°K NeI λ5852 is too weak to give a useful photoelectric signal, so $T_{neon}$

---

†Additive components not intended as subject of study or for diagnosing the plasma not only cause needless spectroscopic interference but also produce an undesirable cooling of the plasma.

††Supplied by Air Products Inc. For each analysis, a set of comparison standards is made which brackets the unknown sample in concentration.

was available for only a small percentage of runs in which $I_{NeI\lambda5852}$ was photographically recorded. Moreover, at these low temperatures $H_\alpha$ is no longer optically thick, so its intensity will scale with temperature like optically thin $H_\beta$ rather than like the Planck function. The drawbacks could have been overcome by using lower initial pressures of test gases containing higher silane concentrations, but this was not possible because it was necessary at that time to relocate our equipment.

In computing the temperatures $T = \frac{1}{3}(T_\beta + T_\alpha + T_{\lambda\frac{1}{2}})$ we discovered a pronounced systematic discrepancy; $T_{\lambda\frac{1}{2}} << T_\beta < T_\alpha$ . The direction and size of these inequalities suggested that silane concentrations were substantially lower than .33%. If actual silane concentrations are lower than assumed, then electron density, because of its nearly linear dependence upon silane concentration, will be proportionately reduced. But electron density is a weak function of temperature in these plasmas because there is little SiI left to ionize at $T > 9{,}000°K$ , so $T_{\lambda\frac{1}{2}}$ will be drastically reduced by the unknown loss of silane. The intensity of $H_\beta$ , however, is a strong function of temperature, so an unknown deficiency in silane concentration reduces $T_\beta$ only slightly. The slit-integrated intensity of $H_\alpha$ will be affected least of all, because lower electron densities imply that more of $H_\alpha$ will fall within the slits, partially compensating for there being fewer hydrogen atoms than assumed.

In view of these discrepancies the mixture was returned to the factory for a second analysis, and we set about using all the information at our disposal: we had not hitherto employed the few photographically recorded intensities of NeI λ5852 . If the assumed silane concentration is too low, then the A-value of $H_\beta$ , measured relative to NeI λ5852 should be too low also. Indeed, the average for the five runs in which

I $H_\beta$/I Ne $\lambda$5852 was available gave the A-value of $H_\beta$ too low by the factor 0.7. Since the A-values of both $H_\beta$ and NeI $\lambda$5852 are known, we can use the measured pressure and I $H_\beta/I_{Ne\lambda5852}$ to deduce source temperature.

Other data we had not used previously were the incident shock speeds $S_1$. During the investigation of CI, SI and SII the temperatures derived from $S_1$ by the Rankine Hugoniot relations were used to check reliability of these equations rather than to improve our best estimated temperature, $T \cong \frac{1}{4}(T_\alpha + T_\beta + T_{neon} + T_{\lambda\frac{1}{2}})$. Given the level of agreement between $\tilde{T}$ and $T_{S_1}$ shown in Fig. 19, and noting $\frac{\partial}{\partial S_1} T_{S_1}$ is less for silane test gases than for .5% $CH_4$ + .5% $CS_2$ test gases, we now use $T_{S_1} \pm {}^{2\%}_{4\%}$ to form:

$$T = \frac{1}{5}(T_\alpha + T_\beta + T_{\frac{I_{H\beta}}{I_{Ne\lambda5852}}} + T_{S_1} + T_{\lambda\frac{1}{2}}) \quad .$$

We also reduced the one successful data run in .5% $SiHC\ell_3$, obtaining an A-value for SiI $\lambda$5948 a factor 2.1 larger than the average from the nine runs in silane reduced using the assumed 0.33% concentration.

The silane concentration, $\gamma$, was estimated in two ways, since an error in the assumed $\gamma$ (0.33%) appeared to be the only plausible explanation for the breakdown of self-consistency in the redundant temperature measurements. The first of these is essentially the method outlined by Boldt. In a given experimental run we measure the variables $I_{H\beta}/I_{NeI\lambda5852}$, $I_{H\beta}$, $\int_{WS/2}^{WS/2} I_\alpha(\lambda)d\lambda$, and $Ne(\lambda\frac{1}{2}$ of $H_\beta)$. These are all functions of the two unknowns, T and $\gamma$, if we assume the pressure is accurately known. Figure 62 graphically represents four equations in two unknowns:

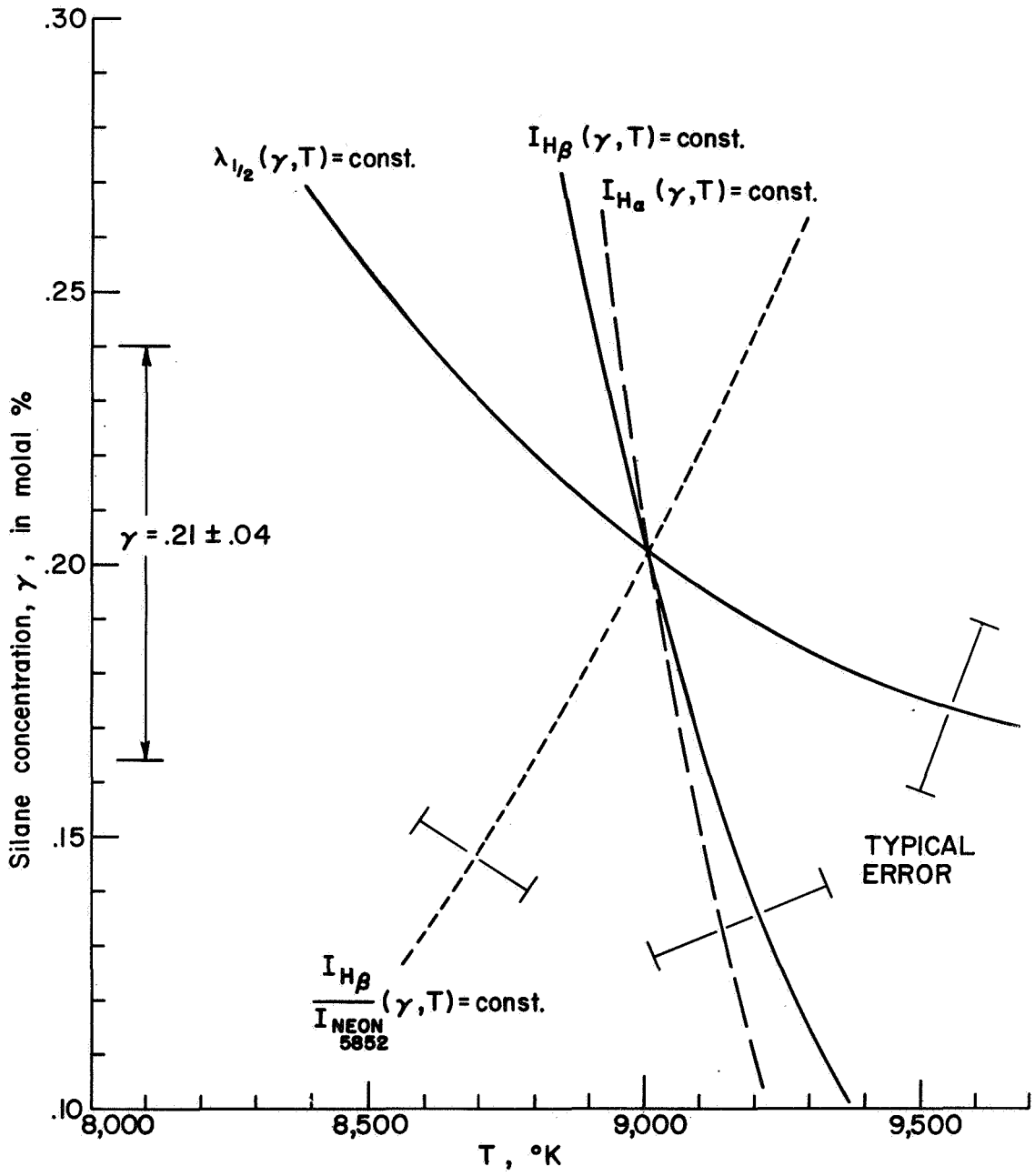


Fig. 62: Graphical Solution (Over Determination) for Temperature and Silane Concentration in Terms of the Four Observables: The Intensities of $H_\alpha$ and $H_\beta$, the Halfwidth of $H_\beta$, and the Ratio of $H_\beta$ to NeI λ5852 Intensities.

$$\frac{I_{H\beta}}{I_{Ne\lambda 5852}}(\gamma,T) = \text{constant} \pm \text{error}$$

$$I_{H\beta}(\gamma,T) = \text{constant} \pm \text{error}$$

$$\int_{-WS/2}^{WS/2} I_{\alpha}(\lambda)d\lambda(\gamma,T) = \text{constant} \pm \text{error}$$

$$Ne(\lambda \text{ of } H_{\beta})(\gamma,T) = \text{constant} \pm \text{error} .$$

The intersection of any two of these curves defines the coordinates $(\gamma \pm \Delta\gamma, T \pm \Delta T)$ the other two equations overdetermine $(\gamma,T)$ , so those points common to all four curves define the most reliable set of coordinates:

$$\gamma = .21\% \pm .04\%$$

$$T = 9{,}000°K \pm 200°K .$$

The data can also be handled in a different way to yield another estimate of $\gamma$ : for every data run compute the quantity

$$\sigma(\gamma) \equiv [(T_{\alpha}(\gamma) - T(\gamma))^2 + (T_{\beta}(\gamma) - T(\gamma))^2 --- (T_{\lambda_{\frac{1}{2}}}(\gamma) - T(\gamma))^2]^{\frac{1}{2}}$$

for a set assumed $\gamma$ values. The minimum in $\sigma(\gamma)$ vs. $\gamma$ should occur at the correct $\gamma$ . Figure 63 illustrates this approach, with the best estimate for $\gamma$ being $\gamma = .22\% \pm 40\%$.

The results of Air Products' reanalysis of the test gas cylinder was $\gamma = .28\% \mp .01\%$ . The reduction in $\gamma$ from .33% to .28% in twenty

$$\sigma(T,\gamma) = \left[T_\alpha^2(\gamma)+T_\beta^2(\gamma)+T_{NEON}^2(\gamma)+T_{\lambda_{1/2}}^2(\gamma)+T_{S_1}^2(\gamma)-\frac{1}{5}\left\{T_\alpha(\gamma)+T_\beta(\gamma)+T_{NEON}(\gamma)+T_{\lambda_{1/2}}(\gamma)+T_{S_1}(\gamma)\right\}^2\right]^{1/2}$$

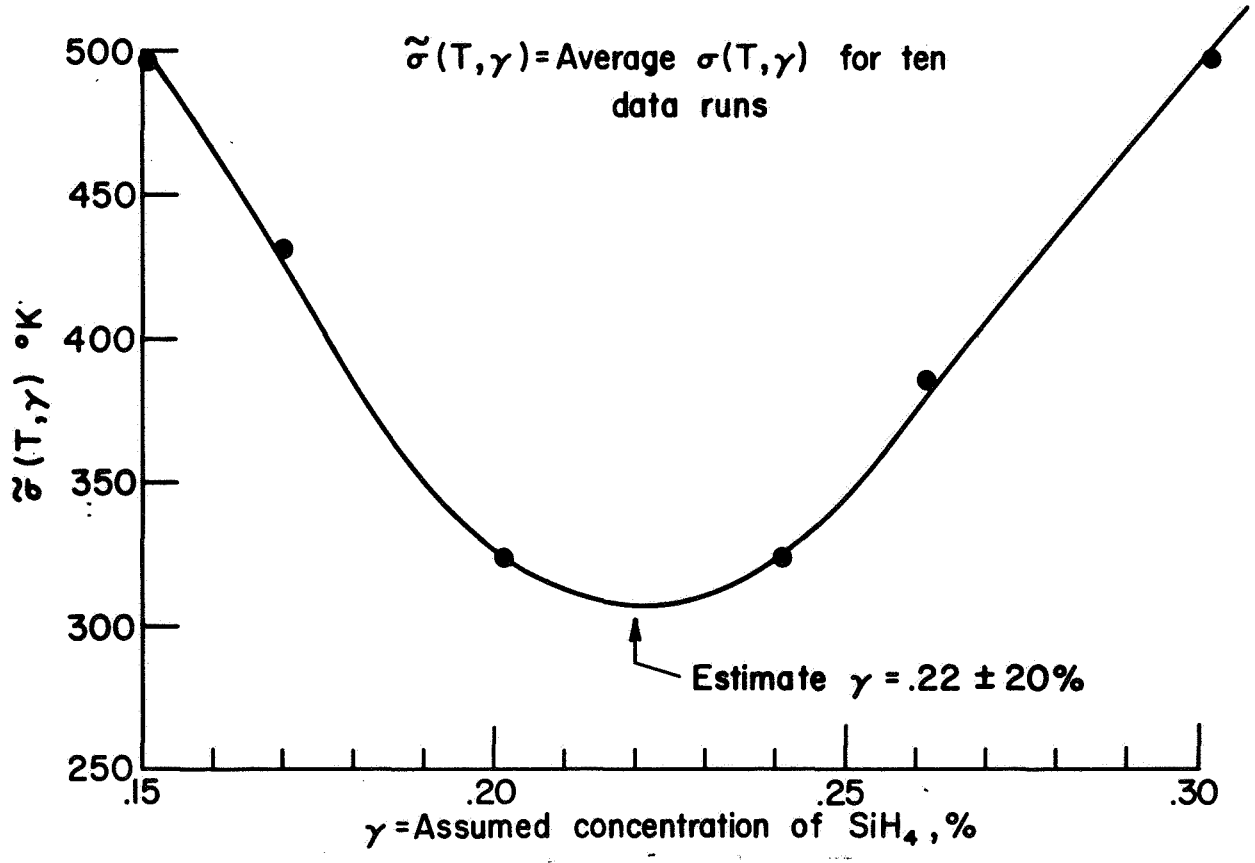


Fig. 63: RMS Scatter Between Five Measured Temperatures as Function of Assumed Silane Concentration in a Silane + Neon Test Gas.

months, was judged by the company's engineers to be normal for low concentrations of test gases in neon carriers, the hypothesized loss mechanism being absorption into the cylinder walls. Assuming $\gamma$ decreased at a constant rate over the twenty months between analyses, the value appropriate to our data runs would be $\gamma = .30 \pm .01\%$.

Faced with the decision to adopt either the results of two infared analyses giving $\gamma = .30$ , or the results of our own determination, $\gamma = .21_5$ , we choose the latter. We can suggest no way to reconcile the disagreement -- neither reaction nor adsorption of silane within the shock tube prior to firing seem plausible†.

The AE-values for SiI $\lambda$5948 deduced with $\gamma = .21_5$ are shown in Fig. 64 . The result from the single run in .5% $SiHC\ell_3$ is cross-hatched. Note that this result agrees to a few per cent with the average of results from runs in $.21_5\%$ $SiH_4$ : if $\gamma = .30\%$ had been employed, there would be instead a factor of 1.9 discrepency. The scatter in these results for the ten runs gives an RMS deviation of 12%, which is not in excess of what is expected from photographic noise. The combined uncertainty from scatter, absolute intensity, and absolute pressure is $\pm$ 25% : this, compounded with a $\pm$ 25% uncertainty in $\gamma$ gives for our absolute A-value of Si $\lambda$5948 :

$$\tilde{A}E = .98\times10^{6}\ \mathrm{sec}^{-1} \pm 35\% \quad .$$

---

†The most likely reaction (which is not probably in a system pumped-down to vacuums of $10^{-6}$Torr) would be hydrolysis:

$$S_iH_4 + 2\ H_2O \rightleftharpoons S_iO_2 \searrow + 4H_2 \quad .$$

For every silicon atom lost, the test gas would be enriched by 4 hydrogen atoms. If a significant fraction of silane reacted in this way, discrepancies between $T_\alpha$ , $T_\beta$ , $\dfrac{T_{IH_\beta}}{I_{NeI\lambda5852}}$ and $T_{S_1}$ , $T_{\lambda\frac{1}{2}}$ would be large enough to be detected.

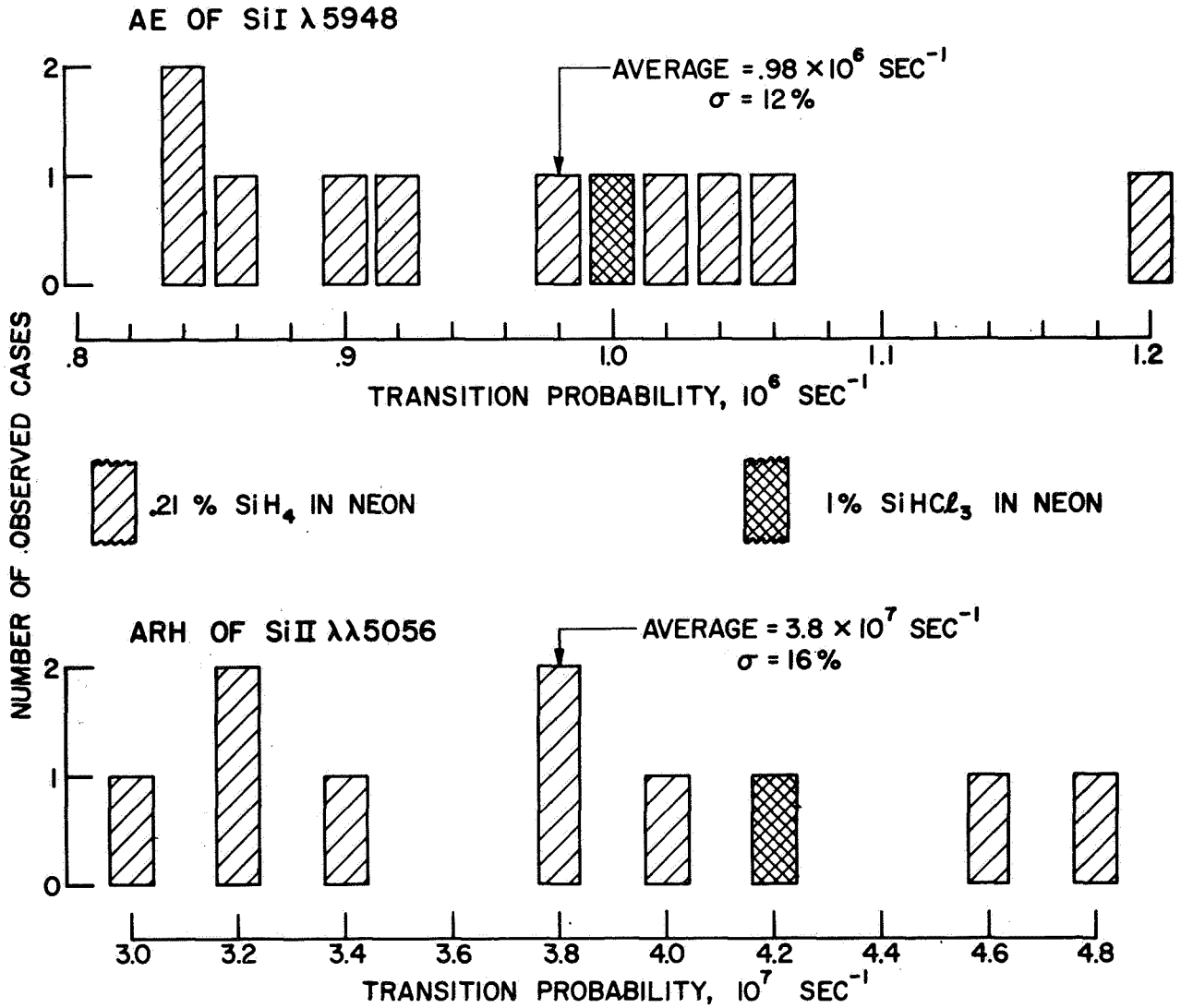


Fig. 64: Histogram of Results for A-Values of SiI λ5948 and SiII λλ5056 .

Figure 64 gives the histogram of ARH-results for SiII λλ5056, where

$$\widetilde{ARH} = 3.8\ 10^{7}\ \mathrm{sec}^{-1} \pm 20\% \ .$$

Although the scatter in these SiI and SiII results are roughly equivalent, the SiII results should be more accurate for two reasons: first, ARH relies on the ratio of photographic intensities, $I_{\lambda\lambda 5056}/I_{H\beta}$ , which is less susceptible to systematic error than the absolute intensity needed for AE of SiI λ5048 . Also, the ratio of silicon to hydrogen number densities has a much weaker dependence on the approximately known $\gamma$ than does the silicon number density alone. That is

$$\frac{\partial}{\partial\gamma}\left(\frac{N_{\mathrm{SiII}\ \lambda\lambda 5056}}{N_{H_\beta}}\right)\Bigg]_T << \frac{\partial}{\partial\gamma}\left(N_{\mathrm{SiI}\ \lambda 5948}\right]_T \ .$$

At the low silane concentrations we used, however, the approximately known impurity concentration of hydrogen (from wall contaminents) can introduce an estimated 10% uncertainty into ARH of SiII λ5056.

3. Results for transition probabilities of SiI and SiII . Current results for SiI and SiII are listed in Table XI . Several SiI A-values could be deduced only by relying on published relative intensity data, since in our spectra the relavent lines merged completely. Under shock tube conditions ($T \approx 10{,}000°K$) they form two broad features (λλ6150, λλ6240) having greater integrated intensities than any other SiI features we measured. To compute the stated A-values we used degeneracies

Table XI. TRANSITION PROBABILITIES FOR SiI

| Multiplet | Transition (n, lower) (m, upper) | $J_n - J_m$ | λ(Å) | Amn $10^7 sec^{-1}$ | $log_{10}gf$ | Tolerance | Remarks |
|---|---|---|---|---|---|---|---|
| 8.01• | $4s\ ^3P^o - 5p\ ^1P$ | 1-1 | 5873.7 | .007 | -2.970 | ±45% | |
| 9 | $4s\ ^3P^o - 5p\ ^3D$ | 2-3 | 5797.9 | .017 | -2.230 | 35% | |
| | | 1-2 | 5793.1 | .022 | -2.252 | 35% | |
| | | 0-1 | 5780.4 | .027 | -2.395 | 35% | |
| | | 2-2 | 5859.2 | <.002 | <-3.306 | — | |
| 10 | $4s\ ^3P^o - 5p\ ^3P$ | 2-2 | 5708.4 | .066 | -1.795 | 35% | |
| | | 1-1 | 5690.5 | .053 | -2.116 | 35% | |
| | | 2-1 | 5754.3 | .005 | -3.146 | 35% | |
| | | 1-0 | 5701.1 | .105 | -2.291 | 35% | |
| | | 1-2 | 5645.7 | .019 | -2.338 | 45% | |
| | | 0-1 | 5665.6 | .038 | -2.262 | 35% | |
| 11 | $4s\ ^3P^o - 5p\ ^3S$ | 2-1 | 5864.5 | .085 | -1.910 | 35% | |
| | | 1-1 | 5622.2 | .006 | -3.086 | 45% | |
| 11.05• | $4s\ ^3P^o - 6p\ ^3P$ | 2-2 | 4792.3 | .008 | -2.861 | 45% } | (3) |
| | | 1-0 | 4792.2 | .006 | -3.685 | 45% } | |
| | | 1-1 | 4772.7 | .016 | -2.782 | 45% | |
| 11.06* | $4s\ ^3P^o - 6p\ ^3S$ | 2-1 | 4782.9 | .011 | -2.958 | 45% | |
| 16 | $4s\ ^1P^o - 5p\ ^1D$ | 1-2 | 5948.5 | .098 | -1.585 | 35% | (1) |
| 17 | $4s\ ^1P^o - 5p\ ^1S$ | 1-0 | 5772.2 | .175 | -2.058 | 35% | |
| 17.02* | $4s\ ^1P^o - 4f'[2\frac{1}{2}]$ | 1-2 | 5517.5 | .008 | -2.739 | 40% | |
| 17.03* | $4s\ ^1P^o - 4f'[1\frac{1}{2}]$ | 1-2 | 5493.2 | .009 | -2.706 | 40% | |
| 17.08* | $4s\ ^1P^o - 6p\ ^1D$ | 1-2 | 5006.0 | .018 | -2.465 | 40% | |
| 21.10* | $3p^3\ ^3D^o - 5f[2\frac{1}{2}]$ | 2-3 | 6244.5 | .061 | -1.601 | 45% | (3) |
| | | 1-2 | 6237.3 | .109 | -1.495 | 45% | (3) |
| 21.11* | $3p^3\ ^3D^o - 5f[3\frac{1}{2}]$ | 3-4 | 6254.2 | .068 | -1.443 | 45% | (3) |
| | | 3-3 | 6254.3 | .010 | -2.400 | 45% | (3) |
| | | 2-3 | 6243.8 | .061 | -1.601 | 45% | (3) |
| 21.12* | $3p^3\ ^3D^o - 5f'[3\frac{1}{2}]$ | 3-4 | 6155.1 | .047 | -1.620 | 45% | (3) |
| | | 2-3 | 6145.0 | .038 | -1.828 | 45% | (3) |
| 21.13• | $3p^3\ ^3D^o - 5f'[2\frac{1}{2}]$ | 3-3 | 6142.4 | .038 | -1.828 | 45% | (3) |
| | | 2-3 | 6131.8 | .034 | -1.873 | 45% | (3) |
| | | 2-2 | 6131.6 | .045 | -1.900 | 45% | (3) |
| | | 1-2 | 6125.0 | .047 | -1.873 | 45% | (3) |
| 21.16* | $3p^3\ ^3D^o - 6f[2\frac{1}{2}]$ | 1-2 | 5747.6 | .010 | -2.615 | 45% | |
| 21.17* | $3p^3\ ^3D^o - 6f[3\frac{1}{2}]$ | 2-3 | 5753.6 | .005 | -2.778 | 45% | |
| | | 3-4 | 5763.0 | .005 | -2.624 | 45% | |
| 21.18* | $3p^3\ ^3D^o - 6f'[3\frac{1}{2}]$ | 3-4 | 5675.4 | .007 | -2.498 | 45% | |
| 21.19* | $3p^3\ ^3D^o - 6f'[2\frac{1}{2}]$ | 3-3 | 5669.7 | .003 | -3.073 | 45% | |
| | | 2-3 | 5660.6 | .008 | -2.582 | 45% } | (3) |
| | | 2-2 | 5660.5 | .008 | -2.722 | 45% } | |

TRANSITION PROBABILITIES FOR SiII

| | | | | | | | |
|---|---|---|---|---|---|---|---|
| 2 | $4\ ^2S - 4\ ^2P^o$ | $\frac{1}{2}-1\frac{1}{2}$ | 6347.1 | 3.10 | - .097 | ±40% | |
| | | $\frac{1}{2}-\frac{1}{2}$ | 6371.3 | 3.87 | - .331 | 40% | |
| 4 | $4\ ^2P^o - 5\ ^2S$ | $1\frac{1}{2}-\frac{1}{2}$ | 5978.9 | 5.27 | - .247 | 30% | |
| | | $\frac{1}{2}-\frac{1}{2}$ | 5957.6 | 3.56 | - .413 | 30% | |
| 5 | $4\ ^2P^o - 4\ ^2D$ | $1\frac{1}{2}-2\frac{1}{2}$ | 5056.0 } | 3.8 | .167 | 20% | (2) |
| | | $1\frac{1}{2}-1\frac{1}{2}$ | 5056.3 } | | | | |
| | | $\frac{1}{2}-1\frac{1}{2}$ | 5041.0 | 4.73 | - .143 | 20% | |

*Revised classification from C. E. Moore, NRDS-NBS 3, Section 2.

(1) All of our SiI lines are measured relative to this line.

(2) All of our SiII lines are measured relative to this blended pair.

(3) Pronounced Stark broadening causes these lines to blend in our plasmas: the relative intensity observations given by Moore are used to deduce the relative strengths of the stronger lines within multiplets.

and the relative intensities as indicated in the table and employed the mean excitation energy of the blended lines, all of which lie within 0.1 eV of their mean.

Lines composing multiplet (10) could not be resolved well because wing blending made determination of the local continuum uncertain.

4. Checks for internal consistency. Because data runs using silane all grouped around the same plasma temperature and pressure, and because all silane came from a single cylinder, we cannot make comparisons analogous to those of Figs. 51 and 52 .

As already noted, the single data run using $SiHC\ell_3$ agreed with the average of the silane results to within joint tolerances.

To check self-consistency we also computed ARH of SiI λ5948 and AE of SiII λλ5056. Both these A-values have an implicit thermal dependence roughly equal to that of the integrated intensity of $H_\beta$ , so the 1.5% - 2% uncertainty in $\tilde{T}$ (for the silane data) leads us to expect about twice the scatter for these A-values as for the thermally insensitive results AE of SiI λ5948 and ARH of SiII λλ5056. The 10% agreement between the averaged AE and the averaged ARH results for both SiII λ5048 and SiII λλ5056 affirms that no gross errors exist in our absolute photometry.

5. Comparison with literature values. In comparisons with both theoretical predictions and previous experimental findings the current SiI and SiII results invariably emerge as the low absolute values.

Table XII compares the current SiI results against Coulomb approximations and the results of Hey's[111] investigation (the sole previous experimental study in the region 4600Å < λ < 6900Å) . We included in this

Table XII. COMPARISON OF SiI TRANSITION PROBABILITIES WITH LITERATURE VALUES.

| Multi-plet | λ(Å) | $A_{mn}, 10^6 sec^{-1}$ | | | |
|---|---|---|---|---|---|
| | | This experiment | Hey (1959) Ref.[111] | NBS adopted (1968) Ref.[13] | Coulomb approximation Griem, Ref.[7] |
| ( 9) | 5797.9 | .17 ± 35% | --- | 1.08 | .75 |
| | 5793.1 | .22 ± 35% | --- | 1.53 | 1.06 |
| | 5780.4 | .31 ± 35% | --- | .98 | .7 |
| | 5859.2 | <.02 -- | --- | .42 | .3 |
| (10) | 5708.4 | .66 ± 35% | --- | --- | 2.9 |
| (11) | 5684.5 | .85 ± 35% | --- | 2.6 | 2.5 |
| | 5622.2 | <.06 -- | --- | 1.6 | 1.6 |
| 11.05* | 4792.2↑ | .11 ± 40% | --- | --- | --- |
| (16) | 5948.5 | .98 ± 35% | 2.16 ± 20% | 2.2 | 4.5 |
| (17) | 5772.2 | 1.75 ± 35% | --- | 8.0 | 7.8 |

↑Blended multiplet.

*Classification from C.E. Moore, Selected Tables of Atomic Spectra, SiI, Nat. Bur. Stand. Ref. Series, NSRDS-NBS 3, Section 2.

| Citations for violet SiI lines | |
|---|---|
| λ4102.9 | |
| ≳ .056 | Woodgate (1966), Ref.[112] |
| .171 | Hey (1959), Ref.[111] |
| .157 | Lawrence and Savage (1966), Ref.[47] |
| λ3905.5 | |
| 19.7 | Allen and Asaad (1956), Ref.[23] |
| 14.5 | Lawrence and Savage (1966), Ref.[48] |
| 28.7 | Corliss and Bozman (1962), Ref.[112] |
| ≳ .75 | Woodgate (1966), Ref.[112] |
| 81.0 | Coulomb approximation, Griem, Ref.[7] |

table a comparison between literature values for λ3905.5 and λ4102.9, two SiI lines we did not measure, to call attention to the unfortunately large disagreements between authors[7,23,47,48,111,112] for this astrophysically important element.

Our SiI results run consistently below Coulomb predictions by factors of 3-5. Coulomb predictions are not expected to be very reliable for these transitions because the lower levels are s-states (penetrating orbitals) and are only moderately excited. The radial wave functions also come very close to cancellation. Still, our CI results agreed closely with Coulomb predictions which are expected to be no more reliable than for these SiI lines.

We fall a factor of 2.1 below Hey's value for SiI λ5948 . Hey's result for SiI λ4102.9 (which we did not measure) agrees to 10% with Lawrence and Savage.[47] The latter authors used intermediate coupling calculations to transfer to SiI λ4102.9 the results of their lifetime measurements on SiI λ2505. It appears that little of the accuracy of the lifetime determination was lost in this transfer because other SiI A-values similarly treated by Lawrence and Savage agree very well with the relative A-values measured by Corliss and Bozman.[48] So there is independent support for Hey's result for SiI λ4102.9. But much the same line of argument raises questions about Hey's result: if Hey's result for SiI λ4103, $.0171\times10^7$ $sec^{-1}$, is scaled by the Lawrence and Savage predictions (cf. Table XII) to give the A-value of SiI λ3905.5 , we get:

$$A_{3905} = \frac{1.45}{.0157} \times .0171\times10^7\ sec^{-1} = 1.5_8\times10^7\ sec^{-1} \quad .$$

Table XII. APPLICATION OF CURRENT RESULTS TO SiI SOLAR ABUNDANCE DETERMINATIONS[+], SHOWING DECREASED SCATTER FROM IMPROVED RELATIVE gf VALUES .

| Multi-plet | λ(Å) | (a) log gf from Coulomb[+] approximation | (b) log gf from Renormalized[*] current results | log [solar[°↑] abundance] based on (a) | based on (b) |
|---|---|---|---|---|---|
| (9) | 5797.9 | -1.25 | -1.54 | 6.79 | 7.08 |
| | 5793.1 | -1.52 | -1.56 | 7.07 | 7.11 |
| (10) | 5645.6 | -1.70 | -1.65 | 7.13 | 7.08 |
| | 5665.5 | -1.79 | -1.57 | 7.27 | 7.05 |
| | 5690.4 | -1.92 | -1.43 | 7.64 | 7.15 |
| | 5701.1 | -1.79 | -1.60 | 7.22 | 7.03 |
| | 5708.4 | -1.22 | -1.11 | 7.16 | 7.05 |
| (11) | 5684.5 | - 1.54 | - 1.22 | 7.34 | 7.02 |
| (16) | 5948.5 | - .89 | - .89 | 7.11 | 7.11 |
| (17) | 5772.2 | - 1.58 | - 1.36 | 7.32 | 7.10 |
| | | | Variance: | 0.22 | 0.04 |

[+]B.J. O'Mara, Thesis California (1967).

[*]Current results renormalized to agree with Coulomb approximations for $Si_I$ λ5948.5 .

[°↑]Absolute (non-normalized) current results would increase solar abundance of $Si_I$ by a factor of 4 over that given in the last column above.

While this A-value is twice as great as predicted by the Coulomb approximation, Hey's result for SiI λ5948 , $.216 \times 10^7$ $sec^{-1}$, is about one half as large as the Coulomb prediction.

Regardless of how closely Hey's results agree with other experiments at 4,000Å , we are really concerned with his results at 5,950Å . Although he measured no SiI lines in the interval between 4,000Å and 5,950Å , both he and the current author measured SiII lines in the vicinity of 5,050Å , 5,950Å and 6,350Å . Our relative SiII A-values disagree by as much as a factor of 2, which is greater than joint tolerance estimates.

In the absence of previous laboratory values with which to compare our relative SiI results, we turn to the solar abundance studies of O'Mara.[2] Coulomb predictions for several of the SiI lines he used to determine the solar abundance of silicon are listed in the third column of Table XIII. As seen in the fifth column of the table, the silicon abundances deduced from these predicted A-values disagreed by as much as $10^{0.42} = 2.6$ . By renormalizing the current results to agree with the Coulomb approximation gf value for λ5048.5 , we obtain the set of gf values listed in the fourth column: substituting these for the Coulomb approximations used by O'Mara scales his abundance determinations into the set shown in the sixth column of the table. Our relative gf values are thus seen to reduce the rms scatter in abundance estimates by a factor of six.

Our SiI results disclose one gross violation of LS coupling: λ5684.5 and λ5622.2 of multiplet (11) should have relative strengths of 5.0 and 3.0, respectively, according to LS coupling. We, in contrast,

obtain a ratio of 7.5 to <0.5. The intensity ratios from which these relative line strengths were deduced was typically 50 to 3, the same intensity ratio as observed by Kiess.[113] However, Radziemski et al obtained the value 50 to 12 for this ratio, more nearly in accord with LS coupling. Both of these authors used low pressure lamps. Regarding the discrepancies in relative intensities we can only remark that excitation in our plasmas is exclusively thermal and that our integrated intensities for SiI λ5684.5 were quite strong enough to insure at least a 30% tolerance for the ratio of strengths for these two lines.

Table XXII also compares with LS coupling the relative strengths for those lines of multiplet (9) which we could resolve. Here too we find departures from LS-coupling, but none so drastic as in multiplet (11). This limited evidence seems to suggest that use of LS coupling predictions is at least partially responsible for the scatter in solar SiI abundance determinations.

Table XIV compares the current SiII results with literature values. There is a bewildering variety of disagreements -- almost all of them large. Our results for multiplets (2) and (5) average a factor of .6 less than the results Hey obtained using a stabilized arc: yet we agree with his result for λ5978.9 to within 8%. With respect to SCF,[114] SOC[115] and Coulomb[7] approximations our results are generally small by factors of 2 to 4; yet we agree with the Coulomb approximation for λ5957.6 to within 10%.

Responsibility for the factor of .6 disagreement with Hey's results for multiplets (2) and (5) cannot be ascribed to the usual causes. Since our results for both SiI and SiII bear essentially the same factor of .6 relationship to Hey's results (cf. Table XII), a temperature

Table XIV. COMPARISON OF SiII TRANSITION PROBABILITIES WITH LITERATURE VALUES.

| Multi-plet | (Å) | $A_{mn}$, $10^7 sec^{-1}$ | | | | | |
|---|---|---|---|---|---|---|---|
| | | This experiment | Hey (1959) Ref.[111] | SOC Froese (1968) Ref.[115] | SOC Weiss (1967)* | Coulomb approximation Underhill & Froese(1966),Ref.[115] | SCF Bates & Damgaard (1948),Ref.[114] |
| (2) | 6347.1 | 3.10 ± 40% | --- | 7.02 | 6.24 | 6.36 | 9.0 |
| | 6371.3 | 3.87 ± 40% | 7.33 ± 25% | 7.47 | 6.64 | 6.81 | 9.0 |
| (4) | 5978.9 | 5.27 ± 30% | 5.64 ± 25% | 11.07 | --- | 7.91 | --- |
| | 5957.6 | 3.56 ± 30% | --- | 5.45 | --- | 3.97 | --- |
| (5) | 5056.0 } 5056.3 } | 3.80 ± 20% | 5.97 ± 25% | 12.92 | 9.41 | 10.18 | --- |
| | 5041.0 | 4.37 ± 20% | 7.30 ± 25% | 16.44 | 11.97 | 12.96 | --- |

*Private communication to Miss Froese.

error in either experiment cannot alone account for the discrepancy. Moreover, referring to Fig. 61 , we find that the ratio of $ARH_{SiII}$ (curve "B") to $AE_{SiI}$ (curve "C") in the current experiment can be varied only 5% by a 5% error in source temperature, so in the current results the ratio of SiII λλ5056 to SiI λ5948 A-values is thermally insensitive. The largest estimated uncertainty in the current work has to do with the relative silane concentration γ : however, if our adopted γ is grossly in error, results for SiI would be affected much more than results for SiII. That is, a large error in γ could not both reduce our results with respect to Hey and yet leave the ratio of SiI to SiII A-values intact. If absolute photometry is at fault, why should our CℓI λ4601 results, obtained with a $SiHC\ell_3$ test gas (cf. Section H), agree to within 5% with Hey's results for this line, which he similarly measured (using $SiC\ell_4$ test gases) simultaneously with silicon lines? Demixing in the arc should not be pronounced since silicon and chlorine differ relatively little in atomic weight.

## G. Transition Probabilities for PI and PII .

1. Introduction. The current results are, to the best of our knowledge, the first experimentally determined visible A-values for both PI and PII . Although Martin[116] made extensive relative intensity measurements covering the near IR , visual, and near UV spectra of both PI and PII , his light source was a hollow cathode lamp, so these data could not be reduced to transition probabilities.

The toxicity[117] of volatile phosphorus compounds (e.g. $PH_3$) and the low vapor pressure of pure phosphorus may have discouraged prior study with sources giving truly thermal excitation.

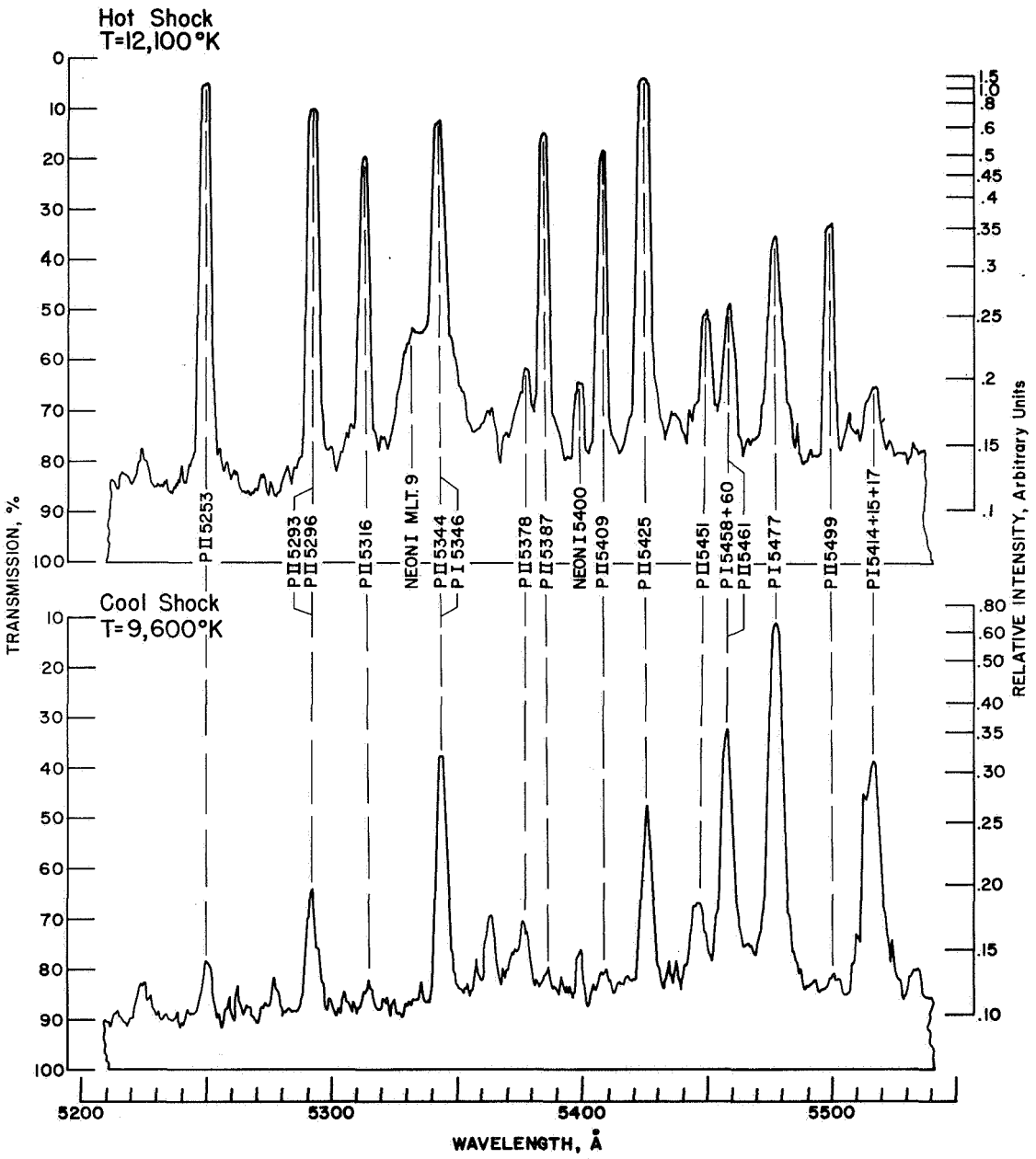


Fig. 65: Densitometer Tracings, 5200Å - 5500Å , for Two Shocks in 0.14% $PH_3$ + 99.86% Neon, Showing Strong Temperature Dependence in the Relative Brightness of PI and PII lines.

However, when a thermal source is employed, one finds that the electron densities which are necessary for LTE also cause almost all of the stronger PI lines to blend with either PII lines or the PI lines in other multiplets.

Fortunately, the shock tube has the capability of producing either spark-like or arc-like spectra, enabling us in several cases to minimize interference between lines of PI and PII . Taking ionization into account, the effective excitation energies of visible PI and PII lines differ typically by a Rydberg. Moreover, their transition probabilities are very dissimilar, being typically $10^6$ $sec^{-1}$ for PI and $10^8$ $sec^{-1}$ for PII . By simply varying the initial test gas pressure we could vary source temperatures from 9,500°K, where PI lines are substantially brighter than PII lines, to 12,500°K, where the PII spectrum is far brighter than the PI spectrum.

The two densitometer tracings in Fig. 65 are for two shocks in .14% $PH_3$ + 99.86% neon test gases. Plasma temperature for the upper spectrum was 9,600°K (corresponding to use of a 45Torr initial pressure of test gas), while source temperature for the lower spectrum was 12,100°K (where initial test gas pressure of 15 Torr was used). The relative brightness of the PI and PII spectra in these two plasmas is strikingly different.

A reproduction of a drum camera spectrogram taken during one of the cooler shocks in $PH_3$ is shown in Fig. 66 .

Owing to the relocation of our equipment, only 9 experimental runs were made using $PH_3$ + neon test gases: of these 9, two resulted in photographic records which were excessively dense and one run was ruined because of an accident during developing of the drum camera

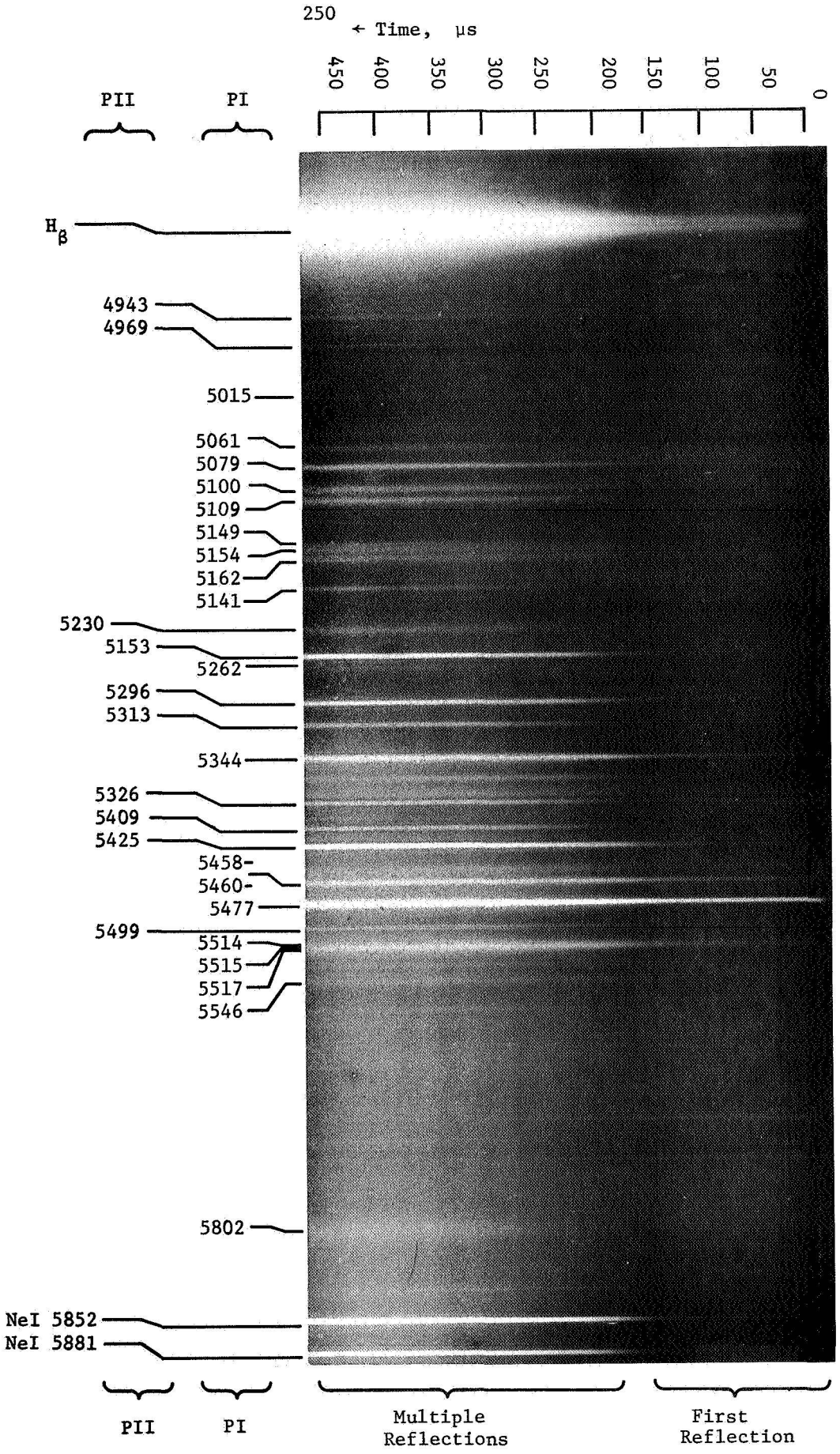


Fig. 66: Time-Resolved Spectrogram of Shock in 0.14% $PH_3$ + 99.86% Neon.

film. Because the number of runs was limited, we concentrated our efforts on the spectral region between 4800Å and 5900Å. This region is spanned by a single drum camera recording and includes both $H_\beta$ and the majority of stronger visual PI and PII lines.

2. Design, execution and reduction of experimental runs. Within the wavelength range studied, the brightest PI and PII lines not seriously blended are PI λ5477 and PII λ5253 .

The spectroscopic additive gas in these studies was $PH_3$ . Because of its toxicity, a lean mixture of $PH_3$ in neon was chosen. This was supplied (Air Products, Inc.) with an IR analysis stating the molal concentration of $PH_3$ as .28%.

Figure 15 shows the relative error propagated into various measured A-values for PII λ5253 ; $AE_{PII}$ , $ARH_{PII}$ , $ARN_{PII}$ and $A(TIB)_{PII} = \frac{1}{2}(ARN_{PII} + ARH_{PII})$ , under our usual shock tube conditions. For only one experimental run could we use $ARN_{PII}$ : for other runs either the recorded wavelengths did not extend up to λ5852Å or else NeI λ5852 was too bright to give a useful photographic density. This one $ARN_{PII}$ result was obtained simultaneously with one of our five $ARH_{PII}$ results.

For the source conditions most commonly used in our study of phosphorus ( Table II ) the thermal dependence of $AE_{PI}$ , (the emission A-value for PI λ5477), is similar to the relative thermal dependence of $AE_{SiI}$ in Fig. 61 . That is, $AE_{PI}$ for $T_o \approx 12{,}000°K$ is similar to $AE_{SiI}$ at $T_o \simeq 9{,}000°K$ .

The great majority of PI and PII lines we studied had significant blending problems. When a blended pair consists of a PI line and a PII line, we could effectively eliminate the mutual interference by first producing spectra where ion line brightness was enhanced

and neutral line brightness suppressed, and then producing much cooler plasmas where the relative brightness of PI and PII lines was reversed. Unscrambling of blended profiles was further aided by the characteristic differences in the shapes of PI and PII lines; the neutral lines are typically ten times broader than the ion lines.

When a blend consists of two ion lines or two neutral lines (of different multiplets) which overlap almost completely we deduce A-values only when one member of the blended pair is at least four times brighter than the other member according to Martin's relative intensity determinations†. In such cases we use Martin's relative intensities to subtract out the weaker line's contribution to the blend; we deduce the A-values only for the dominant members of blended pairs. When the two blended lines are of comparable brightness we do not attempt reduction to A-values unless the lines are sufficiently separated that blending is confined to the wings.

We estimate that blending contributes not more than 10% to our stated tolerances.

In reducing our data for PI and PII we encountered breakdowns in self consistency between redundant temperature measurements. As was the case with our silicon data, the inconsistancies indicated that the relative concentration of spectroscopic additive gas was substantially less than indicated by our supplier.

Except for the fact that most experimental runs made during our study of PI and PII had temperatures in the neighborhood of 12,000°K,

---

†Our relative intensities agree with Martin's to $\pm$ 30% for isolated lines in the same stage of ionization.

Table XV. TRANSITION PROBABILITIES FOR PI

| Transition† (n, lower)(m, upper) | $J_n$-$J_m$ | λ(Å) | Amn $10^6 sec^{-1}$ | $10g_{10}gf$ | Tolerance | Remarks |
|---|---|---|---|---|---|---|
| 4s $^4P$ - 5p $^4S^\circ$ | 1½-1½ | 5015.8 | .24 | -2.438 | ± 45% | |
| | 2½-1½ | 5079.3 | .73 | -1.949 | 30% | |
| 4s $^4P$ - 5p $^4P^\circ$ | ½-1½ | 5061.9 | .48 | -2.129 | 35% | |
| | 1½-½ | 5098.2 | .44 | -1.990 | 30% | |
| | 1½-1½ | 5100.9 | | | | |
| | 2½-2½ | 5109.6 | .48 | -1.945 | 35% | |
| 4s $^4P$ - 5p $^4D^\circ$ | ½-1½ | 5149.4 | .24 | -1.761 | 35% | (3) |
| | 1½-2½ | 5154.8 | | | | |
| | 2½-3½ | 5162.2 | | | | |
| 4s $^2P$ - 5p $^2P^\circ$ | 1½-1½ | 5345.8 | 1.61 | -1.561 | 35% | (3) |
| 4s $^2P$ - 5p $^2D^\circ$ | ½-1½ | 5458.3 | 1.85 | -1.482 | 40% | (2),(3) |
| | 1½-2½ | 5477.7 | 2.92 | -1.103 | 30% | (1),(2) |
| $3p^4$ $^4P$ - 4f $^4D^\circ$ | 1½-2½ | 5514.7 | 1.14 | -1.137 | 30% | (3) |
| | 2½-3½ | 5517.0 | | | | |
| $3p^4$ $^4P$ - 4f $^4D^\circ$ | ½-1½ | 5546.9 | .51 | -2.030 | 39% | (3) |
| 4s $^2P$ - 5p $^2S^\circ$ | 1½-½ | 5905.0 | .37 | -2.408 | 40% | (4) |

†Classification from W. C. Martin, J. Opt. Soc. Amer. 49, 1701 (1959).

Remarks: (1) This transition measured absolutely; other PI transitions measured relative to it. (2) Under shock tube conditions each of these lines is merged with some other PI line belonging to a different multiplet. The results of MARTIN were employed in the analysis of these line pairs which we feel is justified when one of the merged pairs is at least four times stronger than the other according to his relative intensity estimates: only the stronger members of the pair are then reduced to A-values. (3) These PI lines are merged with PII lines, but reduction to A-values is possible for source conditions where the PII line is not more than 1/4 the strength of the PI line. (The PII lines in question can be enhanced to 10 times the brightness of any observed PI line, so their A-values may be obtained by going to higher source temperatures. The PI A-values are small and the PI lines arise from low energy states while the PII A-values are very large but arise from high energy states. By shifting source temperatures ± 3000°K one can effectively suppress or enhance either the PI or PII spectrum.) (4) This line merged with the line Neon I λ5906.4, but approximate correction for this interference is made in an analogous fashion to that given in remark (3).

Table XVI. TRANSITION PROBABILITIES FOR PII

| Multiplet | Transition (n, lower)(m, upper) | $J_n - J_m$ | $\lambda$(Å) | Amn $10^8 sec^{-1}$ | $\log_{10} gf$ | Tolerance | Remarks |
|---|---|---|---|---|---|---|---|
| 5 | 4s $^3P^\circ$ - 4p $^3D$ | 2-3 | 6043.1 | .73 | .447 | ± 30% | (1) |
| | | 1-2 | 6024.1 | .30 | -.043 | 35% | |
| | | 1-1 | 6087.8 | .24 | -.395 | 35% | |
| 6* | 4s $^3P^\circ$ - 4p $^3P$ | 2-2 | 5425.9 | 1.12 | .393 | 25% | |
| | | 1-1 | 5386.9 | .55 | -.142 | 25% | |
| | | 2-1 | 5499.7 | .31 | -.374 | 20% | |
| | | 1-0 | 5409.7 | 1.43 | -.202 | 25% | |
| | | 0-1 | 5344.7 | .66 | -.074 | 30% | |
| | | 1-2 | 5316.1 | .29 | -.207 | 25% | |
| 7* | 4s $^3P^\circ$ - 4p $^3S$ | 2-1 | 5296.1 | .86 | .036 | 30% | |
| | | 1-1 | 5191.4 | .19 | -.638 | 25% | |
| | | 0-1 | 5152.2 | < .02 | <-1.686 | --- | |
| 10* | 4s $^1P^\circ$ - 4p $^1D$ | 1-2 | 5253.5 | 1.15 | .375 | 20% | (2) |
| 13 | 4p $^3D$ - 5s $^3P^\circ$ | 3-2 | 4943.4 | 1.28 | .371 | 25% | |
| | | 2-1 | 4969.6 | .68 | -.121 | 30% | |
| | | 1-0 | 4954.3 | .68 | -.601 | 25% | |
| | | 1-1 | 4927.0 | .36 | -.403 | 30% | |
| 15 | 4p $^3D$ - 4d $^3F^\circ$ | 3-4 | 4602.1 | 1.72 | .692 | 35% | |
| | | 3-3 | 4658.3 | 2.52 | .759 | 35% | |
| 23* | 4p $^3P$ - 5s $^3P^\circ$ | 2-2 | 5450.7 | .85 | .278 | 35% | (3) |
| | | 1-1 | 5507.1 | .53 | -.144 | 35% | |
| | | 2-1 | 5583.3 | .51 | -.146 | 35% | |
| | | 1-0 | 5541.2 | .98 | -.344 | 35% | |
| | | 1-2 | 5378.1 | .39 | -.075 | 30% | |
| | | 0-1 | 5483.6 | .70 | .024 | 35% | |
| 27* | 4p $^3S$ - 5s $^3P^\circ$ | 1-2 | 5588.2 | .38 | -.051 | 35% | |
| | | 1-1 | 5727.7 | .28 | -.377 | 45% | |

*Measurement secured for all members of multiplet.

Remarks: (1) Accuracy for this multiplet is degraded (to ± 35%) because only two observations were made at this wavelength. (2) This transition was measured absolutely; all other PII transitions are measured relative to it. (3) For these multiplets the lines are relatively weak so that the measurements suffer from low signal-to-noise ratios.

Table XVII. COMPARISON OF PI AND PII TRANSITION PROBABILITIES WITH COULOMB APPROXIMATIONS

PI

| λ(Å) | $A_{mn}$ $10^6 sec^{-1}$ This experiment | $A_{mn}$ $10^6 sec^{-1}$ Coulomb* approximation | λ(Å) | $A_{mn}$ $10^6 sec^{-1}$ This experiment | $A_{mn}$ $10^6 sec^{-1}$ Coulomb* approximation |
|---|---|---|---|---|---|
| 5015.8 | .24 ± 45% | 2.0 | 5149.4, 5154.8, 5162.2 | .24 ± 35% | 2.1 |
| 5079.3 | .73 ± 30% | 2.9 | | | |
| 5061.9 | .48 ± 35% | 1.5 | | | |
| 5098.2, 5100.9 | .44 ± 30% | 1.3 | 5345.8 | 1.61 ± 35% | 7.3 |
| 5109.6 | .48 ± 35% | 3.4 | 5458.3 | 1.85 ± 40% | 3.8 |
| | | | 5477.7 | 2.92 ± 30% | 5.7 |

PII

| Multi-plet | λ(Å) | $A_{mn}$ $10^8 sec^{-1}$ This experiment | $A_{mn}$ $10^8 sec^{-1}$ Coulomb* approximation | Multi-plet | λ(Å) | $A_{mn}$ $10^8 sec^{-1}$ This experiment | $A_{mn}$ $10^8 sec^{-1}$ Coulomb* approximation |
|---|---|---|---|---|---|---|---|
| (5) | 6043.1 | .73 ± 35% | .68 | (13) | 4943.4 | 1.28 ± 25% | .63 |
| | 6024.1 | .30 ± 35% | .51 | | 4969.6 | .68 ± 30% | .58 |
| | 6087.8 | .24 ± 35% | .27 | | 4954.3 | .68 ± 25% | .78 |
| | | | | | 4927.0 | .36 ± 30% | .19 |
| (6) | 5425.9 | 1.12 ± 25% | .69 | | | | |
| | 5386.9 | .55 ± 25% | .23 | (15) | 4602.1 | 1.72 ± 35% | 1.9 |
| | 5499.7 | .31 ± 20% | .37 | | 4658.3 | 2.52 ± 35% | .21 |
| | 5409.7 | 1.43 ± 25% | .93 | | | | |
| | 5344.7 | .66 ± 30% | .32 | (23) | 5450.7 | .85 ± 35% | .33 |
| | 5316.1 | .29 ± 25% | .24 | | 5507.1 | .53 ± 35% | .11 |
| | | | | | 5583.3 | .51 ± 35% | .19 |
| (7) | 5296.1 | .86 ± 30% | .55 | | 5541.2 | .98 ± 35% | .45 |
| | 5191.4 | .19 ± 25% | .35 | | 5378.1 | .39 ± 30% | .11 |
| | 5152.2 | <.02 -- | .12 | | 5483.6 | .70 ± 35% | .15 |
| (10) | 5253.5 | 1.15 ± 20% | 1.00 | (27) | 5588.2 | .38 ± 35% | .15 |

*Coulomb approximations calculated by M. W. Smith, private communication, who estimates their reliability as "E" (uncertainty > 50%).

so that $T_{neon}$ was measureable, this situation is analogous to the one we encountered with silicon. Using the same modified techniques of Boldt as we applied to our silicon data, we found the relative $PH_3$ concentration to be .14 ± .03, rather than .28 as stated by the supplier.

3. Checks for internal consistency. Although $AE_{PI}$ and $ARH_{PII}$ are the thermally insensitive A-values for PI λ5477 and PII λ5253, respectively, we also measured $ARH_{PI}$ and $AE_{PII}$ to check for overall consistency. These latter results scattered more than their thermally insensitive counterparts, but agreed with them inside of joint tolerances.

4. Results. Current results for PI and PII are given in Tables XV and XVI respectively.

Tolerances for PII are smaller than for PI because $ARH_{PII}$ has a much weaker dependence on the imprecisely known $PH_3$ concentration than does $AE_{PII}$, and also because the PII lines were usually stronger and narrower (less prone to errors in background corrections) than were the PI lines.

For relative A-values of strong PII lines within the same multiplets, accuracies should be only slightly inferior to the corresponding values for the SII lines studied.

5. Comparison of PI and PII results with literature values. Table XVII compares the current PI and PII results with Coulomb approximations.[118] Relative PII line strengths within multiplets are compared with LS coupling predictions[119] in Table XXII. There are frequent departures from LS coupling which greatly exceed claimed experimental tolerances.

## H. Transition Probabilities for Selected Visible Lines of OI, NeI, AℓII and CℓI .

1. Introduction. Transition probabilities were obtained for 19 lines or blended multiplets from the spectra of OI, NeI, AℓII and CℓI . For all these spectra except AℓII our results emerged as useful by-products of studies intended for other elements, with the consequence that these data usually derive from two to eight runs per element. This is not to say that results for these lines are necessarily less accurate than our results for SI, SiI, PI, etc., for in some cases just the opposite is true -- however, a major portion of assigned tolerances represents the uncertainty in averages over very limited samplings. All of these transitions were measured in a particularly simple way, i.e. by thermally insensitive intensity ratios to lines of well-known A-values, so they are not prone to large systematic errors.

Roughly one half of our OI transitions have been measured previously,[26,120] to claimed accuracies equivalent to those of the current study. Our single CℓI line, λ4601 , has been measured in several studies,[107,111] of which Bengtson's[61] can unquestionably claim accuracies superior to our own. No prior determinations are available for the ten NeI lines, the AℓII line, or for one half of the OI lines currently studied.

Results for OI, NeI, AℓII and CℓI are collected in Table XVII together with assorted comparison values from the literature.

2. Transition probabilities for OI . On two occasions the shock tube was fired using test gases of 2% $O_2$ in neon, with the object of determining contamination concentrations of hydrogen added to our plasmas by impurities coming from the shock tube walls. Temperatures were deduced from absolute intensities of NeI λ5852 and from the half-width of $H_\beta$ , whose brightness (even as an impurity) was adequate for

Table XVIII. TRANSITION PROBABILITIES FOR OI, NeI, AlII AND CII

| Atom Multiplet | | Transition (n, lower)(m, upper) | λ(Å) | $A_{mn}$, $10^6 sec^{-1}$ This experiment | Comparison value(source) | Coulomb approximation |
|---|---|---|---|---|---|---|
| OI | (11) | $3\,^5P - 6\,^5S^0$ | 5436.1 | 3.2 ± 15% | 4.11 ± 25% §<br>3.05 ± 25% ♀ | 3.48 |
| | (12) | $3\,^5P - 5\,^5D^0$ | 5330.0 | 1.8 ± 20% | 1.97 ± 25% ♀<br>1.85 ± 25% § | 2.63 |
| | (13) | $3\,^5P - 7\,^5S^0$ | 5019.5 | 1.3 ± 20% | --- | --- |
| | (14) | $3\,^5P - 6\,^5D^0$ | 4968.1 | .31 ± 25% | --- | --- |
| | (15) | $3\,^5P - 8\,^5S^0$ | 4802.3 | <.15 --- | --- | --- |
| | (16) | $3\,^5P - 7\,^5D^0$ | 4773.3 | <.01 --- | --- | --- |
| | (22) | $3\,^3P - 6\,^3S^0$ | 6064.4 | 2.5 ± 20% | 2.34 25% ♀ | 2.87 |
| NeI | ( 1) | $3s1^\circ - 3p4$ | 6217.3 | 9.9 ± 25% | 7.7 ♀ | --- |
| | | $- 3p5$ | 6143.1 | 29.9 ± 25% | 21.6 ♀ | --- |
| | | $- 3p8$ | 5944.8 | 11.2 ± 20% | 10.5 ♀ | --- |
| | | $- 3p9$ | 5881.9 | 12.7 ± 20% | 12.8 ♀ | |
| | ( 3) | $3s2^\circ - 3p6$ | 6074.3 | 57.0 ± 20% | 61.7 ♀ | --- |
| | | $- 3p10$ | 5400.6 | 1.4 ± 20% | --- | --- |
| | ( 5) | $3s3^\circ - 3p7$ | 6266.5 | 20.4 ± 20% | 22.3 ♀ | --- |
| | | $- 3p9$ | 6163.6 | 19.4 ± 20% | 16.0 ♀ | --- |
| | ( 6) | $3s4^\circ - 3p9$ | 6598.9 | 24.6 ± 20% | 25.1 ♀ | --- |
| | | $- 3p10$ | 5852.5 | 75.6 ± 15% | 71.9 ♀(1) | --- |
| | ( 9) | $3p1 - 4d1^\circ$ | 5343.3 | 10.7 ± 20% | 1.4 ϕ | --- |
| | | $- 4d2^\circ$ | 5341.1 | | 5.1 ϕ | |
| | | $- 4d5^\circ$ | 5330.8 | | 4.0 ϕ | |
| | (11) | $3p1 - 5d1^\circ$ | 4710.1 | 1.1 ± 25% † | --- | --- |
| | | $- 5d2^\circ$ | 4708.9 | | | |
| | | $- 5d5^\circ$ | 4704.4 | | | |
| | (16)† | $3p2 - 6d3^\circ$ | 4712.1 | | | |
| | | $- 6d8^\circ$ | 4715.3 | | | |
| | (13) | $3p2 - 4d3^\circ$ | 5764.4 | 11.4 ± 25% | --- | --- |
| | (14) | $3p2 - 5d3^\circ$ | 5037.8 | 3.8 ± 30% | 4.65ϕ | --- |
| | (19) | $3p3 - 4d4^\circ$ | 5820.2 | 6.7 ± 30% | --- | --- |
| | | $- 4d10^\circ$ | 5562.8 | 2.4 ± 25% | --- | --- |
| | (24) | $3p4 - 4d9^\circ$ | 5656.7 | 5.4 ± 30% | --- | --- |
| | (25) | $3p4 - 5d11^\circ$ | 4957.0 | 1.0 ± 30% | 2.25ϕ | --- |
| | (34) | $3p8 - 5d11^\circ$ | 5145.0 | 3.5 ± 45% | 2.88ϕ | --- |
| | | $- 5d10^\circ$ | 5144.9 | | | |
| AlII | (16) | $4p\,^1P^0 - 5d\,^1D$ | 5593.2 | 227. ± 35% | --- | 110. |
| CII | (15) | $4s\,^2P - 5p\,^2P^0$ | 4601.0 | 3.26 +35% −20% | 3.33 ± 5% Δ<br>4.21 ± 3% ⊕<br>4.24 ± 15% * | 5.3 |

† Two multiples blended; we give $A = \Sigma gA/\Sigma g$ .

♀ Ref. [13], § Ref. [26], Δ Ref. [111], * Ref. [51], ⊕ Ref. [107] .

ϕ Ref. [121]; intermediate coupling calculation, with estimated reliability being typically 1.5 ± 1.0 .

(1) All NeI transitions measured relative to this line.

this purpose. Taking the average of $T_{neon}$ and $T_{\lambda\frac{1}{2}}$, together with measured pressure, permitted us to deduce the relative concentrations of HI and OI from the ratio of $H_\beta$ to OI λλ6157 integrated intensities; the A-values of this blended OI multiplet were regarded as known reliably to 10%.

What is germane here is that several blended OI multiplets, although much weaker than OI λλ6157, showed up with brightness quite adequate for good photographic recording. Because these multiplets have excited states lying within 0.5 ev of OI λλ6157, their A-values measured relative to OI λλ6157 are essentially thermally insensitive. This enabled us to exploit spectra from multiply reflected shock regions in addition to the more homogeneous first reflected shock flows, so that a total of five sets of data were gleaned from the two shock tube firings.

A densitometer tracing covering 5300Å < λ < 6200Å of a spectrogram from a multiply reflected shock flow is given in Fig.67. This tracing shows signal-to-noise ratios (for emission granularity) more favorable that the typical 15% - 25% tolerances of our OI results would indicate. However, the chief error source is not noise but rather interference from other spectral features. The reference line, OI λλ6157, blends with OI λ6106, NeI λ6163 and NeI λλ5338.9 (as seen on the tracing). There is also a fairly serious blending between OI λλ5330 and NeI λλ5338.9, but fortunately we know the relative strength of this neon multiplet compared to nearby unblended neon features from our studies employing "pure" neon test gases, and so can make blending corrections for OI λλ5330.0 which are accurate to perhaps ± 10%. The tracing also shows that OI λλ5958 is "lost" between the wings of the strong NeI lines λ5944 and λ5975, while OI λ5512 and OI λ5555 are so weak as to be hardly distinguishable from grain.

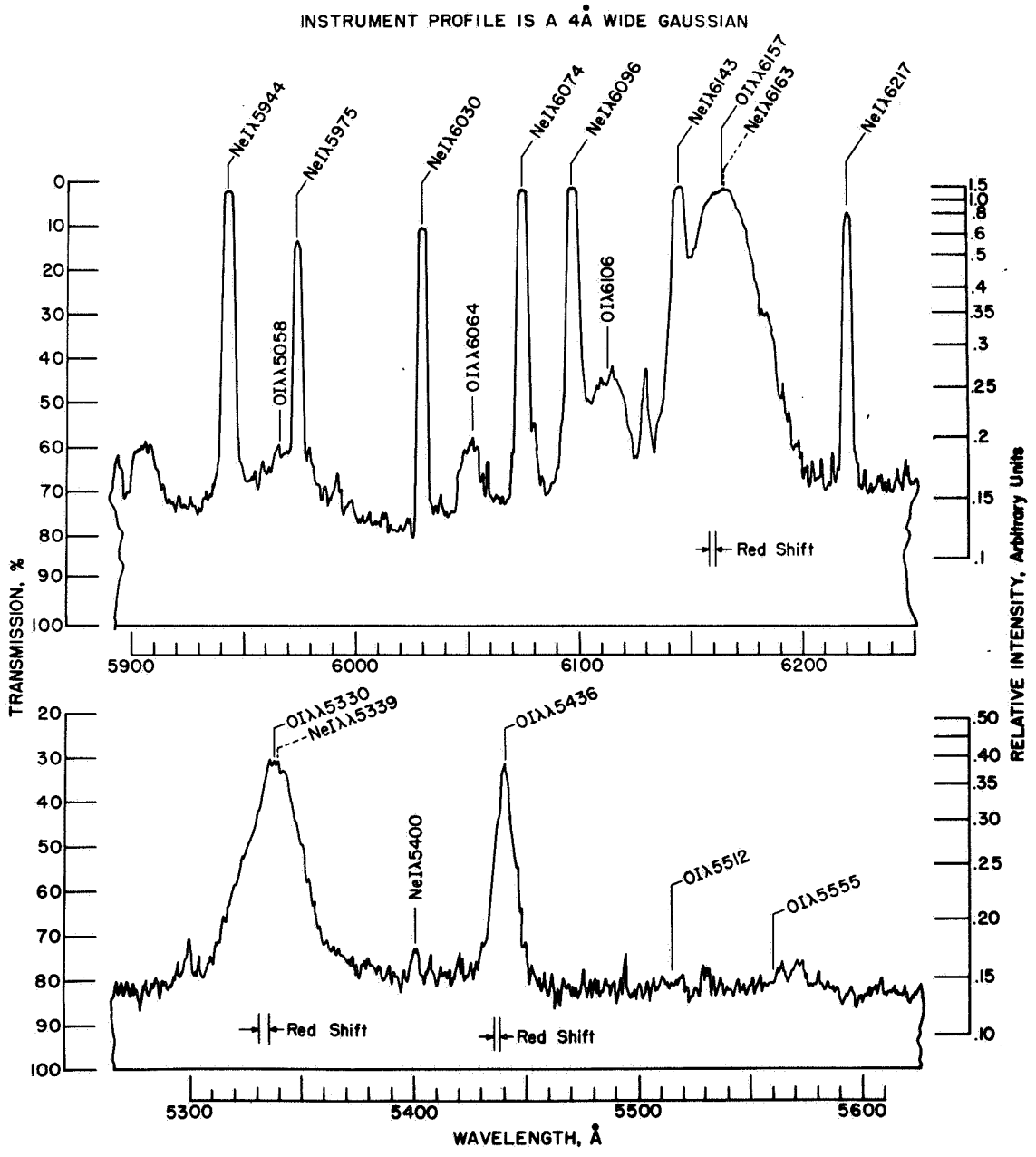


Fig. 67: Densitometer Tracings, 5300Å - 5600Å , and 5900Å - 6200Å , for Multiply-Reflected Shock in 2% $O_2$ + 98% Neon .

The better than 10% agreement between current results and NBS[13] estimates (shown in Table XVII), for OI λλ5436 , OI λλ5330 , and OI λλ6046 is well within the tolerances assigned either set of values.

3. Transition probabilities for NeI . The strong red NeI lines belonging to multiplets (1), (3), (5) and (6) are prominent features of our spectra when source temperatures exceed 11,000°K. We measure NeI λ5852 relative to $H_\beta$ to obtain the absolute A-value. The other neon lines we report are measured relative to λ5852. In previous studies absolute A-values for these lines have been obtained by radiative decay methods.[38] The excellent agreement between several authors[17] who use both relative intensity and hook methods to measure relative A-values, indicates that their combined results should be reliable to a few per cent. Table (XVIII) compares current results with literature values.

No results have been reported for many of the NeI transitions with 20-21 eV excited states. We observe several of these lines in plasmas hotter than 12,000°K, some of which are identified in the densitometer tracing, Fig. 68 ; this covers wavelengths 5200Å < λ < 6000Å for a multiply reflected region ($T \approx 12{,}200$°K) in a .11% $(CH_3)_3$ Aℓ plus neon test gas. This figure gives an impression of how strikingly wide these lines are in a typical laboratory plasma. Their uncommonly large Stark widths may very well be responsible for these lines having been for so long neglected: at T = 12,000°K and $Ne \approx 10^{17} cm^{-3}$ they appear as gentle undulations on top of surrounding continuua.

Figure 69 depicts a portion of a drum camera spectrogram of a first reflected shock in pure neon. Here, the unexpected strengths of these NeI lines, as well as their great widths, are evident.

As with OI , our method here is particularly simple -- using time resolved photographic recording, the intensities of various neon lines

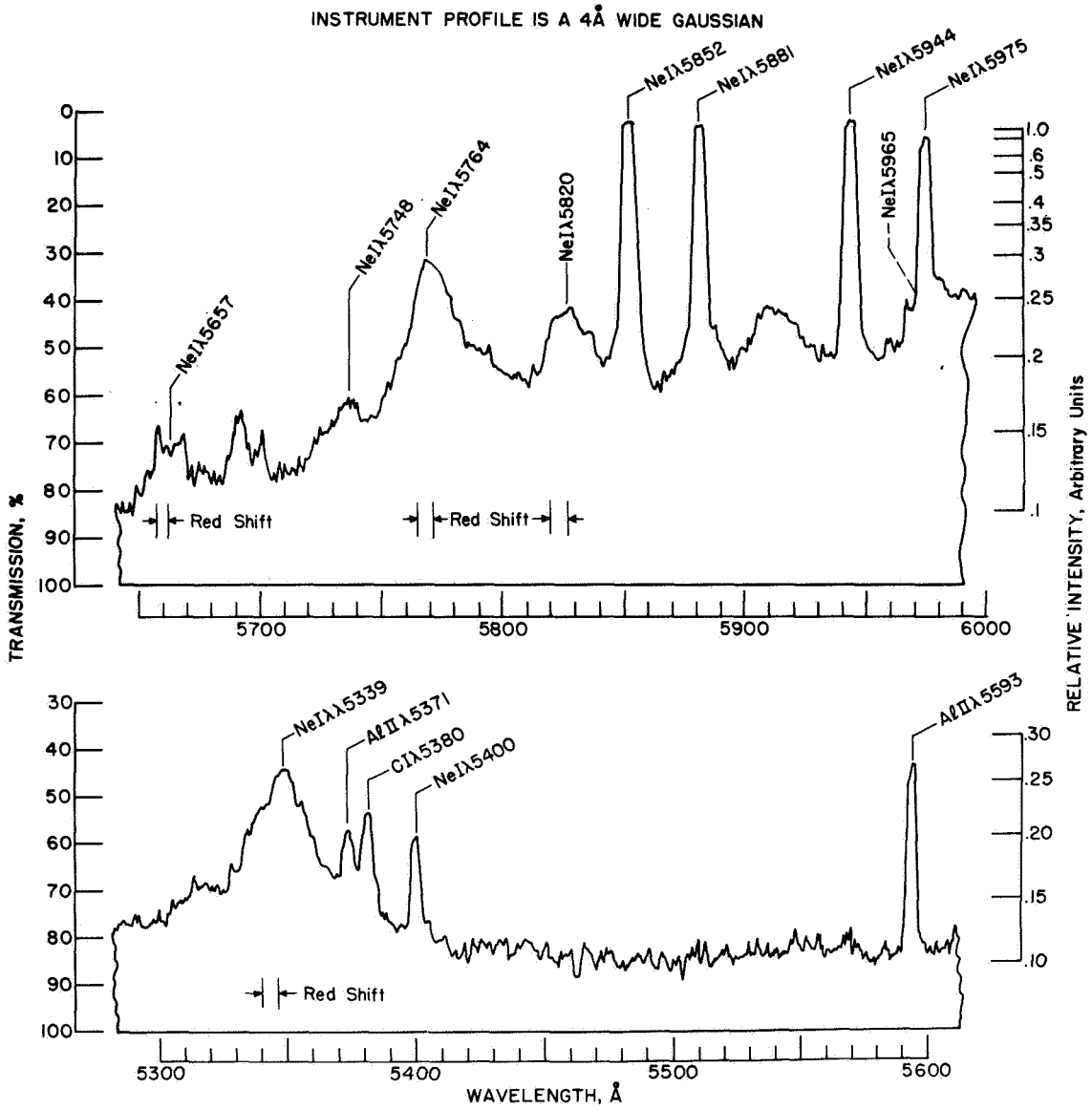


Fig. 68: Densitometer Tracing, 5300Å - 5650Å , for Shock in 0.11% $[CH_3]_3$ Aℓ + 99.89% neon.

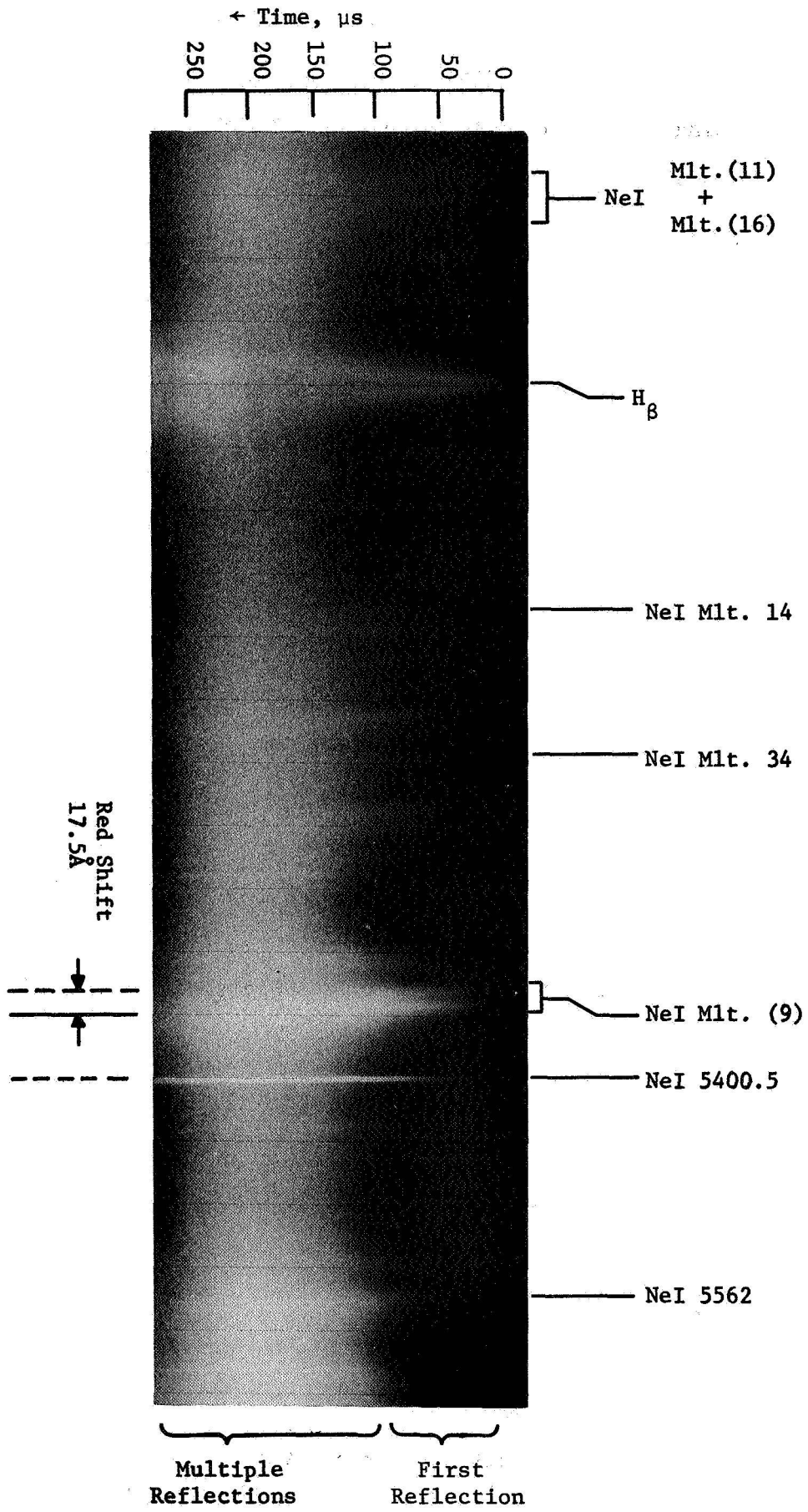


Fig. 69: Time-Resolved Spectrogram of Shock in Pure Neon Test Gas.

were compared to NeI λ5975 , (a comparison seldom spanning more than 500Å). Because the excited level separations between λ5975 and the lines being studied is only 0.2 eV for λ5400 , and 2 eV for λλ5339 , λ5764 , λ5820 and λ5657 , A-values measured relative to λ5975 have only slight thermal dependence. For the transition probability of λ5975 we adopt the NBS[13] recommended value, $4.33\times10^{6}\,sec^{-1}$, whose accuracy† is estimated at "B-" i.e., 10% - 15%. Our results therefore contain this amount of uncertainty compounded with our own experimental error due to both a paucity of data (most lines were measured 3-7 times) and the difficulty in assigning baselines to these broad profiles.

4. Transition probability for AℓII λ5593.2. Just prior to breaking down our equipment, a few runs were made using $[CH_3]_3$ Aℓ as a spectroscopic additive with the hope of measuring AℓII transition probabilities. Although no published experimental work was available for AℓII in the visible,[17] feasibility estimates employing Coulomb approximations indicated we should be able to photographically record at least AℓII λ5593.2 . This transition is ideally suited for study by TIB methods, as Fig. 16 shows, provided the initial partial pressure of $[CH_3]_3A\ell$ is known. $A(TIB)_{A\ell} = \frac{1}{2}(ARH_{A\ell} + ARN_{A\ell})$ is virtually fool-proof†† since it involves only relative intensity measurements, while temperature errors of + 1000°K or -1000°K lead to results erroneous by only + 7% and -1%, respectively. (These same temperature errors would cause AE alone to be erroneous by factors of 1/5 and 5, respectively.)

Our plans for high accuracy were foiled by an air-leak in the line admitting $[CH_3]_3A\ell$ into the system, discovered only after we had

---

†Tabulated transition probabilities of NeI λ5852 and λ6402 are estimated to be slightly more reliable, but these lines are too strong to use for direct photographic comparisons.

††That is, if one does not worry about the ≤ 5% uncertainty in $A(TIB)_{A\ell}$ from the ≤ 10% uncertainty in $A_{mn}$ of the NeI λ5852 reference line.

developed our drum camera photographs for three runs and found they contained lines of OI , but none of AℓII . The main leak source was then eliminated, but the neon remaining was enough for only one additional run.

The one run we did succeed in getting had three distinct flow regions in approximately steady state. Figure 68 shows, as we originally anticipated, that AℓII λ5593 appears with a good brightness. In attempting to reduce these data we found $T_{neon}$ to be greater than $T_\beta$ or $T_\alpha$ by several hundred degrees while $T_\beta < T_{\lambda\frac{1}{2}} < T_{neon}$ . If we disregarded these discrepancies and used $T = \frac{1}{4}(T_{neon} + T_\alpha + T_\beta + T_{\lambda\frac{1}{2}})$ to compute $ARN_{A\ell}(T,p)$ and $ARH_{A\ell}(T,p)$ , we consistently found $ARH_{A\ell} \simeq 3\ ARN_{A\ell}$ for all three flow regions. These discrepancies all point to the same conclusion, namely, that initial partial pressure of $[CH_3]_3A\ell$ was 2-3 times less than assumed. The valve on the lecture bottle containing the trimethyl aluminum sealed erratically, making it possible for it to have sealed during our helium leak checks and yet to have passed air when cracked open for withdrawal of trimethyl aluminum.

Without a reliable initial partial pressure of $[CH_3]_3A\ell$ we could not use $ARN_{A\ell}$ and hence could not form $A(TIB)_{A\ell} = \frac{1}{2}(ARH_{A\ell} + ARN_{A\ell})$. However, the transition probability, $ARH_{A\ell}$ of AℓII λ5593 , is only weakly dependent (at temperatures above 1eV ) on the absolute concentration of trimethyl aluminum, since the hydrogen to aluminum (ion) relative concentrations are set primarily by the stoichiometric ratio, 9:1. The ratio of $H_\beta$- to- NeI λ5975 excited state densities is not critically dependent on temperature, so $T_{neon}$ is good enough to allow us to deduce the absolute concentration of hydrogen to ± 35% (and hence, the absolute concentrations of aluminum and carbon also) from the observed intensity ratio

and known A-value ratio of $H_\beta$ -to- NeI λ5852. Consulting Fig.16 we see that a ± 15% temperature error has no more than a ∓ 20% effect on $ARH_{A\ell}$ .

We found $ARH_{A\ell}$ for all three shock regions (spanning a temperature range of 800°K) agreed with each other to 15%. As a control, we simultaneously measured CI λ5052 using the $ARH_C$ method, noting that (cf. Fig. 5 and Fig.16 )

$$\left|\frac{\partial ARH_C}{\partial T}\right| \simeq \left|\frac{\partial ARH_{A\ell}}{\partial T}\right|$$

These control A-values grouped within 15% of each other for all three shock regions, giving an average A-value 12% higher than our adopted CI λ5052 A-value, $1.7_4 \times 10^6 sec^{-1}$ .

Still, with only three scans available, this procedure does not accurately overdetermine the state of our source. In view of the paucity of data and the uncertainty in the aluminum impurity levels (cf. Chapter VI), we attach a 35% tolerance to our results for AℓII 5593, $A_{mn} = 2.35 \times 10^8 sec^{-1}$.

5. <u>Transition probability for CℓI λ4601</u> . Our chlorine results are limited to the single line CℓI λ4601 , and the data for this consists of that single run using $SiHC\ell_3$ additives that survived mishaps in photographic developing. For this one run, however, the photographic profiles of both $H_\beta$ and CℓI λ4601 were well-defined and the four temperatures $T_\alpha$ , $T_\beta$ , $T_{\lambda\frac{1}{2}}$ and $T_{neon}$ agreed mutually to 2%, so the ARH transition probability, which is not very thermally sensitive anyway, would be accurate to ± 20% if λ4601 did not fall very close to the edge of the drum camera film. Because the amount of vignetting at the edge of the film is only

approximately known, we believe our result, 3.26 $10^6 sec^{-1}$, is reliable to $^{+35\%}_{-20\%}$ . This result agrees to better than 20% with the average of the three previous studies[61,107,111].

## I. Stark Widths and Shifts for Neutral Lines .

1. Introduction. Total Stark widths and shifts were measured for sixteen lines selected from the spectra of CI , OI , NeI , SiI , PI , CℓI and AI . Only the width of CI λ5052 has any relevance to our main objective of securing A-values; measured broadening parameters for this line were employed in calculating wing corrections for the slit-integrated absolute intensities. Broadening studies were not included among the planned objectives of our investigations, but emerged naturally when it was realized that our photographic data contained a wealth of lines that were observed to broaden and shift several Å , or even tens of Å . Since densitometer tracings, reduced to intensity profiles, were already on hand for reduction of A-value data, line shifts and widths could be had essentially by laying a ruler along a strip chart recording. We elected, for the time being, to measure a limited number of lines which exhibited the most pronounced broadening and shifting for a particular spectrum and which had profiles the least complicated by interference with other lines or by low signal-to-noise ratios.

With this limited set of lines we should enjoy high accuracies,† because reading errors and errors in instrumental profiles will generally be very small relative to the large shifts and widths we observe. If our results are to pose a more stringent than usual test of Griem's theory for

---

†We measure the merged multiplet OI λλ6046 in spite of the fact we cannot achieve good accuracy (it is too faint) because it is one of the few lines where we can compare results with previous experiments.

Stark broadening of light neutrals, then our overall tolerances must be less than 20%, since this level of agreement between theory and experiment has been amply demonstrated. The same criterion need not be applied to shift measurements, since even 20% accuracy results will make welcome additions to the handful of previous determinations[122].

The union of a conventional shock tube and time-resolved photographic spectroscopy creates a system well-suited for measuring line shifts and widths as functions of plasma electron density. Between the first and multiple reflected shock regions, temperatures typically increase 500°K to 1000°K (i.e. 5% to 10%) while electron densities typically increase by factors of 1.8 to 2.5, depending on test gases used. So on the same piece of drum camera film a line might be observed, say, at $Ne = 4\times10^{16}cm^{-3}$ and again at $Ne = 9\times10^{16}cm^{-3}$, while the temperature, for line broadening purposes, remains essentially constant. Moreover, by selecting initial conditions purposely to vary plasma temperatures for our A-value studies, we often changed electron densities between different first reflected shocks in the same test gases by more than a factor of two. Altogether then, we often recorded spectra of an element over a range of 4 (or more) in electron density (as can be seen from Fig. 44 and Table II). Had it been our intention, this range of electron densities could readily have been doubled.

Time resolved photographic recording of luminous multicomponent plasmas also provides, in a very simple and direct way, means for determining both the plasma electron density and the absolute wavelengths at a number of points in the emitted spectra: That is, any spectrogram containing $H_\beta$ contains its own record of electron densities since Griem's predictions for the Stark broadening of this line have been verified to 5%.

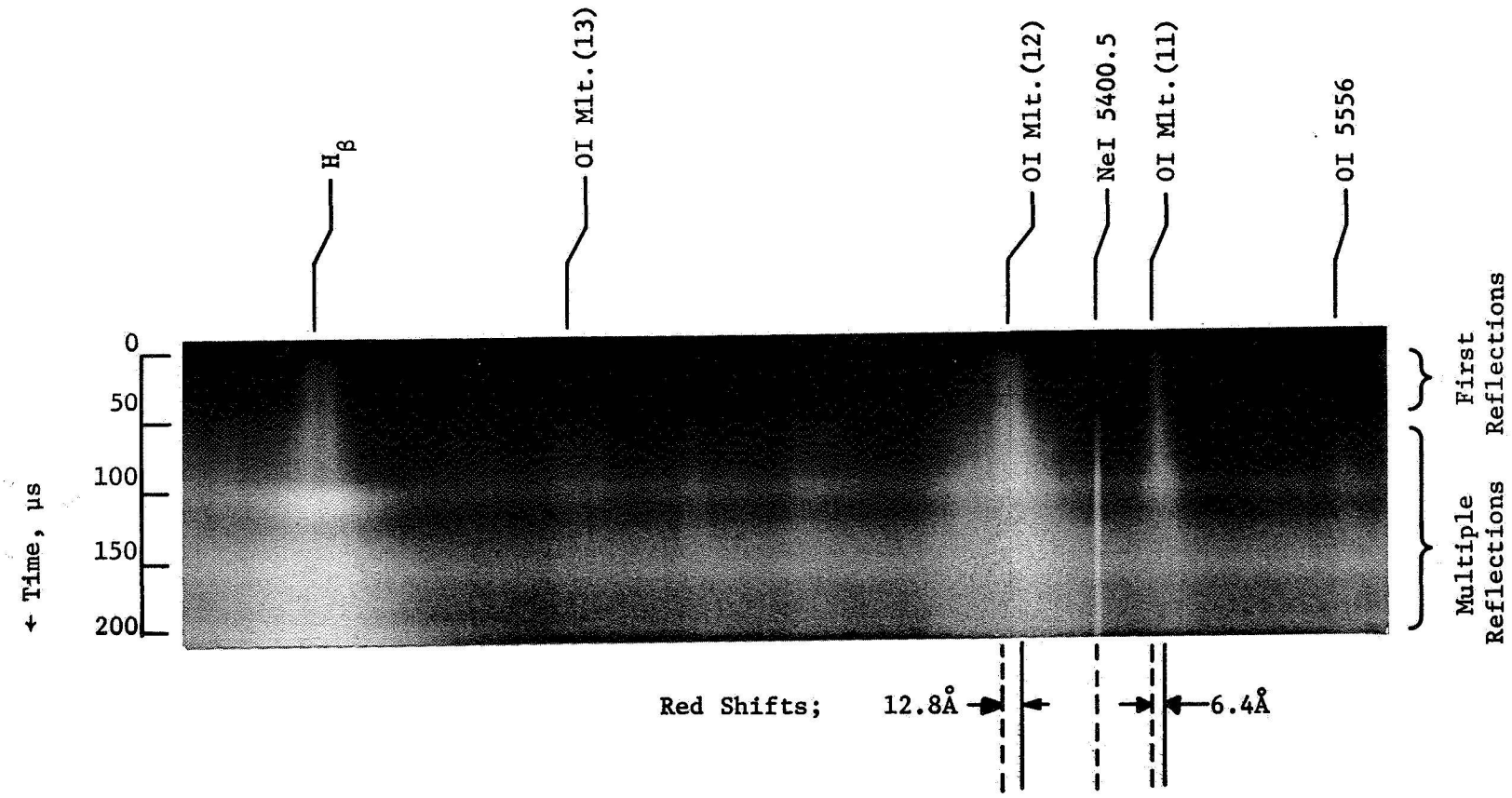


Fig. 70: Time-Resolved Spectrogram of Shock in 2% $O_2$ + Neon.

Many (first) ion lines and neon lines belonging to low-lying multiplets shift no more than 1/10 to 1/100 as much as the broad neutral lines being studied, and hence serve as wavelength fiduciaries for shift measurements. The shifts of the ions themselves can approximately be taken into account when they are significant. Also, there are usually enough ion lines in the proximity of a broad neutral that shifts can be determined relative to several of them and intercompared for consistency.

Figures 69 and 70 provide particularly dramatic examples of how the advantages of conventional shock tube sources mesh with the advantages of time-resolved photographic spectroscopy to yield easily reduced and reliable shift and broadening data. Figure 70 consists of a time-resolved spectrogram of shock tube luminosity from a test gas of 2% $O_2$ in neon. Impurity levels (from wall-borne contaminants) of hydrogen are sufficient to give $H_\beta$ useful photographic densities within most shock regimes shown; only in the late multiple reflected regions does it become difficult to distinguish the $H_\beta$ baseline from the high continuum levels. The subjects of study here are the merged OI multiplets λλ5436.1 and λλ5329.9 . The narrow line between them is NeI λ5400.46 of neon multiplet (3). We use this line as the wavelength marker.

Both the shifting and broadening of the OI lines as time progresses is immediately apparent to the naked eye. By repetitively scanning these spectrograms with a densitometer of slit height extension 5μs in the time direction we constructed the width vs. shift curves for these multiplets shown in Fig. 71 . The plotted points have been corrected for the $\approx$ 2Å separation of components by methods discussed in the next section. We ceased to scan when the full halfwidth of λλ5329.9 reached 60.0Å because for later times (greater widths) the film became so

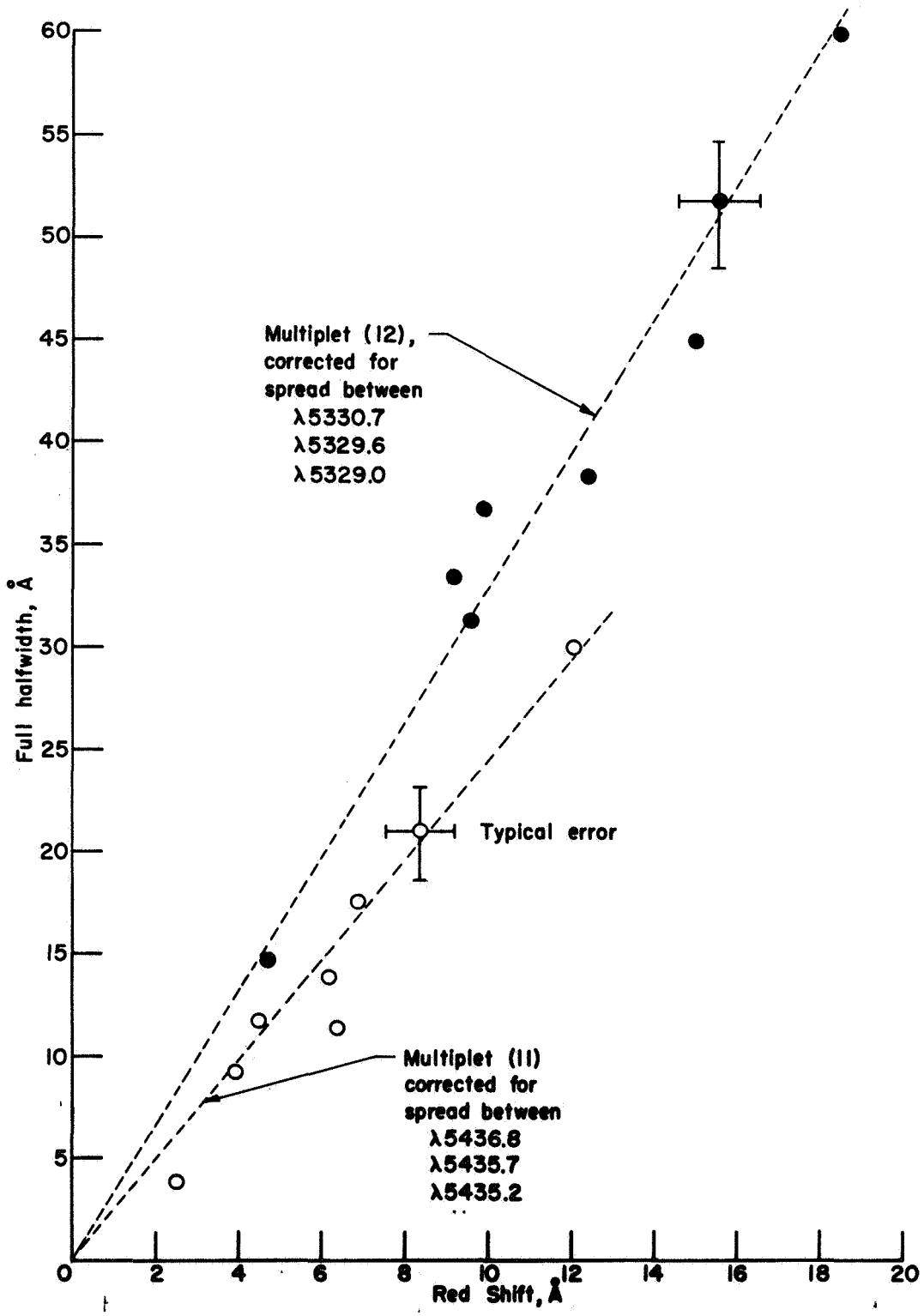


Fig. 71: (Full) Halfwidth vs. Red Shift for Blended Multiplets (11) and (12) of OI .

dense as to spoil the relative intensity calibrations. Out of 16 data points shown, 13 fall within ± 10% of linear shift-to-width relationships.

Figure 69 illustrates another case where large progressive broadening and shifting are observed in a single drum camera exposure: the test gas is pure neon (plus wall impurities). The narrow unshifted line is NeI λ5400.5 and the many broad features that shift to the red with time (increasing electron density) are the highly excited NeI lines listed in Table .

2. Method. Data for CI λ5052 , SI λλ4695 , and Aℓ λ6752 were recorded using the (nominal) 1Å entrance slits whose instrument profile is given in Fig. 72 : all other neutral line broadening was studied with wider slits producing a Gaussian instrument profile of full halfwidth 4.0Å . For the lines listed in Table IXX halfwidth data were collected from shock regions where electron densities gave ratios of line width to instrument width between 1 and 10; the majority of data was taken with this ratio of order 4.

To unscramble the instrumental widths from the true line half-widths, we used tabulated solutions of the convolution integral eqn. [14]. Knowing the instrument halfwidth, these solutions can be applied in a straightforward way to isolated lines, but complications arise for merged multiplets with significant wavelength separations between components. In the present work this complication is serious only for the multiplet SI λλ4695 , where the 2.1Å spread of the three lines comprising the multiplet is not small compared to the 3Å to 6Å widths for the merged multiplet. For other merged multiplets the spread between (the extreme) components amounts to only one-fourth to one-tenth of the merged multiplet full halfwidths, and is more easily corrected for. To treat SI λλ4695

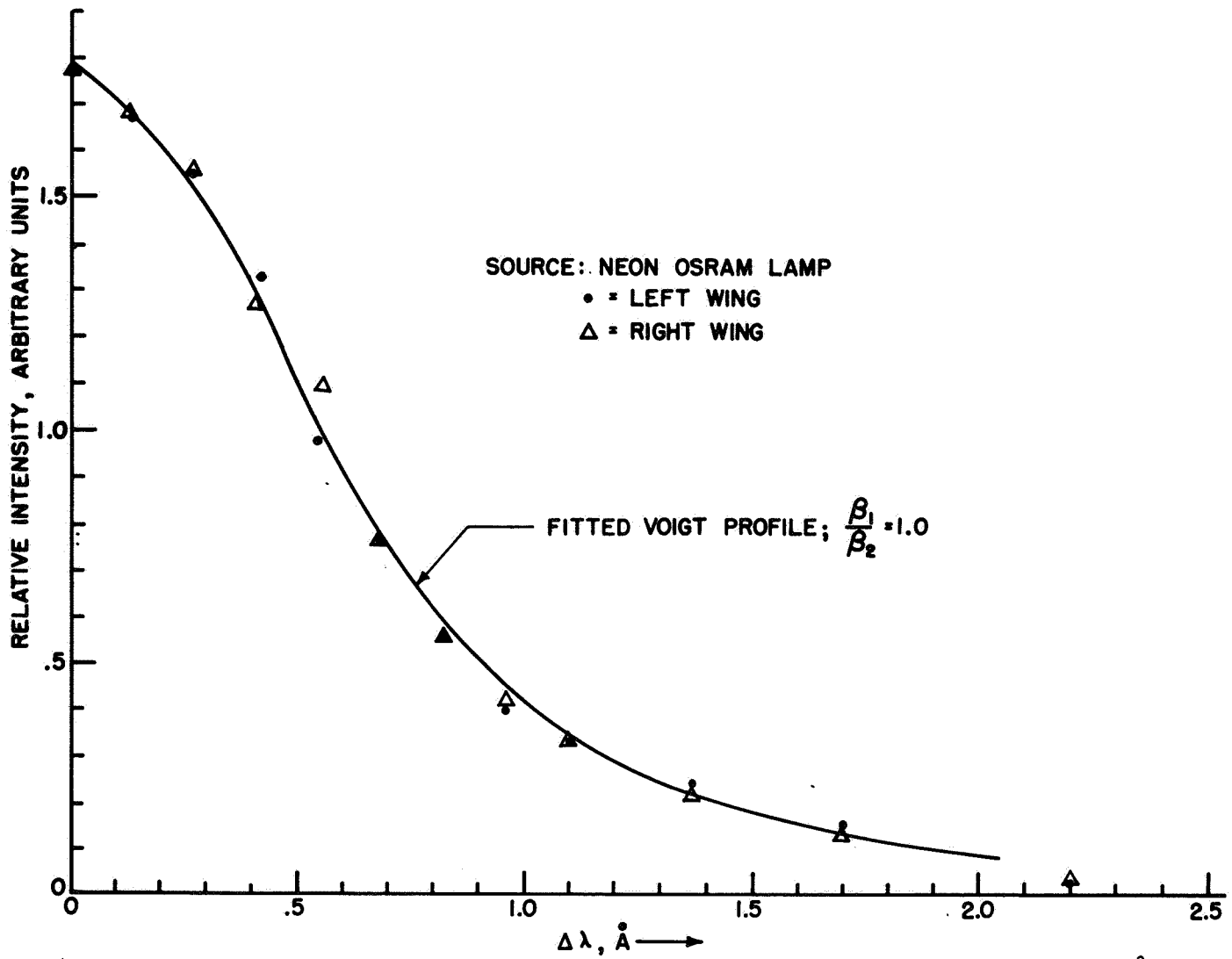


Fig. 72: Instrument Profile for 0.75 Meter JACO Fast Spectrograph Using 50μ Slit (1.0Å Bandpass)

we assume the three blended lines comprising the multiplet broaden equally, and that their relative strengths are governed by LS coupling. Using these assumptions to graphically combine three Lorentzian profiles of equal width, known separation, and known relative peak heights, we establish the relationship between the blended multiplet halfwidth and the halfwidths of its members. Separation of the multiplet's members changes the blended profile's shape, as well as its width, by increasing the Gaussian fraction, so a further correction is necessary to data which was routinely reduced on the assumption that the only Gaussian component† in the observed profiles was the .67Å contribution from the instrument profile. Therefore a second curve was constructed giving the multiplet halfwidth, as it would appear after slit unscrambling, as a function of the Stark halfwidth of its component members. For comparison with theory we used Griem's predicted values for impact and ion broadening parameters to calculate (total) Stark halfwidths as a functions of electron density and then applied the appropriate slit corrections, producing the dashed curve in Fig. 73 which is compatible with the slit-unfolded data points.

The shift of SI λλ4695 was measured using SII λ4716.22 as a wavelength fiduciary. Bridges' value for the observed width (this ion line was too faint to give us profiles reliable enough for halfwidth measurements) was used to scale Griem's prediction for the shift of this ion line. Because λ4716 is quite broad for an ion, error in its calculated shift might be as great as .3Å, an error that can pass directly into the measured shift of SI λλ4695. Unfortunately, no other SII lines were available as fiduciaries in this wavelength region and our

---

†Doppler broadening is completely negligible compared to Stark broadening for these neutrals.

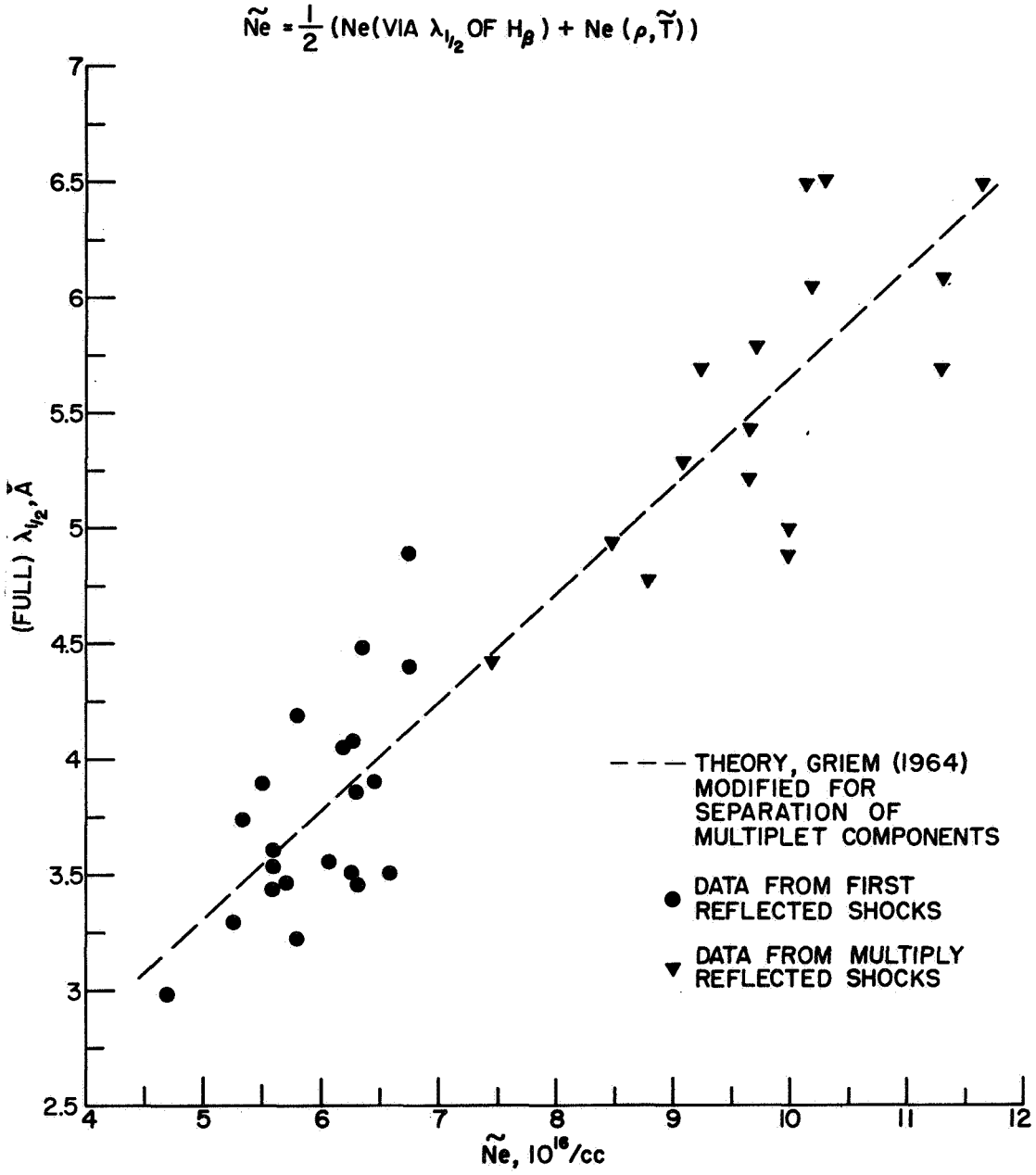


Fig. 73: (Full) Halfwidths of SI λλ4695 Measured as Functions of Electron Density.

densitometer, with its braided-wire drive, cannot be relied upon to maintain constant scanning speed to better than .3%; therefore we could not use narrow SII lines at 5400Å as wavelength fiduciaries.

For other merged multiplets the reduction of profiles was much simpler because the widths of the blended multiplets were 4 to 10 times greater than the spread between the multiplets' members, as we have said, but equally as important, because wide slits producing 4Å wide Gaussian profiles were used. That is, if three lines have comparable strength and are more or less equally spaced within a total 2Å spread, and each of them has a dispersion profile much wider than 2Å , the net effect of their 2Å separation upon the blended profile can be approximated by adding a 2Å Gaussian component, $\beta_1$ , to a single imaginary multiplet member at the center of gravity. Since the 4Å Gaussian component, $\beta_2$ , of the instrument profile is twice as great at $\beta_1$ , the Gaussian component of the convoluted (true + instrument) profile, $\beta_3$ , is little influenced by $\beta_1$ because[64]:

$$\beta_3 = (\beta_1^2 + \beta_2^2)^{\frac{1}{2}}$$

So the wide slit has a greater influence on the observed profiles than does the separation between the multiplets' members. The value of $\beta_3$ was computed for each of the different blended multiplets even though it differed from 2.1Å by only a few per cent in all cases studied.

Electron densities for each densitometer scan (5μs time integrated photographic record) were obtained from the halfwidth of $H_\beta$ , with the exception of the data for AI λ6752.8, where the halfwidth of $H_\alpha$ was used instead. Here $H_\alpha$ was optically thin because hydrogen was present at low impurity concentrations.

The wavelength standard for the shift measurements of NeI λ5764.4 and NeI λ5820.1 was NeI λ5852.5 ; for SiI λ5848.5 and OI λλ6046.4 the standard was NeI λ5975.5 ; while OI λλ6157.3 and AI λ6752.8 rely on NeI λ6143 and NeI λ6698.9 , respectively. The (small) shifts of the neon fiduciary lines were calculated from Griem's tables[7].

The great majority of width and shift measurements were performed at plasma densities between $4\times10^{16}cm^{-3}$ and $8\times10^{16}cm^{-3}$ .

3. Results. Stark shifts and widths for sixteen lines (or blended multiplets) are given in Table IXX together with values predicted by Griem's[7] theory and with whatever previous experimental values are available. Tolerances are 80% confidence limits, usually $1.29\sqrt{\sigma/n}$ , with $\sigma$ and n the standard deviation and number of runs for a set of data. In a few instances the cited tolerances are larger than this to account for the possibility that we might repeatedly misinterpret profiles because of small interferences. We did not check the majority of the slit-unfolded profiles to see if they conformed to dispersion profiles in the wings.

Two sources of systematic error can enter our results and both might cause slight overestimates of line halfwidths. Both potential errors can be commited during the densitometer scanning of time-resolved spectrograms. If there is anything less than perfect alignment between the densitometer slits and the lines being scanned the resulting skewness registers as spurious broadening. Because the Jaco #2310 densitometer provides a 15X magnified image of its slits superimposed on the spectrogram, it is possible to consistently align the slits, of .5 mm height, to within 30' of arc. Since reciprocal dispersion of the spectrograms is 20Å/mm , the spurious broadening from slit misalignment seldom exceeds .05Å . It is therefore altogether negligible for our neutral lines with the possible

Table IXX TOTAL STARK SHIFTS AND WIDTHS FOR NEUTRAL LINES

$Ne = 10^{17} cm^{-3}$ , $T = 11,000^{o}K$

| Multiplet | | λ(Å) | Full-halfwidth, Å: This § experiment | Full-halfwidth, Å: Previous § experiment (Ref.) | Full-halfwidth, Å: Theory Griem(1964) | Red Shift, Å: This experiment | Red Shift, Å: Previous experiment (Ref.) | Red Shift, Å: Theory Griem(1964) |
|---|---|---|---|---|---|---|---|---|
| CI | (11) | 5380.2 | 2.99 ± .2 | --- | 2.54 | .38 ± .3 | --- | 1.39 |
| | (12) | 5052.1 | 3.90 ± .2 | --- | 3.99 | 2.20 ± .3 | --- | 2.25 |
| | (13) | 4932.0 | 4.07 ± .5 | --- | 5.20 | 3.02 ± .3 | --- | 3.04 |
| OI | (10) | 6157.3* | 37.2 ± 4. | --- | --- | 16.6 ± 2. | --- | --- |
| OI | (11) | 5436.1* | 27.2 ± 2. | --- | --- | 10.8 ± 1.1 | --- | --- |
| OI | (12) | 5329.9* | 70.6 ± 4. | --- | --- | 21.6 ± 1.1 | --- | --- |
| OI | (22) | 6046.4* | 27.8 ± 6. † | 35.0 ± 5.3(a) | 34.5 | 13.2 ± 2.6 | 16.2 ± 2.7(a) | 17.4 |
| NeI | ( 9) | 5338.9* | 50.4 ± 5 | --- | --- | 15.0 ± 3. | --- | --- |
| NeI | (13) | 5764.4 | 31.0 ± 2. | --- | --- | 12.4 ± 1.9 | --- | --- |
| NeI | (19) | 5820.1 | 23.8 ± 2. | --- | --- | 13.8 ± 2.8 | --- | --- |
| SiI | (10) | 5645.7 | 7.4 ± .7 | --- | 7.18 | --- | --- | 4.15 |
| | | 5665.6 | 7.3 ± .7 | --- | 7.18 | --- | --- | 4.15 |
| | | 5690.5 | 7.7 ± .7 | --- | 7.18 | --- | --- | 4.15 |
| | | 5701.1 | 6.5 ± .7 | --- | 7.18 | --- | --- | 4.15 |
| | | 5708.4 | 7.1 ± .7 | --- | 7.18 | --- | --- | 4.15 |
| | | Average: | 7.2 ± .3 | --- | 7.18 | --- | --- | 4.15 |
| SiI | (11) | 5684.5 | 7.5 ± .7 | --- | 7.41 | --- | --- | .20 |
| SiI | (16) | 5948.5 | 11.6 ± .8 | --- | 11.10 | --- | --- | 5.95 |
| SiI | (17.08) | 5006.0 | 13.9 ± 1.4 | --- | --- | --- | --- | --- |
| PI | ( 2) | 5515.9* | 11.8 ± 2.0 | --- | --- | 4.6 ± 1.0 | --- | --- |
| SI | ( 2) | 4695.1* | 5.3 ± .7 | 4.86 ± .5(b) | 5.25 | 2.78 ± .3 | 2.44 ± .3 | 2.17 |
| | ( 4) | 5278.9* | 4.8 ± .2 | 4.29 ± .4(b) | 5.08 | 3.10 ± .3 | --- | 2.67 |
| | ( 8) | 6751.0* | 31.8 ± 4.0 | 34.7 ± 2.0(b) | 33.4 | 2.3 ± 1.5 | 1.3 ± 1.5 | 1.91 |
| CaI[x] | (15) | 4601.0 | 5.0 ± .4 | --- | 4.97 | --- | --- | 2.70 |
| AI[x] | (11) | 6752.8 | 9.4 ± 1.0 | --- | 9.17 | 3.1 ± .5 | --- | 3.40 |

*Center of gravity for merged multiplet.

[x]Data (and calculated values) taken at $T = 10,000^{o}K$.

§Corrected for spread in multiplets.

†Estimated accuracy for the single determination available.

(a) W.L. Wiese and P.W. Murphy, Phys. Rev. 135, 2108 (1963).

(b) J.M. Bridges and W.L. Wiese, Phys. Rev. 159, 31 (1967).

exception of the most narrow ones, CI λ5052 , and CIλ5380 . The second source of error arises because the finite densitometer slit height has extension in the time direction of the spectrograms and therefore mixes shifts with widths if plasma conditions vary within the slit-integrated sampling time (typically 6μs). Because the red shifts are numerically about one half as great as full halfwidths, and because electron densities within a given flow region usually do not increase more than 2% in 6μs , we estimate the spurious increase in our halfwidths to be not more than 2%.

Turning to some particular results of Table IXX , we re-emphasize that OI λλ6046.4 is by far our least accurate result. Because of its faintness this blended multiplet could be discriminated above grain only late in the multiply reflected region of a single experimental run where $H_\beta$ was so diffuse, (and background levels so high) that electron density could be determined with no more than 20% - 25% accuracy. Again, our motive for including this result of sub-standard accuracy was to get a comparison against one of the few published shift and width measurements. It should be noted that although the current values for shift width are 20% below those of Wiese and Murphy,[123] we agree to within 3% on the ratio of shift/width.

Results for the other three blended OI multiplets listed should be more accurate because these multiplets have at least ten times the brightness of λλ6046.4 , and therefore could be measured over wide ranges of temperatures (and, correspondingly, electron densities), including several where the $H_\beta$ profile could be very clearly delineated. So electron densities are much more firmly established than for λλ6046.4 .

The tolerances for the Stark widths of CI λ5052 , CI λ5380 and SI λλ4695 are felt to be realistic even though these features are the narrowest (neutral) ones measured, and the lines were often so faint

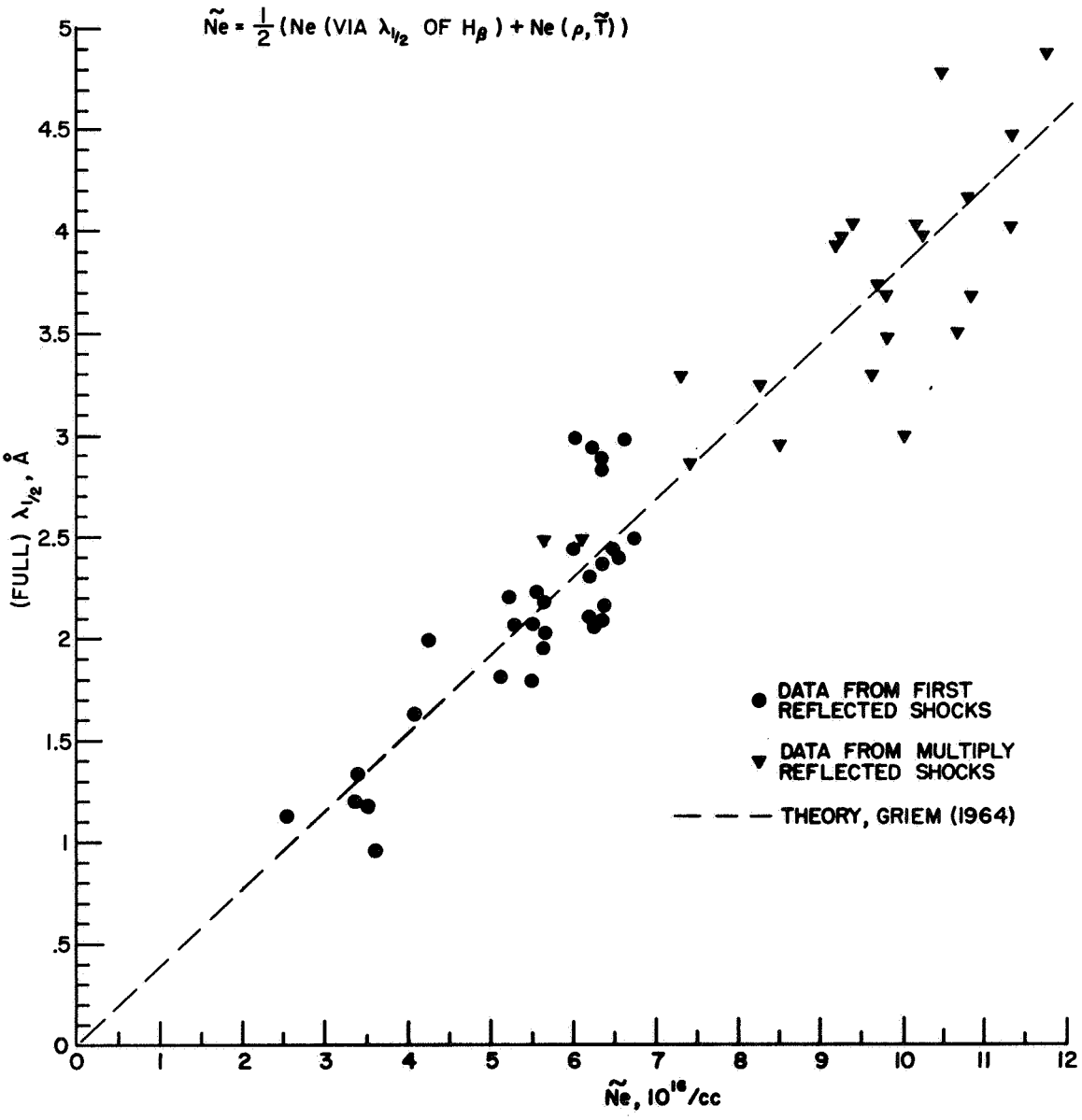


Fig. 74: (Full) Halfwidths of CI λ5052 Measured as Functions of Electron Density.

that grain made the profiles quite ragged (cf. Fig. 47 ). The data for CI λ5052 and SI λλ4695 , shown in Figs. 74 and 73 , respectively, display the 10% - 20% scatter we expect on the basis of photographic signal-to-noise ratios discussed in Section B-7 of Chapter VI . It is the large number of data, and the wide range of electron densities covered, that allows us to extract a precise average value. Measured shifts for CI λ5052 are (relatively) more accurate than for SI λλ4695 because the wavelength reference (SII λ5032.4) for CI λ5052 was available on more runs, and is expected to shift less, than SII 4716.2 , the reference line for SI λλ4695 .

Results for PI λλ5515.9 have a relatively large tolerance to cover possible errors from interference†. The blended multiplet PI λλ5515.9 is composed of the three lines (using Martin's[116] designations):

λ5515.00 , $3p^4\ 4P_{1\frac{1}{2}} - 4f\ 2D^o_1$ , Intensity = 10

λ5514.79 , $3p^4\ 4P_{1\frac{1}{2}} - 4f\ 4D_{2\frac{1}{2}}$ , Intensity = 60

λ5517.01 , $3p^4\ 4P_{1\frac{1}{2}} - 4f\ 4D_{3\frac{1}{2}}$ , Intensity = 80 .

Since the upper state of the LS coupling-forbidden line λλ5515.0 is $^2D$ , it is influenced by a different set of dipole-allowed perturbers than are $^4D$ excited states of the two other lines composing this merged feature. However, the LS coupling-allowed lines comprise more than 90% of the λλ5515.9 total intensity so it is their widths and shifts we are measuring in spite of the slight interference from PI λλ5515.0 .

For all results the ratios of shifts to widths should be as accurate as the shifts themselves, since the line widths were generally determined with

---

†The several other PI lines we observed all had more serious interference, usually from PII lines.

precision not less than 2/3 the precision of the $H_\beta$ halfwidth, i.e. the line widths had precisions comparable with the measured electron densities since $Ne \propto (\lambda_{\frac{1}{2}} H_\beta)^{2/3}$ .

For sixteen of the lines studied Griem has tabulated impact and ion broadening parameters. The total Stark widths calculated with these parameters agree with our results in all cases to 20% or better, while eleven of the sixteen results agree with theory to within 5%. The average ratio of experimental to predicted widths for the sixteen lines is 0.996. Except for CI λ5380 and CI λ4932 , experiment and theory agree well within experimental tolerances of 5% - 20%. CI λ4932 has a particularly large tolerance because this line is situated on the wing of $H_\beta$ which makes it difficult to find the baseline of its profile.

The observed shifts do not agree with theory nearly as well as do the widths. According to Griem and Shen[124] the uncertainties in the calculated shifts should be of order 10% of the calculated full halfwidths. The greatest discrepancy between our measured shifts and Griem's theoretical predictions occurs for CI λ5380 . With the exception of this line, our results agree with predicted shifts to within joint uncertainties.

With respect to previous experiments: our widths and shifts for both SI λλ4695.1 and SI λλ5279 agree with Bridge's results to within either of our claimed tolerances.

## J. Stark Broadening of Ion Lines.

1. Introduction. Stark broadening was measured for lines of SII, SiII, AℓII and PII. Data were taken with instrument profiles several times wider than the lines of interest, so accuracies are not high. At the time the experiments were performed we had no intention of measuring profiles of

of narrow lines, but rather concentrated on taking whatever expedients would optimize our results for transition probabilities. Hence, wide slits were employed to give good emulsion densities to the integrated line intensities.

We were prompted to try to salvage some ion broadening information from our data by reports from several laboratories[125] that the then current theory for Stark broadening of ions underestimated observed widths by factors of 2 to 10. So it appeared, in light of the paucity of precise ion broadening studies, that results of no better than, say 20% - 60% accuracy, could still serve as bases for significant comparison with theory. We were able in some cases to obtain accuracies of this order because of a relatively large number of data at our disposal, the high electron densities of our plasmas, and the fact that narrow neutral lines, (i.e. neon lines of multiplets #1, #3, #6), could often be simultaneously measured as controls.

With regard to the quality, our results divide into two distinct groups: the results for SII Stark broadening were obtained using 1Å (nominal) wide slits, at electron densities between $5\times10^{16}cm^{-3}$ and $11\times10^{16}cm^{-3}$, and upwards of 30 different runs were available. These results are considerably more accurate than our results for Stark broadening in SiII, AℓII or PII , which were obtained using 4Å slits, with electron densities between $3\times10^{16}cm^{-3}$ and $6\times10^{16}cm^{-3}$, and for which only 3 to 12 different runs† are available.

One apparent anomaly has been observed in this work. The broadening of AℓII λ5593.2 is at least a factor of 8 less than predicted by current theory taking into account effects of strong collisions, and a factor of 8 less than Griem's older theory.

2. Method. When instrument profiles are several times wider than line profiles, broadening measurements involve the inaccuracy of a

---

†For purposes of studying broadening a "run" consists of the scan from a steady state flow region--so a time resolved spectrogram from a single firing of the shock tube might provide 2 or even 3 runs.

a difference measurement. That is, if both the line and instrument profiles were strictly Lorentzian, with halfwidths $w_\ell$ and $w_o$, respectively, the halfwidth $w_{tot}$ of the observed profile would be

$$w_{tot} = w_o + w_\ell \quad .$$

If $w_{tot}$ can be measured with an accuracy of $w_{tot}$, then the relative error in $w_\ell$, assuming the instrumental width is known perfectly, is:

$$\frac{\Delta w_\ell}{w_\ell} = \frac{\Delta w_{tot}}{w_{tot} - w_o}$$

so if $\Delta w_{tot} = .2A^\circ$, $w_{tot} = 4.3Å$ and $w_o = 4.0Å$, the relative error in line width would be 67%.

When the instrument profile is a 4.0Å wide Gaussian, the error propagated into $w_\ell$ is actually a bit worse than indicated by the above example. If one plots the Lorentzian fraction, $f_\ell$ against the Gaussian fraction, $f_g$, for the Voigt profile, it is found that

$$\frac{\partial f_g}{\partial f_\ell} \approx -2 \qquad \text{in the}$$

limit $\ell f \to 0$. Since the line profile is essentially Lorentzian†, we have:

$$w_\ell = f_\ell \, w_{tot}$$

---

†Doppler broadening does give ionic line profiles a significant Gaussian component--however, when the Gaussian instrument width is 10 times greater than this component, the Gaussian component of the Voigt profile is increased only 1%.

so that

$$\Delta w_\ell = w_{tot}\ \Delta f_\ell + f_\ell\ \Delta w_{tot}$$

or

$$\Delta w_\ell = w_{tot}\ \frac{\partial f_\ell}{\partial f_g}\ \frac{w_o}{w_{tot}} + f_\ell\ \Delta w_{tot}\ .$$

Assuming $w_o = 4.0\text{Å}$ , $w_{tot} = 4.3\text{Å}$ and $\Delta w_{tot} = .2\text{Å}$ , then:

$$f_\ell = .13\ ,\ f_g = .93$$

and

$$\Delta w_\ell - (.93)\ 2\Delta w_{tot} + .13\ \Delta w_{tot}$$

$$\Delta w_\ell \simeq 1.99\ \Delta w_{tot}$$

so that

$$\frac{\Delta w_\ell}{w_\ell} \simeq 1.99\ \frac{.2}{(.13)(4.3)} \simeq .71\ .$$

So with a reading error of .2Å and using 4Å slits we can measure a .56Å Stark broadening to 71% precision, or a .3Å Stark broadening to only a factor of 2 precision, i.e., $\frac{\Delta w_\ell}{w_\ell} = 1.3$ . If six determinations are made, then the average broadening will be uncertain, from reading errors alone, by 29% for a .56Å broadening and by 53% for a .3Å broadening. The scatter from random error in the simultaneous electron density determinations is negligible compared to these errors.

Of course, there is also ample opportunity to make systematic errors; because of the large astigmatism and large aperture of the Jaco #75,000 spectrograph, the positioning of film in the focal plane of the drum camera is very critical, so that a slight mechanical perturbation might easily change the instrument profile. To guard against this possibility we measured Stark widths of narrow neutral neon lines in the plasma as controls. Comparing these widths with Griem's predicted values, which we assume to be reliable to 20% we confirmed our a-priori estimates of scatter (based on a .2Å precision in reading the densitometer profiles) and could detect no systematic discrepancies to within the 20% significance of our statistics. Any spurious broadening from misalignment of densitometer slits must therefore average to less than .1Å .

The method used to measure the Stark width of AℓII λ5593.2 departed somewhat from that employed on SiII and PII lines. Only three scans were available, one in the first reflected shock region and the other two in multiply reflected shock regions of the same experimental run. However these scans contained, in addition to AℓII λ5593 , both NeI λ5400.5 and CI λ5380.2 . The Stark width of λ5400.5 is predicted by the neutral broadening theory of Griem,[7] and the broadening of λ5380.2 is known from our own previous measurements. These three lines appear in Fig. 68 . All three lines have nearly the same emulsion densities and lie close enough together in wavelength so that there is little chance for making photometric errors in comparing their relative intensity profiles. On the scans for all three shock regions, AℓII λ5593.2 is broader than NeI λ5400.5 and narrower than CI 5380.2 . Hence, without, even knowing the instrument profile or the plasma electron density, we can say the total Stark broadening parameter for this ionic line lies between $2.33\times10^{-2}$ and

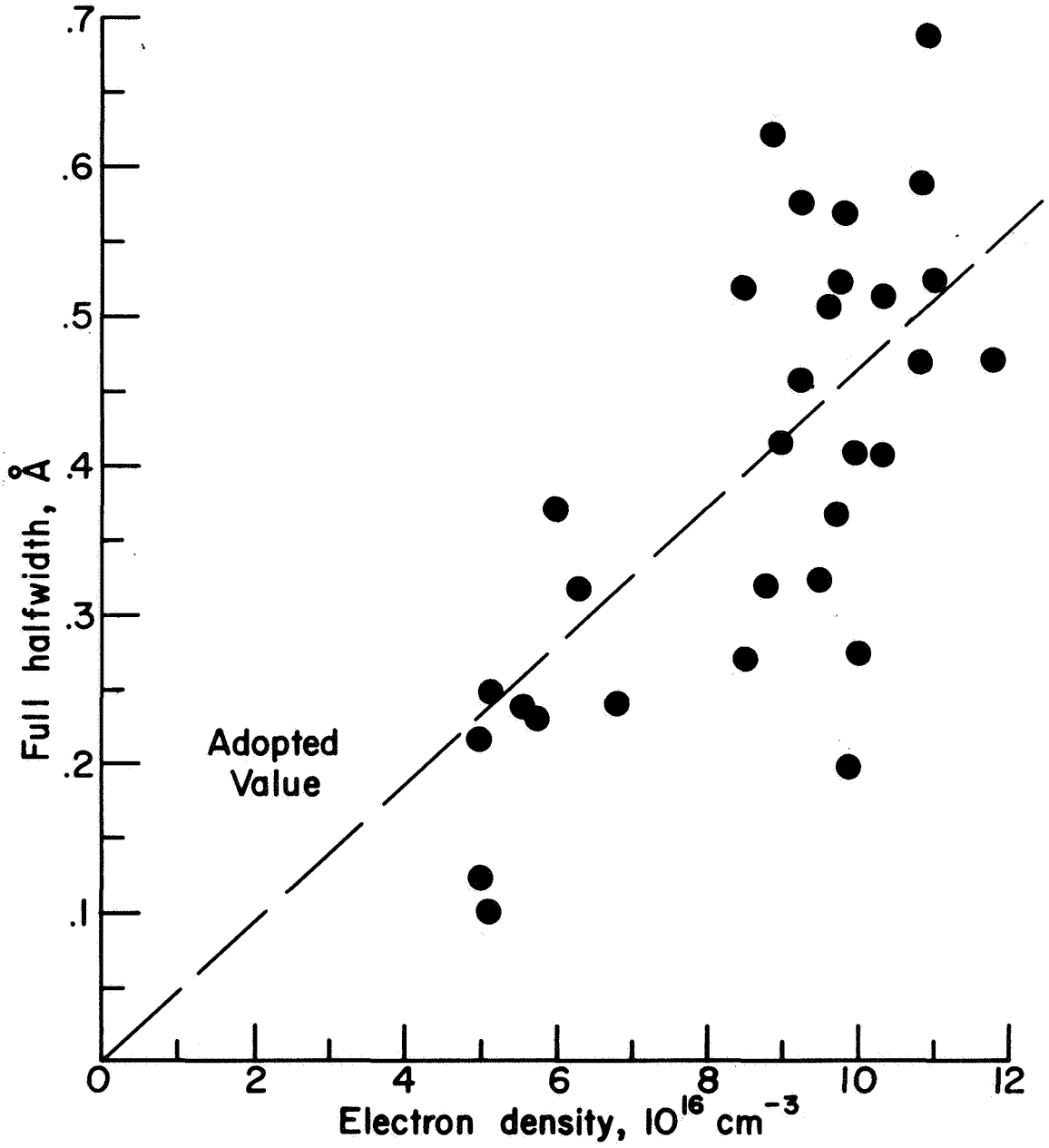


Fig. 75: (Full) Halfwidth of SII λ5453 Measured as a Function of Electron Density.

$1.21\times10^{-1}$ . In all three scans we consistently obtained the CI λ5380.2 halfwidth to within ± 20% of its accurately measured value and deduce the halfwidth of NeI λ5400.5 to believe our result for the total AℓII broadening parameter is reliable to 35%.

Because 1Å wide, rather than 4Å wide, slits were used to take data for SII broadening, we expect these results to be more precise. Assuming $w_{tot}$ = .1Å , we now take $w_{tot}$ = 1.5Å , and $w_o$ = .67Å as the Gaussian component of our nominal 1Å instrument profile and $w_o$ = .806Å as the Lorentzian component of our instrument profile. The relative error in the measured Stark width, $w_\ell$ , is:

$$\frac{\Delta w_\ell}{w_\ell} = \frac{\Delta(f_\ell \cdot (w_{tot} - w_o))}{f_\ell \cdot (w_{tot} - w_o)} \simeq 36\ \% \ .$$

Figure 75 shows our data for the Stark widths of SI 5253 as functions of electron density. Scatter is about 35%, in accordance with the above a priori estimate of precision. For the SII data runs we also measured the Stark widths of narrow NeI lines in the half dozen cases where wavelengths were recorded above λ5852Å and the lines of NeI multiplets (1) and (6) did not have excessively high densities on our emulsions. The average of these determinations gave a total broadening parameter for NeI λ5852 that was 10% below Griem's predicted value, but the significance of this average was limited to ± 15% because of large scatter.

3. Results and discussion. Current results for Stark broadening of SII are given in Table XX , along with the results of Bridges and Wiese and theoretical predictions of several authors.[7,52-54] Results for AℓII , SiII

Table XX. COMPARISON OF SII TOTAL STARK WIDTHS WITH LITERATURE VALUES.

| Multi-plet | λ(Å) | Full-halfwidth (Å) at $Ne = 10^{17} cm^{-3}$, $T = 11,000^{o}K$ | | | | | |
|---|---|---|---|---|---|---|---|
| | | Experiment | | Theory | | | |
| | | This Study | Bridges and Wiese (1967) Ref.[25] | Griem (1964) Ref.[7] | Griem (1968) Ref.[52] | Cooper and Oertel (1967) Ref.[53] | Davis and Roberts (1967) Ref.[54] |
| (1) | 5027.2 | .51 ± .16 | .56 ± .07 | .17 | .35 | --- | --- |
| (6) | 5453.8 | .47 ± .16 | .56 ± .07 | | | | |
| | 5432.8 | .55 ± .16 | .60 ± .07 | | | | |
| | 5428.6 | .45 ± .16 | .56 ± .07 | | | | |
| | 5509.7 | .49 ± .16 | .60 ± .07 | | | | |
| | 5473.6 | .55 ± .16 | .64 ± .07 | | | | |
| | 5564.9 | .60 ± .16 | --- | | | | |
| | Average: | .51 ± .13 | .58 ± .04 | .106 | .52 | .62 | .42 |
| (7) | 5103.3 | .75 ± .15 | --- | | | | |
| | 5009.5 | .60 ± .15 | --- | | | | |
| | 5032.4 | .68 ± .15 | .76 ± .07 | | | | |
| | Average: | .67 ± .13 | .76 ± .07 | .093 | .42 | .52 | .36 |
| (9) | 4815.5 | 1.44 ± . 3* | 1.0 ± .13 | .081 | .40 | .50 | .38 |
| (11) | 5606.1 | .55 .16 | .53 ± .07 | | | | |
| | 5660.0 | .67 .16 | --- | | | | |
| | Average: | .61 ± .16 | .53 | .111 | .34 | .66 | .32 |
| (15) | 5014.0 | .80 ± . 2 | --- | --- | .63† | --- | --- |
| (38) | 5345.6 | .62 ± .13 | .78 ± .07 | | | | |
| | 5320.7 | --- | .66 ± .07 | | | | |
| | Average: | .62 ± .13 | .72 ± .05 | --- | .38 | .40 | .50 |
| (39) | 5212.6 | .62 ± .15 | --- | --- | .42 † | --- | --- |

† Author's estimates using hydrogenic ion value for radial matrix elements.

* Interference from CIλ4817.3 .

and PII are presented in Table XXI, along with predictions from Griem's older theory[7] and his current "semi-empirical"[52] formulation.

To include in these tables the predictions from the older theory is perhaps unnecessary, since it is now recognized that the semi-classical approach, that works well for moderately excited neutral lines, is inadequate to cope with lines of (first) ions where separations between levels are generally far greater (density of states are far less) than with neutrals, and where the ionic Coulomb field accelates perturbing charges. However, we include these older predictions as an aid for those wishing to scale the current results (for both A-values and halfwidths) into existing astrophysical curves of growth that were constructed with the aid of these older broadening predictions.

Table XX shows the current results for SII widths which are generally less than those of Bridges and Wiese by an additive factor of approximately .09Å . This is well inside the overlap of our joint tolerance estimates. We also agree qualitatively on two points. First, the width of λ4815.5 of multiplet (9) is anomalously large with respect to current theories: taken together with our joint findings that the relative strength for this line does not seem to favor either LS or intermediate coupling, this tends to support Bridges' suggestion of a misclassification for this multiplet. The second point of qualitative agreement is that the different members of multiplet (6) have widths differing by as much as .08Å (excluding λ5564.9 , which Bridges did not measure). Since .08Å is within the tolerance in either set of results, this difference in widths within the multiplet might easily be dismissed as scatter were it not for the fact that both experiments find the same pattern for relative widths within the multiplet. Adding .09Å to the current results for this multiplet brings them into nearly

perfect coincidence with Bridges' results. If these apparent .08Å differences between widths of lines in multiplet (6) are real, then they are more than a factor of 3 larger than expected[52] from the small energy separation between excited states of the multiplet.

We list three sets of predicted widths for the SII lines: these were calculated by Davis and Roberts[54] in accordance with the theoretical treatments of Griem[53], Cooper and Oertel[53], and Davis and Roberts[54]. While all three of these treatments have been more successful than the earlier calculations of Griem (1964), (based on the 1962 theory of Griem, Baranger, Kolb and Shen) in estimating widths of isolated ion lines[7], the three theories disagree as to whether elastic or inelastic collisions are responsible for most of the broadening.

Griem uses the Born approximation[52] to treat inelastic collisions; to treat elastic collisions he adopts semi-empirical Gaunt factors to extrapolate inelastic excitation cross sections to below threshold energies. In this treatment inelastic collisions will dominate the broadening for the lines of SII we study because the energy separations between perturbing and perturbed states is typically more that 1 eV: however, for some of the PII lines we study, energy separations are less than 0.1 eV and elastic collisions may dominate.

Cooper and Oertel use the straight-line paths of the earlier theory by Griem <u>et al</u>[7] for strong collisions, but for weaker collisions they adopt hyperbolic orbits to better describe the influence of the ionic attractive field. Elastic collisions typically contribute less than 10% to their total predicted widths.

Davis and Roberts also employ hyperbolic orbits to describe ion-electron collisions, but use <u>ab initio</u> calculations to estimate the

Table XXI. MEASURED STARK WIDTHS FOR STRONG ION LINES, INCLUDING COMPARISON WITH PREDICTED VALUES.

| Ion (Multiplet) | Average Plasma Temperature | λ(Å) | Full halfwidth (Å) at $N_e = 10^{17}$ $cm^{-3}$ | | |
|---|---|---|---|---|---|
| | | | This Experiment | Theory, Griem (1964) Ref.[7] | Theory, Griem (1968) Ref.[52] † |
| AℓII (16) | 12,000°K | 5593.2 | 1.4 ± .4 | 12.2 | 9.6 |
| SiII (4) (6) | 10,000°K | 5979.0 | 2.4 ± .4 | 1.1 | 2.2 |
| | | 5041.0 | 3.0 ± .4 | 1.5 | 3.2 |
| PII* (6) | 12,000°K | 5425.9 | .7 ± .4 | | |
| | | 5386.9 | .6 ± .4 | | |
| | | 5499.7 | 1.0 ± .5 | | |
| | | 5409.7 | .7 ± .4 | | |
| | | 5316.1 | .9 ± .5 | | |
| | | Average: | .78 ± .4 | .78 | 1.05 |
| (7) | | 5191.4 | 1.9 ± .4 | .55 | .94 |
| (10) | | 5253.5 | .8 ± .4 | .65 | 1.90 |
| (13) | | 4943.4 | 1.9 ± .5 | --- | 1.55 |

† Author's estimates based on hydrogenic ion radial matrix elements.

* Energy levels taken from W.C. Martin, J. Opt. Soc. Am. 49, 107 (1956).

contributions of elastic collisions. Their work suggests that elastic collisions will often considerably modify electron impact widths.

The current results do not consistently agree with any set of predictions to within estimated tolerance, even when we exclude λ4815.5 from the comparisons. The average ratio of predicted to observed widths is .71 for the theory of Griem, .93 for Cooper and Oertel, and .67 for Davis and Roberts. (Using the results of Bridges and Wiese these ratios become, respectively, .65, .89, and .62.)

The results in Table XXI show that .4Å is the typical tolerance obtained using 4Å slits. This is essentially the error from scatter that we anticipated at the beginning of this section. The .5Å tolerance on PII λ4943.4 reflects uncertainty in electron density: the two available scans are from plasmas hotter than 12,000°K, where the halfwidth of $H_\beta$ is difficult to measure because of excessive emulsion blackening at the peaks of the $H_\beta$ profiles.

Predicted Stark widths given in the table were calculated by the author using Griem's semi-empirical theory. To save labor we used the approximation that all broadening can be described in terms of interaction with the nearest dipole-allowed perturbing levels of the upper and lower states: according to Griem this approximation may overestimate the widths by as much as 10%.

Four out of seven of our results: SiII λ5979.0 , SiII λ5041.0 , PII λ5191.4 and PII 4943.4 , agree with these predicted widths to within experimental tolerance. The factor of 2 discrepancy between predicted and observed widths for multiplet (6) of PII only slightly exceeds the sum of our 50% experimental tolerance and the 35% uncertainty estimated for the theoretical value. However, our results for PI λ5253.5 and AℓII λ5593.2 disagree with theory by factors of 4 and 8, respectively.

Because the experimental values are too small with respect to theory, these anamalies cannot be attributed to blending with hypothesized unidentified lines. Two reasons that might cause theory to overestimate the AℓII λ5595.2 width are Debye shielding or misclassification of the line, but it does not appear that either of these can cause the factor of 8 discrepancy we observe.

At high electron densities the ionic field builds up a Debye sheath which effectively shields the ion from weak (large impact parameter) encounters with incident electrons. However, it is precisely these weak collisions which effectively induce transitions to the very close-lying perturbing levels. Griem shows[7] that Debye shielding becomes important for perturbing levels lying closer than $\hbar w_p$, where $w_p$ is the plasma frequency. The excited state of AℓII λ5593.2 is 235 $cm^{-1}$ (.029 ev) removed from its nearest dipole-allowed perturbing level, while our plasma frequencies (for plasmas containing Aℓ) never exceeded 90 $cm^{-1}$. Therefore Debye shielding is not expected to strongly influence the broadening of this line.

Now consider the sort of reclassification that would be required to lower the predicted width of AℓII λ5593 by a factor of 8. Griem's semi-empirical Gaunt factors are slow varying functions of the energy separation between perturbing and perturbed levels: so even if the two nearest perturbing levels according to present classifications were removed to infinity, the decrease in predicted broadening will be only a factor of 2, because of the great density of remaining perturbing levels. The radial matrix elements which enter into the predicted halfwidths scale with a quartic dependence on excited state effective principle quantum number, $n^*$ Lowering $n^*$ by $(8)^{\frac{1}{4}} = 1.68$ would make it smaller than the presently classified ground state for AℓII . Moreover, we recall that the A-value we determined for this line was twice as large as the Coulomb approximation

predicts. If AℓII λ5593 were presently misclassified, this evidence would suggest that the principle quantum number should in fact be larger.

### K. Relative Stark Widths of $H_\beta$ and $H_\gamma$ .

The Stark widths of the hydrogen Balmer lines have in recent years been subject to both theoretical[25,29,56,86,125-127] and experimental[29,55,65,128-132] study. There are two reasons for the special interest in the broadening of these lines: because they are frequently bright and tens of Ångstroms wide in laboratory plasmas, the ability to correlate their Stark widths with electron density makes them valuable non-interfering plasma diagnostic probes. Theoretically, these lines provide a rigorous test of proposed broadening models because the hydrogen wave functions are known exactly.

We confine our efforts to measuring the halfwidth of $H_\gamma$ relative to $H_\beta$ . Several authors[29,55,65,128-132] have already measured the halfwidth of $H_\beta$ as a function of electron density and found better than 5% agreement with predictions of Griem, Kolb and Shen.[56] While our attempts to over-determine the state of our plasma lead us, in effect, to duplicate these measurements, our results are not subject to an unambiguous interpretation. That is, comparing the electron densities deduced from the $H_\beta$ halfwidth and the Griem, Kolb, Shen theory with those deduced by applying the Saha-Boltzmann equations to measured temperatures and pressures, we found that for 56 runs (cf. Fig. 76):

$$\left[\frac{Ne(\lambda_{\frac{1}{2}} \text{ of } H_\beta)}{Ne(p,T)}\right]_{avg.} = 1.03 \ , \quad \frac{\sigma}{\sqrt{56}} = .02 \ .$$

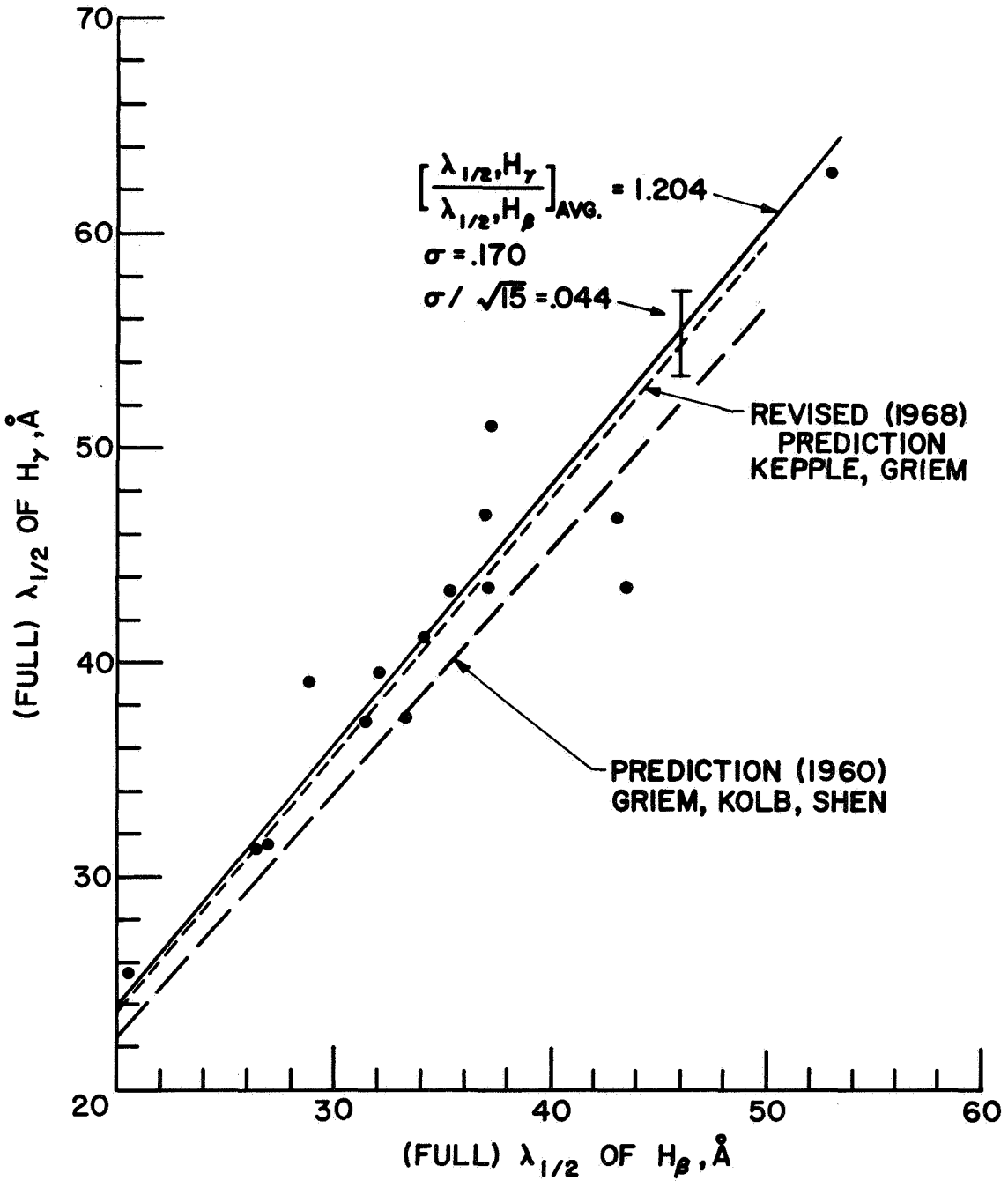


Fig. 76: Comparison of Measured Halfwidths of $H_\beta$ and $H_\gamma$

However, since the concentrations of readily ionized impurities boiled-off the shock tube walls is unknown, this good agreement might be due to theory underestimating the Stark broadening while we underestimate the impurity concentrations. Our results do indicate, at least, that the theory of Griem, Kolb and Shen does not overestimate the Stark width of $H_\beta$ by more than 3% in the electron density range studied.

For comparison of $H_\beta$ and $H_\gamma$ halfwidths, we do not need to know the exact composition of our plasmas. Moreover, previous studies of the relative $H_\beta$ and $H_\gamma$ halfwidths[29,55,65,128-132] disagree by as much as 25%, so results need not be reliable to better than 5% to offer a meaningful test of the theory.

During twenty of our experimental runs drum-camera spectrograms simultaneously recorded the profiles of $H_\beta$ and $H_\gamma$. On almost 1/3 of these spectrograms the emulsion density at the peak of $H_\beta$ was too great to permit reliable reduction to relative intensities, while on a few others plasma temperatures did not excite $H_\gamma$ to a brightness giving good signal-to-noise ratios over the entire profile. Utilizing densitometer scans of both first reflected and multiply reflected shocks, we did obtain fifteen pairs of $H_\beta$ and $H_\gamma$ profiles with good overall emulsion densities.

The full halfwidths of $H_\beta$ and $H_\gamma$ were read directly as the widths at half peak intensity, with no attempt to best-fit entire profiles to theoretically predicted shapes. The peak intensity of $H_\beta$ was taken to be the average of the red and blue peaks. Corrections were made routinely for both optical depth and the influence of the instrument profile: however, both these corrections together never amounted to more than 5% since the slit width was (nominally) 1Å while peak optical depths remained below 0.1.

The estimated uncertainty in the typical $H_\beta$ or $H_\gamma$ halfwidth is $\pm$ 10% . We believe most of this uncertainty is due to random reading error, especially in the choice of background intensities, rather than repeatable error. For our spectra there are no strong lines on the shoulders of either $H_\beta$ or $H_\gamma$ , and we could go arbitrarily far out on the wings to determine the continuum levels. The data conform to our a priori error estimate in two ways. The scatter in the ratio of $H_\beta$ to $H_\gamma$ halfwidths is about 15% , as one would expect if both halfwidths have 10% scatter, and 200°K scatter in $T_{\lambda\frac{1}{2}}$ (cf. Chapter VI, Section C-6 or Fig.43 ) corresponds to approximately a 10% scatter in the halfwidth of $H_\beta$ .

Our results for the full halfwidth of $H_\gamma$ as a function of the full halfwidth of $H_\beta$ are given in Fig. 76 . While data were collected from plasmas with electron densities between $3\times10^{16}cm^{-3}$ and $1.2\times10^{17}cm^{-3}$ , the majority of data came from plasmas with electron densities between $5\times10^{16}cm^{-3}$ and $8\times10^{16}cm^{-3}$. Plasma temperatures ranged between 10,500°K and 12,500°K with most runs grouping around 11,500°K.

Assuming the halfwidths of $H_\beta$ and $H_\gamma$ are linearly related over this range of source conditions, we find:

$$\left.\frac{\lambda_{\frac{1}{2}} \text{ of } H_\gamma}{\lambda_{\frac{1}{2}} \text{ of } H_\beta}\right|_{\text{avg.}} = 1.204 \pm .044$$

The .044 (3.7%) tolerance of our result is the uncertainty due to scatter. As seen in Fig. 76 , this result is 1% greater than the revised (1968) predictions of Kepple and Griem[86] and 7% greater than the (1960) predictions of Griem, Kolb and Shen.[56] The revised predictions take into account

perturbations to the lower state of $H_\gamma$ , which was not done in the earlier work, and also use different cut-off parameters (for weak collisions) and different ion distributions than were assumed in the 1960 predictions.

Because $H_\alpha$ was optically thick in our plasmas, no comparison was made between $H_\alpha$ and $H_\beta$ halfwidths. However, we did observe an apparent red shift in $H_\alpha$ . In one run using "pure" argon as a test gas the impurity level of hydrogen (boiled-off the shock tube walls) allowed us to record $H_\alpha$ in a multiply reflected shock with a peak optical depth less than .7. After correction for optical depth, $H_\alpha$ had a full halfwidth of 24Å $\pm$ 3Å , indicating an electron density of $3.8\times10^{17}cm^{-1} \pm .7\times10^{17}cm^{-1}$ . Using the superimposed spectrum of a neon Osram lamp we measured a red shift of 2.2Å for the peak of $H_\alpha$ .

# CHAPTER VIII

# CONCLUSIONS AND CRITIQUE

## A. Conclusions

We regard this work as a contribution to the field of astrophysics. Both stellar abundance and stellar atmosphere studies will benefit from the more than 200 transition probabilities presented. Because temperatures in our source resemble those of stellar chromospheres, the lines we measured should also be the lines which appear strong in the visual stellar spectra of CI , OI , NeI , AℓII , SiI , SiII , PI , PII , SI , SII and CℓI . For approximately half of these 200 lines our results give the first experimentally determined A-values: few of the lines studied have previously been measured more than once.

Two of the methods we have developed, thermally insensitive balancing (TIB) , and a new way to secure absolute photometric calibrations, should significantly assist the laboratory astrophysicist in the acquisition of more reliable A-values and the plasma physicist in the determination of conditions in high temperature gases.

The TIB method circumvents, in a simple way, the critical implicit thermal dependence usually found in the measured A-values of ions and light neutrals, long recognized as a major source of error in such determinations. This new method is quite general, being valid wherever the Saha-Boltzmann equations are valid and being useful wherever the relative composition of a multi-component plasma is known.

Moreover, in many cases TIB confers the additional advantage of allowing the spectroscopist to perform two relative intensity measurements instead of a more ardous (and often less reliable) measurement by absolute intensity measurement.

Because the new method of absolute intensity calibration requires a high intensity flash lamp, equipment costs are greater than for conventional methods relying on carbon arcs or tungsten filament lamps. However, for the growing number of plasma laboratories that already employ flash lamps for reversal temperature measurements, the new calibration method offers a valuable check on the conventional calibration, and in some cases, a superior alternative to it.

We now collect our results and compare them, collectively, with calculations in the Coulomb approximation and with some of the predictions of LS coupling.[119] The purpose of these comparisons is to make use of the fact that data for all eleven spectra were gathered in much the same way; i.e., since all data were gathered on the same instruments, sharing the same calibrations and methods of source diagnostics, and all A-values were deduced so as to minimize implicit thermal dependence, we expect our "trans-species" relative A-values to be more reliable than if these eleven spectra had been studied by eleven independent workers.

In particular we seek similarities in their behavior with respect to theory for transitions with the same configurations (e.g. 3s - 4p , 4s - 5p , etc.), for transitions in atoms with the same number of valence electrons (e.g. CI & SiI , or OI & SI ) and for transitions in the same isoelectronic sequences (e.g. SiI and PII , PI and SII ).

Fig. 77 shows the ratio of observed A-value to that predicted by the Coulomb approximation: $A_{mlt.}(obs.)/A_{mlt.}(ca.)$ , for 45 multiplets against an ad-hoc parameter $m$ . This parameter is intended to be an index of how hydrogenic the transitions are. The multiplets shown were measured in their entirety, or were missing no more than one of their weaker members whose absence was accounted for using LS coupling. Transitions involving equivalent electrons are excluded. The parameter

$$m \equiv (n_m^*)^2 \cdot (1-e^{-\tilde{\ell}}) \cdot |\sigma|$$

does not derive from rigorous quantum mechanical arguments but is contrived to be large when transitions are hydrogenic. Here $n_m^*$ is the effective quantum number of the lower state: at large values of $n_m^*$ there is less chance of strong interaction between the valence electron and other orbital electrons. The factor $(1-e^{-\tilde{\ell}})$ , where $\tilde{\ell} = \frac{1}{2}(\ell_n + \ell_m)$ , is included in recognition that s-state orbits are core-penetrating, while the factor $|\sigma|$ is included because radial matrix elements are inherently unreliable in the neighborhood of zeros.

The gross pattern of agreement with hydrogenic predictions has one important feature in common with a Coulomb-idealized situation: agreement is best for the most hydrogenic (largest $m$ ) transitions. Since the apparatus draws no distinction between hydrogenic and non-hydrogenic transitions -- tolerance estimates are based on photometric error, thermal dependence, etc., results of higher and lower accuracy

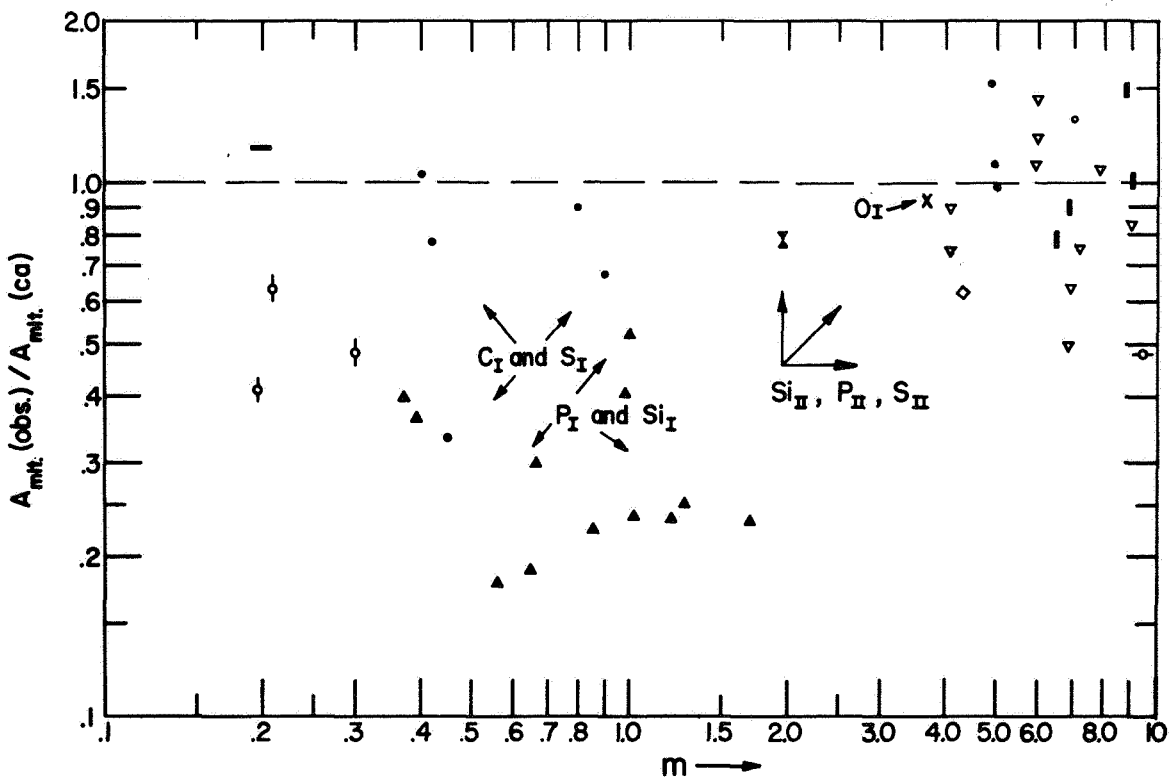


With increasing value of the ad hoc parameter m the transitions should become increasingly more hydrogenic and the coulomb approx. more reliable:

$$m \equiv (n_n^*)^2 \cdot (1-e^{-\tilde{\ell}}) \cdot |\sigma|$$

where: $\tilde{\ell} = \frac{1}{2}(\ell n + \ell m)$

Z = net atomic (ionic) charge (i.e. 1 for ions)

$$n_n^* = \left[\frac{(Z+1)^2 R}{E_\infty - En}\right]^{1/2}$$

n = lower state of transition

R = Rydberg constant

Multiplet origin:
- • 3s – 4p
- ▲ 4s – 5p
- ϕ 3s – 5p
- – 2p – 4p
- ▽ 4s – 4p
- -o- 4p – 4d
- I 4p – 5s
- X 4p – 5d
- ◇ 3s $3p^4$ – $3s^2$ $3p^2$ 4p
- x $2p^3$ 3p – $2p^3$ 6s

. 77: Comparison of Currently Measured Multiplet A-Values with Coulomb Approximation.

are equally distributed between the right and left sides of the figure. But agreement with theory is unmistakably better at the right hand margin where theory is most reliable.

If there is a tendency for the ratios $A_{mlt.}(obs.)/A_{mlt.}(ca.)$ to group together for spectra of such structure related pairs as CI and SiI , OI and SI , or the isoelectronic pairs SiI and PII or PI and SII , it cannot be significantly detected above the already mentioned dependence on m .

Fig. 77 shows one clear correlation between atomic structure and degree of adherence to Coulomb predictions: our results for 4s-5p transitions are markedly less than predicted values, regardless of whether the transitions belong to the spectra of SiI , PI or SI . This curious discrepancy is open to three distinctly different interpretations: either some quantum mechanical effect has an unexpectedly strong influence on transitions between these configurations, or, our results for these transitions are spurious by an average factor of 3, or the lines are presently misclassified.

We can suggest no quantum mechanical effects which might be responsible for this anomaly. While the 4s lower state configuration is expected to be core penetrating, our results for 4s-4p transitions agree well with Coulomb predictions.

While the misclassification of a single line, or even a group of close-lying multiplets, might not be outside of the realm of possibility, one cannot seriously entertain the suggestion that all 4s-5p transitions in three different elements have been misclassified, and in precisely the way necessary to give a consistent factor of 3 discrepancy with respect to Coulomb predictions.

Some workers regard a consistent disagreement between a particular set of results and the corresponding Coulomb predictions as de facto evidence of systematic experimental error. According to this view, consistent disagreement by a factor of 3, as in the present results for SiI , PI and SI , admits of no other interpretation. The estimated tolerances of our results for these three spectra are roughly an order of magnitude too small to cover the disparity with respect to Coulomb predictions. In assigning 15% and 20% tolerances to SI λλ4695 and SI λλ5279 , respectively, we have said all we can say about our certitude for these results. But we should comment on our (typically 35%) tolerances for PI and SiI results. Of all the transitions we studied ,those belonging to PI and SiI are most susceptible to error because they alone were deduced solely from AE (emission) measurements while the very small absolute concentrations of spectroscopic additives had to be deduced by the methods of Boldt . Even so, the tolerances assigned from the data on hand is to the best of our knowledge realistic: it is because the range of our data is less extensive than we would like for ferreting out systematic errors that we have some intuitive reservations about SiI and PI . That is, if we had collected data over a wider range of source conditions using a variety of spectroscopic additives and still found no systematic discrepancies within our data, our confidence in these results would have been stronger because possible systematic errors, as of now unrecognized, would have had a greater chance of being discovered. We should recall here that of the two previous experimental studies of SI , one agreed with our results to within a few percent while the other was a factor 1.7 larger than our result. The single SiI result available for comparison is a factor of 2 greater than our result.

TABLE XXII.

Relative line strengths within multiplets: present results compared with LS coupling.

| Multiplet | | ΔJ | λ(Å) | Relative line strength* LS coupling | This experiment |
|---|---|---|---|---|---|
| $Si_I$ | ( 9) | 2 -3 | 5797.9 | 21.0 | 15.5±10% |
| | | 1 -2 | 5793.1 | 11.25 | 14.7±10% |
| | | 0 -1 | 5780.4 | 5.00 | 8.6±10% |
| | | 2 -2 | 5859.2 | 3.75 | <1.4 -- |
| | (10) | 2 -2 | 5708.4 | 11.25 | 10.92±10% |
| | | 1 -1 | 5690.5 | 2.25 | 5.23±15% |
| | | 2 -1 | 5754.3 | 3.75 | .48±30% |
| | | 1 -0 | 5701.1 | 3.0 | 3.49±15% |
| | | 1 -2 | 5645.7 | 3.75 | 3.13±10% |
| | | 0 -1 | 5665.6 | 3.0 | 3.73±10% |
| | (11) | 2 -1 | 5684.5 | 5.0 | 7.50±10% |
| | | 1 -1 | 5622.2 | 3.0 | .50±30% |
| $Si_{II}$ | ( 2) | ½-1½ | 6347.1 | 4.0 | 3.71±15% |
| | | ½- ½ | 6371.3 | 2.0 | 2.29±15% |
| | ( 4) | 1½- ½ | 5978.9 | 4.0 | 3.58±10% |
| | | ½- ½ | 5957.6 | 2.0 | 2.42±10% |
| | ( 5) | 1½-2½ | 5056.0 } | 20.0 | 20.15±5% |
| | | 1½-1½ | 5056.3 } | | |
| | | ½-1½ | 5041.0 | 10.0 | 9.85±5% |
| $P_I$ | -- | 1½-1½ | 5015.8 | 4.0 | 2.45±25% |
| | | 2½-1½ | 5079.3 | 6.0 | 7.55±15% |
| | -- | ½-1½ | 5061.9 | 5.0 | 6.12±20% |
| | | 1½- ½ | 5098.2 } | 6.6 | 8.47±10% |
| | | 1½-1½ | 5100.9 } | | |
| | | 2½-2½ | 5109.6 | 12.6 | 9.54±20% |
| | -- | ½-1½ | 5458.3 | 10.0 | 8.25±20% |
| | | 1½-2½ | 5477.7 | 18.0 | 19.75±10% |
| $P_{II}$ | ( 5) | 2 -3 | 6043.1 | 21.0 | 24.55±15% |
| | | 1 -2 | 6024.1 | 11.25 | 7.93±15% |
| | | 1 -1 | 6087.8 | 3.75 | 3.52±15% |
| | ( 6) | 2 -2 | 5425.9 | 11.25 | 11.71±8% |
| | | 1 -1 | 5386.9 | 2.25 | 3.41±8% |
| | | 2 -1 | 5499.7 | 3.75 | 2.00±8% |
| | | 1 -0 | 5409.7 | 3.00 | 2.97±8% |
| | | 0 -1 | 5344.7 | 3.00 | 3.98±8% |
| | | 1 -2 | 5316.1 | 3.75 | 2.93±8% |
| | ( 7) | 2 -1 | 5296.1 | 5.0 | 7.32±10% |
| | | 1 -1 | 5191.4 | 3.0 | 1.55±10% |
| | | 0 -1 | 5152.2 | 1.0 | <.13 -- |
| | (13) | 3 -2 | 4943.4 | 21.0 | 25.70±10% |
| | | 2 -1 | 4969.6 | 11.25 | 8.26±15% |
| | | 1 -0 | 4954.3 | 5.0 | 2.73±10% |
| | | 1 -1 | 4927.0 | 3.75 | 4.31±15% |
| | (15) | 3 -4 | 4602.1 | 45.0 | 22.7±15% |
| | | 3 -3 | 4658.3 | 3.9 | 26.3±15% |
| | (23) | 2 -2 | 5450.7 | 11.25 | 9.21±15% |
| | | 1 -1 | 5507.1 | 2.25 | 3.48±15% |
| | | 2 -1 | 5583.3 | 3.75 | 3.46±15% |
| | | 1 -0 | 5541.2 | 3.0 | 2.20±15% |
| | | 1 -2 | 5378.1 | 3.75 | 4.08±10% |
| | | 0 -1 | 5483.6 | 3.00 | 4.57±15% |
| | (27) | 1 -2 | 5588.2 | 5.0 | 5.43±20% |
| | | 1 -1 | 5727.7 | 3.0 | 2.57±25% |

TABLE XXII. (CONTINUED.)

| Multiplet | | ΔJ | λ(Å) | Relative line strength* LS coupling | Relative line strength* This experiment |
|---|---|---|---|---|---|
| $S_{II}$ | ( 1) | 1½- ½ | 5027.1 | 4.0 | 3.21±8% |
| | | ½- ½ | 5142.3 | 2.0 | 2.79±15% |
| | ( 6) | 2½-3½ | 5453.6 | 24.0 | 22.23±7% |
| | | 1½-2½ | 5432.7 | 12.6 | 13.09±7% |
| | | ½-1½ | 5428.6 | 5.0 | 5.19±7% |
| | | 2½-2½ | 5564.9 | 5.4 | 3.77±10% |
| | | 1½-1½ | 5509.6 | 6.4 | 6.10±10% |
| | | ½- ½ | 5473.6 | 5.0 | 5.86±11% |
| | | 2½-1½ | 5645.6 | .6 | <2.24 -- |
| | | 1½- ½ | 5556.0 | 1.0 | 1.52±25% |
| | ( 7) | 2½-2½ | 5032.4 | 12.6 | 12.68±8% |
| | | 1½-1½ | 4991.9 | 1.6 | 3.50±8% |
| | | ½- ½ | 4942.4 | 1.0 | 1.30±15% |
| | | 2½-1½ | 5103.3 | 5.4 | 5.55±8% |
| | | 1½- ½ | 5009.5 | 5.0 | 4.44±8% |
| | | 1½-2½ | 4924.0 } | 10.4 | 8.52±8% |
| | | ½-1½ | 4925.3 } | | |
| | ( 9) | 2½-1½ | 4815.5 | 6.0 | 7.94±10% |
| | | 1½-1½ | 4716.2 | 4.0 | 2.54±10% |
| | | ½-1½ | 4656.7 | 2.0 | 1.52±20% |
| | (11) | 4½-3½ | 5606.1 | 50.0 | 37.70±10% |
| | | 2½-1½ | 5659.9 | 22.5 | 22.80±10% |
| | | 1½- ½ | 5664.7 | 14.0 | 13.19±10% |
| | | 3½-3½ | 5526.2 | 5.7 | 10.60±15% |
| | | 2½-2½ | 5578.8 | 7.3 | 7.3±10% |
| | | 1½-1½ | 5616.6 | 5.6 | 5.49±20% |
| | | 1½-2½ | 5536.7 | .29 | 6.54±20% |
| | | 2½-3½ ? | 5466.5 | .40 | <1.90 -- |
| | (15) | 1½-1½ | 5014.0 | 10.0 | 10.93±10% |
| | | ½- ½ | 4917.1 | 4.0 | 3.07±12% |
| | (38) | 2½-3½ | 5320.7 | 40.0 | 37.63±7% |
| | | 1½-2½ | 5345.6 | 28.0 | 30.37±7% |
| | (39) | 2½-2½ | 5212.6 | 28.0 | 31.45±10% |
| | | 1½-1½ | 5201.0 } | 20.0 | 16.55±10% |
| | | 2½-1½ | 5201.3 } | | |
| | (43) | 3½-2½ | 4463.5 | 24.0 | 23.23±25% |
| | | 2½-1½ | 4483.4 | 12.0 | 8.86±25% |
| | | 1½- ½ | 4486.6 | 5.0 | 9.51±25% |

*Experimental relative strengths are normalized against the multiplet sums of LS coupling predictions.

Comparison of observed line strengths within multiplets with predictions of LS coupling, given in Table XXII*, disclosed a generally better than 25% level of agreement punctuated by a few large discrepancies. Three departures from LS coupling are large enough to suggest misclassification: these occur in multiplet (11) of SiI, multiplet (15) of PII and multiplet (9) of SII . For relative A-values of the stronger lines within the spectrum of the same species the current results generally agree with previous studies to 10% - 15%.

B. Critique of the Experiments Design

In attempting to appraise the current experiment's design it can justifiably be asked whether the instrumentation was suitably or excessively elaborate to accomplish the preliminary objective of measuring the A-value of CI λ5052 to 10%. In particular, are both photographic and photoelectric recording necessary with a source as versatile as the conventional shock tube and when one has developed an independent means of checking carbon arc absolute intensity calibrations? And, why should four redundant temperatures be measured when the TIB method effectively removes the usual implicit A-value dependence on temperature?

To answer such hypothetical questions, we would recall that the redundant measurements disclosed many discrepancies, large and small, in our early results for CI λ5052 . How many of the systematic error sources thus discovered and remedied would have escaped eventual detection with less elaborate plasma diagnosis and photometry is problematical -- but the methods we did use allow us to meaningfully claim 10% overall tolerance for our prime result.

---

*In computing the LS predicted relative line strengths we assumed all members of the same multiplet had equal radial matrix elements and neglected the difference in wavelength for members of the same multiplet.

We also point out that once one gets over the initial hurdles of building and checking-out such a system, its potential for efficiently collecting very extensive data is unsurpassed. For instance, the sum of this authors' results and those of Bengtson* comes to well over 300 transition probabilities. While this number of lines might be found in the spectrum of a typical metal, they here in fact constitute a very substantial fraction of the stronger ($A_{mn} \geq 3\times10^5$ $sec^{-1}$) visible lines from the second and third rows of the periodic table that hitherto either had not been measured at all, or had been measured to reliabilities estimated as less than 50%.

## C. Suggestions for Future Work

The factor of 3 disparity between our PI and SiI results and theory calls for further investigation. If the current results are spurious, then the astrophysical importance of the SiI spectrum demands better values: if the current results are essentially correct, then theory must be updated. Future work on visible SiI spectra should include SiI λ3905 so that the relative A-values of Corliss and Bozman[48] can be utilized as transfer standards into the UV where the radiative lifetime studies of Lawrence and Savage[47] afford reliable SiI A-values for comparison. Solar abundance studies would also profit from the inclusion in future studies of the near - IR SiI lines: some of these are bright enough to compensate for the reduced sensitivity of IR detectors and should be measurable in laboratory sources giving useful brightness to visible SiI lines.

---

*With some modifications to the system we have described, Bengtson[61] obtained the first experimental A-values for FI, BrI, BrII, and the IR lines of CℓI ; his results also encompassed all the stronger visible lines of CℓI and CℓII.

Coming as they did from data never intended for the purpose, our results for Stark broadening (and shifting) hardly do justice, either quantitatively or qualitatively, to our system's capacity for the collection of such information. Moreover, recent development of a new generation of commercial spectrographs claiming both good resolutions and large apertures, together with the availability of faster films*, makes feasible studies of ion line broadening that can be both comprehensive in scope and yet highly accurate. The line broadening theory for ions can well use reliable data at this time[125] and it will be doubly valuable when collecting in a coherent fashion -- i.e., when a single spectrogram, or the output from a single day's operation of the same equipment, might yield data for two or even three different ions. In particular, we suggest starting with PII for time-resolved photographic broadening studies: its visible spectrum is rich in lines readily excitable in 1 eV thermal sources, many multiplets contain several resolvable members, and the predicted Stark broadening for different visible multiplets covers a range of 4 in halfwidth. Our own estimates of broadening have certainly not pre-empted PII as an object for study.

Another candidate for future broadening studies is AℓII, for whose λ5593 line we have observed an anomalously large disagreement with current ion broadening theory.

Three general areas of study that could effectively profit from the methods and techniques we have employed, and which are of sustained astrophysical interest, are: transition probabilities for first ions of the metals, and transition probabilities of the light elements and their first ions in both the near IR and near UV.

---

*For example, Kodak #2485.

## SELECTED BIBLIOGRAPHY


[1] Aller, L.H., Abundances of the Elements, Interscience, New York (1961).

Aller, L.H., Stellar Atmospheres, ed. Greenstein, p. 232, Chicago (1961).

[2] O'Mara, B.J., The Solar Abundance of Light Elements, Thesis U.C.L.A. (1967).

[3] Goldberg, L., Müller, E.A., and Aller, L.H., Ap. J. Suppl., 5, 45 (1960).

[4] Müller, E.A., and Mutschlecner, J.P., Ap. J. Suppl. 91, 1 (1964).

[5] Aller, L.H., The Atmospheres of the Sun and the Stars, Roland Press, New York (1963).

[6] Chandrasekhar, S., An Introduction to the Study of Stellar Structure, Dover, New York (1957).

[7] Griem, H.R., Plasma Spectroscopy, McGraw-Hill, New York (1964).

Cooper, J., Rep. Prog. Phys. 29, 35 (1966).

Robinson, D., and Lenn, P.D., Applied Optics 6, 983 (1967).

Foster, E.W., Rep. Prog. Phys. 27, 469 (1964).

[8] Pai, S.I., Radiation Gasdynamics, Springer, New York (1966).

[9] Kolb, A.C., and Griem, H.R., Chpt. 12 in Atomic and Molecular Processes, ed. D.R. Bates, Academic Press, New York (1961).

McWhirter, R.W.P., Chpt. 5 in Plasma Diagnostic Techniques, Academic Press, New York (1965).

[10] Wing, W.D., Am. Rocket Soc. 32, 90 (1962).

[11] Hunt, B.L., and Sibulkin, M., J. Quant. Spect. Radiat. Transfer 7, 261 (1962).

[12] Addink, N.W.H., Spectrochim Acta, 349 (1959).

[13] Wiese, W.L., Smith, M.W., and Glennon, B.M., Atomic Transition Probabilities, Vol. I: Hydrogen through Neon, Nat. Bur. St. Ref. Ser. 4 (1966).

Ibid. Vol. II: Sodium through Argon, to be published.

[14] Helliwell, T.M., The Nodal Boundary Condition Method Wave Functions and Transition Probabilities for Atoms with Two Valence Electrons, Thesis Cal. Inst. Tech. (1963).

[15] Bates, D.R. and Damgaard, A., Phil. Trans. Roy. Soc. (London) A242, 101(1949).

[16] Varsavsky, C.M., The Calculation of Absolute Line Strengths in Atomic Spectra, Thesis Harvard (1958).

[17] Glennon, B.M., and Wiese, W.L., Bibliography on Atomic Transition Probabilities, Nat. Bur. St. Misc. Pub. 278 (1966).

Ibid., Supplement for May 1966 through December 1967, (1968).

[18] Urey, H.C. The Abundance of the Elements with Special Reference to the Problem of Iron Abundance, Harold Jeffreys Lecture (1966).

[19] King, A.S., Ap. J. 37, 239 (1913).

[20] King, R.B., and King, A.S., Ap. J. 82, 377 (1935).

King, R.B., and Stockbarger, D.C., Ap.J. 91, 488 (1940).

[21] Rozhdestvenski, D.S., Trudy GOI, 2 (1922).

[22] Prokof'ev, V.K., Trudy GOI, 25, 1 (1924).

Prokof'ev, V.K., Trudy GOI, 2-3, 111 (1931).

[23] Allen, C.W., and Asaad, A.S., Month. Nat. Roy. Astron. Soc. 117, 36 (1957).

[24] Lochte-Holtgreven, W., p. 115 of Optical Spectrometric Measurements of High Temperatures, (ed. Dickerman, P.J.), U. of Chicago Press (1961).

[25] Bridges, J.M., Experimental Determination of Transition Probabilities and Stark Widths for SI and SII Lines, Thesis, Maryland (1966).

Bridges, J.M., and Wiese, W.L., Phys. Rev. 159, 31 (1967).

[26] Foster, E.W., Proc. Phys. Soc. (London) A90, 275 (1967).

[27] Wiese, W.L., Present Status of Our Knowledge of Atomic Transition Probabilities, Proc. X Colloquium Spectr. Interntl. (1962).

[28] Turner, E.B., The Production of Very High Temperatures in the Shock Tube with an Application to the Study of Spectral Line Broadening, Thesis, Michigan (1956).

[29] Doherty, L.R., The Measurement of Absolute Spectral Line Intensities with the Shock Tube, Thesis, Michigan (1962).

[30] Wilkerson, T.D., The Use of the Shock Tube as a Spectroscopic Source with an Application to the measurement of gf-Values for Lines of Neutral and Singly Ionized Chromium, Thesis, Michigan (1961).

[31] Charatis, G., Shock Tube Determination of Chromium gf-Values, Thesis, Michigan (1961).

[32] Brown, W.A., Phys. Fluids 9, 1273 (1966).

[33] Byard, P.L., J. Quant. Spectrose, Radiat. Transfer 7, 559 (1967).

[34] Parkinson, W.H., and Nicholls, R.W., Shock Tube Spectroscopy III: Temperature and Intensity Measurements in a Shock Tube, U. of Western Ont. Phys. Dept. Report, AFCRC-TN-59-662 (1959).

[35] Christian, R.H., and Yarger, F.L., J. Chem Phys. 23, 2042 (1955).

Seay, G.E., Los Alamos Sci. Lab. Rep. No. LAM-2125 (1957).

[36] Fowler, R.G., Goldstein, J.S., and Clotfelter, B.E., Phys. Rev. 82, 879 (1951).

Sakuntala, M., Clotfelter, B.E., Edwards, W.B., and Fowler, R.G., J. Appl. Phys. 30, 1669 (1959).

Griem, H.R., and Klob, A.C., J. Quant. Spectrosc. Radiat. Transfer. 2, 503 (1962).

[37] Lawrence, G.M., Radiative Lifetimes in ArI, II Interntl. Confr. on VUV and X-Ray Spectrosc., (1968).

[38] Klose, J., Phys. Rev. 141, 181 (1966).

[39] Heron, S., McWhirter, R.W.P., Rhoderick, E.H., Proc. Roy, Soc. (London) A234, 565 (1956).

Lawrence, G.M., and Savage, B.D., Phys. Rev. 141, 67 (1965).

[40] Bashkin, S., Wangsness, R.K., Heroux, L., Phys. Rev. 151, 87 (1966).

[41] Landau, L.D., and Lifshitz, E.M., Quantum Mechanics, Non Relativistic Theory, Addison Wesley, Reading Mass. (1958).

[42] Hinnov, E., Kohn, H., J. Opt. Soc. Am. 47, 156 (1957).

Kuhn, H.G., and Vaughan, J.M., Proc. Roy. Soc. (London) 277, 297 (1963).

[43] Garton, W.R.S., Autionization Considered in Relation to Excitation and Electron Capture Processes, in the Thershold of Space (ed. Zelikoff, M.), Pergamon, New York (1956).

[44] DeZafra, R.L., and Kirk, W., Am. J. Phys. 35, 573 (1967).

[45] Gallagher, A.G., Phys. Rev. 157, 24 (1967).

[46] Aller, A.H., and Jugako, J., Ap. J. Suppl. 38, Art. 8-7 (1959).

[47] Lawrence, G.M., Ap. J. 148, 261 (1967).
Savage, B.D., and Lawrence, G.M., Ap. J. 146, 940 (1966).

[48] Corliss, C.H., and Bozman, W.R., Nat. Bur. Stand. Monog. 53 (1962).

[49] Woodgate, B., Mont. Nat. Roy, Astron. Soc. 134, 287 (1966).

[50] Slavenas, I.Y.Y., Optics and Spectrosc. (USSR) 16, 214 (1964).

[51] Bengtson, R., The Measurement of Transition Probabilities and Stark Widths in CI, FI, NeI, CℓI, CℓII, BrI and BrII, Thesis, U. of Maryland, in preparation.

[52] Griem, H.R., Phys. Rev. 165, 258 (1968).

[53] Cooper, J., and Oertel, G., Phys. Rev. Letters 18, 985 (1967).

[54] Davis, J., and Roberts, D.E., Proc. Phys. Soc. 92, 889 (1967).

[55] Hill, R.A., and Gerardo, J.B., Phys. Rev. 162, 45 (1967).

[56] Griem, H.R., Kolb, A.C., and Shen, K.Y., Phys. Rev. 116, 4 (1959).
Griem, H.R., Kolb, A.C., and Shen, K.Y., Stark Broadening of Hydrogen Lines in a Plasma, NRL Report 5455 (1960).

[57] Ladenburg, R., and Levy, S., Z. Physik 65, 189 (1930).

[58] Griem, H.R., Phys. Rev. 128, 997 (1962).

[59] Koopman, Computer Programs for the Calculation of Equilibrium States in Reflected Shock Plasmas, U. of Maryland Tech. Note BN-481 (1966).

[60] Rouse, C.A., Ap. J. 134, 435 (1961).

[61] Bengtson, R., A Spectroscioic Study of a Shock Excited Ablator, MS Thesis Virginia Polytech. Inst. (1964).

[62] Davidson, N., Statistical Mechanics, McGraw-Hill, New York (1962).

[63] Day, R., Measurement of the Stark Widths and Shifts for Nitrogen Ion Lines, Thesis, U. of Maryland (1965).

[64] Davies, J.T., and Vaughn, J.M., Ap. J. 4, 1302 (1963).

[65] Linke, R., Measurement of the Oscillator Strength of the Neutral Helium Resonance Line, Thesis, U. of Maryland (1964).

[66] Böldt, G.Z., Z. Naturforsh 18a, 1107 (1963).

[68] Laporte, O., and Wilkerson, T.D., J. Opt. Soc. Am. 50, 1293 (1960).

[69] Wright, J.K., Shock Tubes, Wiley, London (1961).

[70] Glass, I.I., and Hall, G., Shock Tubes, Sect. 18 of Handbook of Supersonic Aerodynamics, NAVORD Report 1438, Vol. 6 (1959).

[71] Gaydon, A.G., and Hurle, I.R., The Shock Tube in High Temperature Chemical Physics, Chapman Hall, London (1963).

[72] Bradley, J.N., Shock Waves in Chemistry and Physics, Methuen, London (1962).

[73] Blackman, V.G., Tech. Report II-20, Princeton Univ. Dept. of Phys. (1963).

[74] Resler, E.L., Lin, S., and Kantrowitz, A., J. Appl. Phys., 23, 1390 (1952).

[75] Wilkerson, T.D., Koopman, D., Miller, M., Bengtson, R., and Charatis, G., Atomic Spectroscopy with the Shock Tube, U. of Maryland Tech. Note. BN-508 (1967): to be published in Phys. Fluids.

[76] Courant, R. and Fredrics, K.O., Supersonic Flow and Shock Waves, Interscience, New York (1948).

[77] Guggenheim, E.A., Boltzmann's Distribution Law, North Holland, Amsterdam (1959).

[78] Simpson, C.J.S.M., Chandler, T.R.D., and Bridgeman, K.B., Phys. Fluids 10, 1894 (1967).

[79] Glöck, E., Proc. VII Intenatl. Confr. on Phenomena in Ionized Gases, Belgrade (1965).

[80] Charatis, G. and Hershey, T.L., U. of Maryland Tech. Note BN-361 (1964).

[81] Chelsea Instruments, 470 Kings Road, London SW-10.

TWR Instruments, 139 Illinois St. El Segundo, Calif.

[82] Garton, W.R.S., J. Sci. Instr. 30, 119 (1953).

Garton, W.R.S., and Rajaratnam, A., Proc. Roy, Soc. (London) A70, 815 (1957).

Garton, W.R.S., Parkinson, W.H., and Reeves, E.M., Proc. Phys. Soc. 88, 771 (1966).

[83] Charatis, G., and Wilkerson, T., Phys. Fluids 5, 1661 (1962).

[84] Faizullov, F.S., Sobo'lev, N.N. and Kudryautsev, E.M., Optics and Spectrosc. (USSR) 8, 311 (1960).

[85] Carnavale, E.H., Wolnik, S., Lason, G., Carey, C., and Wares, G.W., Phys. Fluids, 10, 1459 (1967).

[86] Kepple, P., and Griem, H.R., to be published in Phys. Rev.

[87] Griem, H.R., private communication.

[88] Hattenburg, A.T., Appl. Optics 6, 95 (1967).

[89] Macpherson, H.G., J. Opt. Soc. Am. 30, 189 (1940).

[90] Euler, J., Ann. der Physik 14, 145 (1954).

[91] Null, M.R., and Lozier, W.W., J. Opt. Soc, Am. 52, 1156 (1962).

[92] Mees, C.E.K., The Theory of the Photographic Process, Macmillan, New York (1954).

Crosswhite, H.M., and Dicke, G.H., Simplified Techniques for Calibrating Photographic Emulsions, Johns Hopkins Univ. Bumblebee Rep. 202 (1953).

[93] Turner, E.B., Chpt. 7 in Plasma Diagnostic Techniques, (ed. Huddlestone, R.H. and Leonard, S.L.), Academic Press, New York (1965).

Sawer, R.A., Experimental Spectroscopy, Dover, New York (1963).

[94] Solarski, J., and Wiese, W.L., Phys. Rev. 135, 1236 (1964).

[95] Sampson, D.H., Radiative Contributions to Energy and Momentum Transfer in a Gas, Interscience, New York (1965).

Sampson, D.H., Criteria for the Validity of Local Thermodynamic Equilibrium, TIS Report R64SD90 (1964).

[96] Wilson, R.J., J. Quant. Spectrosc. Radiat. Transfer 2, 477 (1962).

[97] Oxenius, J.J., J. Quant. Spectrosc. Radiat. Transfer 7, 837 (1967).

McWhirter, R.W.D., Chpt. 5 in Plasma Diagnostic Techniques, (ed. Huddlestone, R.H., and Leonard, S.L.), Academic Press, New York (1965).

[98] Griem, H.R., Phys. Rev. 131, 1170 (1963).

[99] Slater, J.C., Quantum Theory of Atomic Structure, Vols. I and II, McGraw-Hill, New York (1960).

[100] Condon, E.U., and Shortley, G.H., The Theory of Atomic Spectra, Cambridge (1963).

[101] Candler, C., Atomic Spectra, Hilger and Watts, London (1964).

[102] Shore, B.W., and Menzel, D.H., Principles of Atomic Spectra, Wiley, New York (1968).

[103] Oertel, G., and Shomo, L.P., Ap. J. Suppl. 145 (1968).

[104] Menzel, D.H., and Pekeris, C.L., Month.Not. Roy, Astron. Soc. (London) 96, 77 (1935).

[105] Moore, C.E., A Multiplet Table of Astrophysical Interest (Revised Edition), Nat. Bur. Stds. Tech. Note 36 (1959).

[106] Richter, J., Z. Physik 151, 114 (1958).

[107] Foster, E.W., Proc. Roy. Soc. (London) 80, 882 (1962).

[108] Foster, E.W., Proc. Roy. Soc. (Lon on) 79, 94 (1962).

[109] Maecker,H., Z. Physik 135, 13 (1953).

[110] Garstang, R.H., Month. Not. Roy. Astron. Soc. 114, 118 (1954).

[111] Hey, P., zZ. Physik 157, 79 (1959).

[112] Woodgate, B., Month. Not. Roy. Astron. Soc. 134, 287 (1966).

[113] Kiess, Nat. Bur. Stds. J. Res. 21, 185 (1938).
Radziemski, L.J., and Andrews, K.L., J. Opt. Soc. Am. 55, 474 (1965).

[114] Bates, D.R., and Damgaard, A., Ap. J. 107, 383 (1948).

[115] Froese Fischer, C., Ap. J. 151, 759 (1968).
Underhill, A.B., and Froese, C., Ap. J. 146, 301 (1966).

[116] Martin, W.C., J. Opt. Soc, Am. 49, 107 (1959).

[117] Sax, N.I., Handbook of Dangerous Materials, Rheinbold, New York (1951).

[118] Smith, M.W., private communication.

[119] Goldberg, L., Ap. J. 82, 1 (1935).
Allen, C.W., Astrophysical Quantities, Althane, Loneon (1955).

[120] Jürgens, G., Z. Physik 138, 613 (1954).

[121] Murphy, P.W., private communication.

[122] Wiese, W.L., Chpt. 6 in Plasma Diagnostic Techniques (ed. Huddlestone, R.H., and Leonard, S.L.), Academic Press, New York (1965).

[123] Wiese, W.L., and Murphy, P.W., Phys. Rev. 131, 2108 (1963).

[124] Griem, H.R. and Shen, C.S., Phys. Rev. 125, 196 (1962).

[125] Doherty, R.L. and Turner, E.B., Ap.J. 60, 158 (1955).

[126] Bogen, P., Z. Physik 149, 62 (1957).

[127] Traving, G., Uber die Theorie der Druckverbrieterung von Spektrallinien, Braun, Karlsruthe, 1960.

[128] Berg, H.E., Ali, A.W., Linke, R., and Griem, H.R., Phys. Rev. 125, 199 (1962).

[129] Wiese, W.L., Paquette, D.R., and Solarski, J.E., Phys. Rev. 129, 1225 (1963).

[130] McLean, E.A. and Ramsden, S.A., Phys. Rev. 140, 1122 (1965).

[131] Frerichs, R., Z. Physik 80, 150 (1933).